Realization of ultrathin Copper Indium Gallium Di-selenide (CIGSe) solar cells

Zacharie Jehl

Thèse de doctorat de l'Université Paris Sud-Orsay (Paris XI)

ED MIPEGE - Modélisation et Instrumentation en Physique, Energies, Géosciences et Environnement

Présentée par

Zacharie Jehl Li Kao

pour l'obtention du grade de docteur de l'Université Paris XI

Elaboration of ultrathin Copper Indium Gallium Di-Selenide based Solar Cells

Présenté, le 4 avril 2012 devant le jury composé de :

Abdelilah Slaoui	Rapporteur
Nicolas Barreau	Rapporteur
Michael Powalla	Examinateur
Marc Burgelman	Examinateur
Isabelle Gérard	Examinatrice
Jean-Paul Kleider	Président
Negar Naghavi	Co-Directrice de thèse
Daniel Lincot	Directeur de thèse

Acknowledgements

The making of this thesis would not have been possible without Dr. Daniel Lincot, my PhD director. I am grateful for his remarkable scientific culture, his innovative ideas and his ability to express complicated concepts with simple sentences. I am thankful to Dr. Negar Naghavi, coordinator of the UltraCis project and co-director of this study. She supported me and encouraged me during the harsh times that every PhD student goes through. Her knowledge of alternative buffer layers was precious, and she spent hours and hours to review my articles and this thesis.

I wish to thank Dr. Abdelilah Slaoui and Dr. Nicolas Barreau for accepting to review this thesis. I know that they both are very busy scientists with many responsibilities and i really appreciate that they took time working on this thesis. I am also very happy that Dr. Michael Powalla could join the jury. Having such renowned person in the jury is an honor. Similarly, it is a real honor that Dr. Marc Burgelman is part of the jury. I worked for three years using the software that he and his team designed, and so I am thankful both for his presence, and his indirect scientific contribution. I gratefully thank Dr. Jean Paul Kleider for being part of the jury; his expertise in the field of electrical characterizations is precious to bring new insights on this thesis. And finally, I am more than thankful to Dr. Isabelle Gérard both for being part of this thesis jury, and for her work during the UltraCis project. She taught me the CIGSe etching technique, without which this thesis would not even exist. I also acknowledge Dr. Jean-François Guillemoles, for his advices, explanations, and general scientific contribution to this study. I particularly appreciated his availability and constant good mood. I am more than thankful to Dr. Felix Erfurth who was a post-doc at IRDEP for one year, and worked in close collaboration with me. His scientific qualities, hard work, and enthusiasm led us to significant breakthrough.

I would like to thank all the partners involved in the UltraCis project: “Institut Lavoisier de Versailles”, “Laboratoire de Photonique et Nanostructures”, “Laboratoire de Génie Electrique de Paris”, “Würth Solar/ZSW”, and last but not least, the “Laboratoire Charles Fabry” of “Institut d'Optique”; thank to their work, original ideas and collaboration with us, we were able to move forward with this project. I particularly thank Dr. Nir Dahan from “Institut d'Optique” who I worked with for the past two years. I appreciate you both as a scientific and as a person. I also acknowledge Dr. Jean Rousset from IRDEP, who worked with me in the

beginning of this thesis on the Zinc Oxide nanorods subject. I really had a great time with you.

Je remercie toute les personnes que j'ai pu côtoyer à l'IRDEP ces trois dernières années et tout particulièrement Arthur Lebris, inventeur de la contrepèterie la plus drôle depuis celle du Fakir, Frédérique Donsanti, dont l'aide fut précieuse dans les labos et la compagnie agréable à l'extérieur, Marie Jubault, ma "voisine d'en face" avec qui j'ai pu partager ma passion de la Nu-Soul, Myriam Paire, qui ne sait toujours pas calculer un pH, Jacqueline Destombes, dont la patience à mon égard concernant toutes les démarches administratives force le respect, et enfin Servane Haller, pour tant de choses que je n'aurais pas assez de ces 270 pages.

J'ai la chance d'avoir une famille qui s'est toujours souciée de moi, et je les remercie pour tout car ils sont à n'en pas douter la meilleur part de moi même. Merci à mes Grands Parents, merci à mon Frère, merci à mon Père et à ma Mère, et bien sur à tout(e) mes Cousin(e)s (Thierno, Simon, Nastunia, Jess…), Oncles, Tantes. J'ai une pensée toute particulière pour ma grand mère J. Li-Kao qui hélas n'aura pas vu cette thèse s'achever.

Mes amis sont tous une part très importante de ma vie et leur présence, certains depuis plus de 23 ans, m'a sans aucun doute apportée la stabilité et l'équilibre nécessaire pour achever mes études. Pape aka « Man of Stile », Sadat aka « Mâle Alpha», Menad aka « Le meilleur d'entre nous », Bren-ya aka « Bren de la P-loche », François aka « Freaka », Benjamin aka « casse toi que je mate mon Berserk », Jeff aka « Swagg-man », Harry aka « la Suisse », Hervé aka « Kyano_Thunderfury », Oumar aka « le mec balaise », André aka « B3NTO », Lev aka « le mec qui jette des pizzas par la fenêtre », Gihan aka « le futur marié », Habib aka « Satan », Baptiste aka « le dragueur de la tour C », ainsi que tout ceux que je n'ai pas la place de citer (Maxime, Christophe, Jean-Jacques etc. je vous ai pas oublié!). Merci, pour tout, et pour le reste. Je remercie également Bernard et Jean-Christophe, mes voisins profs! Et enfin, je remercie Wilaï, pour tout.

GENERAL INTRODUCTION **9**

MOTIVATION **9**

SCIENTIFIC APPROACH **10**

CHAPTER I: **13**

STATE OF THE ART **13**

I) THE COPPER INDIUM GALLIUM DISELENIDE ($Cu(In,Ga)Se_2$) SOLAR CELL **14**

II) STATE OF THE ART IN THINNING OF CIGSE ABSORBER **19**

CHAPTER II **27**

THEORETICAL ANALYSIS: EFFECT OF THINNING OF CIGSE ABSORBER LAYERS ON SOLAR CELLS CHARACTERISTICS AND POTENTIAL IMPROVEMENTS FOR ULTRATHIN DEVICES **27**

II.1) INTRODUCTION **28**

II.2) MODELING OF A STANDARD CIGSE SOLAR CELL **29**

II.2.A) DEFINITION OF THE INPUT PARAMETERS 29

II.2.B) MODELING OF CURRENT-VOLTAGE AND SPECTRAL RESPONSE 33

II.3) INFLUENCE OF CIGSE THICKNESS ON PHOTOVOLTAIC PARAMETERS **35**

II.3.A) MODELING OF THE CURRENT-VOLTAGE CURVES 35

II.3.B) MODELING OF SPECTRAL RESPONSES 40

II.3.C) CONCLUSION 43

II.4) ANALYSIS OF POTENTIAL IMPROVEMENTS FOR ULTRATHIN CIGSE SOLAR CELLS **45**

II.4.A) INTRODUCTION 45

II.4.B) FRONT AND BACK SIDE OPTICAL ENGINEERING FOR EFFICIENT LIGHT MANAGEMENT 45

II.4.C) REDUCTION OF THE BACK CONTACT RECOMBINATION BY ENERGY BAND ENGINEERING 49

II.4.D) POTENTIAL IMPROVEMENTS FOR AN ULTRATHIN 100 NM CIGSE SOLAR CELL 58

II.5) CHAPTER CONCLUSION **62**

CHAPTER III 67

EXPERIMENTAL RESULTS ON CHEMICALLY ETCHED THIN OF CIGSE ABSORBERS LAYER; SOLAR CELLS ELABORATION AND CHARACTERIZATIONS 67

III.1) INTRODUCTION 68

III.2) STATE OF THE ART IN THINNING OF CIGSE ABSORBERS 69

III.3) CHEMICAL ETCHING OF CIGSE 76

III.3.A) EXPERIMENTAL SETUP 76

III.3.B) RESULTS 77

III.4) CHARACTERIZATION OF ETCHED CIGSE FILMS 82

III.4.A) MATERIAL CHARACTERIZATION 82

III.4.B) OPTICAL CHARACTERIZATION OF ETCHED CIGSE FILMS AND SOLAR CELLS BY SPECTROSCOPIC REFLECTIVITY AND PHOTOLUMINESCENCE 94

III.5) ELECTRICAL CHARACTERIZATION OF CIGSE SOLAR CELLS WITH ABSORBER THINNED BY CHEMICAL ETCHING 101

III.5.A) EXPERIMENTAL SETUP 101

III.5.B) CURRENT-VOLTAGE CHARACTERIZATION 102

III.5.C) SPECTRAL RESPONSE 106

III.5.D) CONCLUSION 110

III.6) INFLUENCE OF THE SURFACE ROUGHNESS ON THE CIGSE SOLAR CELLS 111

III.6.A) DEVICE CHARACTERIZATION 111

III.6.B) DISCUSSION 115

III.6.C) ANALYTICAL EXPRESSION OF THE SPECTRAL RESPONSE 118

III.6.D) CONCLUSION 122

III.7) CHAPTER CONCLUSION 124

CHAPTER IV 127

FRONT CONTACT ENGINEERING OF THIN CIGSE SOLAR CELLS 127

IV.1) INTRODUCTION 128

IV.2) STATE OF THE ART 130

IV.2.a) Anti-reflecting coating layers 130
IV.2.b) Light scattering effect by texturation of the front ZnO:Al window 132
IV.2.c) Alternative ZnS/(Zn,Mg)O buffer layer for CIGSe solar cells 142
IV.2.d) Conclusion 144
IV.3) Experimental Results 145
IV.3.a) Light scattering and antireflection effect for ultrathin CIGSe solar cells by ZnO:Al chemical texturation and electrodeposition of ZnO nanorods 145
IV.3.b) Comparative study between standard CdS and alternative ZnS buffer layers on chemically thinned CIGSe absorber solar cells 164
IV.4) Chapter Conclusion 169

CHAPTER V 171

BACK CONTACT ENGINEERING FOR THIN AND ULTRATHIN ABSORBER CIGSE SOLAR CELLS 171

V.1) Introduction 172
V.2) State of the art 174
V.2.a) Metallic back contact 174
V.2.b) Transparent back contact 181
V.2.b) Conclusion 184
V.3) Metallic back contact 185
V.3.a) Introduction 185
V.3.b) Experimental 185
V.3.c) Chemical analysis of the Mo/CIGSe back contact interface 188
V.3.d) Optical characterization of the Mo/CIGSe interface and alternative back contact interface 191
V.3.e) Electrical characterization by Transmission Line Measurements of the metal/CIGSe interface for different metals 194
V.3.f) Electrical characterization of thin absorber solar cells with Au back contact and comparative study with standard Mo back contact 199
V.3.g) Conclusion 207
V.4) Transparent back contact based on ZnO:Al 208
V.4.a) Introduction 208

V.4.b) Electrodeposited thin Cu layer at the CIGSe/ZnO:Al interface 210
V.4.c) Electrodeposited Cu_2O interfacial buffer layer 216
V.5) Ultrathin CIGSe solar cell with lambertian light scattering back reflector 220
V.5.a) Optical simulation of a 100 nm CIGSe slab with lambertian back reflection 221
V.5.b) Light absorption in an ultrathin 200 nm CIGSe solar cell structure 223
V.5.c) Conclusion 228
V.6) Chapter Conclusion 229

GENERAL CONCLUSION AND PERSPECTIVES 233

REFERENCES 241

APPENDIX 253

I) Modeling parameters of the reference solar cell 253
II) Characterization tools 260
Scanning Electron Microscopy (SEM) 260
Atomic Force Microscopy (AFM) 260
X-Ray Photoelectron Spectroscopy 261
Electrical Characterization 262
III) State of the art insights for ZnS/(Zn,Mg)O) deposition 264
IV) Optical simulation of a solar cell stack using the radiative transfer equation 267

General Introduction

Motivation

Copper indium gallium diselenide ($CuIn_{1-x}Ga_xSe_2$ or CIGSe) solar cells present the highest conversion efficiency ever reported in thin film technology, with a record value of 20.3% recently reported by ZSW [1]. Over the past decade, the CIGSe field experienced an increasing industrial development with the commercialization of high efficiency modules [2]. It is now considered as one of the most promising alternative technology to silicon-based solar cells, and to meet the production milestone of 0.5 $ per watt for cost parity with other energy sources. In the scope of increasing the development of the CIGSe technology up to the Giga-Watt, the issue of possible material scarcity arises. While copper and selenium are abundant materials, gallium and more importantly indium are limited resources, and their availability may become a problem for future development of CIGSe-based solar cell [3]; moreover, indium is already a widely used material for indium tin oxide (ITO) production which is strongly related to the overwhelming flat screen industry. Therefore, the future of the CIGSe technology seems closely tied with the question of materials savings.

In this scope, several alternatives have been proposed in the recent years, such as replacing In and Ga by more abundant materials such a Zn and Sn (kesterite material). Although recent improvements have been achieved (with efficiencies up to about 11% [4]), the efficiency of these solar cells is still 2 times lower than record CIGSe solar cells. Another idea to reduce the material utilization in CIGSe solar cells is to reduce their dimensions, either by reducing the lateral dimensions [5] of the device, or the thickness of the device. In recent review [3], V. Fthenakis suggested that an extensive R&D is needed on developing thinner layers, which has not been sufficiently studied so far.

In this PhD thesis, we will focus on developing CIGSe solar cells with very thin and ultrathin absorber layers, down to 100-200 nm, while the standard thickness of CIGSe layers is 2500 nm. Besides using 25 times less indium in the fabrication of a solar cell, such an achievement will markedly reduce the deposition time of the material, and thus significantly increase the throughput of the process and the machinery utilization, leading major cost reduction.

However, the competitiveness of the CIGSe material relies on its high efficiency compared to other thin film technologies; therefore, the reduction of the CIGSe absorber thickness must not be linked to an efficiency decrease of the solar cell. It is thereby necessary to develop innovative theoretical and experimental designs that could allow to maintain the efficiency of ultrathin absorber solar cells at the same level as the current thick absorber solar cells. The main objective of our researches is to propose new front contact and back contact engineering on ultrathin absorber solar cells, to overcome the various efficiency limitations that exists when reducing the CIGSe thickness in a solar cell. For that, we will propose a novel approach combining chemical etching of the absorber, and low temperature back contact processing.

Scientific approach

In the first Chapter of this thesis, we will introduce the general state of the art of thinning the CIGSe absorber for very thin and ultrathin solar cells, with a short overview of the available literature on this subject. In a second Chapter, we will study from a theoretical point of view the effect of reducing the absorber thickness in a CIGSe solar cell by using numerical tools (SCAPS, and optical simulation). New solution to increase the performances of the very thin and ultrathin absorber CIGSe solar cells will be proposed, and theoretically evaluated. In the third Chapter of this thesis, we will experimentally reduce the CIGSe thickness using a chemical bath etching based on a bromine solution. The resulting CIGSe films will be characterized by various tools in order to evaluate the chemistry, the crystallinity, the composition and the optical properties of the etched CIGSe films. Solar cells with very thin and ultrathin absorber thickness down to 200 nm will be realized and electrically characterized, in order to compare the experimental photovoltaic parameters with our simulations. In Chapter IV, we will investigate on the front contact engineering to improve the light absorption of very thin absorber CIGSe solar cell. Various solutions will be tested, including the introduction of new materials in the stack and nanostructuration of layers. In the final Chapter (V), we will study the back interface engineering of very thin and ultrathin absorber CIGSe solar cell. We will propose an innovative methodology for the replacement of the back contact of the CIGSe solar cell by alternative materials and structures, and demonstrate the feasibility of high efficiency ultrathin devices with proof of concept devices. At the beginning of each chapter, a specific state of the art of the current literature on the topic will be presented, in complement of the short overview from Chapter I.

Chapter I:

State of the art

I) The Copper Indium Gallium DiSelenide ($Cu(In,Ga)Se_2$) solar cell

Copper indium gallium diselenide ($CuIn_{1-x}Ga_xSe_2$ or CIGSe) solar cells is a multi layer thin film technology which has been increasingly developed in the last decade thanks to its relatively low cost combined with high efficiencies [1,6]. CIGSe is a direct bandgap semiconductor with a chalcopyrite structure, a p-type doping and a bandgap varying continuously with the gallium content x from about 1 eV (for pure $CuInSe_2$) to about 1.7 eV (for pure $CuGaSe_2$). Thanks to the very high absorption coefficient of more than $10^5.cm^{-1}$ for 1.5 eV and higher energy photons [7], CIGSe solar cells require a much thinner film (~2 μm) than most of the other semiconducting materials. Although alternative plastic or metallic substrate can be used [8,9], we focus in this work on the study of CIGSe solar cells deposited on soda lime glass (SLG) which is both the most widely used substrate and the one giving the best efficiencies. The solar cell stack is presented figure 1. A Mo layer is deposited on the glass substrate by sputtering with a thickness of about 500 nm. This layer is the back contact of the solar cell. Mo has been chosen because of its excellent chemical compatibility with CIGSe (no interdiffusion of the species throughout the absorber during thermal stress) and its ability to form an ohmic contact with the CIGSe, because of the presence of a thin $MoSe_2$ layer at the interface between the two materials [10–13]. The p-CIGSe layer can be grown by several vacuum and non vacuum methods, such as co-evaporation [1,6], sputtering [14,15], electrodeposition [16,17] or nano-particles based techniques [18]; in this work, we focus on the study of a 2.5 μm CIGSe layer deposited by co-evaporation using an industrial three stages process described in reference [2]. This process allows to obtain high efficiencies along with a very good reproducibility. A n-doped buffer layer is deposited on top of the absorber; the most widely used is chemical bath deposited cadmium sulfide (CdS) [19] with a bandgap of 2.4 eV and a thickness of 50 nm. This layer allows the formation of the p-n junction with the CIGSe and passivates the absorber surface which strongly reduces recombination at the p-n interface. The band offset of the CdS on CIGSe is particularly suitable for the following ZnO:i/ZnO:Al bi-layer. However, the relatively low bandgap of this material has been highlighted as a major issue to overcome for increasing the photon absorption in the CIGSe. Cd toxicity is also pointed out as a reason for replacing this buffer layer by an alternative buffer. The top zinc oxide bi-layer is deposited by sputtering as a transparent front contact for

the solar cell. The thin (between 50 and 70 nm) intrinsic n-doped ZnO:i layer (IZO) provides an efficient isolation of potential small shunt conductance, along with protecting the CIGSe/CdS interface from the rest of the process. Degenerate n-doped ZnO:Al (AZO) with a thickness of about 400 nm is the most commonly used transparent conducting oxide in the CIGSe field, and act as a transparent front contact.

The band diagram of the complete solar cell under illumination is presented in figure 2. We see that the p-n junction between p-CIGSe and n-CdS/ZnO creates a space charge region which extends in the p-region of the structure, due to the much lower doping level of the p-region compared to the n-region. The difference in the work function between the p and the n materials creates a built-in potential V_{BI}. Incident light passes through the wide gap ZnO:i/ZnO:Al ($E_g = 3.3ev - 3.5eV$) front window, and through the CdS buffer layer ($E_g = 2.4eV$) where high energy photons are partly absorbed but do not contribute to the photocurrent output. When the photons reach the CIGSe absorber, they are absorbed in the material, which separates the holes and the electrons by exciting them in the conduction band. This increases the density of electrons and holes above their equilibrium values leading to a splitting of the quasi Fermi levels (i.e. a difference in the chemical potential of electrons and holes). Migration of the electrons from the p-doped region to the n-doped region creates a minority carriers current, and the electrons are collected at the ZnO:Al front contact while the hole reach the metallic back contact.

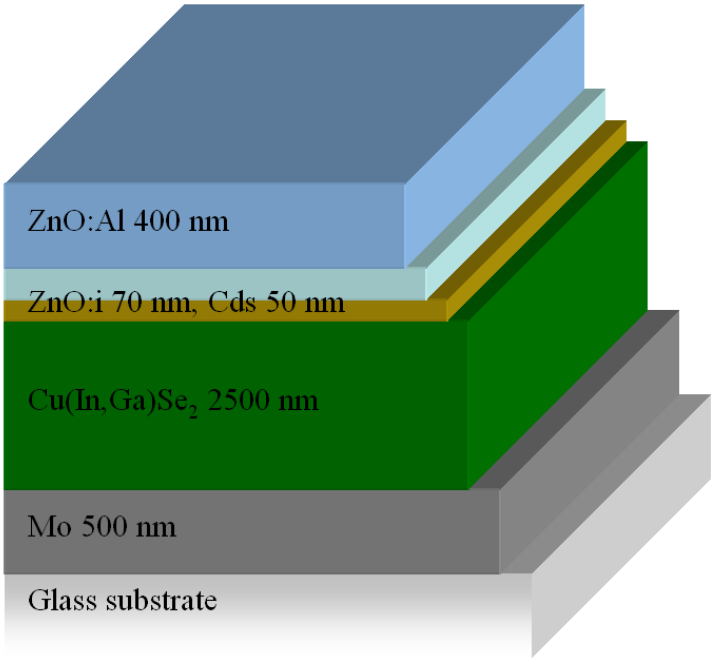

Figure 1. Material stack of a standard CIGSe solar cell

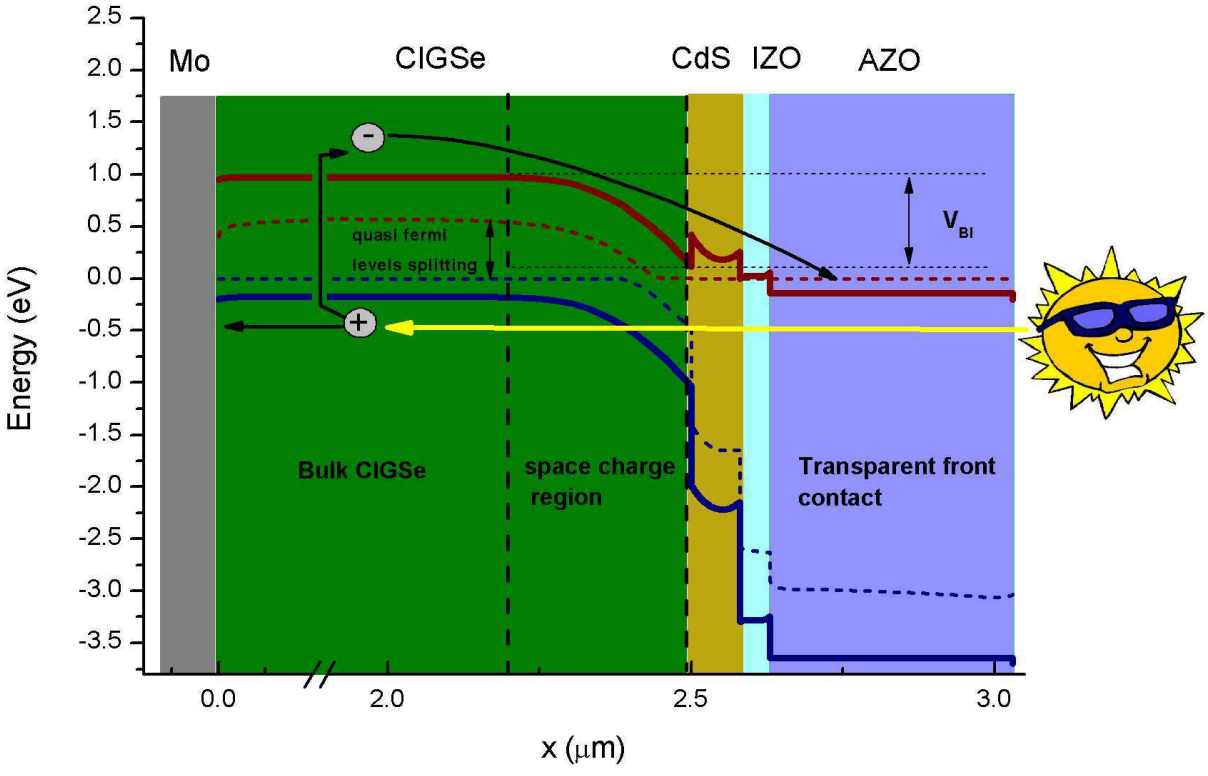

Figure 2. Band diagram of a standard CIGSe solar cell with no polarization and under illumination.

The quasi fermi level splitting drives the maximum value of the Open-Circuit Voltage (V_{oc}) of the solar cell. The short circuit current (J_{sc}) is defined as the current delivered by the cell at 0 voltage. When the diode is polarized in direct, the maximum power output $P_m = V_m.J_m$ is reached, also called the operating point, for a voltage $V_m < V_{oc}$ and a current $J_m < J_{sc}$. The Fill Factor FF is defined as $FF = \frac{V_m.J_m}{V_{oc}.J_{sc}}$. The efficiency η of the solar cell is the ratio between the maximum power output P_m and the incident power P_s. Under standard A.M. 1.5 solar radiation, $P_s = 1000\, W.m^{-2}$. Therefore, in standard conditions, we have $\eta = \frac{V_m.J_m}{1000} = \frac{V_{oc}.J_{sc}.FF}{1000}$. Several factors may limit the solar cell efficiency; the most important ones are shunt resistance arising from leakage of current through the cell, series resistance coming from each layer composing the solar cell and the interfaces between the layers, and carrier recombination that may occurs in the stack. The main recombination processes in solar cells are schematized figure 3. The band to band recombination process is basically the inverse process of the electron-hole pair generation from light absorption in the material (Figure 3.a). An electron from the conduction band falls back to the valence band and releases its energy in the form of a photon $h\nu$. Another very important recombination process is the recombination by phonon emission (Figure 3.b), also called Shockley-Read-Hall (SRH) recombination. This type of recombination is trap-assisted utilizing a defect at the energy E_t within the material bandgap E_g. The excess energy during the recombination of the carrier is transferred to the crystal lattice by phonons. The theory describing this effect can be found in references [20,21]. Interfaces, because of their higher defect density, are often region of high SRH recombinations. Back contact recombination (Figure 3.c), occurring when electron reach the metallic back contact, are often neglected for standard CIGSe solar cell due to the important thickness of the absorber. However, their influence becomes of major importance for thinner absorber layer, particularly for low energy photons that are absorbed deeper in the CIGSe, and thus closer to the back contact. Finally, recombination at the CIGSe/CdS interface which could be assisted by tunneling can also occur, due to interface defects (Figure 3.d).

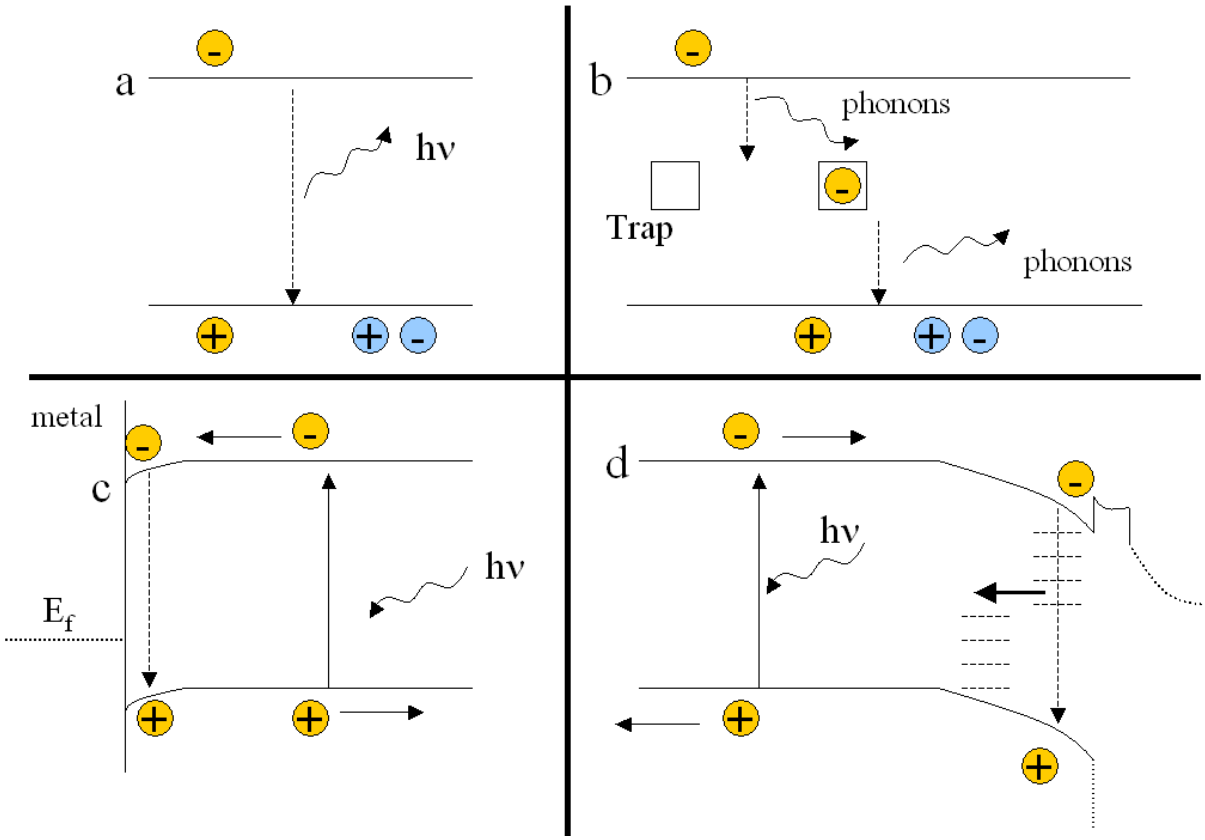

Figure 3. Schematic representation of the major recombination processes in a CIGSe solar cell. (a) radiative band-to-band; (b) Shockley-Read-Hall; (c) back contact; (d) interface recombination with possible tunneling

When reducing the absorber thickness, the device becomes more sensitive to various parameters such as the material absorption, the increased recombination etc… In the following, we will expose a general overview of previous studies related to thinning the CIGSe absorber, which will give us leads to follow throughout our experiments.

II) State of the art in thinning of CIGSe absorber

Since reducing the absorber thickness in CIGSe solar cell has been pointed out as a key issue in this sector, several groups have tackled the task both from a theoretical and experimental points of view and designed devices with thinner absorbers. Systematic study of the reduction of the absorber thickness was first reported by Shafarman et al. in 1997 [22] and Negami et al. in 1998 [23]. Since then, the most active groups have been the NREL group [24] [25] [26] and the Uppsala University group [27] [28] with extensive studies on this topic. Those two groups proposed the same approach for reducing the absorber thickness, consisting in directly growing the CIGSe layer at a lower level, thus adapting the existing process to a lower thickness.

When reducing the absorber thickness of a photovoltaic device, the most expected problem is the reduction of the light absorption and so the decrease of the photocurrent generation in the solar cell. Although the absorption coefficient of the CIGSe material is very high, all the studies have shown that the amount of light absorbed is strongly affected when decreasing the absorber thickness to the sub-micrometer level. Moreover, other problems may appear due to the ultra-low scale of the devices. Negami [23] reported that the solar cells were electrically shunted when the absorber thickness became close to 0.5 μm; this was related to the natural roughness of as-grown CIGSe layers which was of the same order as the film thickness itself. Shafarman et al. [22] also reported a strong decrease of the parallel resistance when reducing the CIGSe thickness, most likely related to an increased shunt effect due to pinholes in the absorber. However, Karpov et al. predicted, in a theoretical simulation study, the existence of a critical device thickness in the submicron region, below which the leakage currents will harm the device performance [29]. Gloeckler and Sites [30] also investigated on the properties of very thin and ultrathin absorber CIGSe solar cells from a theoretical point of view. Their simulations indicated that reducing the absorber thickness leads to a reduction of the short circuit current due to a combination of a reduced light absorption and increased back contact recombination. When the absorber is fully depleted however (thickness lower than the space charge region width), the authors state that the back contact recombination become negligible and the current of the cell depends only on the absorption in the CIGSe.

The Uppsala group's first publication [27] on the topic used a Cu-poor fabrication process giving a relatively smooth surface (RMS ~ 40 nm), which strongly reduces the risk of shunting for thin CIGSe absorbers. However, a much smaller grain size is achieved when compared to a classical three stage process. In this study, a 1.8 μm solar cell with an efficiency of about 16 %, a Fill Factor (FF) of 75 % and an Open Circuit Voltage (V_{oc}) of 650 mV is taken as a reference thick absorber solar cell, and solar cells with thinner absorbers are realized using the same process, down to 0.15 μm. Efficiencies close to 13 % are achieved down to 0.8 μm, showing a moderate decrease when reducing the absorber thickness; however a more pronounced decrease is observed for the lower thicknesses down to 8 % for a 0.36 μm absorber solar cell. The results indicate that the dominant loss is seen in short circuit current. External Quantum Efficiency (EQE) and absorption measurements are performed on the devices (figure 4), showing that the light absorption is only slightly reduced when decreasing the absorber thickness from 1.8 μm to 0.8 μm; the EQE was however strongly affected in the long wavelength range. This reduced carrier collection for low energy photons is interpreted to an increased back contact recombination, thus confirming the simulations from Gloeckler & Sites [30]. For the ultrathin 0.36 μm device, the absorbed light was strongly reduced compared to a thick CIGSe layer in the red and infrared range. Moreover, the difference between absorbed light and collected carriers is even more important and a high fraction of the generated carrier do not contribute to the current. On the other hand, the V_{oc} and the FF are essentially not affected down to ~0.5 μm absorber thickness, maintaining high values close to 650 mV and 73 % respectively. At the ultrathin scale however ($d < 0.4$ μm), the Voc and the FF are reduced although still at relatively high values (600 mV and 70 % respectively).

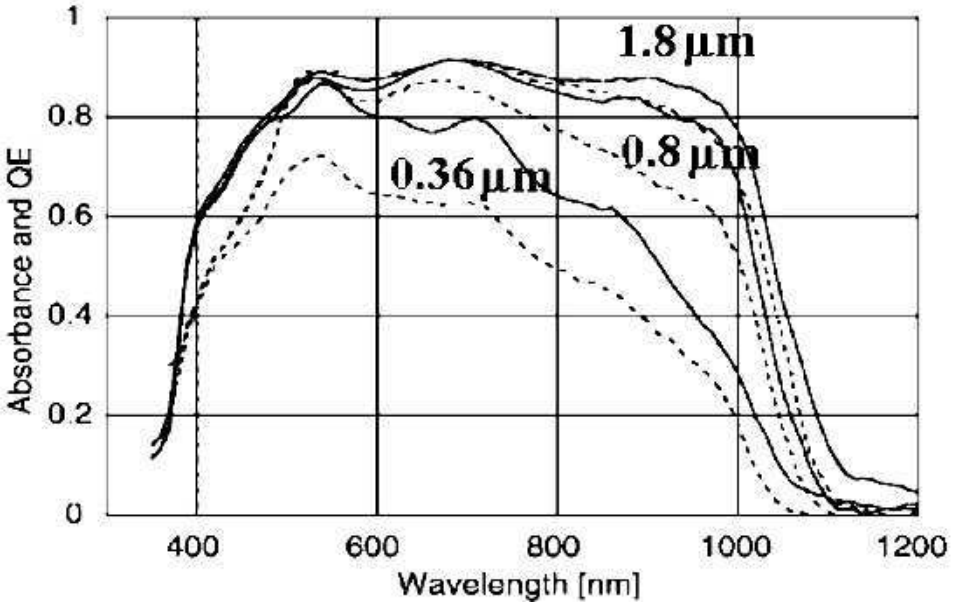

Figure 4. Comparison between the calculated absorption curves (solid) and the corresponding QE curves (dotted) for CIGS thicknesses of 1.8, 0.8 and 0.36 µm [27]

This paper also studies the influence of a back surface field (BSF) on the devices created by inserting a $CuGaSe_2$ layer. It has been shown that by using graded compositional profiles, i.e. increasing the Ga content at the back side of the solar cell, the conduction band level in the CIGSe increases [31]. This leads to a reduced back contact recombination as reported in reference [32]. With the introduction of this layer, the FF increases above 75 % while the V_{oc} is increased by about 30 mV, whatever the CIGSe thickness. The short circuit current however, which is the dominant loss responsible of the efficiency drop, is not improved by the introduction of the BSF. Diode analysis using a 1-diode model with dark and illuminated J-V measurements revealed that reducing the absorber thickness leads to a gradual increase of the saturation current J_0, which is governed by the recombination processes, and an increase of the diode ideality factor A. This is interpreted as related to the reduction of the V_{oc} of thinner absorber devices, while the reduction of the FF is accounted to the increase of J_0 and a decrease of the shunt resistance R_{sh}. The authors attribute the increase of the saturation current to a combination of different phenomena; firstly, thinner absorber increases the back contact recombination and thus reduces the carrier collection. The fact that the FF is improved by the back CGSe layer is an indication that some loss mechanism can be reduced with a BSF, but the losses observed in the EQE curves remain however unchanged with the BSF. The thinner CIGSe layers also have smaller grain and thus larger grain boundaries than thick layers, which

could also account for the increased recombination losses. Finally, according to reference [33], the fact that the EQE of the 360 nm absorber solar is reduced in the short wavelength range combined with an increased ideality factor indicates tunneling recombination in the region close to the CIGSe/CdS interface.

Ramanathan et al. [24] investigated the influence of the thermal evaporation growth process on 1 µm thick CIGSe solar cells; they compare a three stage process with simultaneous co-evaporation of all the elements in one step. The three stage process consists here in the deposition of a $(In, Ga)_2Se_3$ layer, then reacted with Cu and Se. The composition is controlled by detecting the temperature change of the substrate during Cu-poor to Cu-rich transition at the end of the second stage. The third stage is the evaporation of In and Ga in the presence of Se. The reduction of the CIGSe thickness in the three stage process is achieved by reducing the thickness of the precursor film in the first stage. On the other hand, several co-depositions were made, starting with a Cu-rich CIGSe layer or a $CuGaSe_2$ layer, and the flux were adapted to obtain films with the desired element ratio.

These different methods were successfully adopted to deposit absorbers in the thickness range of 0.4-1 µm and a bandgap grading was achieved in all the scenarios. Table 1 presents the best solar cell results as a function of the absorber thickness. A reference thick absorber solar cell is also presented.

Thickness (µm)	V_{oc} (V)	J_{sc} (mA/cm^2)	FF (%)	Eff (%)
1.0 (3-stg)	0.678	31.9	79.2	17.1
1.0 (codep)	0.699	30.6	75.4	16.1
0.6 (codep)	0.658	26.1	73.1	12.6
0.4 (3-stg)	0.565	21.3	75.7	9.1
Control (3 stg, 2.5 µm)	0.728	31.87	80.3	18.7

Table 1. Photovoltaic properties of thin CIGSe solar cells [24]

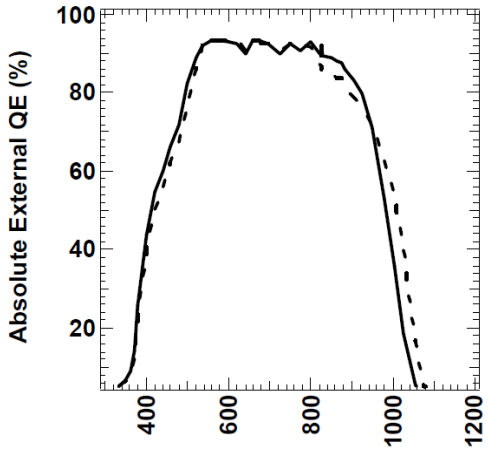

Figure 5. External Quantum Efficiency for a thin 1000 nm CIGSe solar cell (solid line) and thick 2500 nm CIGSe solar cell (dotted line) [24]

The highest efficiency for a 1 μm CIGSe solar cell was achieved for a three stage process absorber with 17.1 %. When comparing the EQE of this solar cell with the thick 2.5 μm solar cell (figure 5), they notice that the long wavelength energy edge is at higher energy for the thin absorber, which is an indication of a higher Ga content. The V_{oc} is however lower than expected in this configuration by about 50 mV, which is the most significant loss that contribute to the difference in the efficiency between a thin and a thick absorber solar cell as seen on table 1. Dark J-V curves analysis shows that while the diode ideality factors are identical between a thin and a thick solar cell, the reverse saturation current is slightly higher in the case of a thin absorber (8.10^{-11}A.cm^{-2} versus 3.10^{-11}A.cm^{-2}) which partly explains the decrease in V_{oc} observed for thin absorbers. Drive-level capacitance profiling (DLCP) measurements were performed on three stage absorbers with different thicknesses in order to evaluate their free carrier and defect density. This characterization reveals an increasing trend in both the carrier and defect density when decreasing the absorber thickness. The increase in the free carrier density does not results in an increase of the V_{oc} due to the counter effect of the increasing defect density. This is attributed to a non-optimum growth of the thinner CIGSe layers.

Instead of directly growing the absorber to a thinner scale, which may lead to the problems previously reported, more fundamental studies can be performed by reducing the thickness of a standard absorber by chemical etching. The chemical etching of CIGSe surface was first introduced by Birkmire and McCandless in 1988 [34], who realized specular CIGSe surface

with this technique. This paper was followed by a publication from Canava et al. who reported a method to reconstruct the surface termination of CIGSe after etching by using a KCN post treatment [35]. Based on these results, Shafarman's team also investigated the etching of CIGSe films, but for reducing the absorber thickness [36]. They performed a systematic comparative study between etched absorbers and as-deposited absorbers of the influence of reducing the CIGSe thickness on the photovoltaic parameters of the solar cells (Figure 6). They reported a similar trend for the J_{sc} when etching absorber as what was observed for as-deposited CIGSe, with a progressive decrease due to the reduction of the thickness of the active material. However, in the case of etched absorbers the FF is found much more stable when reducing the CIGSe thickness than for as-deposited absorbers. On the other hand, the Voc of etched absorber solar cells is reported as slightly lower although the important dispersion of the results makes it difficult to interpret. Overall, the efficiency trend and value is identical between etched and as-deposited absorbers.

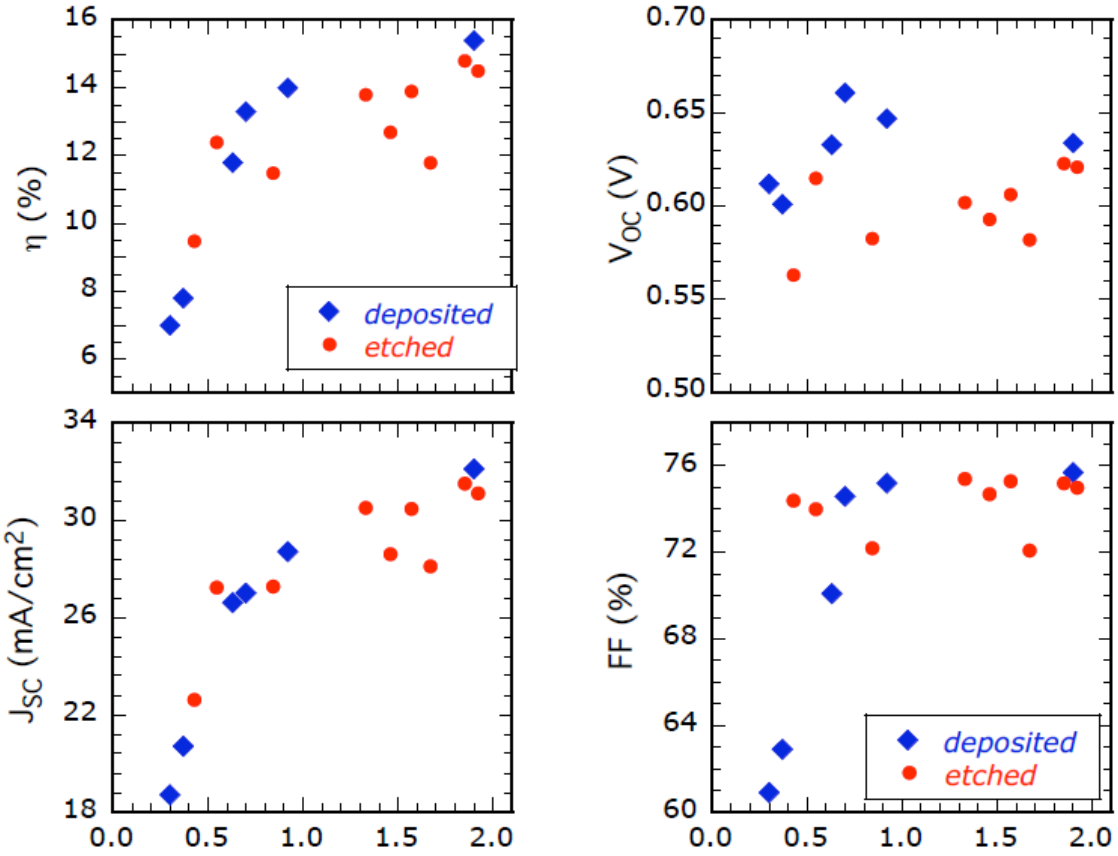

Figure 6. Compared photovoltaic parameters for CIGSe solar cells with different absorber thicknesses realized with two different techniques: direct deposition of the absorber (blue dots), and chemical etching of thick absorbers (red dots) [36]

In this Chapter, we had an overview of the general literature on CIGSe solar cells with thinned absorber. When reducing the CIGSe thickness, the short circuit current has been identified as the dominant loss in the solar cell. This has been attributed to a contribution of both incomplete absorption of incident photons due to the thinning of the absorber, and increased back contact recombination due to the increased proximity of the back interface for thin CIGSe layers. Open Circuit Voltage and Fill Factor are also affected although in much lower proportions, especially for very thin CIGSe absorber (less than 500 nm).

In this work, our goal is to study the feasibility of very thin and ultrathin absorber device with photovoltaic properties comparable to standard thick absorber solar cells. In the following Chapter, we will firstly study the influence of reducing the absorber thickness in a state of the art CIGSe solar cell by numerical simulation. We will try to investigate the physical factors that are involved in the decrease of the performances of the device, in order to address new and adapted techniques to significantly enhance the photovoltaic parameters of very thin (down to 400 nm) and ultrathin (down to 100 nm) absorber CIGSe solar cells. These materials and structures will be implemented in a numerical modeling to evaluate their potential in the scope of future application to experimental proof of concept devices.

Chapter II

Theoretical Analysis: Effect of thinning of CIGSe absorber layers on solar cells characteristics and potential improvements for ultrathin devices

II.1) Introduction

As presented in the previous chapter, thin film solar cells and especially chalcogenide thin film solar cells have been extensively studied in the last three decades, and significant advances have been achieved leading to an increasing development of this technology. We however pointed out that although the current material cost is only a small fraction of the total solar panel cost, this rising evolution may lead to a major increase of the material price (both for CIGSe and CdTe) in a near future [3] [37], and the limited material resources (for In and Te) may become an important limitation to upcoming developments of the sector. In order to limit the bottleneck due to the availability of the material, recent researches have been carried out to reduce the material consumption by thinning the absorber layer, both in CdTe [37] [38] [39] and CIGSe [22] [23] [24] [27]; this is the topic of our present study. In order to evaluate the influence of reducing the absorber thickness in a CIGSe solar cell, it is important at first to perform numerical simulations of very thin and ultrathin absorber solar cells, and to establish interpretations and hypothesis that will give us a trail to follow in the experiments.

In this Chapter, we focus on modeling a standard CIGSe solar cell using SCAPS 2.904, that will be used as a baseline. We will then study the influence of progressively reducing the CIGSe absorber thickness down to 100 nm. SCAPS is a worldwide recognized simulation software created by Prof. Burgelman from the University of Gent [40]. Numerical simulations allow us to discriminate the key parameters of the solar cell that are affected by the absorber thickness reduction, and SCAPS, being both a user-friendly and a powerful tool for 1-D simulation of thin films solar cell, is a very well suited program for this study.

Previous theoretical work shows that sub-micrometer CIGSe solar cells could be greatly improved with a suitable engineering of the device [30, 41]. To supplement these results, we will suggest some realistic improvements to the solar cell and evaluate their potential in the perspective of a performance improvement. Optical simulations of novel CIGSe solar cell structures with very thin absorbers will be presented.

II.2) Modeling of a standard CIGSe solar cell

II.2.a) Definition of the input parameters

The first stage in modeling the influence of the absorber thickness on the photovoltaic parameters of a CIGSe solar cell is to establish a "baseline" solar cell; the parameters used to model this state of the art solar cell are either taken from literature [42] [43] or from direct characterizations of a standard CIGSe solar cell from Würth Solar [2]. The modeled baseline solar cell should match as close as possible the experimental solar cell.

Numerical simulations were performed using the program SCAPS in order to theorically evaluate the influence of the absorber thickness on the properties of the solar cell, and to investigate possible improvements of the device both with an optical and an electrical engineering of the solar cell. SCAPS is a free program developed at the Gent university by M. Burgelman et al. designed for thin film solar cells 1-D modeling [40] and made available to university researchers in the photovoltaic community in 1998. The version used in this work is the 2.904. SCAPS allows to model the main electrical characterizations of solar cells, i.e. Current-Voltage (dark and illumination), Spectral Response, and Capacitance-Voltage and Capacitance-Frequency which will not be used in this work. The user enters electronic and optical parameters to define the different materials and interfaces that compose the solar cell. Recombination model including different types of defects (Neutral, Single/Double Donor/Acceptor, Amphoteric…) are also input parameters. The main limitation of this software simulation tool is that a very good knowledge of the parameters of the materials composing the cell is needed, and experimental characterizations must be performed as much as possible to sharpen the simulations results.

In order to establish a reference solar cell, which will be used as a baseline for the study of the influence of the absorber thickness reduction, the electrical and optical parameters of each layer of the solar cell have been chosen according to experimentally measured parameters and compared to reference [42] and [43]. Table 1 shows the main material parameters used in this study, and the Appendix I summarizes the complete parameters set for simulation of a standard CIGSe solar cell. Repeated simulation by varying each parameter highlighted the fact that some parameters such as the doping level of the CIGSe absorber are of the utmost importance and need to be determined with high precision and reliability. For example, the majority carrier concentration in CIGSe that we use in our simulation is 2.10^{16} cm^{-3}; this

carrier concentration was deduced from an experimental Capacitance-Voltage curve of a standard CIGSe solar cell at room temperature (no illumination). It is in perfect agreement with the references [42] and [43] and thus can be used as one of our baseline parameter for further simulations. Different set of parameters may lead to similar results in the photovoltaic parameters, this is why the user has to be very cautious.

	CIGSe	CdS	ZnO:i	ZnO:Al
ε_r [-]	13.6	10	9	9
χ [eV]	4.5	4.2	4.45	4.65
E_g [eV]	1.15	2.4	3.3	3.5
μ_e [$cm^2.V^{-1}.s^{-1}$]	1.00E+02	1.00E+02	1.00E+02	1.00E+02
μ_h [$cm^2.V^{-1}.s^{-1}$]	25	25	25	25
N_c [cm^{-3}]	2.20E+18	2.20E+18	2.20E+18	2.20E+18
N_v [cm^{-3}]	1.80E+19	1.80E+19	1.80E+19	1.80E+19
N_A [cm^{-3}]	2.00E+16	1.00E+00	1.00E+00	1.00E+00
N_D [cm^{-3}]	1.00E+01	1.00E+17	1.00E+18	5.00E+20
ν_e [$cm.s^{-1}$]	1.00E+07	1.00E+07	1.00E+07	1.00E+07
ν_h [$cm.s^{-1}$]	1.00E+07	1.00E+07	1.00E+07	1.00E+07

Table 1. Material parameters used for the simulation of a reference CIGSe solar cell. ε_r: dielectric permittivity (relative); χ : electronic affinity; E_g: bandgap; $\mu_{e/h}$: electron/hole mobility; $N_{c/v}$: conduction/valence band density of states; $N_{A/D}$: acceptor/donor density; $\nu_{e/h}$: electron/hole thermal velocity.

An accurate definition of the optical properties of the different layers is needed for sharp simulation to match well the experimental characterizations. Some baseline absorption coefficients (Numos) are included in the SCAPS folder, coming from different sources: Numos_ZnO [44], Numos_CdS [44] and Numos_CIGS [28]. Although these data showed good agreement with our experiments, it is also possible to input absorption coefficients from spectroscopic ellipsometry in the simulation for a better accuracy; the reflectivity/transmission at the front and at the back contact of the solar cell are also parameters that can be implemented in the definition of the solar cell. Finally, it is also possible to include a generation function G(x), which can be simulated using an optional program that we developed in our laboratory [45] and included as a .txt file in the SCAPS simulations. In our simulations, however, G(x) was calculated by SCAPS, and Numos files will be used for ZnO and CdS absorption. The absorption of the CIGSe layer is determined from ellipsometry measurements and is presented figure 1.a. The reflectivity R_i of the back contact at the CIGSe/metal interface is also determined using spectroscopic ellipsometry (see Chapter V) for the CIGSe and the back contact (see figure 1.b), and it is calculated using the Fresnel's equation:

$$R_i = \left| \frac{\tilde{n}_{Metal} - \tilde{n}_{CIGSe}}{\tilde{n}_{Metal} + \tilde{n}_{CIGSe}} \right|^2$$

where $\tilde{n}_{Metal}$ and $\tilde{n}_{CIGSe}$ are the complex optical indexes of the CIGSe and the metal determined from spectroscopic ellipsometry measurements. The reflectivity of the front side of the solar cell is experimentally determined by reflectivity spectroscopy measurements of a complete CIGSe solar cell stack (ZnO:Al/ZnO:i/CdS/CIGSe/Mo) in our laboratory using an integrating sphere and implemented in the SCAPS simulations (figure 1.b).

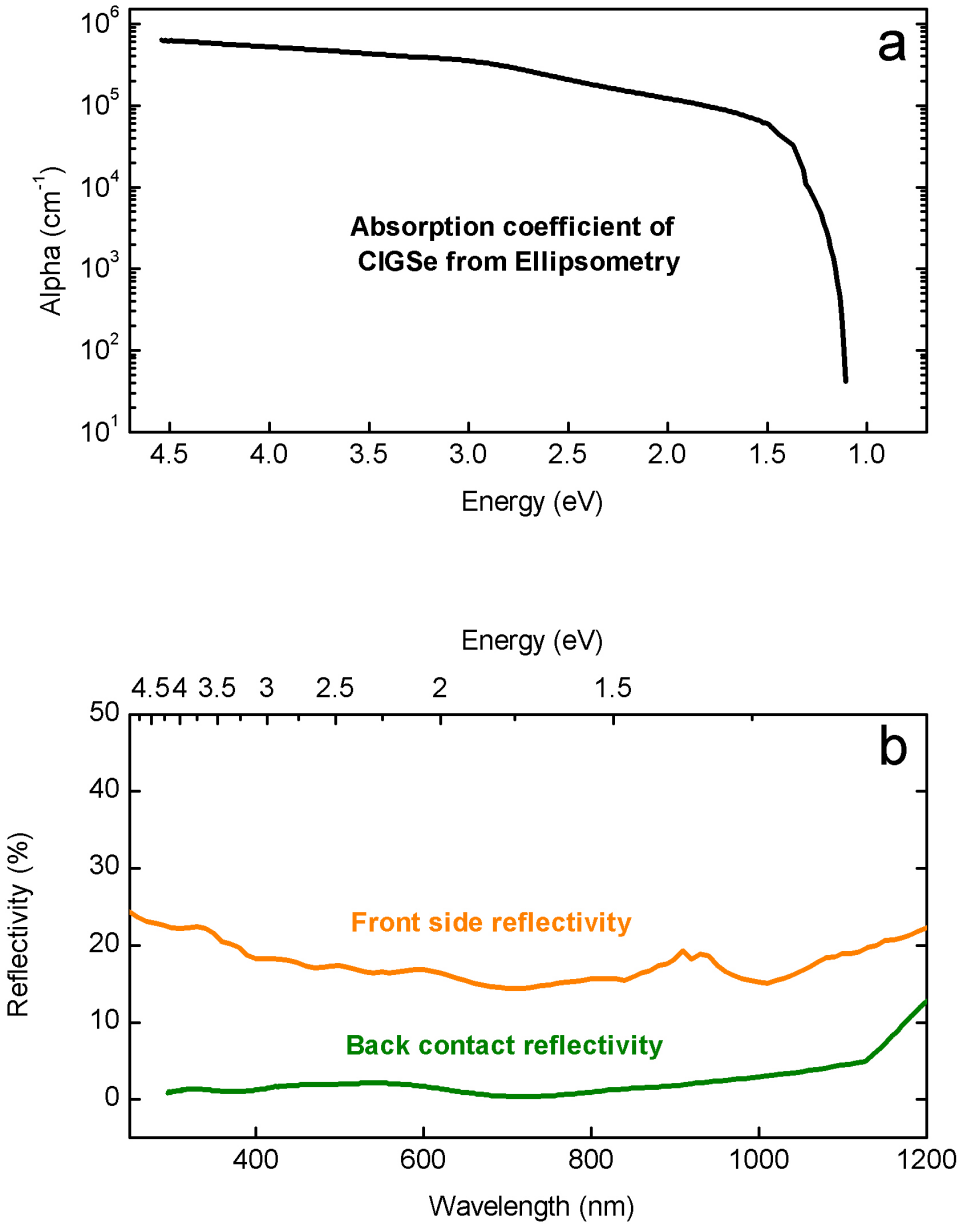

Figure 1. (a) Absorption coefficient of a standard CIGSe layer from spectroscopic ellipsometry measurements; (b) Measured front side reflectivity of a standard CIGSe solar cell (orange curve) and calculated back contact reflectivity (green curve) from ellipsometry data

After the complete definition of the material and optical properties of the solar cell stack, we perform simulations of the Current-Voltage (J-V) curve and Spectral Response, and compare the results with the measurements performed on a reference 2500 nm CIGSe solar cell.

II.2.b) Modeling of current-voltage and spectral response

The CIGSe absorber thickness taken as the default thickness for a reference solar cell is 2500 nm. Figure 2.a shows a superposition of the J(V) curve of an experimental (dots) and a simulated (solid line) reference CIGSe solar cell and Figure 2.b shows the corresponding external quantum efficiencies.

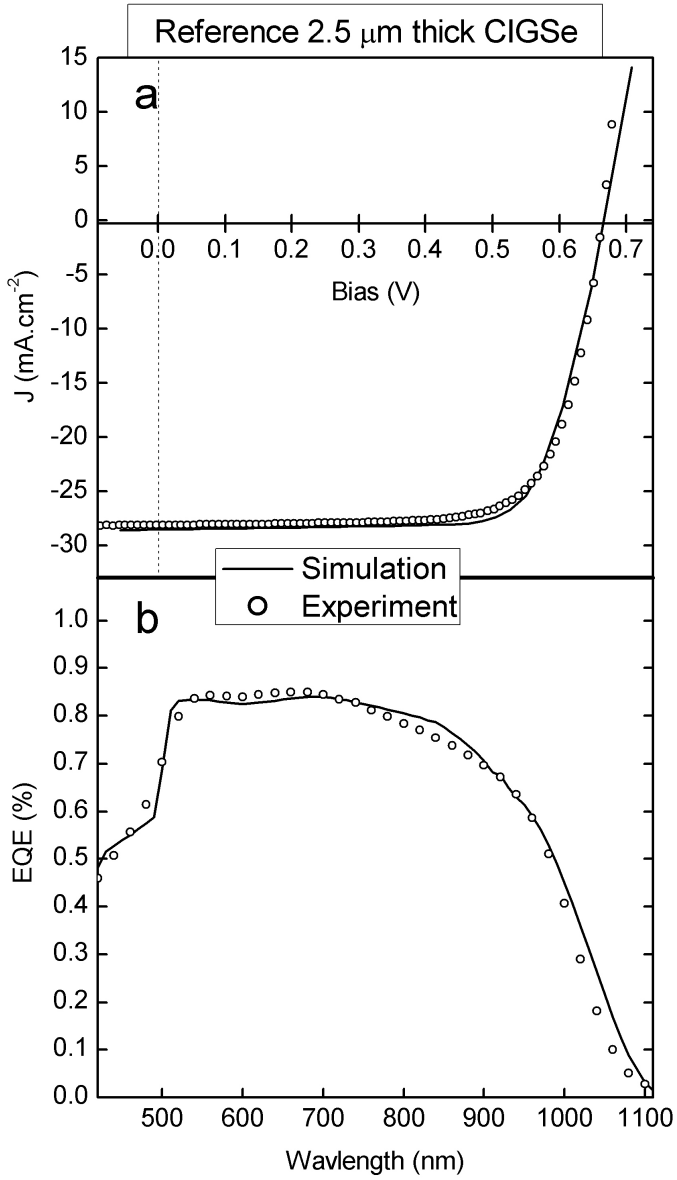

Figure 2. Comparison between a state of the art 2500 nm CIGSe solar cell from Würth Solar (solid line) and our baseline simulated solar cell (circles). a: J-V curve; b: Spectral Response.

From the J-V curves presented figure 2.a, the photovoltaic parameters of the SCAPS baseline solar cell are:

$$V_{oc} = 667 \text{ mV}, FF = 73.9\%, J_{sc} = 28.6 \text{ mA.cm}^{-2} \text{ and } Eff = 14.1\%$$

Which are similar to those of the experimental reference CIGSe solar cell are:

$$V_{oc} = 663 \text{ mV}, FF = 73.3\%, J_{sc} = 28.1 \text{ mA.cm}^{-2} \text{ and } Eff = 13.7\%$$

We can achieve a very good agreement between the simulated and the experimental results; we can also note that the slight differences are much lower than the usual spreading of the parameters observed on standard solar cells.

In addition, the Spectral Response curves presented in figure 2.b show a very close match between the experimental and the simulated curves. The CdS absorption in the UV range is well reproduced, along with the CIGSe absorption plateau in the visible range. The curves however slightly differ in the 800 nm to 900 nm, maybe due to some small interference effects that may appear in the ZnO layer for the experimental solar cell, even if the interfaces of a standard CIGSe solar cells is relatively rough. Also, the bandgap between the two curves seem slightly different. This is attributed to the fact that the ellipsometry data that are used to input the absorption coefficient has to be extrapolated in the vicinity of the bandgap due to the very low absorption of the material in the region, and therefore may lead to a lack of precision.

The agreement between experiments and simulations being good both for the J(V) characteristic and the spectral response, this validates our set-of parameters as a baseline state-of-the-art solar cell for simulating the influence of the absorber thickness on the photovoltaic parameters of the device. However, it is important to highlight the fact that the array of parameters to input in SCAPS is very large; As pointed by M. Burgelman et al. [40], one cannot be sure that another set of parameters does not exist and may lead to calculations which could be judged equally well as the one in figure 2. To prevent this from happening, we performed as many possible characterization on our material and compared it to state-of-the-art literature.

In the following, the thickness of the absorber will be progressively reduced and we will investigate on the evolution of the photovoltaic parameters together with proposing some interpretations.

II.3) Influence of CIGSe thickness on photovoltaic parameters

In this section, we study the effect of the progressive reduction of the absorber thickness from the reference 2500 nm down to 100 nm on the J-V characteristics, the recombination currents in the device and the External Spectral Response (EQE). The doping level of the CIGSe, the mobility μ and the density of states in the conduction band and the valence band are considered homogenous throughout the layer. Using SCAPS 2.904, the absorber thickness is reduced from 2500 nm down to 100 nm starting from the baseline reference solar cell previously established in part I.

II.3.a) Modeling of the current-voltage curves

The figure 3 shows the simulated J-V curves (3.a) and the corresponding photovoltaic parameters (3.b and 3.c) for the different absorber thicknesses. We clearly see that two different regimes in the variation of the parameters emerge. The first one is from 2500 nm to around 500 nm, where the variations of the parameters is moderate. In this configuration, the absorber thickness is roughly higher or of the same order than the mean absorption length of the photons. The absorber layer can still be considered as relatively optically thick. In the second regime, from 500 nm to 100 nm, the variation of the parameters is much more abrupt; in this case, the absorber thickness and so the mean absorption length and the layer cannot be considered as optically thick anymore.

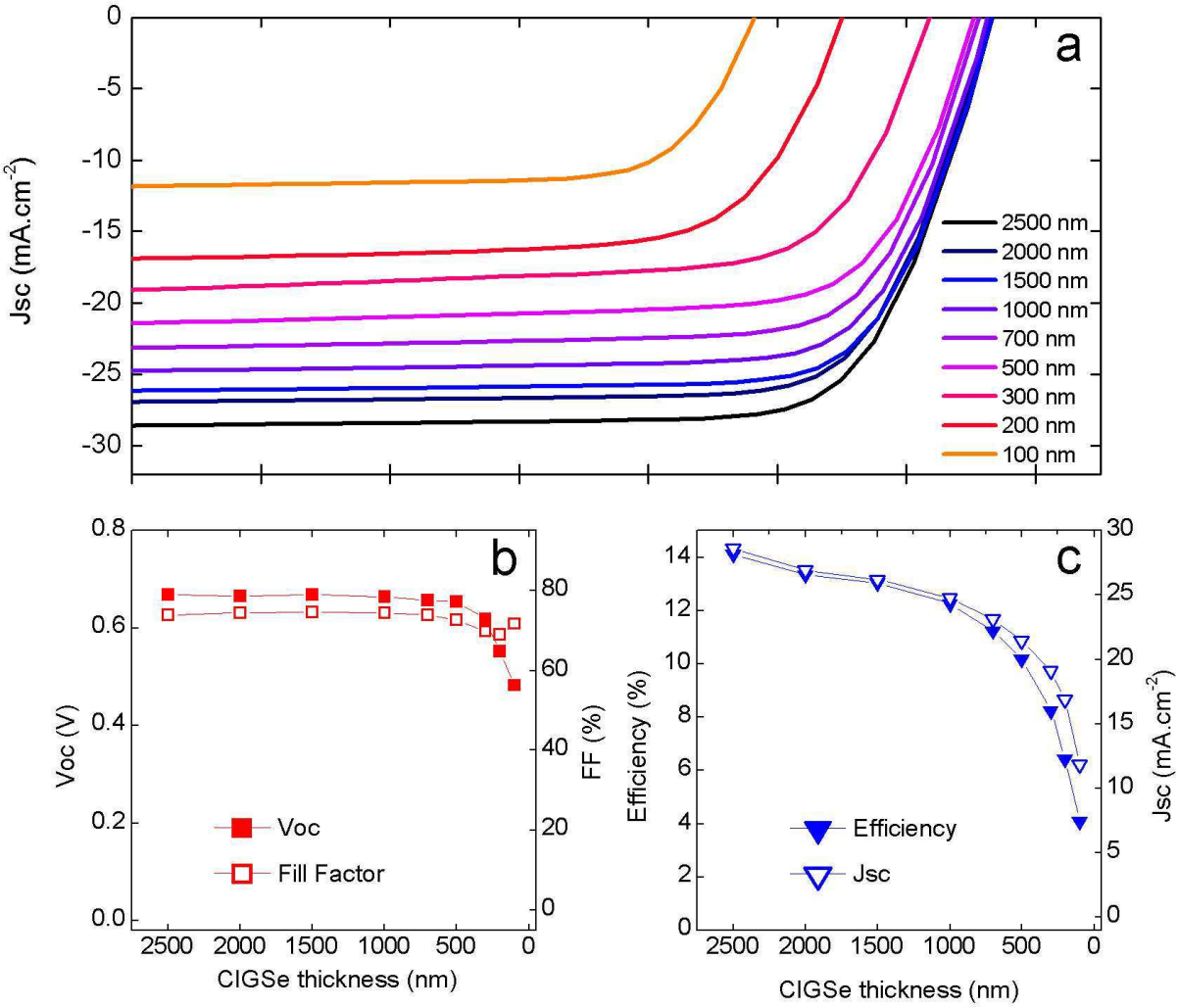

Figure 3. Simulated J-V characteristic (a) of CIGSe solar cells with different absorber thicknesses from 2500 nm down to 100 nm (from dark blue to orange); (b) and (c) are the photovoltaic parameters of the solar cells extracted from the J-V curves.

In the first regime, both the open circuit voltage and the fill factor remain stable down to 500 nm absorber thickness with respective values close to 650 mV and 72-73 % respectively (figure 3.b). On the other hand, the short circuit current is linearly reduced from 28 mA.cm^{-2} for a 2500 nm thick absorber down to 20 m.A.cm^{-2} for a 500 nm absorber (figure 3.c). This drop is both related to non absorption of the photons due to the reduced absorber thickness and to an increased recombination current at the back contact (J_{back}). To illustrate quantitatively the effect of an increase of the recombination current at the back contact when the efficiency decreases, we plot on figure 4.a the calculated back recombination current (calculation by SCAPS). The recombination current J_{back} increases from 1.2 mA.cm^{-2} at zero

voltage for the reference 2.5 μm thick absorber up to 2.8 m.A.cm^{-2} for the 0.5 μm absorber solar cell, so an absolute loss of 1.6 mA.cm^{-2}. The rest of the losses are therefore attributed to non absorption of the photons due to an insufficient absorber thickness. The observed loss is however moderate, with a 29% relative decrease of the current for a removed thickness of about 80 % relatively to the initial 2500 nm absorber. Ultimately, the efficiency drops down to 11 % for a 500 nm thick absorber solar starting from a 14 % reference efficiency for a 2500 nm thick absorber; this efficiency loss is only related to the decrease of the J_{sc} as shown on figure 3.c when reducing the absorber down to 500 nm.

Since the majority carrier concentration in the CIGSe is fixed at 2.10^{16} cm^{-3}, it is possible to evaluate the space charge region width SCRW when no voltage is applied to the diode with the simplified formula $SCRW = \sqrt{\frac{2\varepsilon_r \varepsilon_0}{qN_a} V_{BI}}$ where V_{BI} is the built-in potential (V_{BI}~1 V), N_a the acceptor density, ε_r the relative permittivity of the CIGSe (ε_r = 13.6), and ε_0 the absolute vacuum permittivity (ε_0 = $8.85.10^{-12}$ F.m^{-1}). In our case, we obtain SCRW = 275 nm; therefore, when the second regime is reached and the absorber thickness is lower than 500 nm (ultrathin absorber), it becomes of the magnitude (or even smaller) than the space charge region width and is fully depleted. This results in a ΔV shift of the conduction band that limits the V_{oc} (460 mV for a 100 nm absorber solar cell) of the cell as it is illustrated figure 5. In this case, the quasi fermi level separation is incomplete because of the early “cut” of the band bending region. This particular effect becomes noticeable for an absorber thickness at about 300 nm, thus very close to the value of the space charge region width. The Fill Factor is also slightly affected, although only for the 300 nm and 200 nm samples, where it decreases from its previously stable value of 72% down to 68%, before returning to its ~72% value for the 100 nm sample. The J_{sc} is dramatically decreased for the ultrathin absorbers (300 nm, 200 nm and 100 nm), and drops down to 12 mA.cm^{-2} for a 100 nm absorber solar cell.

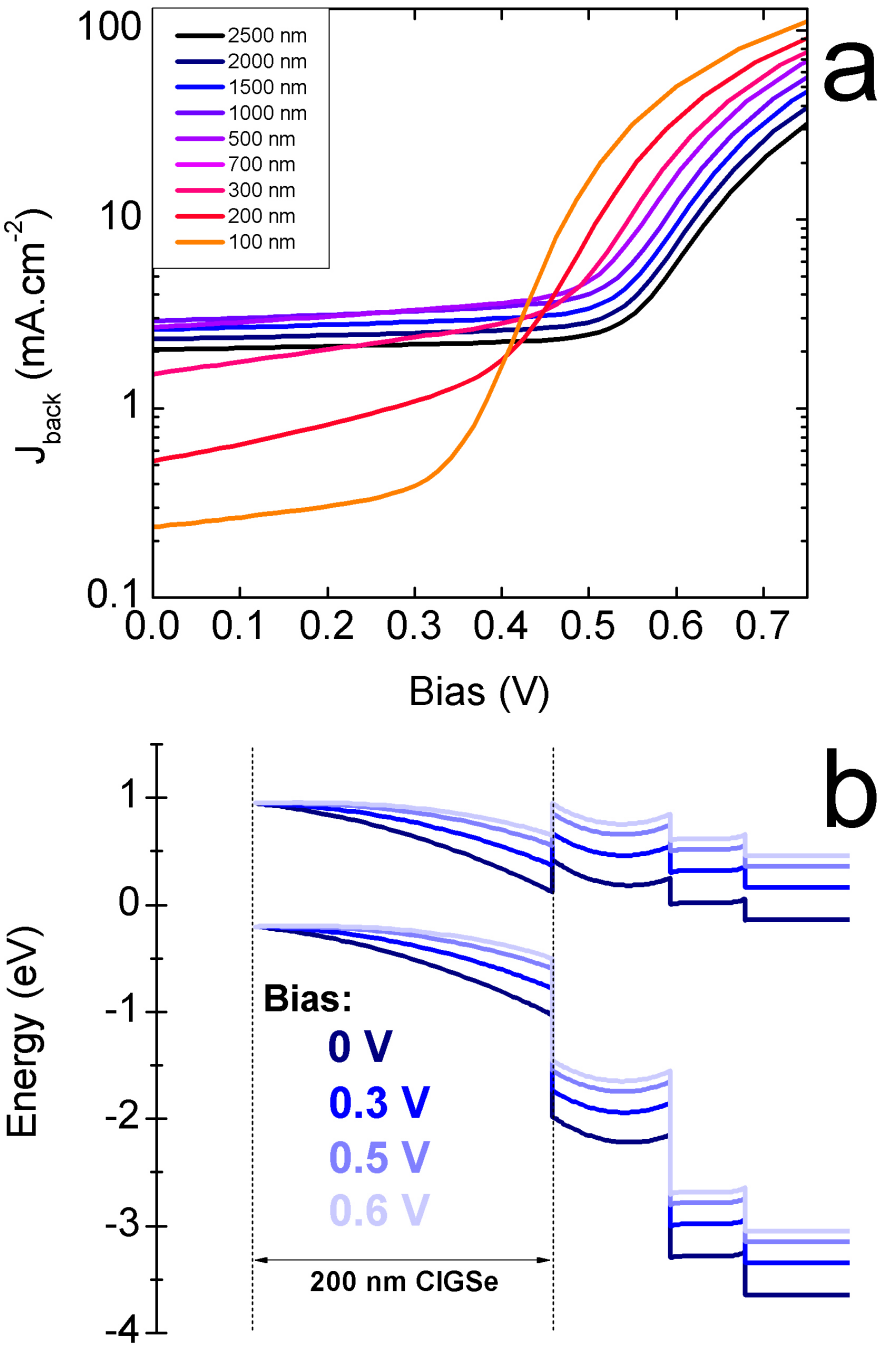

Figure 4. (a) Back recombination current calculated for CIGSe solar cells with different absorber thicknesses, from reference 2500 nm (dark blue curve) to 100 nm absorber (orange curve); (b) calculated band diagram of a 200 nm CIGSe solar cell under 4 different bias: 0 V, 0.3 V, 0.4 V and 0.6 V (from dark blue to light blue).

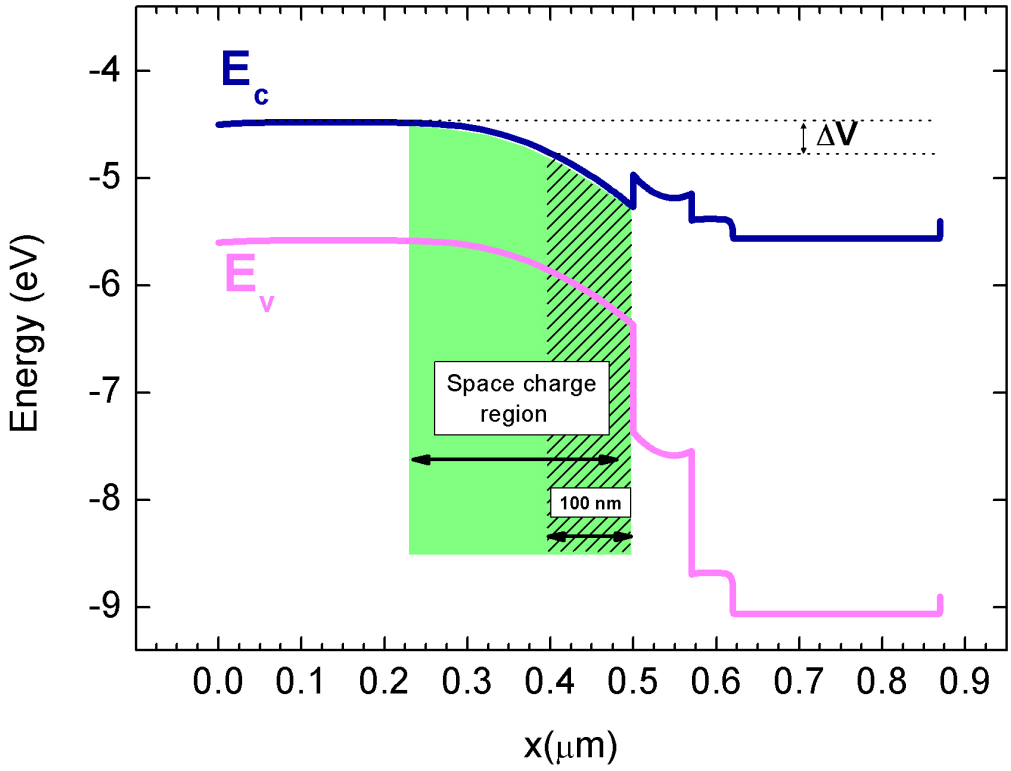

Figure 5. Band diagram of a thinned (500 nm) CIGSe solar cell, illustrating the effect on V_{oc} that has an ultrathinning of the absorber.

It might seem surprising that the back contact recombination is greatly reduced in our simulations for the samples 300 nm, 200 nm and 100 nm, as shown Figure 4.a; there is however a very consistent explanation to this. The absorber being completely depleted, every generated carrier is being driven to the p-n junction by the band bending and the strong electric field in the absorber prevents the generated carriers to drift to the back contact. Gloeckler & Sites [30] already highlighted this phenomenon when the absorber thickness is lower than the space charge region width and they showed that the J_{sc} is nearly independent of the back contact and is only governed by the absorption of the CIGSe layer. The back recombination current curves figure 4.a for fully depleted absorbers are however not parallel to the rest of the curves (absorbers thicker than 500 nm) and they increase with a much more important slope: close to the operating point (450-500 mV), the back recombination currents of the ultrathin solar cells with fully depleted absorbers (300 nm, 200 nm and 100 nm) increase and exceed the recombination currents of the thicker absorber solar cells (> 500 nm). This is due to the fact that the positive polarization of the diode tends to reduce the band bending in the absorber by leveling the -p and the -n sides as it is schematized Figure 4.b.

Therefore, an increasing proportion of photons are absorbed in a quasi flat band region for ultrathin solar cell when applying a positive bias to the diode. While the 100 nm sample is still fully depleted at its much lower operating point, this is not the case for the 200 nm and 300 nm sample where a flat band region appears in the absorber. Therefore, back contact recombination is possible and it slightly reduces the photocurrent at this voltage; it directly affects the FF, which drops from 72% to 68% for the 200 nm and 300 nm sample as shown figure 3.b. For the 100 nm sample, the photocurrent is almost unchanged between V = 0V and the operating point, and so the FF recovers its initial level. As a result from the combined decrease of the V_{oc} and the accelerated decrease of the J_{sc}, the efficiency is strongly reduced from 11% for a 500 nm CIGSe solar cell down less than 4% for a 100 nm.

Eventually, the decrease of the short circuit current is clearly the dominant parameter limiting the efficiency of thinned solar cell although the open circuit voltage becomes an issue at ultrathin scale. In the perspective of using optical management techniques to improve the properties of the solar cell, it is important to investigate the spectral region where the losses occur and so spectral response of the solar cell.

II.3.b) Modeling of Spectral Responses

In this part, we simulate the External Spectral Response (External Quantum Efficiency EQE) of the solar cells when varying the absorber thickness. For these simulations, we used SCAPS 2.904 with exactly the same parameters as used previously for the J-V simulations. No interference effects within the device are being taken into account in these simulations. The obtained EQE curves are presented on figure 6. In the short wavelength region (λ = 400-600 nm), the absorption and carrier collection is almost not affected down to 500 nm of absorber thickness (first regime), with the EQE slightly decreasing from 83% for the reference 2500 nm thick CIGSe to 80% for the 500 nm thick CIGSe solar cell at λ = 550 nm. For the lower thicknesses however (second regime/ultrathin), an accelerated decrease of the EQE is observed. Despite the high energy of the incident photons, the film thickness is insufficient for a complete absorption on the whole spectrum. When the wavelength is increased, the losses due to the absorber thickness reduction become more important. From thicknesses between 2500 nm to 2000 nm, almost no change is observed; however, as the thickness is reduced down to 500 nm, the EQE is significantly reduced especially in the low energy range.

According to reference [30], this is partly due to an increased back contact recombination for carriers generated outside the depletion region close to the back contact, the non-absorption of the thinned CIGSe absorber being the other limiting factor. To support this assumption, we plot on figure 7 the photon absorption depth $\delta_p = \frac{1}{\alpha}$ in the CIGSe versus the wavelength, and the CIGSe thickness is schematically shown on the right side of the graph; this figure clearly illustrates the fact that a non negligible part of the spectrum is not absorbed when the CIGSe thickness is reduced from 2500 nm to 500 nm. In this range, the average absorption depth decreases by 100 nm on the spectrum (from about 1000 nm down to 900 nm). This is in direct relation with the decrease observed in this wavelength range in the EQE curves. Moreover, it confirms the fact that a non negligible part of the photons are also absorbed very close to the back contact, which tends to enhance the back contact recombination. For absorber thicknesses lower than 500 nm, the non absorption by the CIGSe becomes nearly the only parameter limiting the EQE as the back contact recombination is strongly reduced as previously stated. We see on figure 6 that for the 100 nm thick absorber, the EQE is dramatically lowered and it becomes less than 30% after 750 nm. Figure 7 shows that the absorber thickness is significantly lower than the absorption depth and so that the intercept between those two is at 510 nm (dark grey square); after this wavelength, the absorption of the 100 nm film is very poor as confirmed by the EQE simulation figure 6.

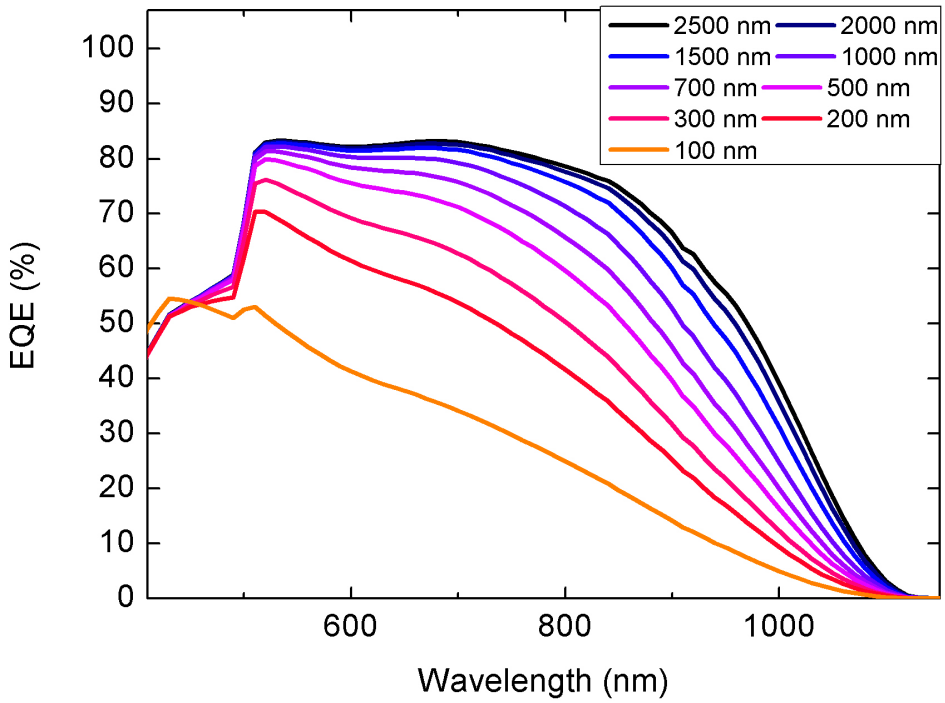

Figure 6. External Quantum Efficiencies of CIGSe solar cells with different absorber thicknesses from 2500 nm down to 100 nm (from dark blue to orange).

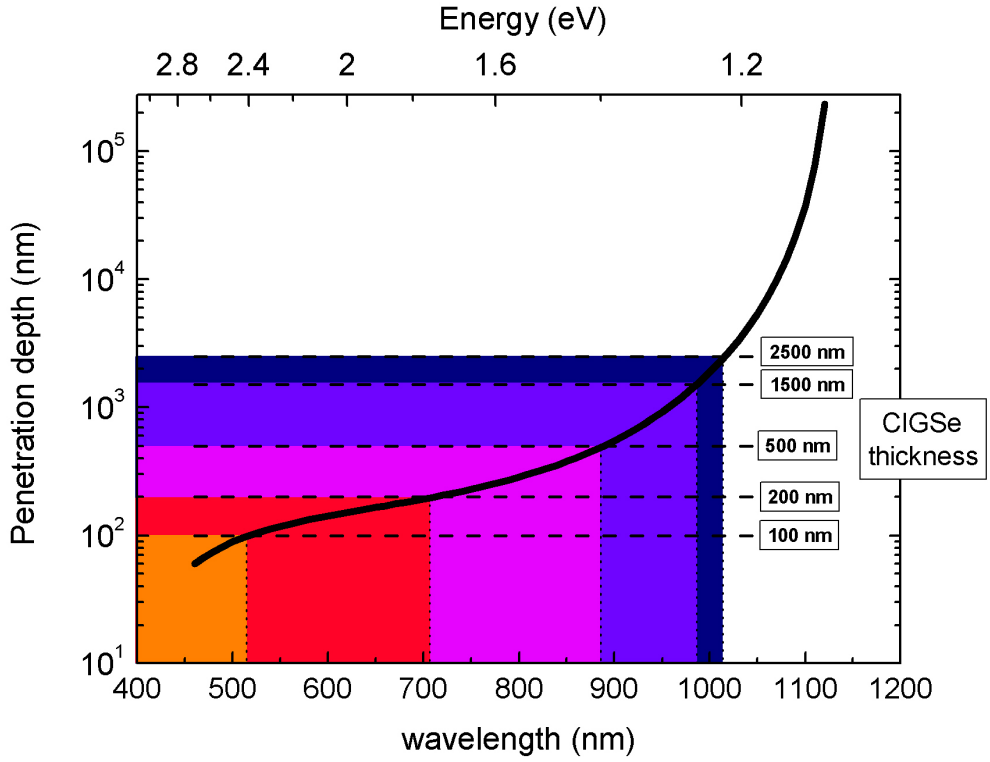

Figure 7. Penetration depth in the CIGSe plotted with the photons incident wavelength. The colored rectangles and the right side of the figure are illustration of the potential absorption of CIGSe layers with different thicknesses.

II.3.c) Conclusion

We have evaluated with numerical simulations the influence of reducing the absorber thickness in a CIGSe solar cell. It was possible to establish a “baseline” state of the art solar cell with SCAPS by using realistic parameters most of the time deduced from experimental data or from literature for the different layers composing the device. The baseline solar cell is in very good agreement with our state of the art experimental solar cell. In our simulations, the absorber thickness was varied from 2500 nm down to 100 nm while keeping constant the other parameters of the device. These simulations, although one-dimensional, gave us a fairly clear idea of the influence of the absorber thickness on the photovoltaic parameters of the solar cell. Two different regimes were identified:

- From 2500 nm down to 500 nm absorber thickness, the short circuit current is the only parameter that is affected by the absorber thickness reduction, decreasing from 28 $mA.cm^{-2}$ (2500 nm CIGSe) down to 20 $m.A.cm^{-2}$ (500 nm CIGSe). We attribute this drop to a combination of non absorption of low energy photons and back contact recombination affecting the carriers that are generated close to the back contact. Accordingly to the evolution of the J_{sc}, the efficiency decreases from 14% (2500 nm CIGSe) down to 11% (500 nm). Although substantial, this variation is rather moderate when one considers the amount of active material that is removed, and at this stage, the CIGSe absorber could still be roughly considered as optically thick.

- From 500 nm down to 100 nm absorber thickness, the absorber becomes fully depleted, being thinner than the space charge region. The intense electric field forces the generated electrons to migrate to the p-n junction and almost completely prevents back contact recombination when no voltage is applied; accordingly to previous results from Gloeckler & Sites [30], the short circuit current is in this case only dependent on the absorption of the CIGSe. The absorption of ultrathin CIGSe layer is very low, which results in very important decrease of the photocurrent down to 12 $mA.cm^{-2}$ for the 100 nm absorber solar cell; moreover, the fact that the absorber is thinner than the space charge region leads to an incomplete separation of the quasi fermi levels which limits the V_{oc} (~460 mV for a 100 nm absorber solar cell). The combination of these different losses dramatically reduces the efficiency of the solar which decreases down to 4% for a 100 nm CIGSe solar cell.

We have highlighted the main issues encountered when one reduces the thickness of the CIGSe absorber down to 100 nm. Both optical (light absorption) and electrical (limited voltage and back recombination) aspect are impacted in the perspective of very thin (500 nm) and ultrathin (100 nm) absorber solar cell. In the following part, optical simulations are done to suggest potential solutions that may allow to overcome the parameter's limitations previously reported. Our solutions will first focus on the intermediate 500 nm CIGSe thickness (first regime), which already provides a substantial saving of material where the photocurrent is the only parameter that needs to be improved compared to a state of the art thick solar cell. Solutions to increase the efficiency of an ultrathin 100 nm CIGSe solar cell will also be presented.

II.4) Analysis of potential improvements for ultrathin CIGSe solar cells

II.4.a) Introduction

In order to improve the performances of thinned absorber solar cells, an engineering of both the front and the back side of the device is needed. In this part, our study will focus on an intermediate 500 nm CIGSe, which cannot be considered as ultrathin, but offers interesting experimental short and mid-term perspectives along with a need for optimizations that can be realized as a first step in efficient thinner CIGSe solar cells. The purpose here is to improve the carrier collection and to increase the broadband light absorption in the active layer (CIGSe), which will allow the J_{sc} of the thinned CIGSe solar cell to match the J_{sc} of a standard thick absorber device. The effect of reducing the losses in the supporting layers (front and back side) is modeled, by using an anti-reflection coating (ARC), a buffer layer with a wider bandgap, and a more reflective back contact. In addition, the effect of a p+ doped electron blocking back layer to reduce the back contact recombination is also presented.

II.4.b) Front and back side optical engineering for efficient light management

Identifying the regions of the thinned absorber solar cell where the optical losses occur is a key issue for designing light management solutions. In the following, a complete CIGSe solar cell stack Mo-500 nm/CIGSe-500 nm/CdS-50 nm/ZnO:i-70 nm/ZnO:Al-400 nm is modeled and the light absorption of each layer depending on the wavelength is calculated. These calculations were performed at the Institut d'Optique by Dr. Nir Dahan and Prof. Jean-Jacques Greffet. For the optical modeling, the structure is considered as a stratified media with flat interfaces where the electromagnetic waves can be calculated at each position for any wavelength λ, incident angle θ_i, and polarization p. Here, the transfer-matrix method is used to calculate the spectral absorption in layer m with thickness L by

$$A_\lambda(\theta_i, m, p) = \frac{[\mathbf{S}(m,0) - \mathbf{S}(m,L)] \cdot \hat{z}}{\mathbf{S}_i(\lambda, \theta_i, p) \cdot \hat{z}}$$

where $\mathbf{S}(m,l)$ is the Poynting vector of the electromagnetic field in layer m at position l, $\mathbf{S}_i$ is the Poynting vector of the incident field, and $\hat{z}$ is a unit vector normal to the interface (here in direction z). It is assumed that the solar light is unpolarized; therefore, the spectral absorption is given by an average of both polarizations

$$A_\lambda(\theta_i,m) = \frac{1}{2}\left[A_\lambda(\theta_i,m,\mathrm{TE}) + A_\lambda(\theta_i,m,\mathrm{TM})\right]$$

where TE and TM are the transverse electric and magnetic modes respectively. The back contact is regarded as a semi-infinite layer since its thickness is much larger than the penetration depth of light. It is found that the absorption in the layers does not depend on the angle of incidence up to almost 80° (not shown here). Therefore, for simplicity, only calculations when illuminating light in normal direction are shown.

Figure 8.a presents the simulated absorption in each different layers of a 500 nm thick standard CIGSe solar cell. In this default configuration, the total absorption in the CIGSe layer is only 57 % (grey area) which corresponds to a J_{sc} of 25.03 mA.cm^{-2} if a 100% internal quantum efficiency in the CIGSe is considered. We can identify two major sources of loss (yellow area and black area). As can be seen on the yellow area, a significant part of the incident photons is absorbed in the 400-500 nm wavelength range and these photons do not contribute to the J_{sc}; this is due to the CdS buffer layer, which has a relatively low bandgap (2.4 eV). This problem has been extensively studied in the past decade based on the development of alternative buffer layers such as ZnS or In_2S_3 [46]. In this study, the use of the buffer bilayer ZnS/ZnMgO [47, 48] has been proposed. Thanks to its higher bandgap compared to CdS (3.6 eV versus 2.4 eV), the ZnS/CIGSe junction efficiently collects the carrier generated by the 400-550 nm photons. When changing the initial stack to the Mo-500 nm/CIGSe-500 nm/ZnS-50 nm/ZnMgO-70 nm/ZnO:Al-400 nm stack, the absorption in the complete device increases up to 63% as shown figure 8.b. In this configuration, the absorption in CIGSe is greatly enhanced in the 400-550 nm wavelength range without affecting the rest of the spectrum which leads to a total absorption increase of +6 % in the active layer. This leads to a significant improvement of the short circuit current which increases from 25.03 for the default configuration up to 27.78 mA.cm^{-2}. Figure 9.a summarizes the expected photocurrent increase depending on the CIGSe thickness when the CdS buffer layer is replaced by ZnS. Electrical losses are not taken in account in these calculations. Whatever the CIGSe thickness, the J_{sc} increase is roughly constant.

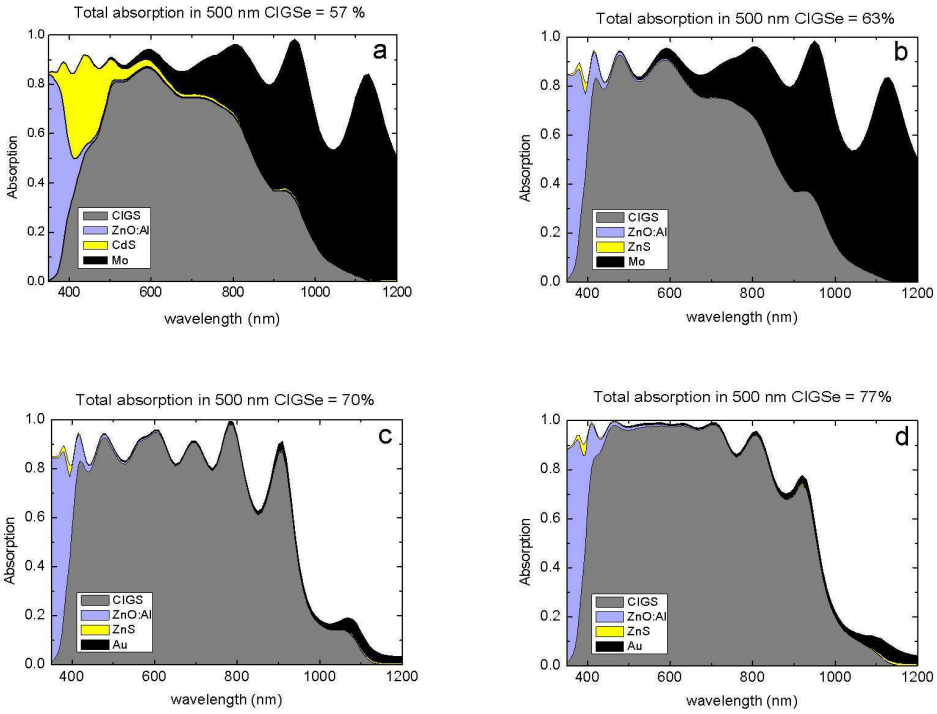

Figure 8. Spectral absorption calculated in the different layers of (a) a standard CIGSe structure (CdS buffer and Mo back contact); (b) alternative ZnS buffer layer; (c) ZnS and Au back contact; (d) ZnS, Au and ARC

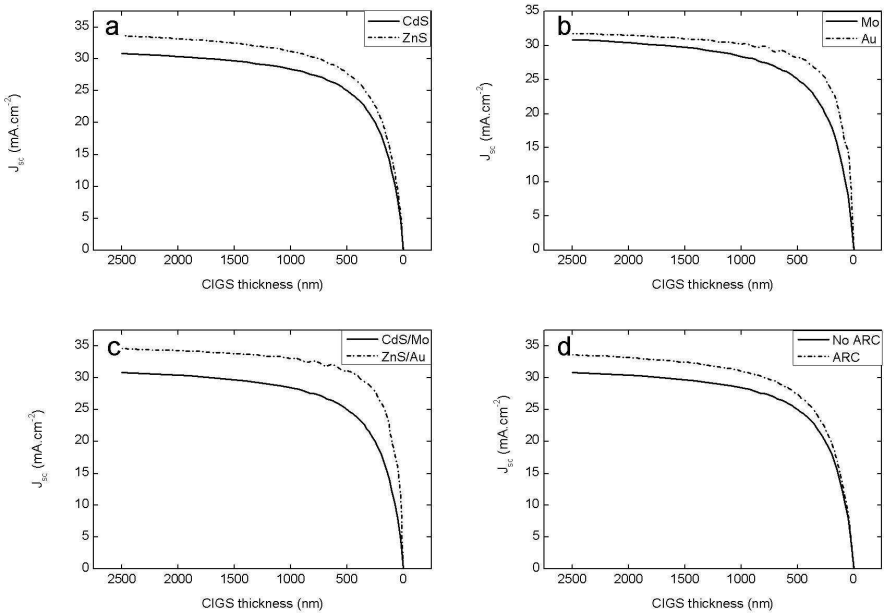

Figure 9. J_{sc} of CIGSe solar cells when varying the absorber thickness with standard and modified conditions: (a) CdS versus ZnS buffer layer: (b) Mo versus Au back contact; (c) Cd/Mo versus ZnS/Au; (d) No Arc versus ARC.

In Figure 8.a, we can also observe that another important loss in a standard CIGSe solar cell stack occurs in the 600 nm to 1100 nm (CIGSe bandgap) range due to light absorption by the Mo back contact (black area); a significant part of the low energy incident photons is not absorbed in the first pass through the thinned 500 nm absorber (see the penetration depth in the CIGSe figure 6) and decays into the back contact due to the poor reflectivity of the metal [49]. To overcome this, it is required to replace the Mo by a more reflective metal as it was suggested by different groups [3041]. When replacing Mo by a reflective metal such as Au as back reflector, we clearly see on figure 8.c that the absorption in the back contact vanishes almost completely and the total absorption in CIGSe increases up to 70 % if combined with ZnS buffer layer. Figure 9.b presents the J_{sc} comparison between a Mo back contact and an Au back contact for a CIGSe solar cell with different absorber thickness. We see that the Au mirror allows to maintain the J_{sc} of a 500 nm thick CIGSe solar cell to a high value (28.3 $mA.cm^{-2}$) close to the reference thick solar cell J_{sc} (30.8 $mA.cm^{-2}$) while the J_{sc} progressively decreases for the Mo back contact solar cell and is only 25 $mA.cm^{-2}$ for a 500 nm CIGSe solar cell. While the replacement of CdS by ZnS leads to a constant gain in the J_{sc} whatever the CIGSe thickness, replacement of Mo by Au leads to a shift in J_{sc} that increases when reducing the CIGSe thickness. Figure 9.c illustrates the direct impact on the J_{sc} of the combination of an Au back contact with a ZnS buffer layer compared to the default Mo back contact with CdS buffer layer configuration. In this case, the J_{sc} is maintained at 31.1 $mA.cm^{-2}$ for a 500 nm CIGSe solar cell, which is higher than the reference thick CIGSe solar cell with CdS buffer layer and Mo back contact (30.8 $mA.cm^{-2}$).

Figure 8.d shows the impact of the addition of an antireflection coating (ARC) on the stack with a ZnS buffer layer and an Au back contact. The total absorption in CIGSe is increased up to 77 % and the only remaining parasitic absorption comes from the ZnO:Al in the U.V. range (~3.4-3.5 eV bandgap); the complete ZnS buffer layer-Au back contact-ARC stack increases the Jsc of a 500 nm CIGSe solar cell up to 33.80 $mA.cm^{-2}$. Figure 9.d shows the direct impact on the photocurrent of an ARC on a CIGSe solar cell with different absorber thicknesses and a standard CdS buffer layer – Mo back contact. Similar to the case of ZnS, the improvement due to the ARC is constant whatever the thickness of CIGSe.

We have demonstrated that it is possible, in a 500 nm CIGSe solar cell, to fully recover and even to exceed the absorption and the short circuit current of a standard 2500 nm thick CIGSe

solar cell with CdS buffer layer and Mo back contact. This was made possible thanks to the replacement of the CdS buffer layer by a higher bandgap material (ZnS), but more importantly to the replacement of the poorly reflective Mo back contact by a more reflective back contact (Au), while the addition of an ARC on top of the solar cell allows an increase of the CIGSe almost equally over the entire spectrum. While the ARC and the ZnS buffer layer lead to a roughly constant increase of the J_{sc} independent from the absorber thickness, the replacement of the Mo back contact by Au leads to a greater J_{sc} increase for thinner absorber. However, the J_{sc} that we calculated here does not take in account the recombinations that take place in the device. We have previously seen that the reduction of the absorber thickness substantially increases the back contact recombination (figure 4.a), due to the increasing proximity of the back interface with the absorption region of the low energy photons particularly (figure 6 and figure 7). In the following, we study the effect of reducing this back contact recombination with energy band engineering at the rear interface of the solar cell.

II.4.c) Reduction of the back contact recombination by energy band engineering

We previously observed that when reducing the absorber thickness down to 500 nm, the back contact recombination becomes an important factor that has to be overcome in order to maintain an efficient carrier collection in the solar cell and the short circuit current. The idea is to realize a contact which would block the electrons (electron mirror) while having an ohmic behavior with the holes, as schematically illustrated in figure 10. This type of effect is similar to the $CuGaSe_2$ back layer that was introduced by Lundberg et al. [27] [32]. Several options are available; the most direct is to adapt the work function of the back metal in order to obtain the desired band bending on a p-doped semiconductor as CIGSe. This will be developed in a first part. In a second part, we will discuss on the introduction at the back contact of an interfacial p+ doped semiconductor layer with an ideal energy band positioning that will act as a perfect electron mirror at the rear side of the solar cell and so blocking the back contact recombination.

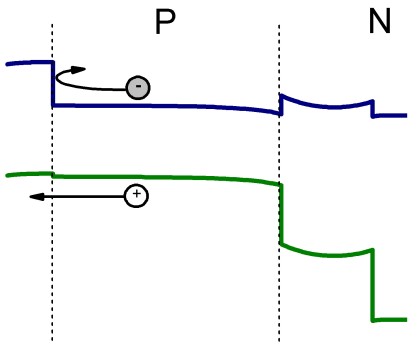

Figure 10. Illustration of the effect of an ideal electron blocking at the rear side of a CIGSe solar cell. The hole is transmitted to the metal while the electron is "reflected" toward the n-doped region

II.4.c.i) Tuning the energy bands with the metal work function

If we don't consider any intermediate layer between the CIGSe and the back contact, and without any surface state or other anomalies, the semiconductor-metal contact can be described as shown in figure 11.a [50]: the electronic energy relations of a high work function metal and a p-type semiconductor which are not in contact. As shown in figure 11.b and based on the Anderson model approach [51], when they are brought together, charge will flow from the semiconductor to the metal and thermal equilibrium is established as a single system, and the Fermi level on both sides lines up. Relative to the Fermi level in the metal, the Fermi level in the semiconductor is lowered by an amount equal to the difference between the two work functions (figure 11.b).

In the vacuum, the work function is denoted ϕ_M for the metal and ϕ_{SC} for the semiconductor, with $\phi_{SC} = \chi + |E_F - E_C|$ where χ is the electronic affinity of the semiconductor, E_c is the edge of the conduction band and E_F is the Fermi level of the semiconductor in the vacuum. The potential difference between the two work functions is called the contact potential. When the metal and the semiconductor are brought into contact, the junction becomes transparent to the holes, and the electrons are blocked by the barrier in the conduction band of the semiconductor, which thus acts as an electronic mirror. The built-in potential φ_{BI} represents in this case a barrier for the electrons, whereas the holes can transfer from the semiconductor to the metal. This example is the ideal case where the work function of the metal is slightly

higher than the work function of the semiconductor. When $\phi_M < \phi_{SC}$, the band bending of the semiconductor at the junction is reversed and in this case, the back contact acts as a sink for the electrons which can therefore drift from the semiconductor to the metal and recombine. In addition, a wrong sided band bending may reduce the V_{oc} of the solar cell because of incomplete quasi-Fermi level separation. It is the case for an ultrathin absorber where the influence of both the back contact and the p-n junction are close enough to overlap within the absorber.

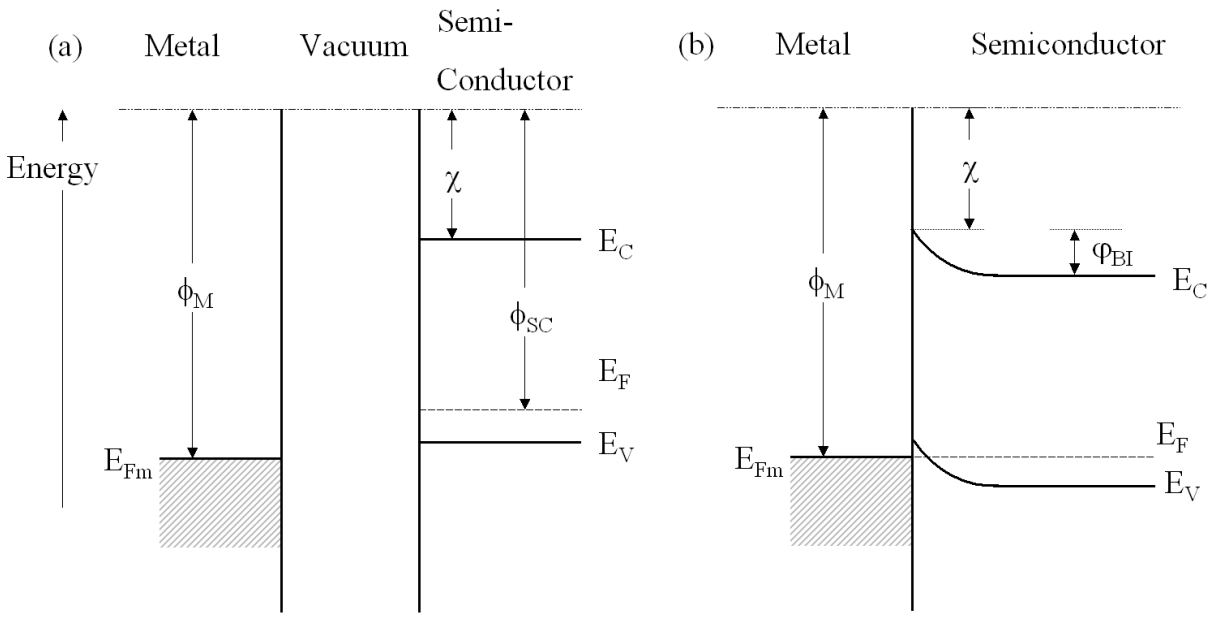

Figure 11. Illustration of the metal / p-doped semiconductor contact. (a) before the contact; (b) after the contact

The electronic affinity of the CIGSe is $\chi = 4.5\,eV$ (see Gloeckler baseline [42]), the bandgap is $E_g = 1.1\,eV$ and the majority carrier concentration is $n_p = 2.10^{16}\ cm^{-3}$. The CIGSe being p-doped, its Fermi level is $5.05\,eV < E_F < 5.6\,eV$ at equilibrium. The only metal which work function is high enough to achieve $\phi_M > \phi_{SC}$ is the platinum Pt ($\phi_{Pt} = 5.7\,eV$) whereas Au that was used previously for the optical simulation has a lower work function ($\phi_{Au} = 5.1\,eV$) [52]. Mo, the most commonly used back contact, has an even much lower work function ($\phi_{Mo} = 4.6\,eV$).

Using SCAPS, we plot the band diagram of CIGSe solar cells with a Pt back contact, an Au and a Mo back contact (Figure 12 a., b. and c. respectively). When using Au or Mo as back contact, we obtain a rectifying diode at the back side, whereas Pt allows an ohmic contact formation for the holes with a small barrier for the electrons. This results is in contradiction with experimental observations where both Mo and Au are reported to form an ohmic contact on CIGSe. This is an indication that in the case of these two metals, the Anderson model fails to describe their electrical interface with CIGSe, and the formation of additional interfacial layer needs to be considered.

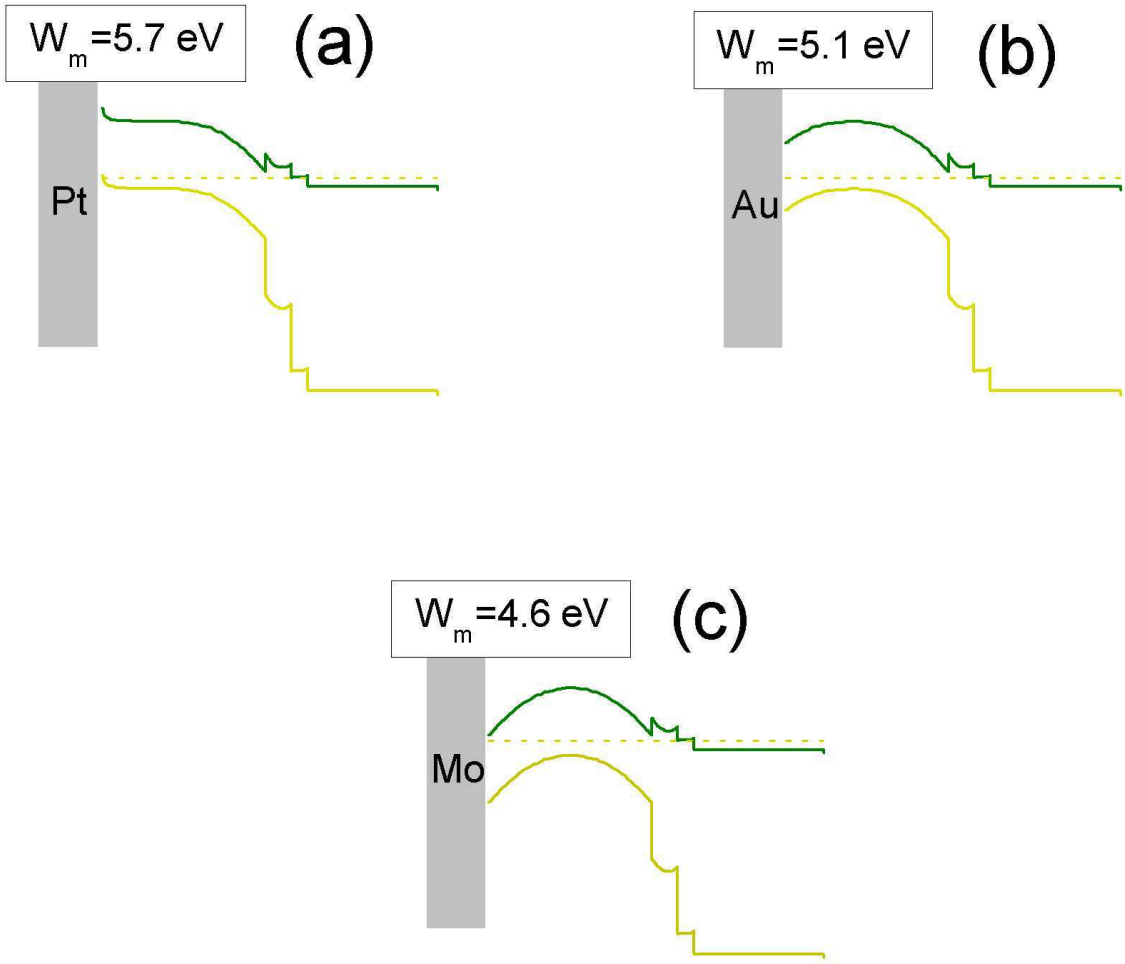

Figure 12. Influence of the work function of the back metal on the band bending of the CIGSe. (a) ohmic Pt back contact; (b) rectifying Au back contact; (c) rectifying Mo back contact

In the case of Mo, the modeling of a 500 nm solar with the $\phi_{Mo} = 4.6\ eV$ work function led to a 0.06% efficient solar cell and presenting the results here would not be of any interest. Therefore, only Au will be taken as an illustration of a rectifying back contact on CIGSe for the following discussion.

The simulated J-V characteristic along with photovoltaic parameters of the 500 nm CIGSe solar cells with Au and Pt back contact are presented on figure 13.a, and the back contact recombination current is presented figure 13.b. The reflectivity of the different back contacts is not taken in account in these simulations in order to decouple the optical and the electrical issues. In this configuration, the J_{sc} of the Pt solar cell is much higher than the Au solar cell (25 $mA.cm^{-2}$ versus 21 $mA.cm^{-2}$); this 4 $mA.cm^{-2}$ difference perfectly matches the shift between the two solar cells observed in the back contact recombination currents presented on figure 13.b. The recombinations also impact the FF of solar cells which is reduced from 75 % for the Pt back contact down to 68 % for the Au back contact. As expected from the band diagram of figure 12, the V_{oc} is reduced for the Au back contact at 520 mV, compared to the Pt back contact (700 mV) because of the overlapping influence of the Au rectifying back contact and the p-n junction. The back contact recombinations are clearly visible on the EQE curves of figure 13.c, where the low energy photons are much more affected in proportion with the Au back contact because of their more important penetration depth, whereas the barrier with the Pt back contact prevents the electrons from reaching the metal; in the case of the Pt back contact, the photocurrent is only dependent on the absorption of the 500 nm CIGSe layer.

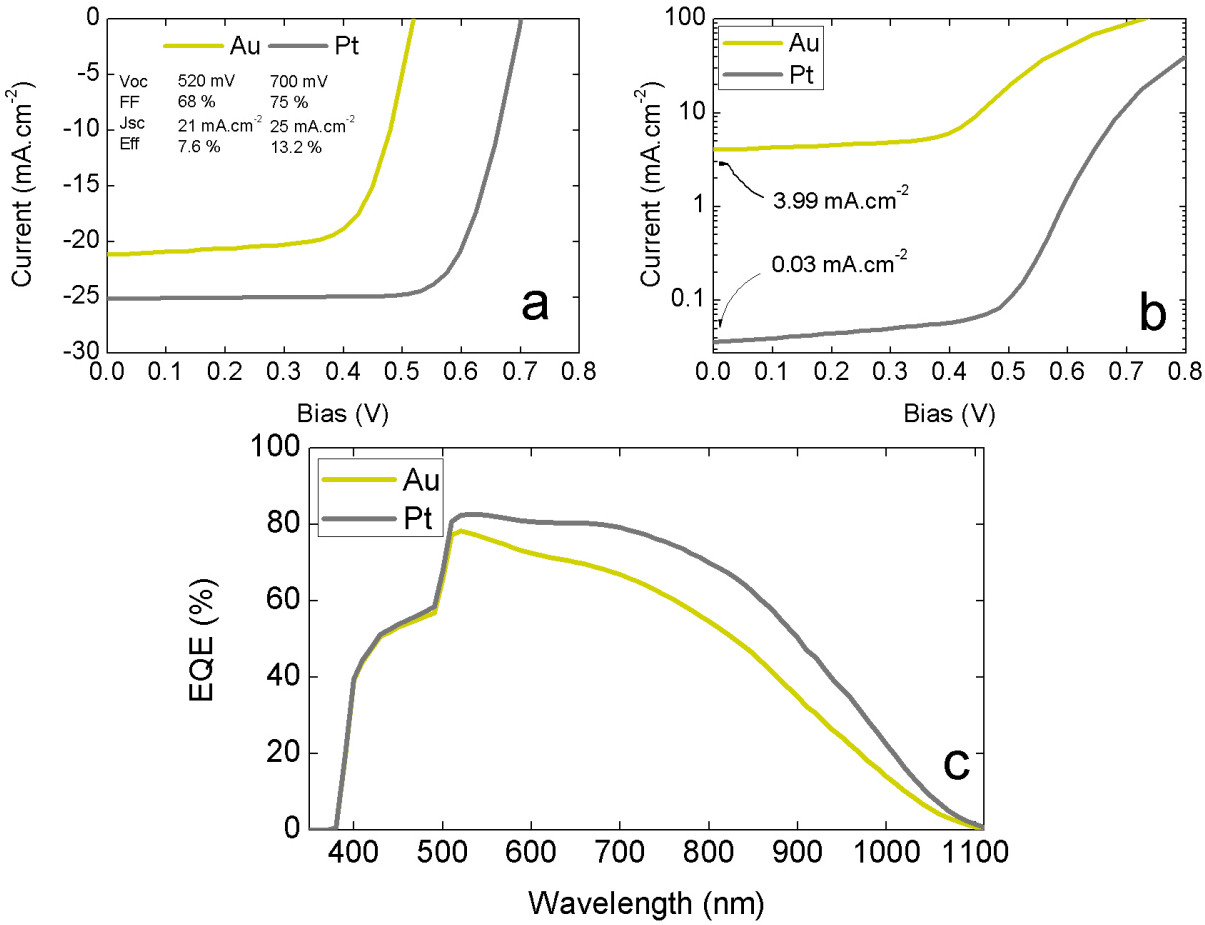

Figure 13. (a) Simulated J-V characteristic of a 500 nm CIGSe solar cell with Au and Pt back contact. The reflectivity of the back contact is fixed a 0% in each case; (b) corresponding back recombination currents; (c) corresponding External Spectral Response curves.

In this part, we have investigated on the influence of the metallic back contact work function in the back contact recombination process of a 500 nm CIGSe solar cell. We have seen that when no interfacial layer is considered, a high work function metal is required to achieve a good ohmicity and not degrading the photovoltaic properties of the solar cell. In addition, if the work function of the metal is lower than the Fermi level of the CIGSe, the overlap of the influence of both the p-n junction and the back contact becomes a problem by affecting the quasi-Fermi level separation and thus reducing the V_{oc}, which would less be the case for a thick 2500 nm CIGSe solar cell. However, the Anderson model that we used in this study does not consider any interfacial layer that may results from the reaction between the metal and the semiconductor. Experiments showed that a perfect metal-semiconductor interface like we considered here almost never occurs in a real device; when the Mo/CIGSe is studied using

the Anderson model only ($\phi_{Mo} = 4.6\,eV$), the quality of the back contact would be very poor compared to what it is in reality. The well known $MoSe_2$ interfacial layer greatly improves the ohmicity of the metal/semiconductor in the CIGSe solar cell. Similarly, Moons et al. [53] reported a good ohmicity for the Au/CIGSe contact. Therefore, some relatively low work function metals offering interesting optical properties should not be excluded from the experiments.

Instead of relying on tuning the back contact with the metal work function, another idea is to introduce a p-doped interfacial layer with the desired band positioning. In the following, we will discuss on the influence of this so called electron blocking layer or back surface field (BSF) at the back contact of a 500 nm CIGSe solar cell.

II.4.c.ii) Introduction of an electron blocking layer (back surface field)

The introduction of a very thin interfacial layer between the CIGSe and the metal may help to reduce the increasing influence of the back contact recombination when reducing the absorber thickness. This "back surface field" (BSF) should act as a perfect electron mirror while being an ohmic contact for the holes; a p+ doping ($N_a = 2.10^{18}$ in our simulations) along with a relatively wide gap ($E_g = 1.4eV$ in our example) for a good transparency is required. This layer should be as thin as possible. SCAPS simulations of a 500 nm thick CIGSe solar cells are performed and the influence of a 10 nm BSF is studied. The parameters of the BSF are summarized in Appendix I of this chapter. Figure 14.a shows the band diagram of a 500 nm thick CIGSe solar cell where an BSF is introduced at the back side of the device, and a comparison of the J-V characteristic, the EQE and the back contact recombination with and without the BSF are shown on figure 14.b, 14.c and 14.d respectively. For the default configuration without BSF, the band alignment between the CIGSe and the metallic back contact is meant so that the bands of the CIGSe are relatively flat; the work function of the metal is taken at a value close to the fermi level of the CIGSe(~5.5 eV). The short circuit current increases from 22.6 $mA.cm^{-2}$ without the electron blocking layer up to 25.2 $mA.cm^{-2}$ with the BSF (figure 14.b). As can be seen figure 14.d, this 2.6 $mA.cm^{-2}$ increase corresponds exactly to the reduction of the back contact recombination by the ideal electron mirror at the back contact, compared to the flat band default configuration. Moreover, the introduction of this large bandgap interfacial buffer layer enhances the quasi fermi level separation, and the

open circuit voltage increases from 600 mV without BSF up to about 680 mV. The overall efficiency increases from 9.9% without BSF up to 12.9% with the BSF.

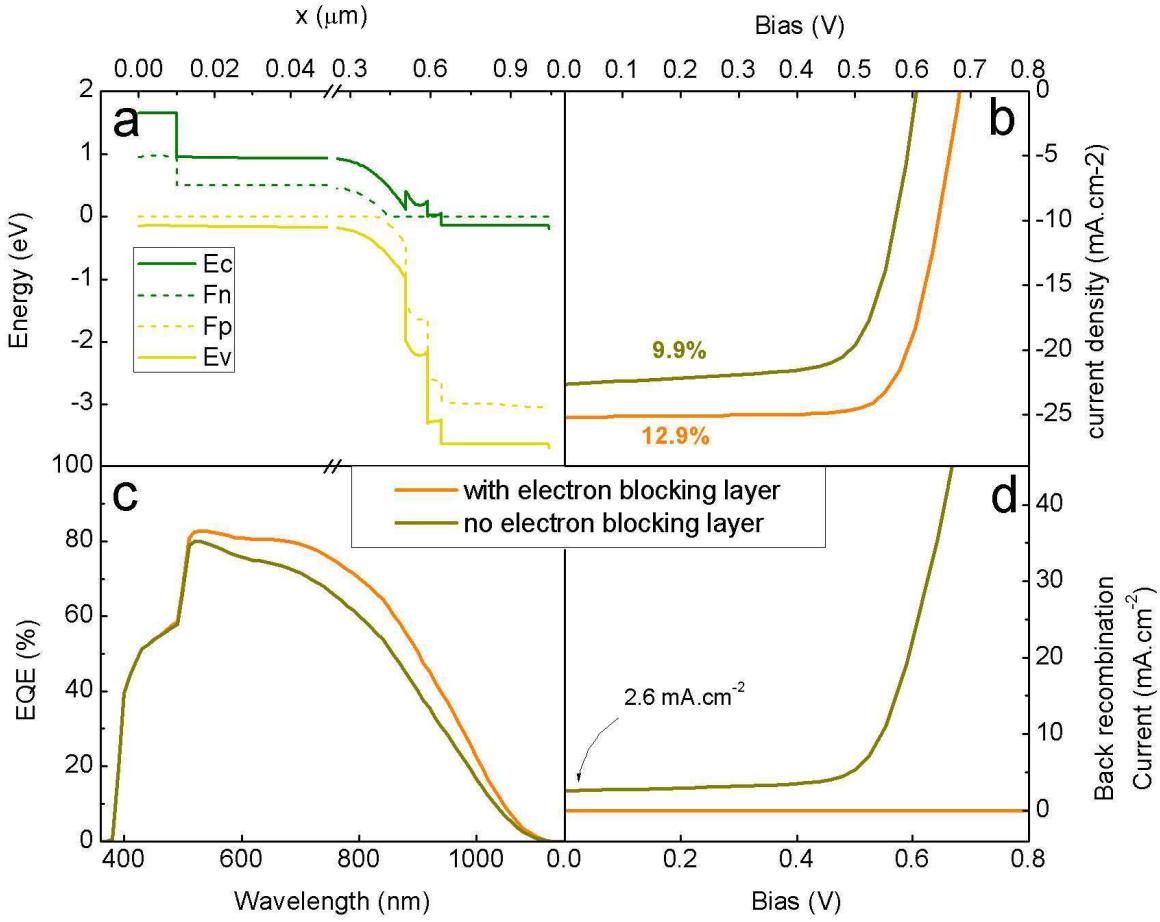

Figure 14. (a) band diagram of a 500 nm CIGSe solar cell with an interfacial 10 nm thick back surface field (BSF); (b) External Quantum Efficiency of a 500 nm CIGSe solar cell with and without BSF; (c) corresponding back recombination currents.

In order to fully take advantage to both electrical and optical improvement, the ideal situation is to combine a reflective back contact with an electron blocking layer. Moreover, achieving a good ohmicity at the back side with an interfacial buffer layer allows one to use a back contact which has a higher reflectivity than a metal. This situation is illustrated in the following. Figure 15.a present the SCAPS simulated EQE of a 500 nm CIGSe with no reflectivity at the back contact and no electron blocking layer. In this case, the combination of non absorption of low energy photons and back contact recombination dramatically reduces the EQE in the IR wavelength range as previously discussed. The short circuit current in this configuration is 22.4 $mA.cm^{-2}$. The EQE of a 1000 nm CIGSe solar cell without BSF and no back reflectivity is plotted as a comparison, showing an absolute current increase of 2.9

mA.cm^{-2} (at 25.3 mA.cm^{-2}) compared to the 500 nm solar cell. This increase is only related to the absorption of the extra +500 nm of material. When a back surface field and an ideal 100 % reflective mirror are added to the 500 nm solar cell, it largely outperforms the 1000 nm solar cell and the Jsc is 28.1 mA.cm^{-2}, representing an increase of + 5.7 mA.cm^{-2}. The corresponding J-V characteristic are shown figure 15.b. The combination of both a perfect optical and electrical management allows to fully recover the current of the standard thick solar cell that was previously presented at the beginning of this chapter (figure 2). As a result, the efficiency of the 500 nm CIGSe solar cell with BSF and 100 % back reflectivity is $\eta = 14.2\%$ (9.8% for 500 nm CIGSe 0% reflectivity and no BSF, and 11.7% for the 1000 nm CIGSe). It is very important to highlight the fact that these improvements have been achieved with simple one-dimensional structures and realistic material properties for the BSF.

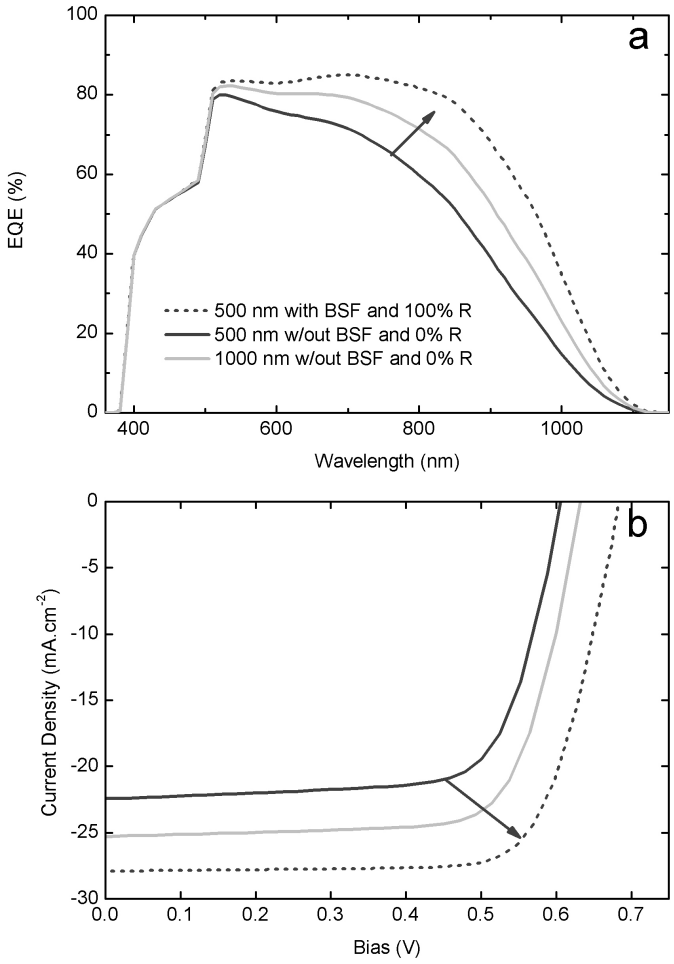

Figure 15. (a) External quantum efficiency curves of a 500 nm CIGSe solar with no reflectivity at the back contact and no electron blocking layer (dark solid grey line); same solar cell with a BSF and a 100 % reflective back contact (dark grey dotted line). Light grey line: 1000 nm CIGSe, no BSF, 0% reflectivity; (b) J-V characteristic

II.4.d) Potential improvements for an ultrathin 100 nm CIGSe solar cell

To increase the efficiency of an ultrathin 100 nm CIGSe absorber solar cell, the challenge is to overcome the very low absorption of the material along with the limitation of the V_{oc} that appears when the absorber thickness is lower than the space charge region width. In the following part, we address potential solutions to significantly enhance the performances of ultrathin CIGSe solar cells by focusing on back side engineering of the device.

II.4.d.i) Increasing the light absorption in the 100 nm CIGSe solar cell

We previously reported the use of very reflective metals as alternative back contact on very thin 500 nm CIGSe absorber solar cells, with a significant increase of the absorption of low energy photons. Figure 16.a presents the simulated EQE curve for a 100 nm CIGSe solar cell with a 0% reflectivity at the back side, confronted to a 100% reflective back contact. The following simulations have been performed using SCAPS. We see that with a 0% back contact reflectivity (solid green line), the EQE curve is very low, even for the high energy photons. The curve peaks at $\lambda = 450nm$ with a value of 55%, before decreasing down to less than 20% at $\lambda = 900nm$. We see on the J-V curve figure 16.b that the corresponding J_{sc} is very poor ($J_{sc} = 12.2mA.cm^{-2}$). While the FF is maintained at a relatively high value (71%), the Voc is also very low (480 mV) which leads to a $\eta = 4.2\%$ efficiency.

When a 100% reflectivity is added at the rear interface of this 100 nm CIGSe solar cell (dotted green line), the J_{sc} increases up to $J_{sc} = 17.8mA.cm^{-2}$ due to the double pass of the light through the absorber. We see on the EQE curve that there is still room for a lot of improvements in the red and infrared spectral regions. Since the FF and the V_{oc} are unchanged, the efficiency only increases up to $\eta = 6.2\%$.

Standard flat 2-D mirrors, even with an ideal 100% reflectivity, are therefore found to be insufficient to achieve an efficient light absorption is a 100 nm CIGSe layer. This is of course not surprising as a flat mirror can only “double” the optical path through the absorber.

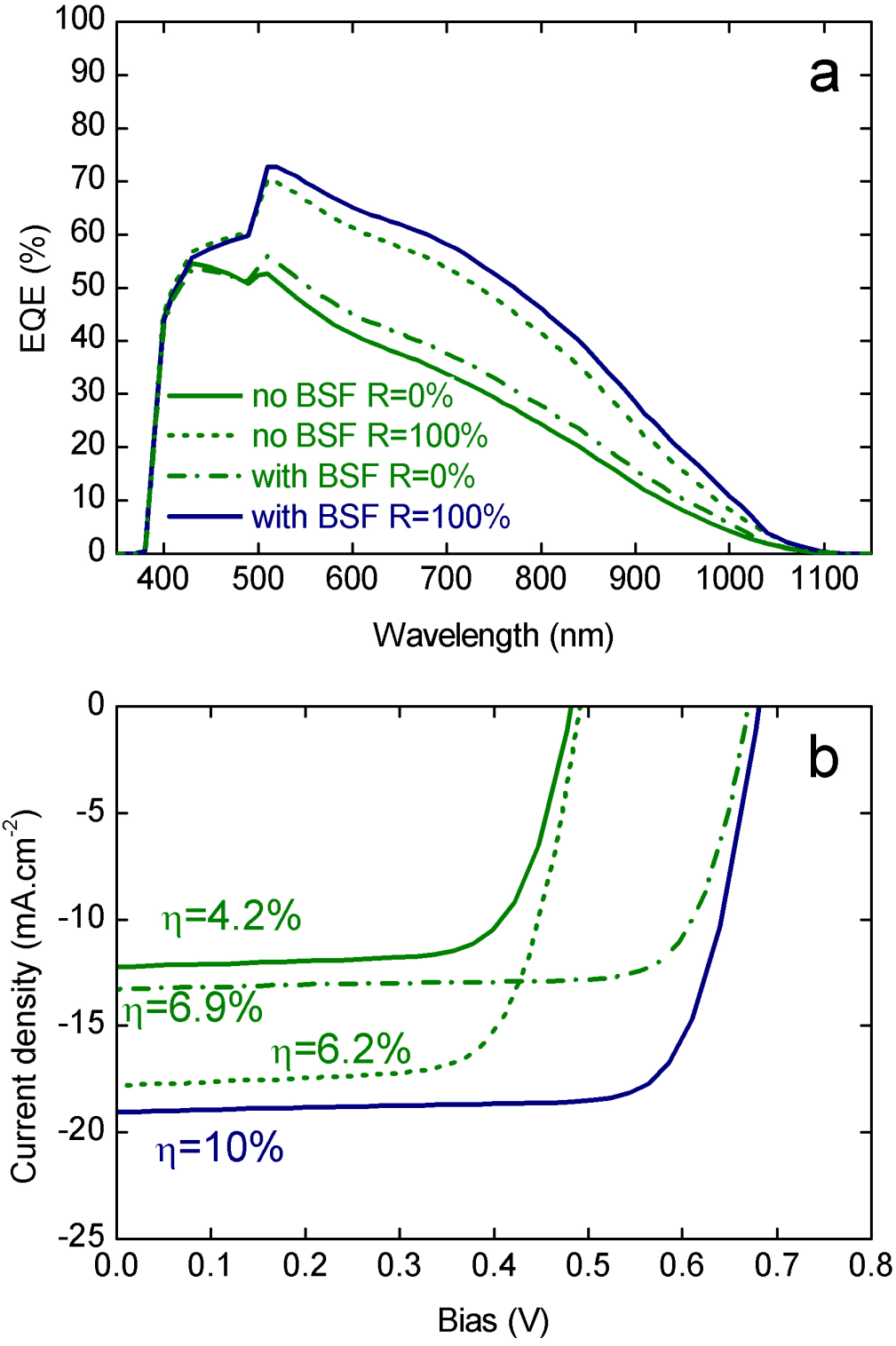

Figure 16. (a) EQE curves of a 100 nm CIGSe solar cell with: no BSF and a 0% reflectivity at the back side (solid green line); no BSF and 100% reflectivity (dotted green line); Bsf and 0% reflectivity (dot-dash line); BSF and 100% reflectivity (solid blue line). (b) Corresponding J-V curves.

In his PhD thesis, Malmström suggested the use of a lambertian back reflector to increase the light pathway through the absorber ([28], page 46 of his Thesis). Considering a lambertian reflection with an Ag mirror, he simulated the current generated in the absorber layer J_{gen}, without taking into account electric losses, and found that a 100 nm CIGSe with an Ag lambertian back reflector had a J_{gen} of 30 mA.cm^{-2}. If this ideal value is combined with the Voc and the FF we simulated for a 100 nm CIGSe solar cell without BSF, the efficiency becomes $\eta = 10.2\%$. In this case, the Voc is the only parameter limiting the efficiency of the ultrathin 100 nm CIGSe solar cell. To overcome this, we introduce the same BSF as previously done for very thin absorber solar cells.

II.4.d.ii) Increasing the voltage of the 100 nm CIGSe solar cell

The parameters of the BSF are identical to that from part II.4.c.ii) (with the 500 nm CIGSe solar cell). The SCAPS simulated EQE curve of a 100 nm CIGSe solar cell with a BSF and a 0% back surface reflectivity is presented Figure 16.a, and the corresponding J-V curve is shown Figure 16.b. We see that the J_{sc} of the solar cell is in this case only slightly affected at 13.2 mA.cm^{-2}, unlike what was observed in a 500 nm. This is consistent with the previous assessment whereby the back side recombination only has a minor influence in the case of fully depleted absorber [30]. We see on the J-V curve that the V_{oc} increases up to 680 mV, equivalent what was observed in the 500 nm CIGSe solar cell, and the FF is significantly increased up to 77%. As a result, the efficiency of the 100 nm CIGSe solar cell with the BSF and 0% back reflectivity is $\eta = 6.9\%$. When the BSF is combined with an ideal 100% reflective flat mirror, the addition of both effects leads to an efficiency of $\eta = 10\%$. Although much higher than what is obtained without any modification, this efficiency is still insufficient to compete with a reference 2500 nm thick absorber CIGSe solar cell. If we use the J_{sc} value from Malmström with lambertian back reflector [28], the efficiency of the solar cell becomes $\eta = 15.4\%$. In this ideal case, our simulations indicate that the 100 nm CIGSe solar cell can outperform the reference thick solar cell.

The simulated photovoltaic parameters of the 100 nm CIGSe solar cell with the different configurations are presented Table 2.

Configuration	Voc (mV)	FF (%)	Jsc (mA.cm^{-2})	Eff (%)
no BSF R=0%	480	71.5	12.2	4.2
no BSF R=100%	490	70.3	17.8	6.2
with BSF R=0%	680	77	13.3	6.9
with BSF R=100%	670	77	19	10
with BSF and Lambertian	670	77	30	15.4

Table 2. Photovoltaic parameters of a SCAPS simulated 100 nm CIGSe solar cell with different configurations.

II.5) Chapter Conclusion

In this Chapter, we firstly achieved the realistic simulation of a standard thick absorber (2500 nm) CIGSe solar cell using SCAPS. The material parameters have been introduced from experimental data wherever possible, and compared to state of the art solar cells parameters. Our simulated reference solar cell showed a good agreement with a reference CIGSe solar cell from Würth Solar, and so the input parameters are taken as a baseline for further simulations.

Our purpose was to study the influence of reducing the absorber thickness only (down to 100 nm) of a CIGSe solar cell on the photovoltaic parameters, and to identify the different sources of loss that affect the efficiency of the device. Two different regions, depending on the remaining absorber thickness, were identified:

- In the first regime from 2500 nm down to 500 nm, the short circuit current is the only parameter that is affected by the thickness reduction, dropping from 28 $mA.cm^{-2}$ down to 20 $mA.cm^{-2}$. Simulation of the back recombination current shows that a non negligible part of the J_{sc} comes from the increasing proximity between the region where the photons are absorbed when reducing the CIGSe thickness and the back contact which acts as a recombination surface for the electrons. The other source of loss in the J_{sc} is due to the reduced absorber thickness: despite the high absorption coefficient of the CIGSe, reducing its thickness increasingly affects the absorption of low energy photons.

- In the second regime, where the thickness is reduced from 500 nm down to 100 nm, the absorber thickness is of the same magnitude of the space charge region, and the absorber is fully depleted. The consequence is that the back contact recombinations are blocked by the strong electric field inside the absorber and the current depends only on the absorption by the CIGSe. However, the absorption of such an ultrathin layer is very low which results in an extremely poor current for the 100 nm solar cell (12 $mA.cm^{-2}$). On the other hand, the fact that the absorber is fully depleted also impact the Open Circuit Voltage which is reduced from 650 mV approximatively down to 460 mV. This is due to the early “cut” of the band bending by the extreme thickness of the absorber, which leads to an incomplete separation of the quasi Fermi levels in the CIGSe.

In order to increase the efficiency of thinned CIGSe solar cells, we decide in a first stage to focus on the absorber thickness down to 500 nm thickness; at this scale, the only issue is to increase the current of the device, and the absorber being of the same magnitude as the wavelength, simple geometrical optics engineering is still possible to apply. An optical model that calculates the different regions of the solar cell where the absorption occurs depending on the incident wavelength is used and shows that the two major losses are due to the CdS buffer layer that absorbs a non negligible part of U.V. photons, and to the poorly reflective Mo back contact. We show that by replacing the CdS buffer layer by a wider bandgap material, i.e. ZnS, it is possible to increase the absorption in the CIGSe layer by an absolute 6% value, corresponding to the U.V. photons that previously did not contribute to the photocurrent. This corresponds to an absolute 2.5 $mA.cm^{-2}$ photocurrent increase. Similarly, replacing the Mo back contact by a more reflective Au back contact allows a 7% absorption increase inside the CIGSe, which leads to a 3.3% absolute increase of the photocurrent of the solar cell. Finally, we showed that combining the alternative ZnS buffer layer with the Au back contact and an antireflection coating on a 500 nm CIGSe solar allows to outperform the J_{sc} of a standard thick CIGSe solar cell. However, these J_{sc} values don't take in account the recombination that reduces the current. Since the back contact recombination has been identified as the dominant electrical mechanism that impacts the short circuit current, we theoretically investigated on solutions that would reduce or block its influence. An illustration of the importance of the back metal work function in the p-CIGSe/metal contact is proposed using the Anderson model. We demonstrate that a high work function metal such as Pt (5.7 eV) is required in order to achieve both a good holes ohmicity and an electron barrier to prevent recombination at the back contact. In addition, we study the impact of a thin wide gap interfacial layer at the back contact with an ideal band positioning as an electron mirror. The back contact recombination is reduced to 0 and the wide gap of this material allows to increase the quasi Fermi level separation inside the CIGSe which leads to a substantial V_{oc} increase. By combining electron blocking and full solar light reflection at the back side of a 500 nm CIGSe solar cell, we show that it is possible to increase the photocurrent to the value of a standard thick device. The solutions that have been proposed are either well controlled (ZnS, ARC…) or 1D optical and electrical engineering (Mirror at the back side, electron blocking layer).

In a final part, we have investigated on improving the efficiency of an ultrathin 100 nm CIGSe solar cell. Standard flat mirrors are found insufficient to achieve a good light absorption in the CIGSe at this scale, and only the use of a lambertian back reflector leads to a

light absorption that is equivalent to that of a standard 2500 nm CIGSe solar cell. Combined with an efficient back surface field to increase the Voc, it is theoretically possible to achieve a 100 nm CIGSe solar cell with an efficiency of $\eta = 15.4\%$, starting from a reference 2500 nm solar cell with an efficiency of $\eta = 14.2\%$.

In the next Chapter, we will investigate on the effect of reducing the absorber thickness from an experimental point of view. A comparison between simulations and experience results will be proposed.

Chapter III

Experimental results on chemically etched thin of CIGSe absorbers layer; solar cells elaboration and characterizations

III.1) Introduction

In the previous Chapter about modeling the influence of the thinning of the CIGSe absorber on the solar cell, we found that the light absorption and carrier collection were the parameters limiting the efficiency of the device. These simulations have been performed assuming flat interfaces and homogeneity of the optical and the transport properties of the absorber, and no parasitic change in the properties of the material were considered. When reducing the CIGSe absorber thickness, one can unfortunately expect unwanted spreading of the material properties of the films, especially as it was reported with a direct growth method [22 23 24 27 39]. It is important to develop a technique that would allow to only reduce the absorber thickness without affecting its intrinsic properties; moreover, the well known natural texturation of the as-grown CIGSe may be a problem both for fundamental understanding of the phenomena occurring in a thinned device, as well as for the actual reduction of film thickness itself, and achieving sub-micrometer CIGSe with relatively flat interfaces is one of the challenges that must be addressed. In this chapter, we propose an alternative approach for thinning the CIGSe without altering the properties of the material. This chemical based approach allows us to have a better control of the thinning parameters, and so to get closer to the conditions of the numerical simulations.

III.2) State of the art in thinning of CIGSe absorbers

The first studies on the influence of the absorber thickness on CIGSe-based solar cells were based on a process where the absorber is directly grown at the desired thickness [22] [23]. In Chapter I, we reported the recent progresses on the study of thinned and ultrathin CIGSe solar cells with a direct growth process [24] [27]. Although directly growing the absorbers as it is done in those two studies has the advantage of being directly industry-compatible, while reducing the material use and the deposition time, it forces one to adapt its deposition process to the reduced thickness of the CIGSe layer. It results in an absorber with a quality that does not necessarily match the quality achieved for standard thick CIGSe layer: pinholes due to the surface roughness [23], smaller grain size with an increased defect density [24] [27]. This lack of control in the quality of the absorber layer makes fundamental study of the properties of the solar cells more complicated. A solution to maintain the quality of the film while reducing its thickness is to carve a reference thick layer down to the desired thickness, starting from a standard 2.5 μm CIGSe absorber. This allows to maintain the high quality of the as-grown film (large grains, controlled composition, good electronic properties) while reducing the thickness of the absorber with a high precision. However, it is important to prevent the films from any damage that the etching could cause, and an advanced characterization of the film's surface chemistry after etching is needed.

The first study on etching a $CuInSe_2$ (CISe) surface was carried out by Birkmire and McCandless [34] in 1988, using 3μm-thick CISe films that were deposited by physical vapor deposition on glass/Mo substrates in two steps as described in reference [54]. In this work, the authors reported a technique to produce specular $CuInSe_2$ films by etching the surface of the absorber with a bromine-based solution with a $[Br_2]$ concentration which was varied in the range of 0.02 $mol.L^{-1}$ to 0.25 $mol.L^{-1}$; by varying the bromine concentration, the etching rate of the surface at room temperature varied from ~0.1 $\mu m.min^{-1}$ to ~5.5 $\mu m.min^{-1}$. The nominal as-deposited surface texture was in the 1-5 μm range. The changes in the surface morphology due to the chemical etching were monitored both by scanning electron microscopy (SEM) of a fractured cross section, and by total reflectivity measurements over the 400-1400 nm wavelength range. After etching, the surface texture decreased down to less than 0.25 μm, and the total front surface reflectivity was increased from 4 % to 15 %. Energy dispersive x-ray

spectroscopy (EDX) and x-ray diffraction (XRD) measurements showed that little or no change in bulk composition or structure occurred due to the etching. The authors fabricated CuInSe2/CdZnS solar cells from which 3 % to 50 % of the as deposited 3-μm-thick films was removed. The photovoltaic parameters are presented on table 1. These results show that the open circuit voltage V_{oc} is comparable to what is measured on as-deposited CISe films, but the short circuit J_{sc} is lower. This is attributed the increased reflectivity of etched CISe films; when corrected with the reflectivity difference, the J_{sc} of etched CISe films become comparable to as-deposited CISe. Moreover, since more than 50 % of the initial thickness is removed without affecting neither the V_{oc} or the J_{sc} in large proportions, it is possible to make the assumption that both the bulk generation and collection properties of the CuInSe2 films must be uniform. This is in contradiction with the results from Noufi et al. [55] who showed that two steps grown CuInSe2 films were compositionally inhomogeneous, having a low-doped surface layer of about 0.2 – 0.4 μm (Ordered Vacancy Compound OVC).

V_{oc} (V)	J_{sc} ($mA.cm^{-2}$)	Fill Factor (%)	Efficiency (%)	Thickness of CISe layer (μm)
0.39-0.43	33.6-34.4	63.2-67.2	8.3-9.9	3
0.431	31.4	60.6	8.2	2.6
0.415	29.5	64.6	7.9	2
0.4	29.5	50.1	5.9	1.5
0.41	30	58.6	7.2	1

Table 1. Best cell parameters for CuInSe2/CdZnS devices, by Birkmire and McCandless [34]

In this study [34] however, the purpose was more to study the feasibility of smoothing CISe surface without altering the performances rather than reducing the absorber thickness in the perspective of studying its influence over the photovoltaic parameters. However, we can note that (excepted for lower Voc), the results are in relative agreement with the theoretical study showing no important decrease of the photocurrent down to 1 μm CISe.

A chemical etching process derived from the previously described method was used in 2003 by Canava et al. [35] on CIGSe surfaces; the purpose was to prepare well defined surfaces of CIGSe thin films in order to answer to basic questions about the relationship between bulk and surface composition. The CIGSe surface used were deposited by co-evaporation at ZSW [56] in order to take advantage of the well controlled industrial process which allows to obtain very reproducible CIGSe films with a composition in atomic per cent of: Cu 21.5 %, In 17.9 %, Ga 8.8 % and Se 51.8 %. In this study, the CIGSe surface was etched using a KBr/Br_2 solution with a bromine concentration in the range of 0.001-1 $mol.L^{-1}$. After etching of the surface, the authors observed the same surface morphology modification as Birkmire et al. [34] with an average roughness decreasing from 75 nm for non etched samples down to ~ 2 nm as determined with a mechanical Profilometer (Figure 1). The film thickness is also determined using the same characterization tool.

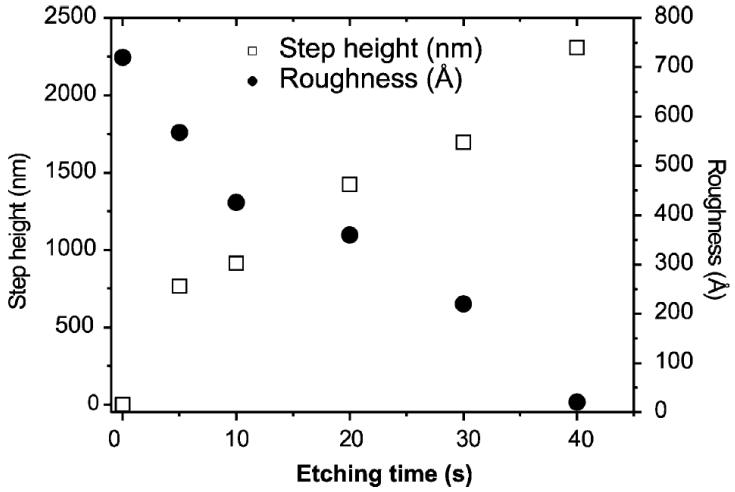

Figure 1. Step height and surface roughness variations as function of etching time in a bromine solution. Concentration of bromine in solution: 0.02 $mol.L^{-1}$ [35]

The CIGSe film remains compact after etching, without pinholes thanks to the lack of any preferential etching along the grain boundaries. The measured etching rate is about $\approx 3.5 \mu m.\min^{-1}$ with a 0.02 $mol.L^{-1}$ bromine concentration. In a previous paper, the authors showed that Br_2 etch leads to the formation of a thin Se^0 layer on the CIGSe surface which can be specifically removed using a KCN treatment [57]. The KCN treatment slightly increases

the roughness of the films. The authors focus their study on the surface composition of the CIGSe during the Br_2 etching process, and on the influence of the KCN treatment; this study was carried out using high resolution XPS (VG 220i XL system). The surface composition of Br_2 etched surface is different from the bulk CIGSe composition; the atomic compositions and atomic ratios are summarized in Table 2.

Treatment	Etching time (s)	Atomic composition (%)				Atomic ratios		
		Cu	Se	In	Ga	Cu/(In + Ga)	Cu/Se	2Se/(Cu + 3In + 3Ga)
As grown (EDX)	–	21.50	51.80	17.90	8.80	0.805	0.415	1.020
As grown	–	10.26	66.70	17.25	5.79	0.445	0.154	1.681
KCN	–	6.54	43.71	46.10	3.65	0.131	0.150	0.561
Br	5	6.93	70.85	18.57	3.65	0.312	0.098	1.925
Br	10	5.07	71.91	18.24	4.78	0.220	0.071	1.940
Br	20	10.52	44.86	38.05	6.58	0.236	0.235	0.621
Br	40	10.22	45.01	36.54	8.24	0.228	0.227	0.623
Br + KCN	5	5.63	41.70	50.34	2.34	0.107	0.135	0.510
Br + KCN	10	9.29	49.22	37.36	4.14	0.224	0.189	0.736
Br + KCN	20	8.48	52.18	35.76	3.58	0.216	0.163	0.825
Br + KCN	40	10.58	57.55	26.66	5.21	0.332	0.184	1.084

Table 2. Global composition of CIGSe surfaces. Bromine solution concentration: 0.2 $mol.L^{-1}$
35

The formation of the thin Se^0 layer after Br_2 etching explains the excess in Se for etched surfaces; the KCN treatment (70°C, 2 hours) allows to obtain a CIGSe stoichiometric surface by removing Se^0 via the formation of $SeCN^-$ complexes, and possible Cu_xSe phases since CN^- is also a strong complexing agent for Cu^+ and Cu^{2+} species. After etching, the surface composition is situated on the Cu_2Se-$(In,Ga)_2Se_3$ pseudo binary tie line, which is remarkable since this composition was found for the first time after etching, while it was so far only been found on as grown surface in ultra high vacuum. Under specific conditions, the surface composition was close to that of the defect compound $Cu(In,Ga)_3Se_5$ which is indeed observed for as grown CIGSe. This can be interpreted by the fact that affinity of CN^- ions for Cu is probably able to remove Cu from CIGSe. Therefore, KCN treatment after Br_2 etching showed a great potential in driving the surface chemistry back to the situation of the as-grown co-evaporated surface, which is of a great importance for devices on etched CIGSe films, since the CdS/CIGSe interface is known to be very sensitive to changes in the absorber surface composition.

A fairly preliminary study of the photovoltaic properties of Br_2-etched CIGSe solar cells was performed by Shafarman et al. in 2006 [58]. Etching the absorber allowed a precise determination of the optical constants n and k by using Spectroscopic Ellipsometry data, which requires a relatively smooth surface. The calculated values of n and k show a good agreement with previous results [59] obtained on CIGSe peeled from the Mo substrates (figure 2). The small differences in magnitude might be due to different surface contamination (oxidation for peeled CIGSe, Se excess for etched CIGSe). Working with flat interfaces also allowed to characterize with a higher precision the CdS grown by Chemical Bath Deposition (CBD) on CIGSe as it is deposited in the device; significant differences in the n and k between single crystal CdS and CBD CdS deposited on CIGSe are found, which suggest a poorer crystallinity of the CBD grown films as opposed to the bulk single crystals.

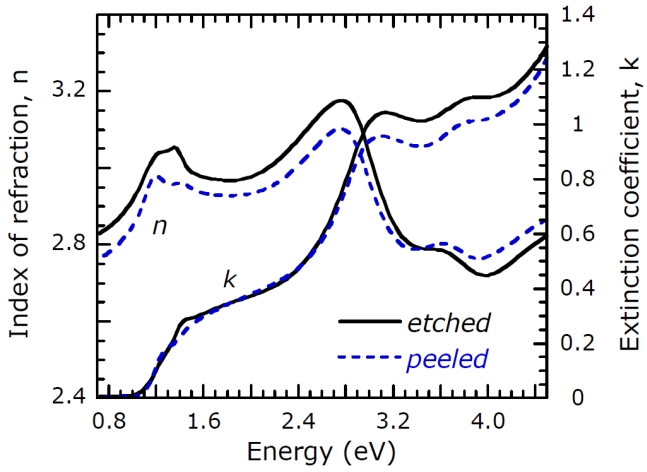

Figure 2. Index of refraction and extinction coefficient for Cu(In,Ga)Se_2 samples from a single run with smooth surfaces created by peeling and Br-etching [58]

In the work by Shafarman et al. [58], a comparison was carried out between etched samples and as-grown samples with the same thickness d, from 1.8 µm down to 0.4 µm. The results for the as-grown samples are mostly comparable to those obtained by Lundberg et al. [27]. The complete set of results comparing etched and as-grown samples is presented Figure 3. There is no decrease of the Voc which remains close to 650 mV for the as-grown samples, and close 600 mV for the etched samples except for $d < 0.5\mu m$ where it decreases in both cases. The FF remains remarkably constant at about 75 % for etched absorbers down to 0.4 µm, whereas

it decreases at about $d \approx 0.8\mu m$ for the as-grown samples, down to 60 % for the 0.4 µm sample. The decrease in Jsc observed for $d < 1\mu m$, although expected due to incomplete light absorption, is greater than expected from device simulations [30]. There is no difference between etched and non etched samples for this parameter, which suggests that the unaccounted loss in current is not due to light scattering effects which would be greater in the case of as-grown absorbers. To conclude, the authors stated that the surface termination of the as-deposited film is not as critical for the device as one could have imagined, and it can be chemically reconstructed by the KCN treatment. No change in the electronic properties of etched samples were observed compared to standard as-grown thick samples.

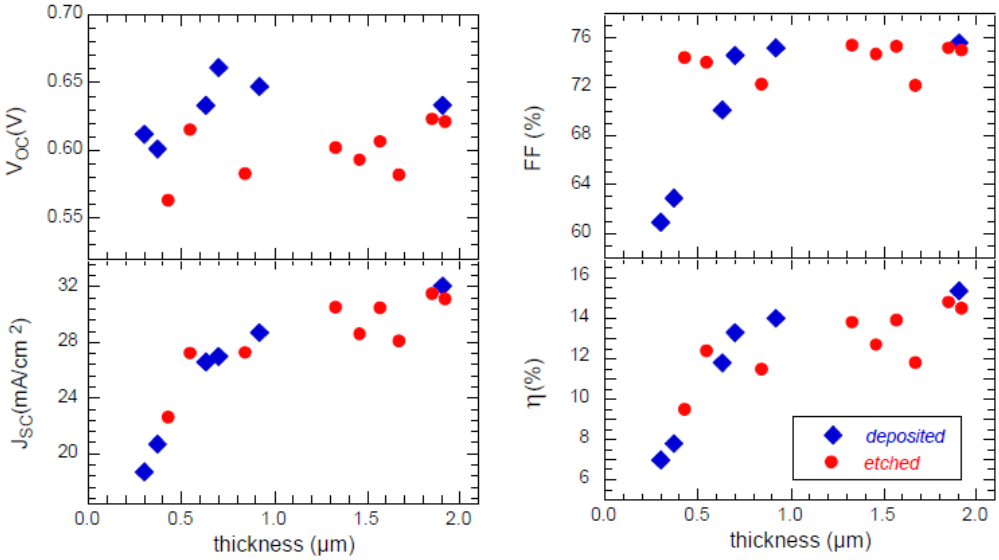

Figure 3. J-V parameters comparing devices with etched Cu(In,Ga)Se2 and with as-deposited absorber layers grown for different times [58]

On the basis of these previous studies, we have seen that for fundamental investigations, etching the CIGSe absorber in order to reduce its thickness presents numerous advantages compared to directly growing the film at the desired thickness. The chemical etching does not degrade the electronic properties of the material and allows to work with flat interface which will facilitates the theoretical investigations of the devices properties. This method gives the opportunity to work with a constant grain size and crystallinity, and “carving” the absorber permits to precisely select a slab of the CIGSe. Moreover, the smoothing effect of the

chemical etching may allow to decrease the absorber thickness to a lower level than as grown CIGSe without increasing too much the shunt effect due to the pinholes that have been observed for ultrathin as-grown CIGSe films [23].

Based on the results from literature, in this chapter we will investigate the chemical HBr/Br_2 etching on CIGSe from Würth Solar [2]. The surface chemistry will be investigated, along with the optical properties of the absorber prior and after the chemical etching. Solar cells on etched absorber using a standard CdS/ZnO:i/ZnO:Al process will be realized then optically and electrically characterized. We will also investigate on the specific influence of the CIGSe roughness over the photovoltaic properties of the solar cells.

III.3) Chemical etching of CIGSe

III.3.a) Experimental setup

In this study, we used the chemical Br_2 based etching process developed at Institut Lavoisier de Versailles by A. Etcheberry and his team and first described on CISe films by Birkmire and McCandless in 1988 [34], and further investigated on CIGSe by Canava et al. in 2003 [35]. However, HBr is preferred to KBr as a stabilizing additive for Br_2: previous experiments [60] have shown that although the dissolution rate and the asymptotic roughness remains the same between the two solutions, the surface roughness decreased significantly faster when using HBr instead of KBr. Moreover, some In and Ga oxides on the etched CIGSe surface have been observed when using a KBr/Br_2 solution; using HBr instead of KBr allows the dissolution of these oxide and leaves the CIGSe surface almost unchanged compared to a non etched surface.

The chemical process of the etching consists in an oxidation of the CIGSe surface by Bromine in two steps, as described in reference [35]. The first step is a preferential dissolution of the metals, leaving Se^0 on the surface:

$$Cu\{In,Ga\}Se_2 + \frac{5}{2}Br_2 \rightarrow Cu(II) + \{In(III) + Ga(III)\} + 2Se^0 + 5Br^- \qquad (1)$$

The oxidation of the Se^0 occurs in a second step, which is rate determining, following the equation:

$$Se^0 + 2Br_2 \rightarrow Se(IV) + 4Br^- \qquad (2)$$

Etching experiments have been carried out in a thermostated cell in order to keep the temperature close to 273 K; it has been demonstrated [60] that the etching rate of the CIGSe is temperature dependent. The samples were fixed on a horizontal rotating disk at a rate of 40 rpm. After etching, the samples were carefully rinsed in high purity de-ionized water (18.3 MΩ.cm) and dried under Nitrogen flux. The etching process was studied by titration using graphite furnace atomic absorption spectrometry (GF-AAS) for the quantification of the Ga, In and Cu dissolved during the etching treatment, and so to determine the kinetics of the etching process depending on the experimental parameters, which is a critical step when one

wants to reach ultra-thin layers without deteriorating the surface. In this study, the CIGSe surfaces are etched from the front side, but back side etching using the same process is also possible.

Before completing the etched sample with the standard solar cell process, i.e. deposition of the CdS buffer layer and ZnO front contact, the surface was superficially treated using the following [KCN] = 0.1 M process: ambient temperature and 5 minutes of treatment. This treatment does not influence the layer thickness nor its bulk composition; it is used to clean the surface from binaries compounds and Se^0, and allows to reconstruct the initial surface chemistry of as-deposited CIGSe films.

III.3.b) Results

During this study, we work on co-evaporated CIGSe coming from industrial lines of Würth Solar. Different batches of samples have been studied, and small variations appeared in their morphology or chemical composition; it is however possible to identify certain general trends that we will outline in the following.

The most critical parameter to investigate when the purpose is to reduce the absorber thickness to less than 500 nm is the etching rate, which depends on the parameters of the etching, especially the Br_2 concentration. A systematic study was carried out at the Institut Lavoisier de Versailles, by varying the Br_2 concentration in a thermostated medium, and following the concentration of the dissolved species in the solution by AAS. The [HBr]/[Br_2] concentration ratio is maintained constant at about 125. The bromine etching allows a large concentration range for the [Br_2] concentration: concentrations from $[Br_2] = 0.002M$ to $[Br_2] = 0.2M$ have been investigated.

Figure 4 presents the etching kinetics calculated determined for different [Br_2] concentrations. This figure shows the etched thickness versus etching time extracted from the titration of the Cu, the Ga and the In. The resulting CIGSe thickness is calculated using the formula $e = \frac{m}{Sd}$ where e is the resulting CIGSe thickness, m is the mass of the element that has been

dissolved, S is the surface of the sample and d is the density. When the solution is highly concentrated (0.04M in our example), the surface roughness is rapidly etched and full dissolution is reached in less than 10 minutes. For a bromine concentration of $[Br_2]$ = 0.02 M, the full dissolution of the CIGSe occurs after about 16 minutes. For this experiment, we used a different CIGSe batch, and so the thickness of CIGSe is slightly different than for other experiments. For lower Br_2 concentration however ($[Br_2] = 0.002M$), working with low Br_2 concentration increases the effect of Br_2 evaporation: the etching velocity is significantly reduced in this case and after 180 minutes, the dissolution of the sample is still incomplete. Moreover, the evaporation of Br_2 leads to higher uncertainty in the data.

As we can see on figure 4, the etching rate is roughly constant throughout the complete dissolution of the CIGSe, whatever the Br_2 concentration; the etching rates are summarized in table 3. We see that the etching rate is roughly linear with the Br_2 concentration.

Br_2 concentration ($mol.L^{-1}$)	0.04	0.02	0.01	0.001
Average rate ($nm.min^{-1}$)	345.9	176.7	80.7	6.3

Table 3. Average etching kinetics calculated from AAS measurements of Cu, Ga, Se and In species in the dissolution solution

In the following, we use $[Br_2]$ = 0.02M; this concentration presents the advantage of being important enough so that the Br_2 evaporation is not much of a problem, and the dissolution rate is stable enough to control precisely the amount of CIGSe that is removed. A serie of samples from the same batch is etched with thicknesses evaluated ranging from 0.3 μm to 2.5 μm (the complete set of results is presented in reference [61]).

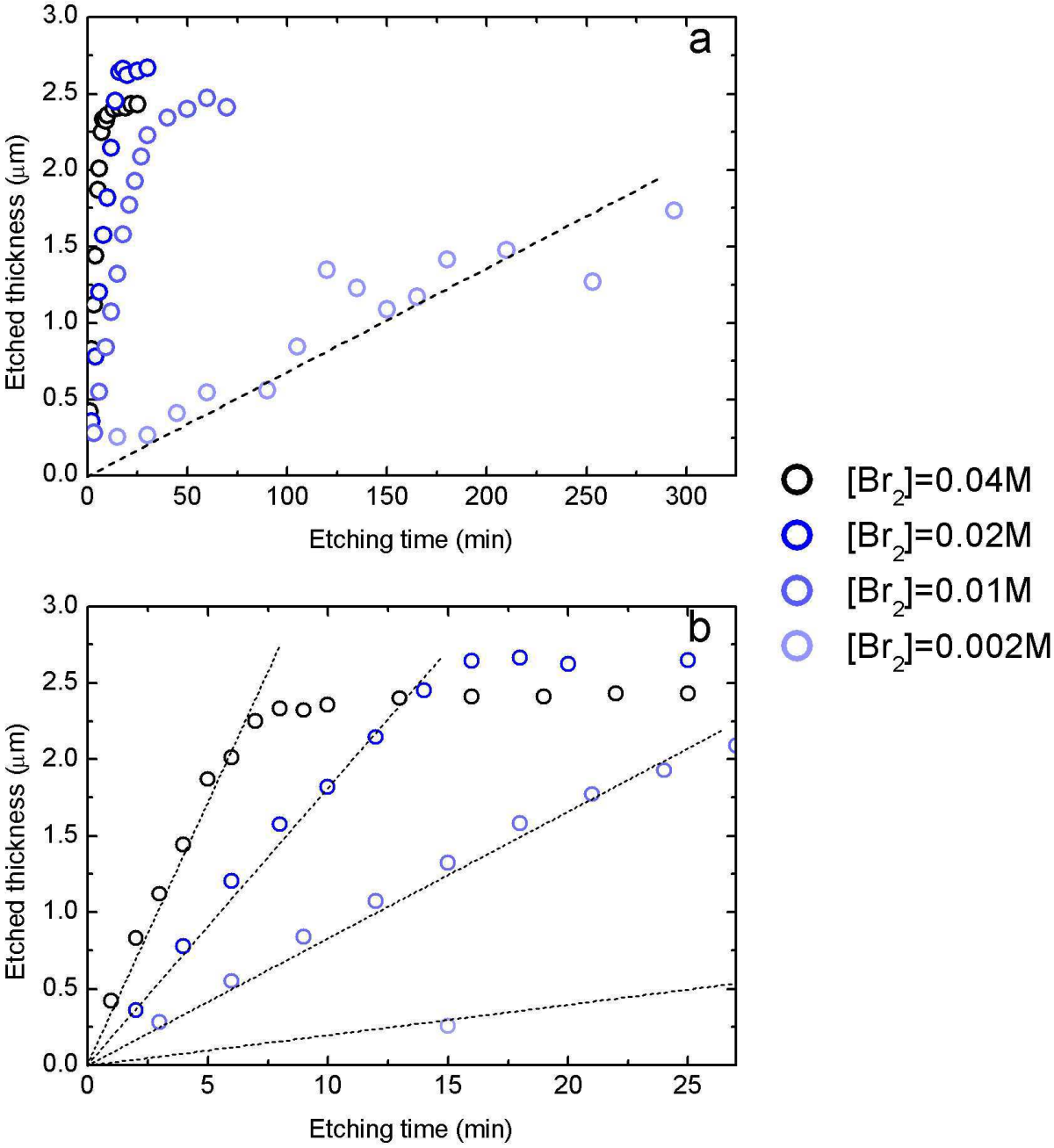

Figure 4. etched "thickness" for Cu, Se, Ga and In elements deduced from the GF-AAS titration of these elements. (a) x-axis up to 300 minutes to show the evolution of $[Br_2]$ = 0.002M; (b) x-axis up to 25 minutes.

The quasi linear time dependency of the amount of dissolved species supports the steady state character of the process which can be considered as constant on the basis of the chemical data provided by the titration procedure. We have however observed that for short etching times, the etching rate is much higher than the calculated rate for the whole CIGSe dissolution; such

observations have previously been reported by Canava et al. [35], and are attributed to the higher surface roughness of the non etched sample compared to etched sample. The determination of the etching velocity for a given batch is very important to carve the films with a very high precision, in the magnitude of $\pm 50nm$ which is perfectly suitable in the perspective of achieving ultrathin CIGSe layers. However, some edge effects on the sample are visible when the film thickness becomes lower than 1 µm; it is possible to reduce this effect by working at a temperature close to 0°C and with a relatively high Br_2 ($\geq 0.01M$) concentration.

GF-AAS allows to monitor, during the etching process, the composition of the CIGSe throughout its thickness by dosing the Cu, Ga, Se and In; we present the atomic percentage of each element in the CIGSe throughout the complete etching of the film in Figure 5.

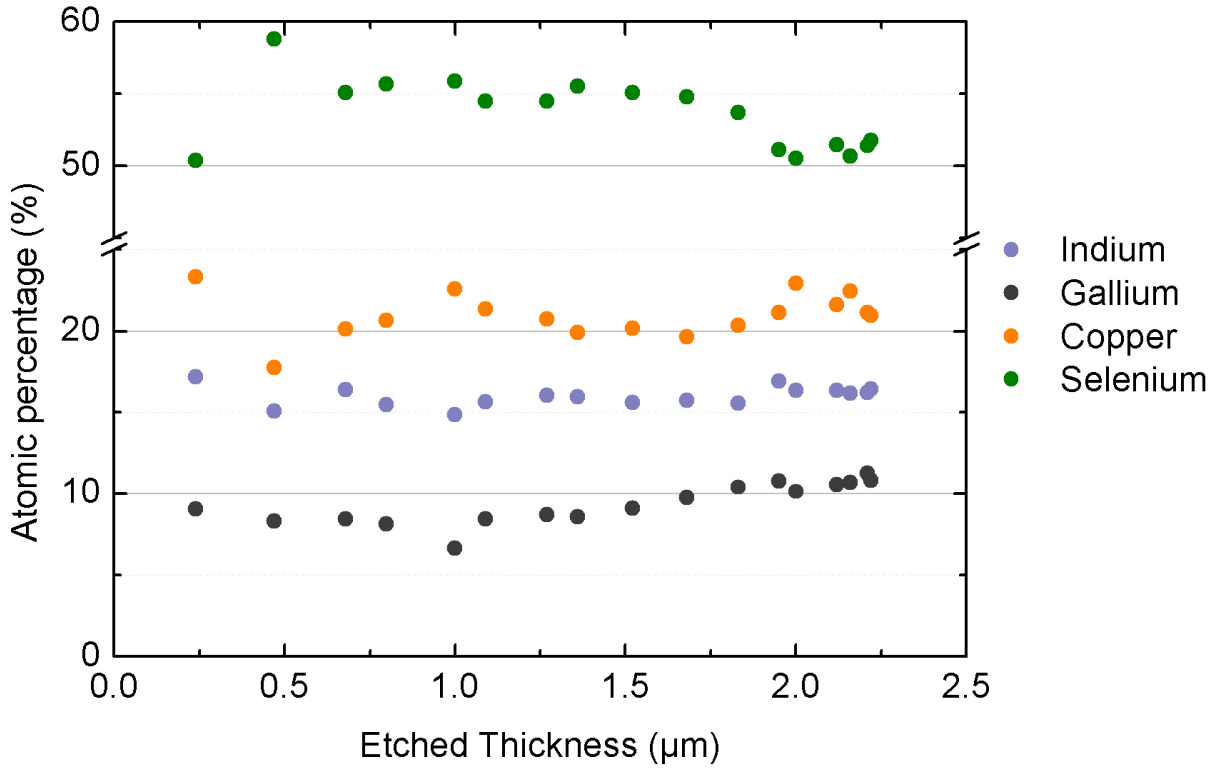

Figure 5. Atomic percentage for Cu, In and Ga elements deduced from SAA dosage

Both Cu and In content exhibit a stable trend throughout the etching, with atomic percentage of about $20.5\% \pm 2.5\%$ and $16\% \pm 1\%$ respectively. The Se content is also stable down to 1.7 µm of etched absorber, at about $55\% \pm 1.5\%$ which is slightly higher than expected from the stoichiometric composition of CIGSe. There seems to be a small Se content decrease down to

$51\% \pm 0.5\%$ at the back of the CIGSe after 1.7 µm of etched material. The Ga content is roughly stable at $8.5\% \pm 1\%$ down to 1.7 µm of etched CIGSe, before increasing up to about $11\% \pm 1\%$ at the back side of the absorber. Such Ga enrichment at the back side of the absorber is well known in CIGSe, and has also been observed more markedly in different batches during our study. The Ga grading in the CIGSe leads to a variation of the bandgap of the material from 1 eV to 1.7 eV (from pure $CuInSe_2$ to pure $CuGaSe_2$) [62].

After etching, the CIGSe seems undamaged and increasingly reflective with naked eye. A systematic analysis of the evolution of the surface with the etching is needed to investigate the potential implication that the absorber etching will have on the solar cells properties.

III.4) Characterization of etched CIGSe films

III.4.a) Material characterization

Analyzing the CIGSe films evolution (roughness, thickness, composition) is a key point in understanding the variation of the parameters of etched solar cells, since it will influence directly the light absorption/carrier collection, dependent both from the surface roughness and the doping profile of the CIGSe, and also the p-CIGSe /n-CdS interface which is highly dependent on the surface chemistry of the CIGSe. Potential damages on the CIGSe film, that may include chemical pollutions or pinholes occurrence in the layer, need to be evaluated for both validation and potential improvements of the chemical etching process.

Moreover, a precise characterization of the CIGSe thickness evolution is also needed in the perspective of the preparation of ultra-thin CIGSe layers; homogeneity and accurate etching rate are binding condition for below-500 nm thick layers in order to avoid shunts in the final solar cell stack.

Several characterization techniques have been used in this work, to monitor from surface chemistry to the layer geometry, and will be detailed in the following. More details on the characterization tools can be found in Appendix II

III.4.a.i) Surface analysis by X-Ray Photoelectron Spectrometry (XPS)

X-Ray Photoelectron Spectroscopy (XPS) is a quantitative spectroscopic non-destructive technique which allows sharp measurements of the empirical formula of chemical compounds, elemental composition, chemical state and electronic state of the elements within a material. The basic principles are described in Appendix II.

XPS surface chemical analyses were achieved in “Institut Lavoisier de Versailles” with a Thermo Electron K-Alpha spectrometer using a monochromatic Al-Kα X-Ray source (1486.6 eV). The Thermo Electron K-alpha spectrometer procedure was used to calibrate the spectrometer. It was verified using Cu and Au (Au $4f_{7/2}$ at 84.0 eV) samples following the ASTM-E-902-94 standard procedure. Charge compensation was requisite to overcome the

charging effects induced by the glass substrate. Acquisition parameters imposed in this study were the following: 400 µm spot size, 12 kV primary energy, 6.0 mA emission intensity, CAE mode (50 eV or 10 eV for high energy resolution) and 0.1 or 0.05 eV energy step size. The quantification of analyses and high energy resolution spectra fitting procedure was performed with the Thermo Fisher scientific Avantage© data system.

In order to obtain reference spectra and a reference XPS composition, the non etched CIGSe surface has been analyzed after a 2 min HCl treatment ([HCl] = 1 M) and the global survey of the surface is presented figure 6. The HCl treatment allows to deoxidize the surface, without affecting the global composition as it was demonstrated by our colleagues from "Institut Lavoisier de Versailles". In the following, the HCl treated de-oxidized surface will be taken as the reference CIGSe surface.

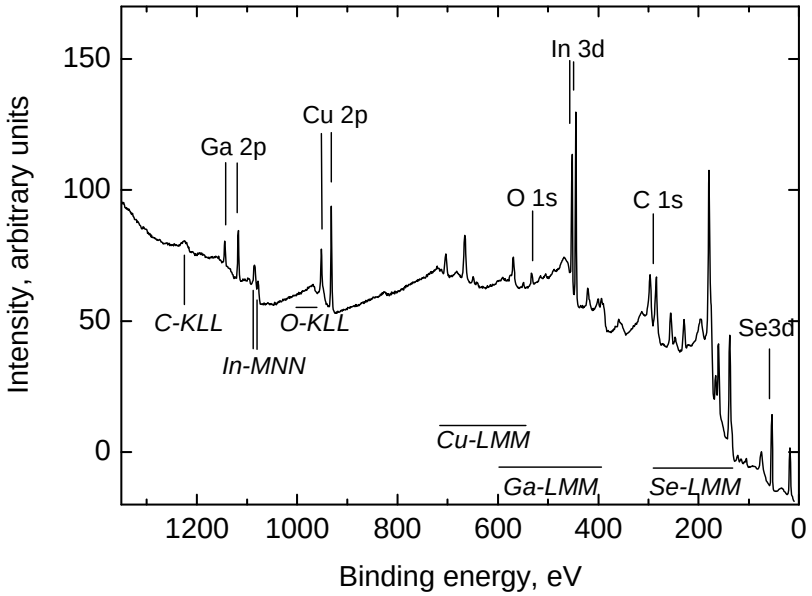

Figure 6. XPS survey of an as deposited CIGSe after a HCl treatment.

For clarity reasons, only the major peaks, used for species quantification, are mentioned in the figure: Cu 2p, Ga 2p, In 3d, Se 3d (core levels). Auger lines which interfere with some of the peaks are also mentioned (especially the Auger line Se-L3M23M45 which interferes with C

1s), along with the O 1s and C 1s peaks that are also visible and are attributed to an almost impossible to avoid carbon contamination. Na is also observed on this reference sample, but it is however not reproducible. Besides the presence of carbon, no pollution are observed on the HCl treated CIGSe surface.

An XPS analysis of the CIGSe surface after the HBr/Br_2 etching is performed for different etching durations. The figure 7 shows a comparison of the XPS spectra of Cu 2p, Ga 2p, In 3d, Se 3d and O 1s from the reference surface to a surface etched for 15.3 min (~1.2 µm of etched CIGSe) in a solution with a concentration of $[Br_2]$ = 0.01M. The binding energies and width at half maximum (FWHM) are presented on table 4. The spectra are presented after normalization in intensity. These spectra and the shape of the peaks highlight a remarkably constant surface chemistry throughout the chemical etching of the CIGSe.

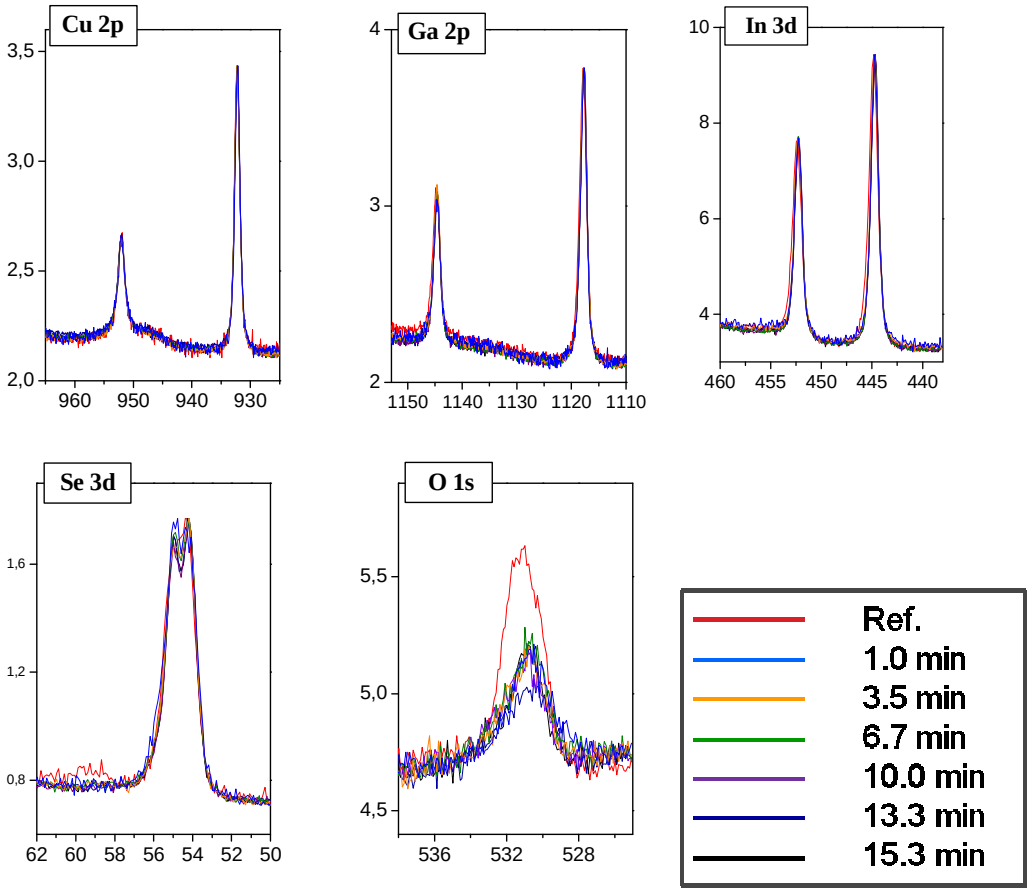

Figure 7. Superposition of the XPS spectra of Cu 2p, Ga 2p, In 3d, Se 3d and O 1s from thinned CIGSe samples in a HBr/Br_2 solution for different etching times

Peak name	Binding Energy, eV	FWHM, eV
Cu $2p_{3/2}$	932.25 ± 0.05	1.00 ± 0.05
Ga $2p_{3/2}$	1117.80 ± 0.05	1.40 ± 0.05
In $3d_{5/2}$	444.75 ± 0.05	0.90 ± 0.05
Se 3d	54.45 ± 0.05	1.60 ± 0.05

Table 4. Binding energies and width at half maximum for different elements (15.3 min of etching)

The Se 3d peak from figure 7 presents a particular shape with a splitting that highlights an additional contribution; a peak reconstruction, using the Avantage© software is presented figure 8. This additional contribution is attributed to the Se^0 already mentioned by Canava et al. [35] [57], which is a chemical intermediate in the surface oxidation process shown with equation (1) and (2). The ratio between Se_{mat} and Se^0 evolves between 0.1 and 0.2, closer to 0.1.

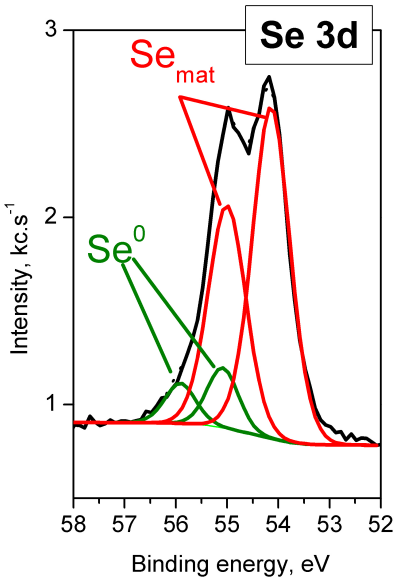

Figure 8. Reconstruction of the Se 3d peak based on a two components set : the Se 3d matrix peaks (red) and the Se0 superficial peaks (black)

The surface composition determined with XPS analysis is presented figure 9. This composition is in good agreement with the composition determined previously by GF-AAS, and also very close to the stoichiometric composition of CIGSe. During the first stages of the etching however, we notice some variations in the XPS composition; they may be related to the original surface roughness of the as-deposited CIGSe which decreases quickly with the bromine etching. An important surface roughness produces a scattering of the photoelectrons and therefore impacts the measurements, particularly by broadening the peaks.

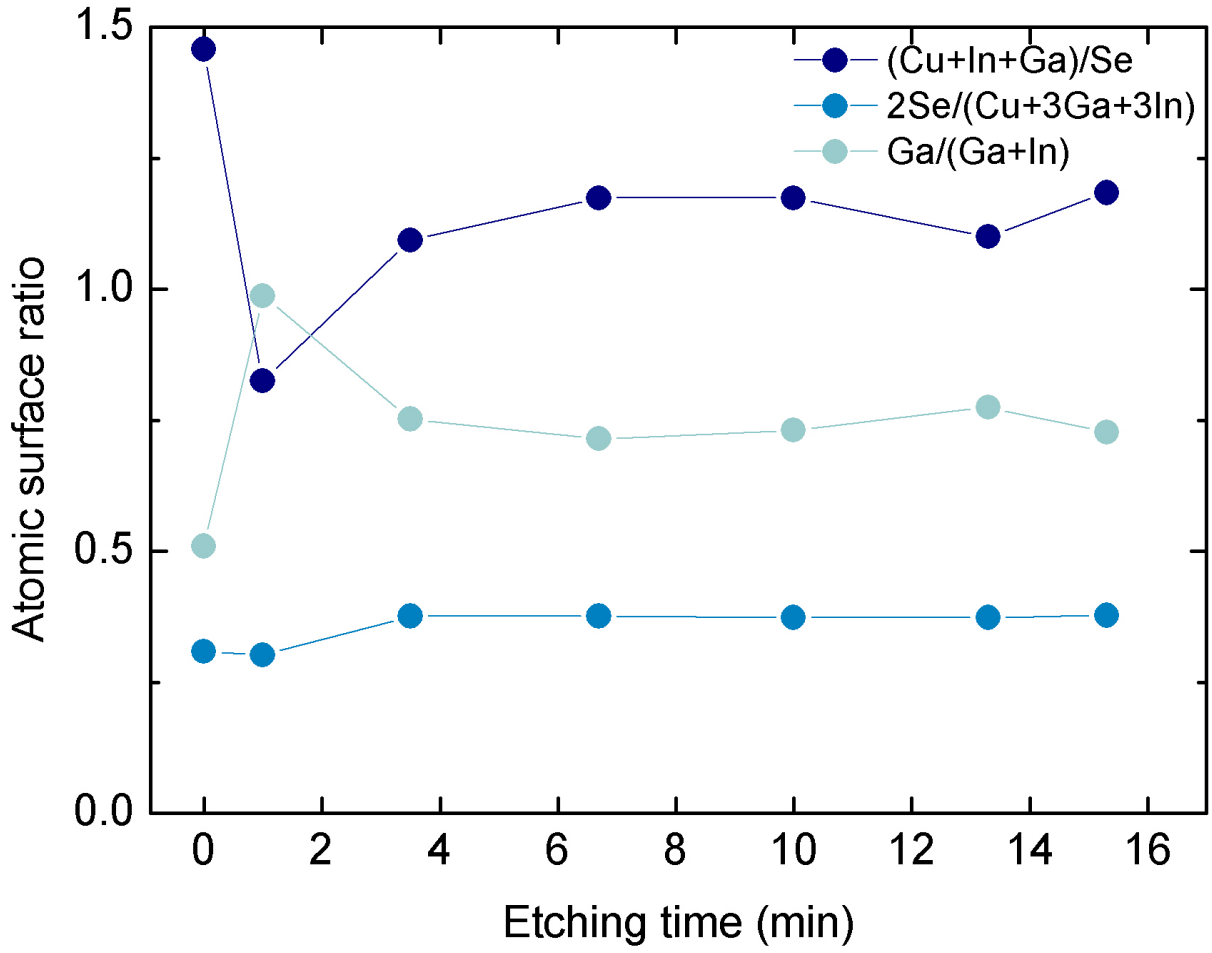

Figure 9. XPS composition of the CIGSe surface at different etching stages of the thinning of the film

These XPS measurements show that the chemical HBr/Br_2 etching does not degrade the CIGSe surface, whatever the etched thickness. No pollution was observed and the films after etching are almost not oxidized. Previous studies [35] have shown that the Se^0 issue is resolved with a KCN treatment which allows to create the p-n junction with a specific and well controlled surface chemistry. Chemical etching of the CIGSe films is therefore perfectly suited for the realization of thinned and ultrathin solar cells and will permit to fabricate proof of concept devices starting from a state of the art solar cell.

III.4.a.ii) Raman spectroscopy and X-ray diffraction analysis

In order to push further the comparison between etched and non etched absorbers, a Raman spectroscopy study was performed on the samples. The Raman Spectra of a raw non etched absorber and a 4 minutes flat etched ($[Br_2]$ = 0.02 M) CIGSe absorber (etched thickness of about 500 nm) are very similar as observed on figure 10. The chalcopyrite characteristic mode A1 frequency is observed at about 177 cm^{-1}. Extra mixed B2/E modes at 220 cm^{-1} and 250 cm^{-1} and a broad mode at about 150 cm^{-1}, are also observed which are typical of CIGSe absorbers deposited by co-evaporation with composition of $Cu/(In+Ga)<0.8$ and $Ga/(Ga+In)= 0.3$.

X-Ray Diffraction analysis were also performed both on non etched and 4 min etched flat CIGSe absorbers. Figure 11 presents XRD spectra through grazing incidence angle of a non etched and a 4 minutes etched CIGSe surface. As can be seen the XRD spectra are very similar and the absorbers present, whatever the thickness, a (112) preferential orientation with additional odd reflections such as (101), (103) and (211) indicating a chalcopyrite structure typical of coevaporated CIGSe absorbers. These considerations about XRD and Raman spectroscopy both support the fact that the HBr/Br_2 etching has only a minor influence on the CIGSe absorber crystalline structure and composition, and only reduces the film thickness and roughness.

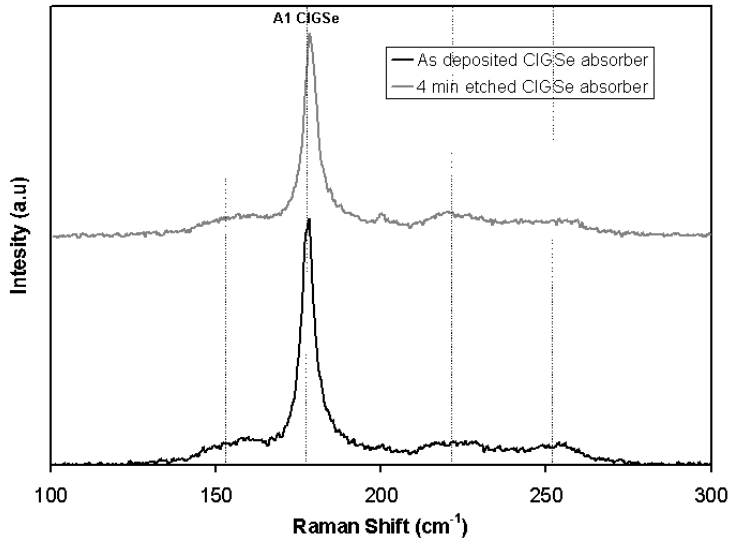

Figure 10. Raman spectra of an as deposited CIGSe absorber and a 4 min etch CIGSe absorber

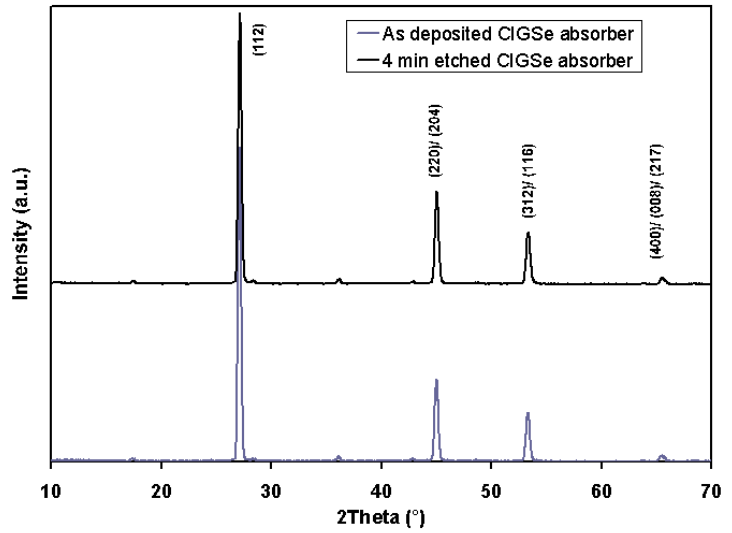

Figure 11. X-ray diffraction patterns of an as deposited CIGSe absorber and a 4 min etch CIGSe absorber

III.4.a.iii) Observation of the surface by Scanning Electron Microscopy

Besides the thickness reduction, the first purpose for which chemical Br_2 etching of the CIGSe surface was develop was to take advantage of the smoothing effect resulting from the etching and obtain quasi-specular films [34]. The smoothing effect of the etching is indeed remarkable and needs an accurate characterization.

The films were observed using Scanning Electron Microscopy (SEM) for an overview of the effects of the etching on the geometry of the CIGSe surface. The SEM setup used was a Leo Supra 35 field emission gun (FEG). The Br_2 concentration is 0.02 M. Two different series of etched samples from the same batch are realized, in order to separate the specific study of the smoothing effect of the etching on the CIGSe surface from the reduction of the absorber thickness. For the first serie (1), the purpose was to observe the smoothing effect of the chemical etching on the absorber while maintaining the CIGSe thickness higher than 2 µm. Short etching steps of 30 seconds are used up to 4 minutes etching, which is equivalent to approximatively 500 nm of etched material for $[Br_2]$ = 0.02M. The SEM cross section pictures of the samples are shown in figure 12. We observe progressive smoothing of the surface, with the sharp tips of the grains being preferentially etched. The average thickness of the absorber is not significantly modified, remaining at about 2 µm after 4 minutes of etching, which from an optical point view won't affect the global light absorption in the film compared to an as-deposited 2.5 µm CIGSe. The apparent original roughness is almost vanished after 4 minutes of bromine etching.

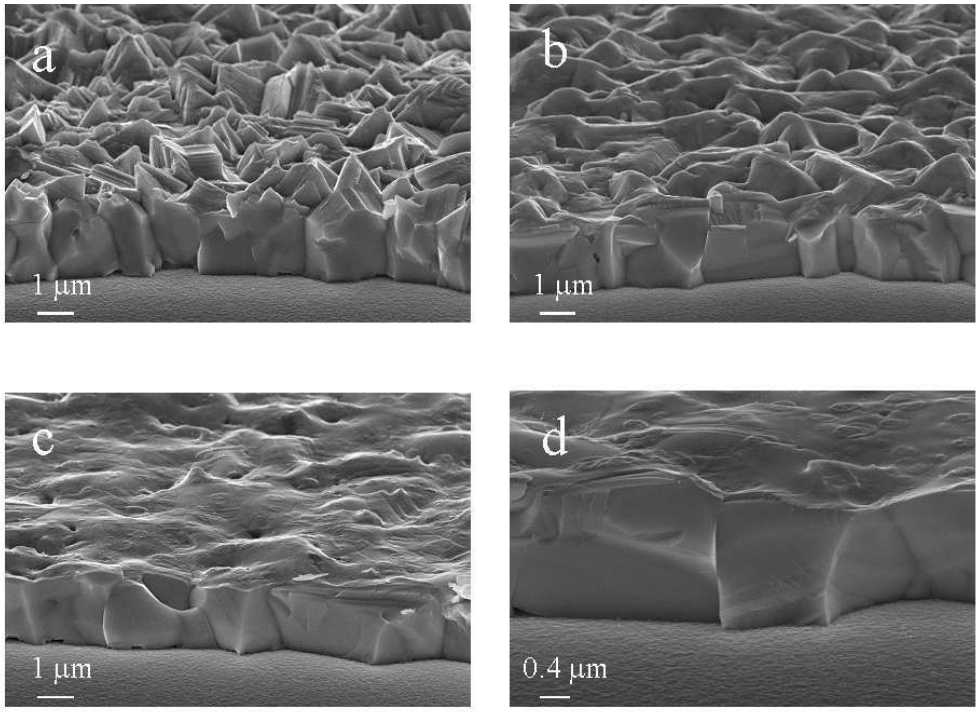

Figure 12. SEM images (cross sections, 65° tilt) of (a) standard non etched (2500 nm) as-deposited CIGSe absorber; and etched CIGSe surfaces after (b) 30 seconds; (c) 2 minutes and (d) 4 minutes of etching.

In the second serie (2), we aim to reduce significantly the CIGSe thickness, from the non etched 2.5 µm initial absorber down to 2 µm, 1.5 µm, 1 µm, 0.7 µm and 0.5 µm. The SEM pictures in figure 13 show the 65° tilted cross sections of the initial absorber surface and of two etched absorber layers with a nominal thickness of 2 µm and 0.5 µm, respectively (a, b and c). In addition the cross sections of the same samples are shown after the deposition of the standard CdS/i-ZnO/n-ZnO layer structure (d, e, f). In contrast to the rough surface of the as-deposited absorber, the surfaces of the etched samples are much smoother. As previously observed, a strong surface modification already occurs within the first minutes of etching, as can be seen for the 2 µm sample compared to the reference non-etched sample. With increasing the etching time, this effect continues and a further smoothing of the surface is observed. Small cavities are also randomly observed at the basis of the CIGSe grains, at the CIGSe/Metal interface as highlighted in figure 13.b. They are most likely reminiscences of the 3-dimensionnal nucleation of the CIGSe crystals on the Mo surface at the early deposition stages, and their impact on ultrathin layers will be discussed in Chapter V. A very thin

superficial layer for the 0.5 µm sample is observed on top of the etched absorber whose origin is not clear. It seems to be caused by the etching process, but it is very unlikely that it is related to the residual Se^0 that was observed on XPS. Up to now, no convincing interpretation has been proposed.

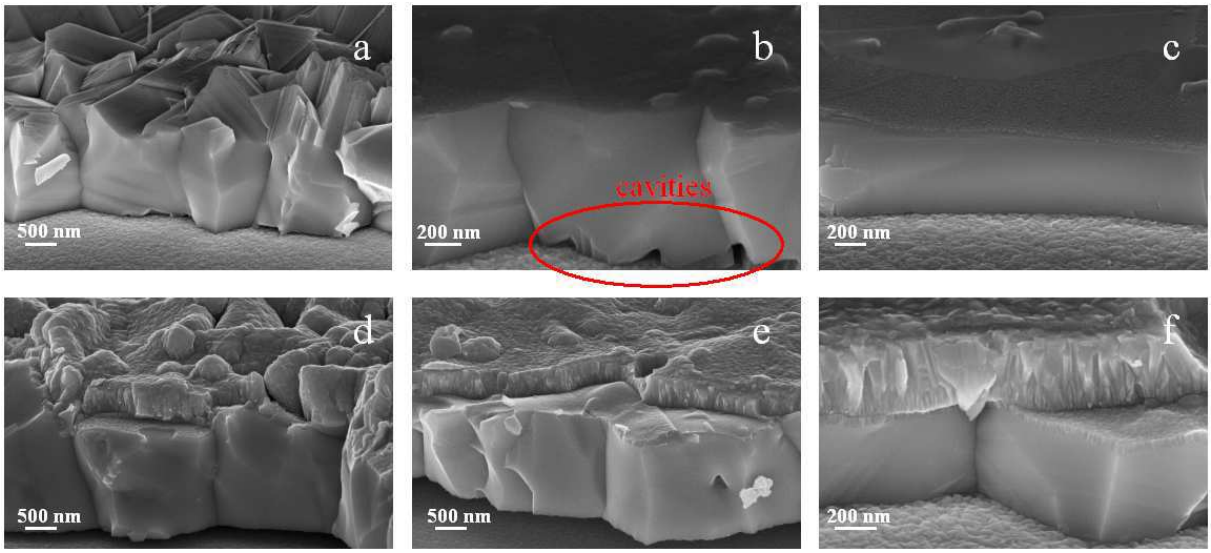

Figure 13. SEM images (cross sections, 65° tilt) of: (a) (b) (c) standard non etched (2500 nm) and etched (2000 nm and 500 nm) CIGSe surfaces respectively. (d) (e) (f) standard non etched (2500 nm) and etched (2000 nm and 500 nm) CIGSe surfaces respectively with CdS/ZnO/ZnO:Al windows layer

III.4.a.iii) Surface roughness characterization by Atomic Force Microscopy

Atomic Force Microscopy AFM is used on non etched and etched CIGSe surfaces in order to follow the evolution of the CIGSe films roughness during the etching process. Two different batches are used for this study (ZI and ZG), and the Br_2 concentration is $[Br_2] = 0.02M$. The AFM principle is described in Appendix II. In this study, the AFM images are obtained on 50 x 50 μm^2 zones with a D3100 microscope and nanoscope IIIa controller, using contact mode with DNP-20 tips (20 nm nominal tip radius). Figure 14 presents the AFM images of the evolution of the surface roughness; based on these images, the Root Mean Square (RMS) of the surface is calculated as defined:

$$RMS = \sqrt{\frac{\sum_{i=1}^{n} (Z_i)^2}{n}} \qquad (1)$$

Where n is the number of total data points and Z_i is the ordinate of the data point i. Figure 15 presents the evolution of the RMS throughout the etching of the CIGSe surface. As expected from the SEM observations, the roughness decreases very fast during the first stages of the etching, with a RMS dropping from about 230 nm for the reference non-etched 2.5 µm CIGSe down to about 90 nm for the short etched 2 µm thick CIGSe. This phase corresponds to the preferential etching of the sharp tips of the grains which was observed in the sample serie (1). In a second phase, from 2 µm to the complete dissolution of the CIGSe absorber, the RMS continues to decrease and reaches a quasi asymptotic value of about 70 nm for ~1 µm of CIGSe left (it is possible that the CIGSe layer is fully dissolved for the last two measurement points). The RMS obtained after etching are slightly higher than those from literature; Shafarman et al. reported a RMS of about 21 nm after Br_2 etching, and even as low as 8 nm after KCN treatment of the surface [58]. This may be related to the much larger scanning area (50 x 50 µm) of this study compared to the scanning area (5 x 5 µm) in the work by Shafarman et al. The three different series of CIGSe samples presented on figure 15 show a remarkable reproducibility in the evolution of their roughness with the etching, even for sample from different batches (ZI and ZG batches).

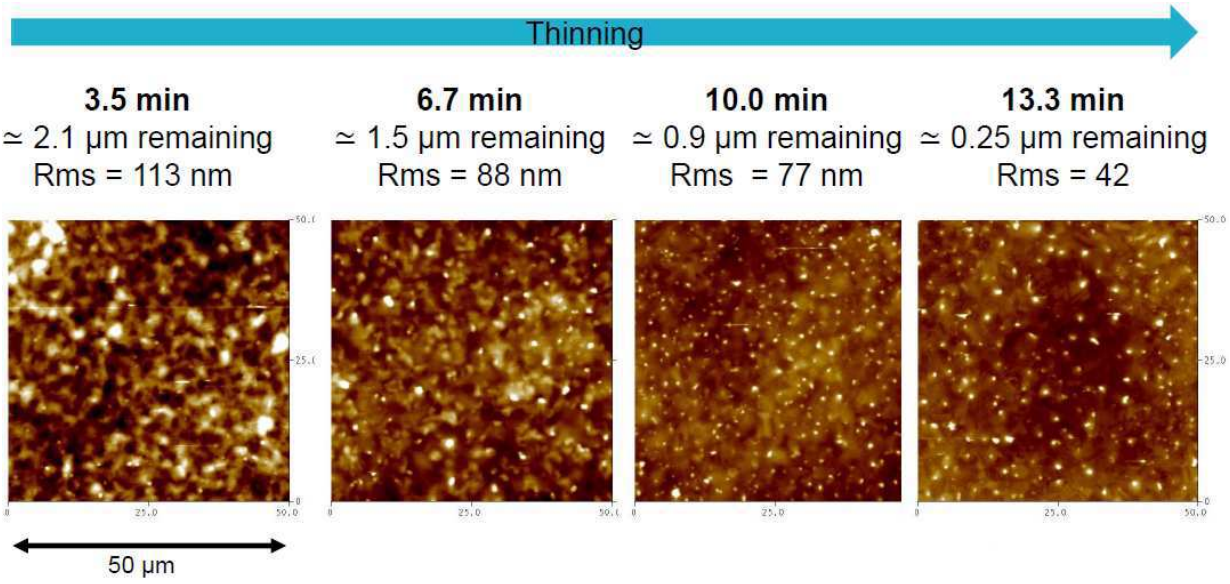

Figure 14. AFM images for different etching times. The remaining CIGSe thickness is also indicated. The initial RMS is about 230 nm.

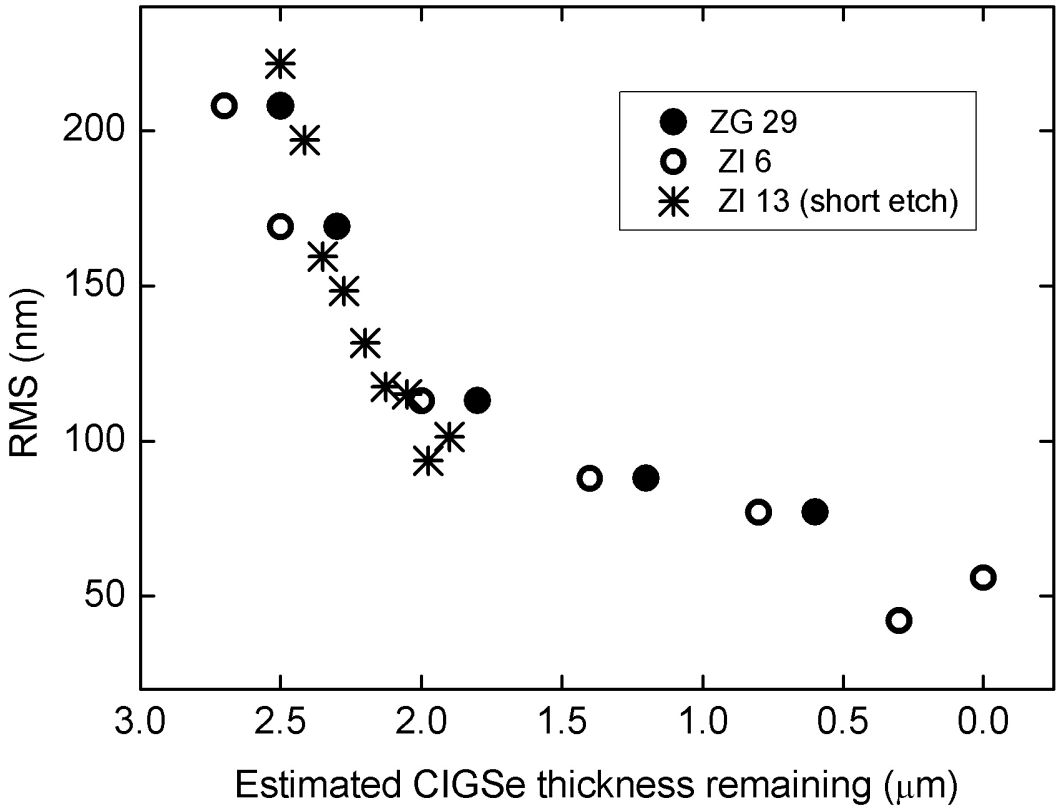

Figure 15. RMS measurements versus CIGSe thickness reduction on different batches (ZI and ZG).

III.4.a.iiiii) Conclusion

We performed several analyzes on the CIGSe surface before and after the chemical etching. XPS measurements show that the surface chemistry is almost not affected by the chemical etching, which leaves a very "clean" surface free from oxides and pollution. Raman spectra and XRD measurements did not indicate any other modification of the film composition or the crystalline structure. Ultimately, the only parameter that is affected by the HBr/Br_2 solution, beside the film thickness, is the surface roughness. Both SEM observations and AFM measurements showed that the smoothing of the surface occurs much faster than the effective thickness reduction, which allows the de-correlation of both parameters (film roughness and thickness).

Etching of the CIGSe absorber has been performed on the front side and after the etching, the visual aspect of the film is strongly modified: being smoother, the surface looks much more specular and reflective. Moreover, SAA measurements allowed to characterize the well known Ga grading in the CIGSe. Successive etching of the Ga-poor top region may result in different optical properties of the film. Based on these considerations, a systematic study of the optical properties before and after etching is needed, and is presented in the following.

III.4.b) Optical characterization of etched CIGSe films and solar cells by spectroscopic reflectivity and Photoluminescence

III.4.b.i) Reflectivity measurements

The first observation that can be made when comparing an etched CIGSe surface to a standard as deposited CIGSe, without any characterization tool, is the higher and more specular apparent reflectivity of the etched surface. AFM confirmed that the roughness of the surface was strongly decreased when etching the CIGSe and so this observation with the naked eye is consistent. In order to quantitatively evaluate the evolution of the reflectivity properties of the CIGSe layers, we performed total and diffuse reflectivity using a Perkin-Elmer Lambda 900 UV/VIS/NIR spectrometer with an integrated sphere. Figure 16 shows the total reflectivity of three absorber films with a thickness of 2500 nm (non etched), and etched 2000 nm and 500 nm, respectively. As the thickness is reduced, interference fringes emerge in the IR range after the bandgap ($\lambda \geq 1050nm$). In this wavelength range the light is not absorbed by the CIGSe material; the appearance of these fringes is caused by the smoothing of the absorber surface providing a more homogeneous thickness of the absorber film, which thus acts as an interference layer. From the interferences, it is possible to calculate the thickness of the films using the formula [63]:

$$m_1 = \frac{3\lambda_2 - \lambda_1}{2(\lambda_1 - \lambda_2)} \rightarrow d = \frac{\lambda_1 (m_1 + ½)}{2n} \qquad (2)$$

where d is the film thickness, $\lambda_2 - \lambda_1$ are two adjacent maxima, and n is the real part of the refractive index of the material. On the other hand, the as-deposited CIGSe sample does not

exhibit any interference fringes in this range due to its high texturation. In the CIGSe absorption range (i.e. wavelength between 1100 nm and 400 nm), the total reflectivity increases with increasing the etching time. The enhancement of the reflectivity for the 500 nm sample represents a relative loss of light intensity penetrating the absorber of about 25% compared to the as-deposited non etched CIGSe sample. The difference between etched and non etched sample is roughly constant with the wavelength. Figure 17 shows the ratio of diffusive reflectivity with the total reflectivity (Haze factor). As it is anticipated for a smoother surface, the etched samples show a much lower diffuse reflectivity compared to the rough as deposited CIGSe. The ratio strongly decreases due to the reduced light scattering effect, especially for non absorbed photons when $\lambda \geq E_g \approx 1050nm$. This is expected from the mirror-like aspect of etched CIGSe samples.

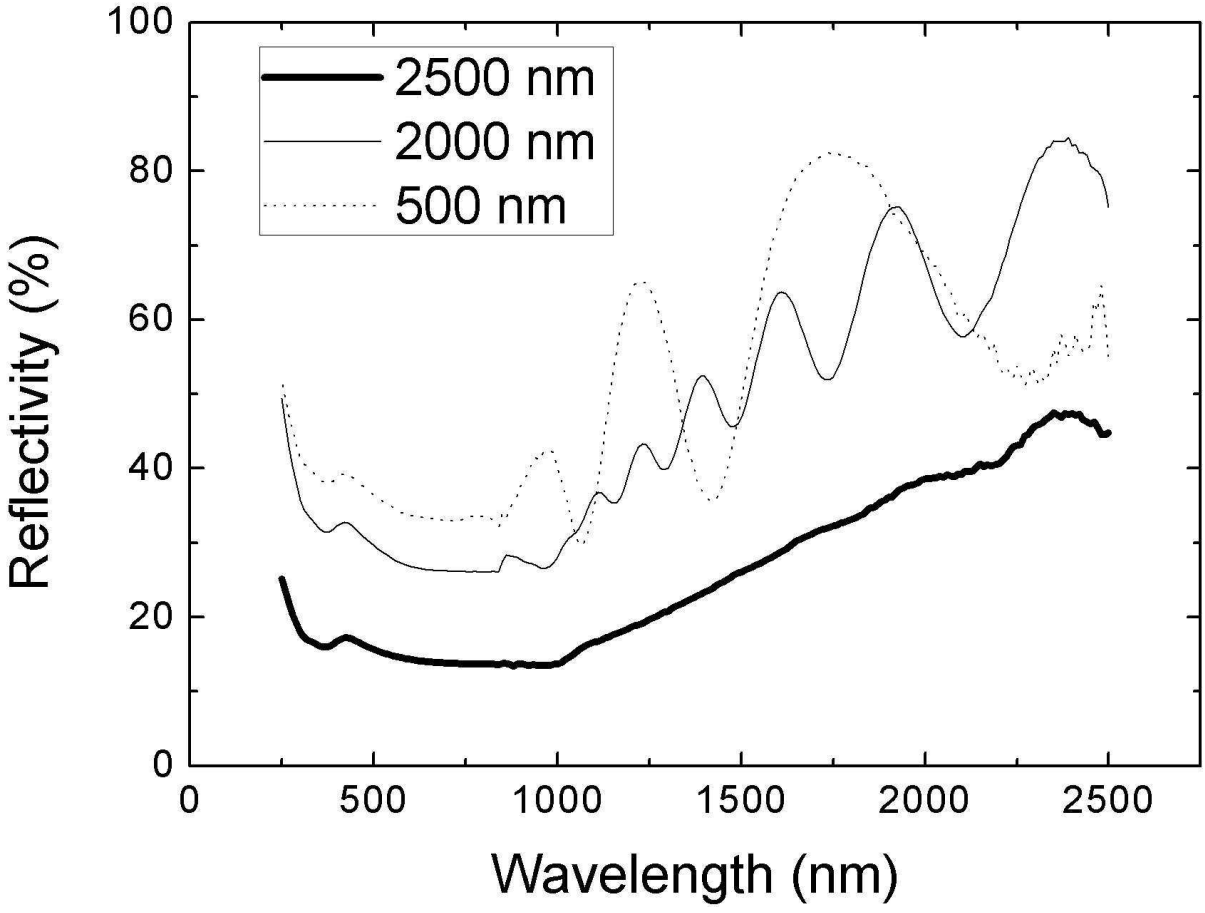

Figure 16. total reflectivity of CIGSe absorbers with different thicknesses; the thick black solid line is the reference non etched 2500 nm absorber; the thin black solid line is the etched 2000 nm thick absorber; the dotted line is the etched 500 nm absorber.

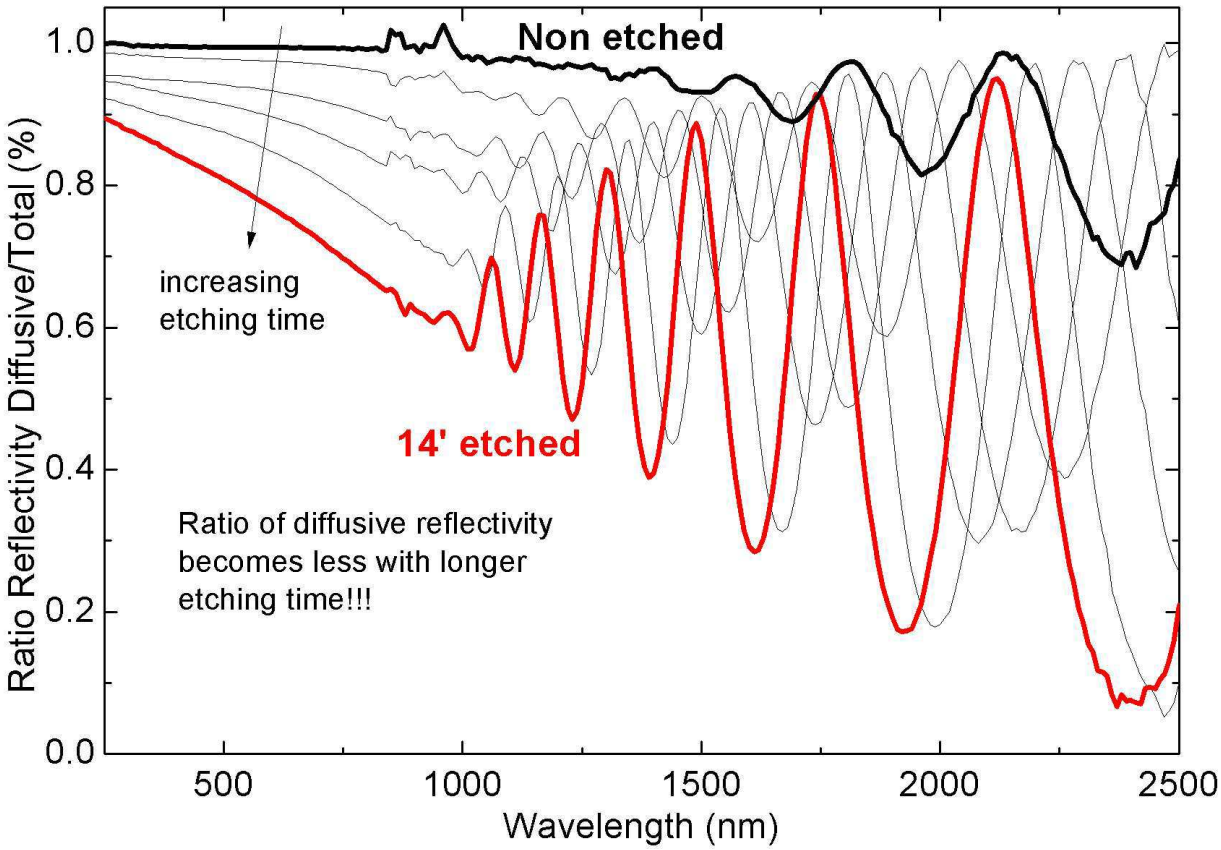

Figure 17. Ratio of the diffusive reflectivity with the total reflectivity when increasing the etching duration (from the black curve to the red curve)

These observations about the different light scattering properties of the etched and non etched sample, are forecasting different light trapping and carrier collection effects between etched and non etched samples.

It is interesting to note that when the cells are completed by deposition of the standard CdS/i-ZnO/ZnO:Al layer structure, the difference in reflectivity between standard and etched CIGSe is strongly reduced (figure 18). This pseudo anti-reflecting effect occurs due to the improved adaptation of the optical indexes at the interfaces air/ZnO/CIGSe compared to the interface air/CIGSe, as the real part of the optical index of the ZnO is about 2 on the whole analyzed wavelength spectrum and the index of the CIGSe is about 2.9 [64]. The ZnO window layer causes additional interference fringes even in the CIGSe absorption range due to the multi-

reflection occurring in the window layer, and affect the effective light intensity penetrating the absorber bulk. It is possible to verify that the spacing between two successive maxima of the reflectivity curve matches the ZnO layer thickness using the formula (2). In the non absorption range, these fringes superpose with the interference fringes originating from the absorber layer, giving the non periodic fringe structure observed.

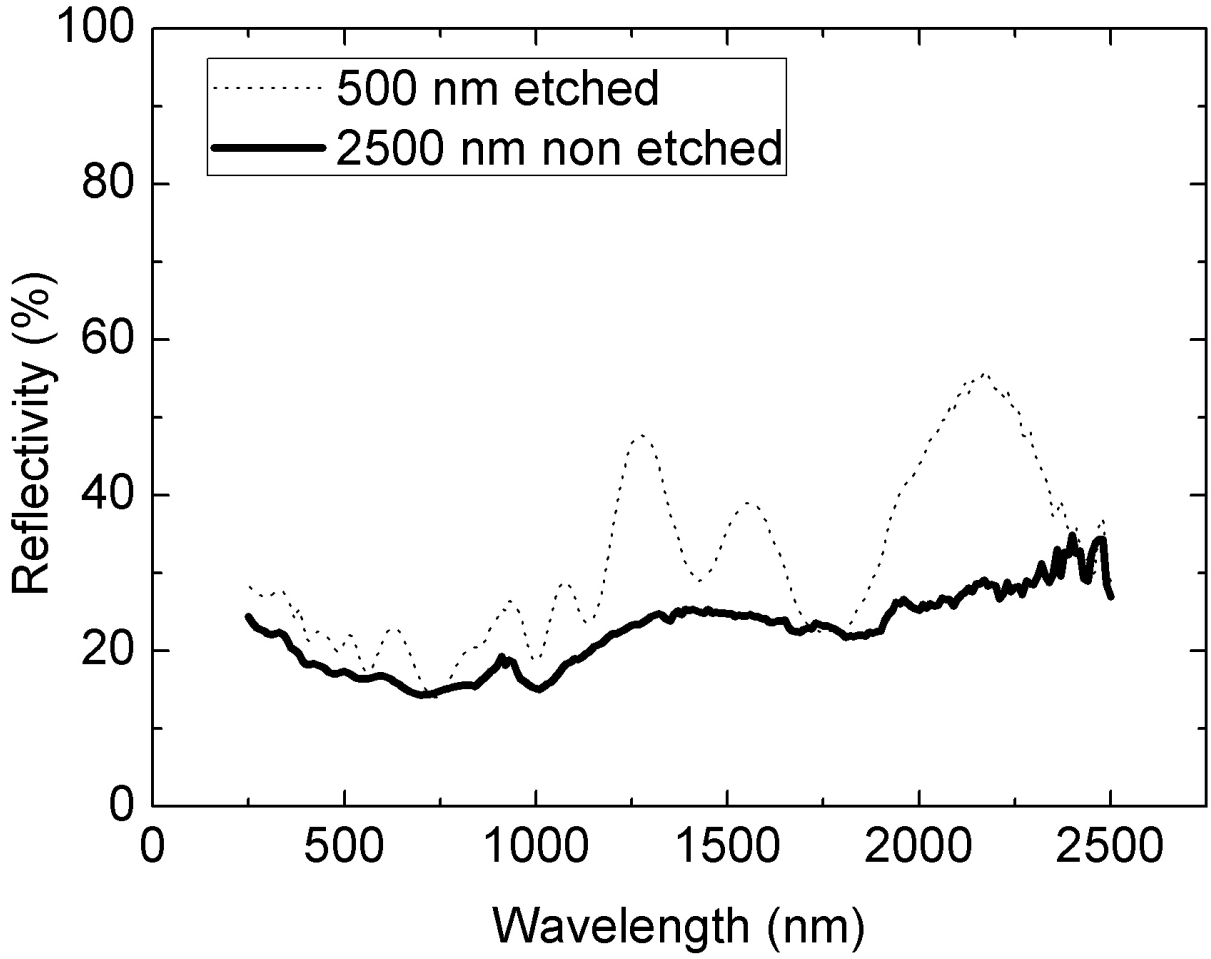

Figure 18. Total reflectivity of the complete solar cell stack for a non etched thick absorber solar cell (solid black line) and a etched 500 nm absorber solar cell (dotted line)

Even if the absorber reflectivity is increased by the etching of the surface, this effect is strongly reduced in the complete solar cell stack; therefore, the absorption of both etched and non etched solar cell is comparable.

III.4.b.ii) Photoluminescence measurements

Another optical phenomenon which needs investigation is the relation between the gallium grading throughout the CIGSe layer and the resulting bandgap grading. From this grading may result both a change in light absorption, and in the voltage of the complete solar cell device. Photoluminescence using a home made setup was performed on CIGSe samples with different etching time. These experiments have been carried out with Dr. Laurent Lombez from IRDEP. The measurements are performed with a laser at an excitation energy of 514 nm. Figure 19 shows the photoluminescence spectra obtained for differently etched sample from the reference 2500 nm thick CIGSe down to 500 nm. The photoluminescence intensity is governed by the generalized Planck law:

$$I_{PL} = A(\nu)\frac{E}{e^{\frac{E-\Delta\mu}{kT}} - 1}$$

where A(ν) is the absorption depending on the frequency ν of the incident photon, E is the energy, k is the Boltzmann constant, T is the temperature and Δμ is defined as $\Delta\mu = E_{Fn} - E_{Fp}$ where E_{Fn} and E_{Fp} are the quasi Fermi level energies for the electrons and the holes respectively, in the CIGSe absorber. On the left edge of the peak in figure 19, the energy of the photons is high enough to be fully absorbed by the material so we can consider the absorption term to be A(ν)~1; moreover, we consider that $e^{\frac{E-\Delta\mu}{kT}} >> 1$. Therefore, in this wavelength range, the shift between the different curves is governed by the $e^{\frac{E-\Delta\mu}{kT}}$ term, i.e. the open circuit voltage of the solar cell V_{oc} depends on $e\Delta\mu$ where e is the elemental charge 1.6 10^{-19} C. When the thickness of the CIGSe is chemically reduced from 2500 nm to 1000 nm, we notice on figure 19 that the high energy edge of the peak (left) increases, meaning that the open circuit voltage should increase in the photovoltaic device. Between 1000 nm and 500 nm however, no variation of the high energy edge of the photoluminescence peak is observed, leading to the assumption that the V_{oc} should be roughly constant in this CIGSe thickness range.

When the wavelength is increased and gets closer to the bandgap, after the maximum of the photoluminescence peak, the shape of the peak is governed by the absorption term A(ν) which cannot be considered equal to 1 anymore, and so is related to the bandgap of the

material. For CIGSe, the penetration depth of the λ=514 nm laser is about 100 nm. Hence, the observed shift toward higher energies of the right part of the peak (low energy) with increasing the etching time (i.e. etching depth) indicates an increase of the bandgap within this surface region. This bandgap grading is consistent with the previously highlighted gallium grading throughout the CIGSe, as an increase of the Ga/(In+Ga) ratio results in larger bandgap in the absorber. However, the effect in the PL spectra is very strong between etched 2000 nm and etched 1000 nm, while in figure 5, the effect seems to appear sooner. It is important to notice that the shape of the bandgap grading, from small to large, leads to re-absorption and re-emission of emitted photons from the deep large bandgap region by the surface small bandgap region; this makes the PL spectra difficult to interpret in a quantitative point of view. Bandgap grading in CIGSe is a well known property that has been found to be benefic to improve light absorption in CIGSe [65].

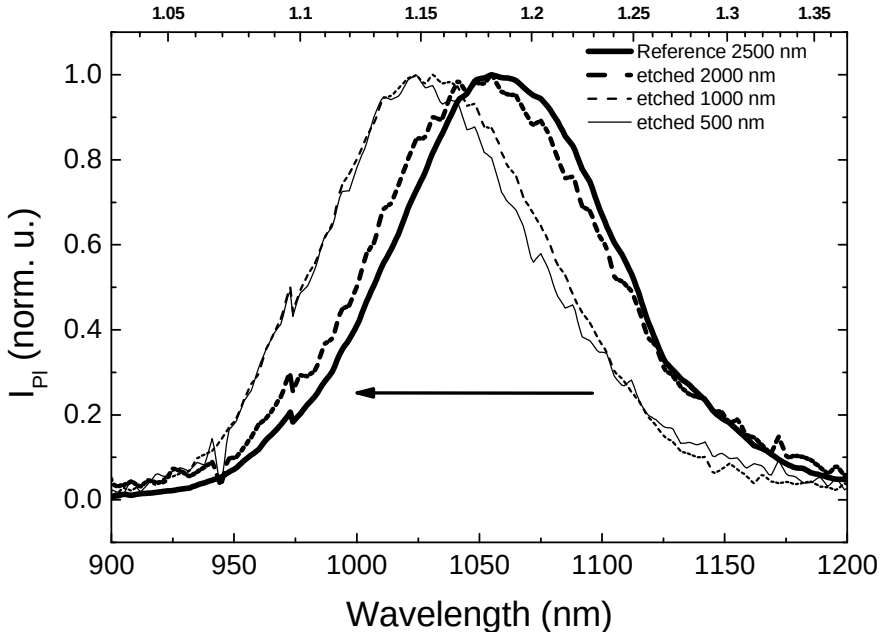

Figure 19. Photoluminescence spectra for a reference non etched CIGSe 2500 nm absorber (thick solid line), and three etched absorbers with different thicknesses : 2000 nm (thick dotted line), 1000 nm (thin dotted line) and 500 nm (thin solid line)

III.4.b.iii) Conclusion

The characterization of etched absorbers revealed that the surface chemistry was almost not affected by the chemical etching, while the surface roughness was strongly reduced. This leads to an increased reflectivity and more specular surfaces. Photoluminescence analysis indicates a shift toward higher energies (increased bandgap) of the right part of the photoluminescence peak; this is consistent with the variation of the Ga content in the layer that was previously highlighted by GF-AAS.

In the next part, both the etched and non etched CIGSe solar cells are electrically characterized in order to extract the main photovoltaic parameters, and evaluate the influence on the device of the different parameters that are modified by the etching: absorber thickness, bandgap and surface roughness.

III.5) Electrical characterization of CIGSe solar cells with absorber thinned by chemical etching

To investigate the impact of the etching on the solar cell parameters, electrical characterizations on etched-absorber CIGSe solar cells have been performed. The samples are co-evaporated from the same batch, with a Ga grading, and are processed with the standard CdS/ZnO:i/ZnO:Al stack. The two electrical characterizations performed are Current Voltage (J-V) measurements under illumination, and Spectral Response (EQE).

III.5.a) Experimental Setup

The investigated $Cu(In,Ga)Se_2$ absorbers (CIGSe) are deposited on Mo covered glass by coevaporation at Würth Solar [2]. The absorber layers with a standard thickness of 2.5μm are chemically etched using an aqueous solution of HBr/Br_2. A KCN treatment on the CIGSe surface is applied before the deposition of the CdS buffer by chemical bath deposition. By increasing the etching time stepwise from 4 min to 18 min, we obtain layers with a nominal layer thickness of 2 μm, 1.5 μm, 1 μm, 700 nm, 500 nm, 300 nm, and 200 nm respectively, estimated by GF-AAS during the etching process. The electrical properties of cells were characterized by current voltage measurements at 25 °C under illumination (AM 1.5 global spectrum). Individual cells of 0.1 cm2 were delimited by mechanical scribing. Absolute spectral response measurements were made with a monochromator (Spectral Products CM 110) under chopped illumination and a lock-in technique. These two characterization tools are described in the Appendix II. Numerical Simulations using SCAPS 2.9 of photovoltaic parameters from J-V curves and Quantum Efficiency Curves are also presented as a comparison to the experimental data. In these simulation, the reflectivity of the surface has been implemented according to the surface reflectivity measured for each corresponding experimental sample.

III.5.b) Current-Voltage characterization

The J(V) measurements are performed under illumination using standard conditions (AM 1.5, 25°C). The obtained photovoltaic parameters as a function of CIGSe thickness are shown in figure 20, and compared to simulated parameters using SCAPS 2.9 [40], figure 21. As predicted by the simulations, the Fill Factor (FF) remains roughly constant at a high value between 70 % and 75 % for all samples down to 500 nm (figure 20.a and 21.a), which indicates the good quality and homogeneity of the material throughout the thickness. For thinner absorber, and contrary to the simulations, the FF dramatically decreases and the 100 nm thick CIGSe solar cell is not functional. The simulations do not highlight such a decrease (figure 21.a) and the simulated FF has an almost constant trend throughout the absorber thickness reduction. Back contact investigations on the sample reveal the presence of pinholes (cavities) on the back side of the absorber (figure 12), which can strongly decrease the shunt resistance and so the FF by some short-circuit pathways for the carriers between Mo and CdS. This particular point will be discussed in chapter V and cannot be modeled using SCAPS.

The open circuit voltage (figure 20.a) slightly increases with increasing etching time when thinning the absorber down to 500 nm, which can be attributed to the grading of the band-gap inside the absorber. The band-gap of the absorber surface is smaller than the bulk value; when the “original” absorber surface is removed, the band-gap of the “new” surface increases, approaching the bulk value with increasing etching time. This is in good agreement with the results from photoluminescence measurements previously discussed. The shift of a few 10 meV in the Photoluminescence spectra between the non-etched absorber and the 500nm sample matches very well the increase of V_{oc} between both samples. No bandgap grading is introduced in the SCAPS simulations and so no effect on the V_{oc} is observed. For thicknesses thinner than 500 nm CIGSe however, the V_{oc} shows a strong decrease in our experimental data, from 0.67 V for the 500 nm absorber down to 0.4 V for the 200 nm, and 0 V (no working solar cell) for the 100 nm. This is consistent with the SCAPS simulations where a Voc decrease is also visible, although it is not so important (figure 21.a).

Two interpretations can be addressed for the strong V_{oc} decrease for thicknesses under 500 nm: the first is related to the width of the space charge region (SCR). As it was shown on chapter II, when the absorber thickness becomes lower than the SCR width, the quasi Fermi level separation does not reach its maximum amplitude and therefore limits the V_{oc} compared to a thicker absorber. The second possible interpretation is related to the previously mentioned

"pinholes" at the back side of the absorber, that are revealed by the etching to ultrathin values of the CIGSe. This last problem is specific to the use of an etching technique and will be discussed in chapter V.

The J_{sc} evolution for the experimental solar cells can be divided into three parts; in a first stage from 2500 nm to 2000 nm of CIGSe thickness, we observe a strong decrease of the current from 28.1 $mA.cm^{-2}$ to 25 $mA.cm^{-2}$. This decrease is stronger than expected from the simulations, since the CIGSe thickness is much more important than needed for a complete absorption of the photons; the increased reflectivity of etched solar cells is not sufficient either to explain this J_{sc} drop. It could be related to the roughness decrease that was previously highlighted. In a second stage, where the CIGSe thickness is reduced from 2000 nm down to 500 nm, the Jsc value decreases from 25 $mA.cm^{-2}$ down to 21 $mA.cm^{-2}$. This decrease occurs rather slowly linearly compared to the first one, and is consistent with numerical SCAPS simulations presented on figure 21.b. The reduction of the CIGSe thickness is the main parameter involved in the J_{sc} drop, since both the reflectivity and the surface roughness remain unchanged. Thinning the layer leads to an increased back contact recombination along with non absorption of low energy photons. The bandgap shift also contributes to the absorption decrease by excluding the lower energy photons from the absorption edge. When the absorber thickness is below 500 nm, a strong drop of the Jsc is observed, from 21 $mA.cm^{-2}$ for 500 nm of CIGSe down to 16 $mA.cm^{-2}$ for 200 nm CIGSe. This decrease is observed both in the simulations and experimentations, and as showed Chapter II, it is only related to incomplete absorption of the photons in the ultrathin layer whereas back contact recombination is not involved; the electric field in the fully depleted absorber allows a complete separation and collection of electron hole pairs in this case.

The fact that V_{oc} does not decrease with reduced thickness is a strong advantage of the etching technique. In comparison Ramanathan et al. showed that the absorber layer thickness has a strong impact on V_{oc} for directly grown thin CIGSe films with a strong degradation in the efficiency by about 50 % for sub-micron CIGSe absorber films was reported [24]. In our study, the efficiency decreases from 13.7 % for the reference 2500 nm sample to 10.3 % for the 500 nm etched sample. As both FF and V_{oc} remain at high values, this efficiency drop is only correlated to the J_{sc} decrease (Figure 20.b). For thinner absorbers, all the parameters are dramatically degraded and so the efficiency rapidly drops to 0%.

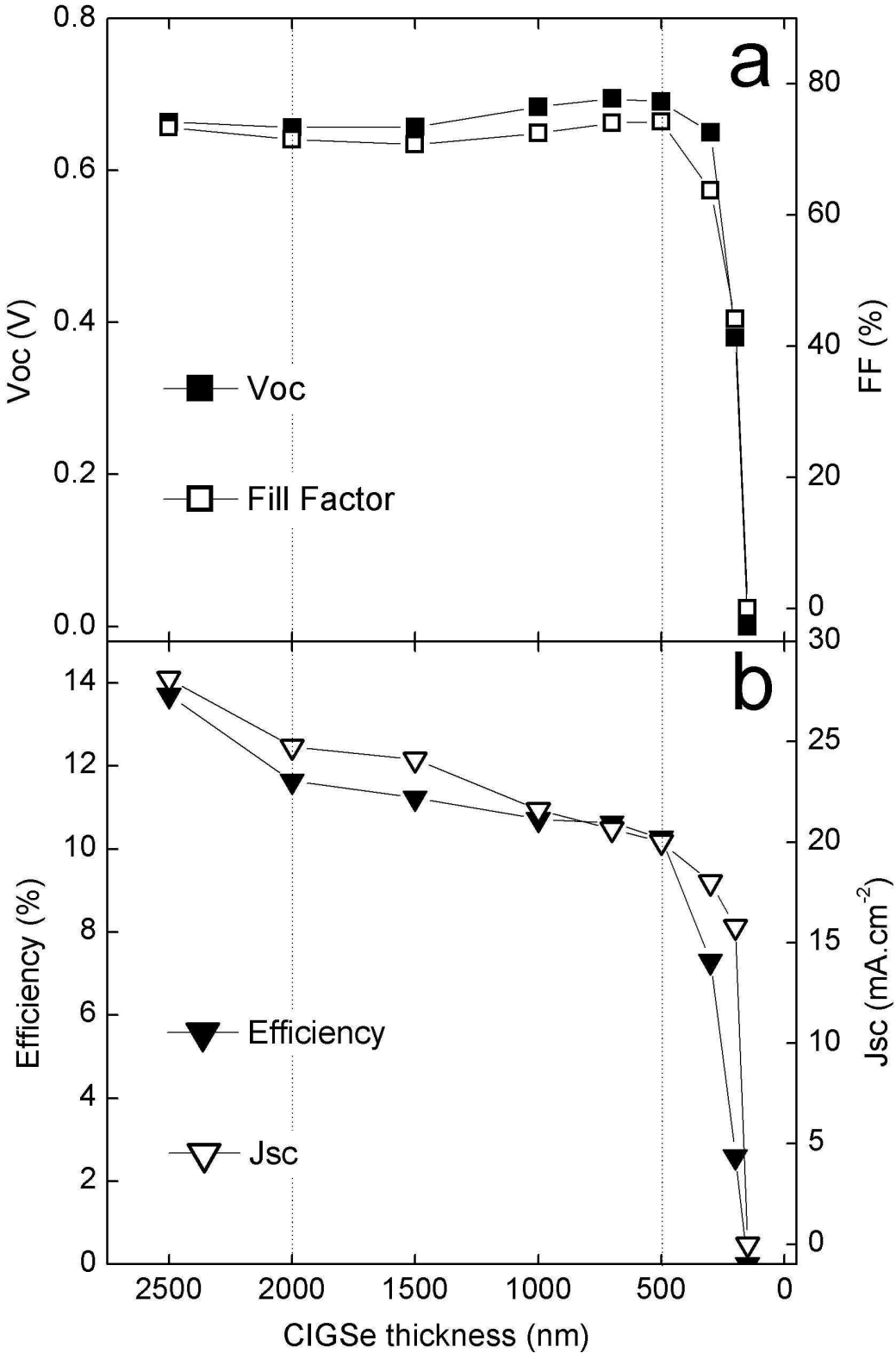

Figure 20. (a) experimental Open Circuit Voltage (filled squares) and Fill Factor (empty squares) Vs CIGSe thickness deduced from J(V) measurements under AM 1.5 illumination; (b) experimental Short Circuit Current (empty triangles) and Efficiency (filled triangles) Vs CIGSe thickness

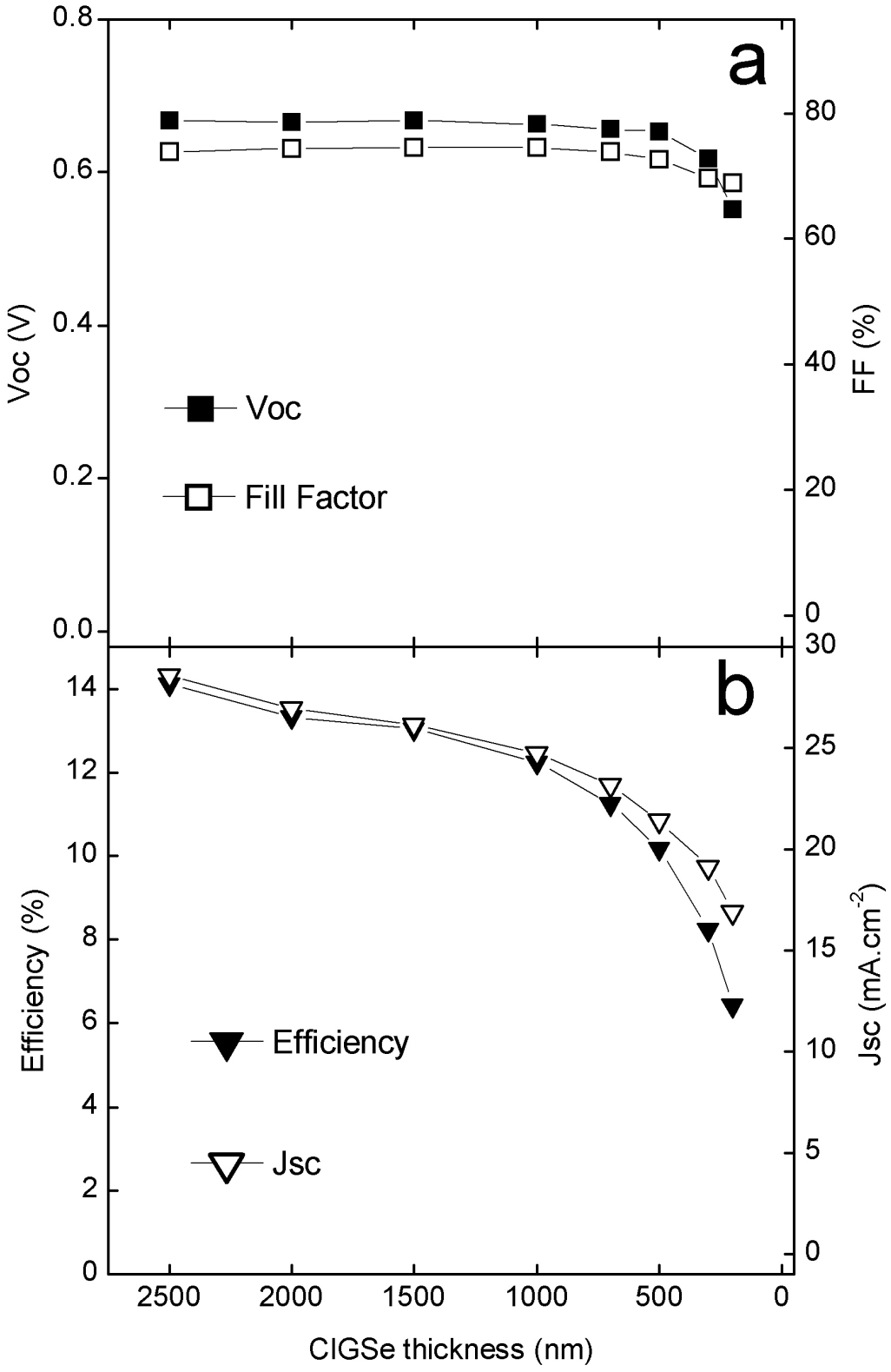

Figure 21. (a) SCAPS simulated Open Circuit Voltage (filled squares) and Fill Factor (empty squares) Vs CIGSe thickness deduced from J(V) measurements under AM 1.5 illumination; (b) SCAPS simulated Short Circuit Current (empty triangles) and Efficiency (filled triangles) Vs CIGSe thickness

III.5.c) Spectral Response

The J_{sc} is found to be the key parameter driving the efficiency decrease when thinning an absorber down to 500 nm, and so EQE measurements are performed on the samples for a better analysis of the absorption and carrier collection in these solar cells (figure 22.a). Corresponding simulated EQE are presented on figure 22.b. Interference fringes can be observed for the etched CIGSe samples originating from the ZnO layer. The positions of the maxima correspond to the positions of the minima of the reflective curves (compare figure 19), and vice versa. Figure 22.a also shows EQE spectra which are corrected for the reflectivity losses (dotted lines) compared to the non-etched sample. Therefore the EQE data was multiplied by the adjusted ratio of the reflectivity data of the standard absorber $R_{standard}$ and the etched sample R_{etched} $(1-R_{standard})/(1-R_{etched})$. These data show the direct impact of the absorber layer thinning on the EQE, the interference fringes of the ZnO are vanished. From the reference 2500 nm thick absorber solar cell down to 500 nm, the UV part of the EQE is relatively unaffected, with a drop from 0.83 to 0.74 at a wavelength of 550 nm; this is consistent with the well known high absorption coefficient of the CIGSe at those wavelength (Chapter II, Figure 1.a) and it is nicely reproduced in the EQE simulations (Figure 22.b). As the energy of the photons decreases, the absorption in the CIGSe is less efficient and so carriers are generated deeper in the absorber. Therefore, when the penetration depth $L_{penetration}$ becomes larger than the space charge region (SCR) width, some carriers generated outside of the SCR may recombine in the CIGSe before reaching the p-n junction. If the absorption occurs at a distance larger than $L_{eff} = W + L_n$, a higher fraction of the generated electrons can recombine in the CIGSe. For an ultrathin absorber, the low energy photons may not even be absorbed in the CIGSe and so be absorbed in the Mo back contact, which has a very low reflectivity. These simplified mechanisms are illustrated in figure 23, showing the calculated penetration depth deduced from α measurements by ellipsometry. In the EQE curves, we observe a strong decrease of the carrier collection for etched absorber as the wavelength increase (i.e. energy decreases), the EQE of the solar cell dropping, at a wavelength of 900 nm, from 0.7 for the reference thick absorber down to 0.3 for the 500 nm absorber and 0.2 for the 200 nm absorber. The EQE SCAPS simulation are slightly overestimated compared to the experimentation for the samples with a reduced absorber thickness. This is attributed to the surface morphology which is not taken in account by the SCAPS simulations and will be discussed later in this chapter. However, we obtained a good agreement between the

experiments and the simulations concerning the evolution of the quantum efficiency when reducing the absorber thickness.

For thicknesses higher than 500 nm, the decrease of the EQE in the IR range is most likely due to back contact recombination combined with non-absorption of the photons; when low energy photons are absorbed in the flat band region, the increasing proximity of the back contact leads to a situation where $L_b < L_n$, where L_n is the diffusion length of the generated photon in the absorber, L_b is the distance from the absorption point to the back contact of the cell, which is defined as $L_b = d - L_{penetration}(\lambda)$ where d is the absorber thickness and $L_{penetration}(\lambda)$ is the penetration depth before absorption for a photon of a given wavelength λ.

For the ultrathin absorber devices ($d < 500$ nm) where the SCR width is approximatively as large as the absorber thickness (fully depleted absorber), it is most likely that most of the low energy photons are not absorbed in the absorber and so are absorbed in the Mo, which explains why the EQE drops down to 0.6 at a wavelength of 550 nm for the 200 nm CIGSe sample. We showed in chapter II that a fully depleted absorber was nearly independent of back contact recombination and that the CIGSe absorption was the only parameter limiting the quantum efficiency of the cell.

The bandgap shift from reference to etch absorber is also evident in figure 22.a and is calculated using the onset of the reflectivity data or the position of the inflection point of the EQE curve. As illustrated in figure 24, both methods are in very good agreement. The calculated bandgap varies from 1.21 eV to 1.26 eV for the 500 nm thick sample; bandgap determination was impossible both for the 300 nm and 200 nm thick samples due to the low value of their EQE curves which leads to interference fringes becoming preeminent over the general shape of the curve. According to reference [62] and the Ga content measured by SAA in part III.3.b., the band gap should vary from 1.17 eV to 1.25 eV. These differences with the experimentally found values are most likely due to the relative inaccuracies in the EQE measurements, even though they are in the same range.

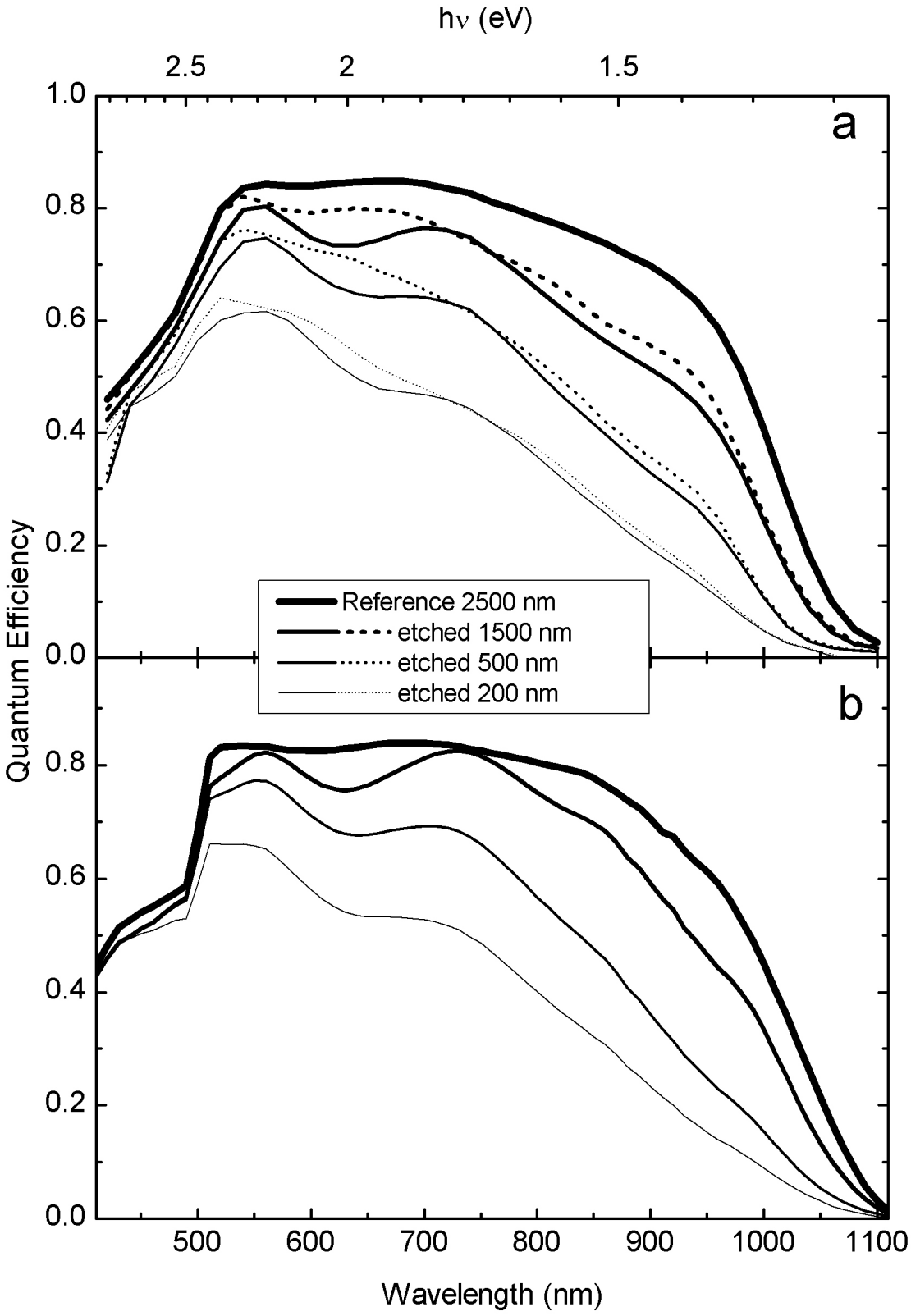

Figure 22. Experimental (a) and SCAPS simulated (b) EQE of four samples with different CIGSe thickness. The dashed lines show the EQE data after correction of the reflectivity losses caused by surface smoothing

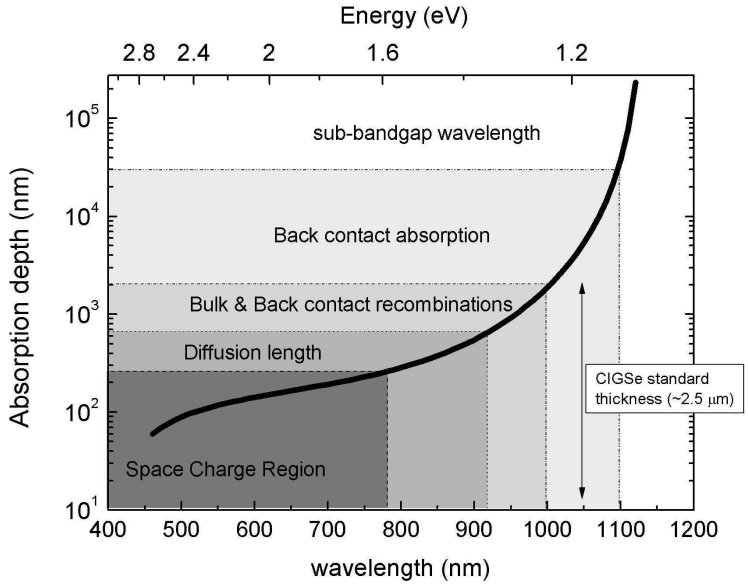

Figure 23. Absorption Depth as a function of the wavelength of the incident photons. The different absorption regions in the absorber are represented with shades of grey. The space charge region width and the diffusion length are determined for a flat interface using a method described in chapter III part d.

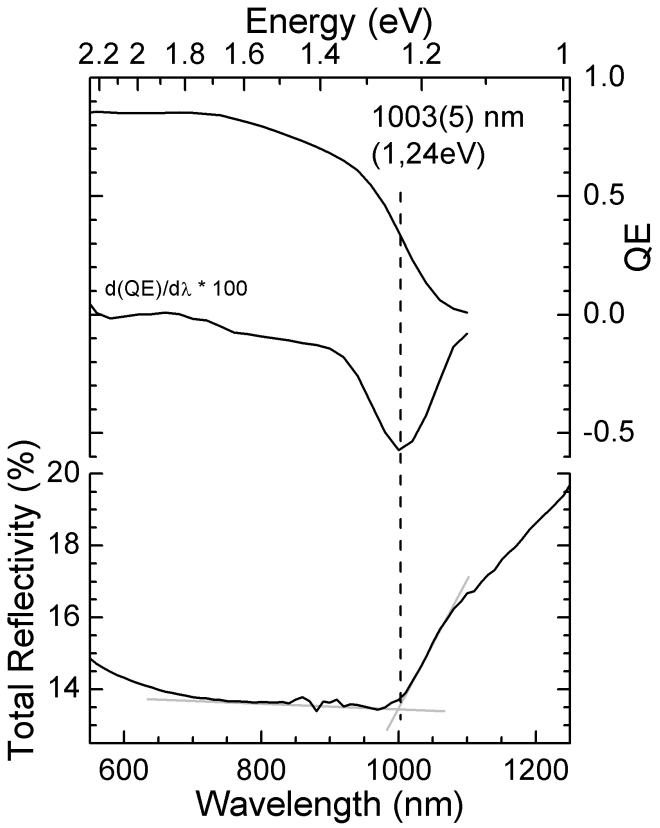

Figure 24. Bandgap determination using the Quantum Efficiency derivative and compared to the reflectivity of the absorber.

III.5.d) Conclusion

The decrease of the efficiency of the solar cell when reducing the absorber thickness has been mostly attributed to reduced short circuit current (figure 20.b); however, the CIGSe thickness is not the only parameters that is influenced by the chemical etching of the absorber. In the part III.4.a.iiii), we showed with AFM measurement (Figure 14 & 15) that the surface roughness was strongly reduced during the etching process, leading to a more specular surface for the etched samples compared to the reference as-deposited CIGSe. This evolution of the morphology strongly influences the solar cell. In the next part of this chapter, we will investigate on the specific influence of the surface roughness of the absorber on the photovoltaic parameters of the solar cell, while keeping the CIGSe thickness at a roughly constant value.

III.6) Influence of the surface roughness on the CIGSe solar cells

As it was previously highlighted, the reduction of the absorber thickness and the enhanced reflectivity of the solar cell due to etching are not sufficient to explain the strong J_{sc} drop that is observed within the first stages of the etching. This important decrease of the J_{sc} corresponds to the thickness decrease from 2.5 µm down to 2 µm and the etching time between 0 min to 4 min with a $[Br_2]$ = 0.02 M. In this range, we previously highlighted an important decrease of the surface roughness (AFM observations Figure 14 & 15).

The surface roughness of the CIGSe is a key parameter for the solar cell which needs to be investigated independently from the absorber thickness variation. In this part, we focus on the study of short etched solar cells with an almost constant absorber thickness, but with a progressive smoothing of the surface. An interpretation of the evolution of the photovoltaic parameters with the surface roughness regarding theorical hypothesis is proposed.

III.6.a) Device characterization

The studied solar cells are from the serie (2), batch ZI 13, previously presented in the part III of this chapter. The bromine concentration is $[Br_2]$ = 0.02M, and the etching times is varied by steps of 30 seconds from 0 to 4 minutes. A KCN treatment was done on the absorbers prior to the deposition of the standard CdS/ZnO:i/ZnO:Al stack. The solar cells are characterized by spectroscopic reflectivity, J-V measurements and Spectral Response.

III.6.a.i) Current-Voltage characterization

The photovoltaic parameters of the solar cells, extracted from the J-V curves, as a function of the CIGSe surface roughness (RMS) are presented on figure 25. Each measurements are separated by 30 seconds of etching. As observed on Figure 25.a, both the open circuit voltage (V_{oc}) and the fill factor (FF) remain remarkably constant, which is a strong indication that the

chemical etching of the surface does not degrade the quality of the CdS/CIGSe interface. This is in good agreement with the constant surface chemistry of the CIGSe after etching deduced from XPS measurements. However, the solar cell efficiency decreases, from 14 % for the rough non etched CIGSe solar cell (RMS = 230 nm) down to 11 % for a smooth surface solar cell (RMS = 90 nm) (Figure 25.b). This decrease is clearly related to the decrease of the short circuit current (J_{sc}) from 29 mA.cm^{-2} to 24 mA.cm^{-2} as shown figure in 26.b. This corresponds to a drop of about 17 % which is much higher than the increase of the reflectivity of the complete solar cell with the etching (Figure 26). These key results are a strong indication that the decrease in the short circuit current is directly related to the effect of CIGSe smoothing on photocurrent generation in the CIGSe layer.

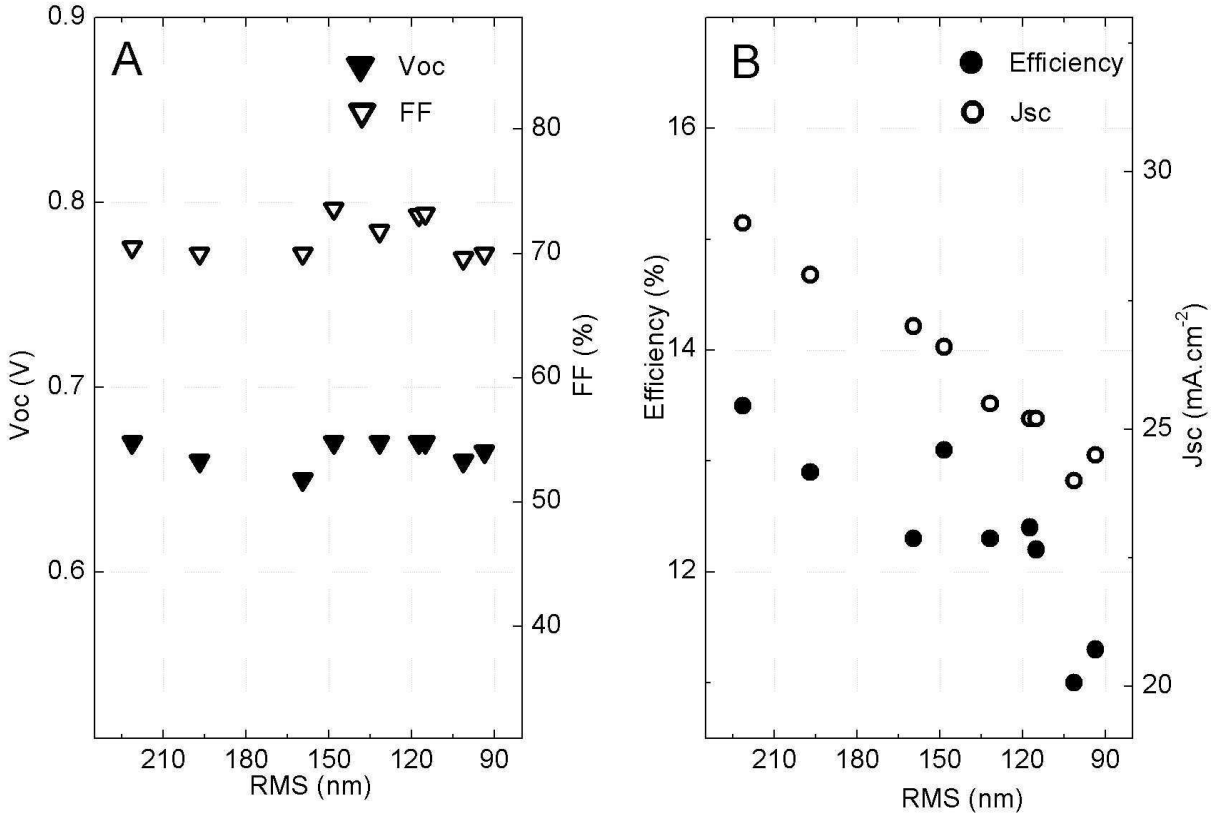

Figure 25. Photovoltaic parameters from J(V) characterization for CIGSe solar cells as function of the surface roughness of the CIGSe absorber: (a) Open Circuit Voltage (Voc) and Fill Factor (FF); (b) Efficiency and Short Circuit Current (Jsc).

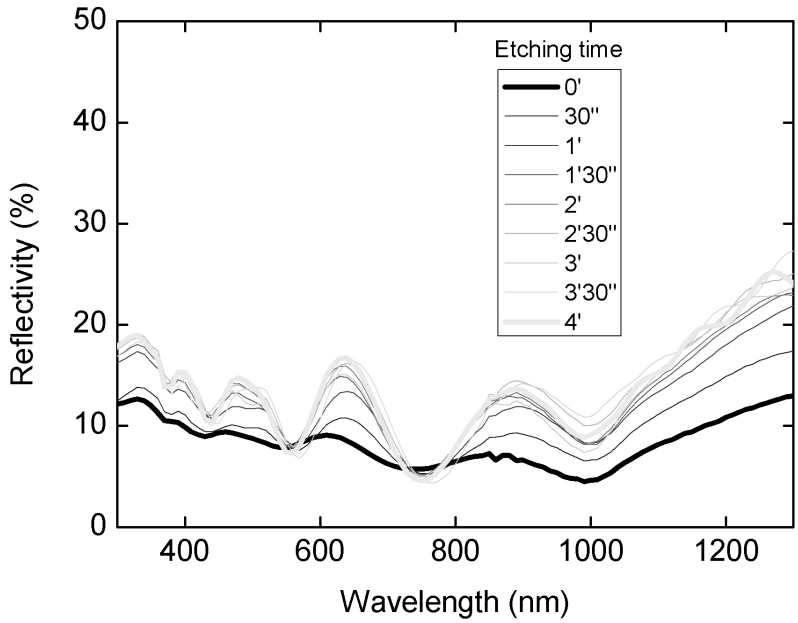

Figure 26. Evolution of the total reflectivity of the completed solar cells stack with different CIGSe roughness

III.6.a.ii) Spectral Response

EQE measurements have been performed on the solar cells (Figure 27.a) as a function of the roughness surface of the CIGSe absorbers. As can be seen, with the decrease of the CIGSe roughness, there is a small downward shift in the overall spectrum corresponding to the drop of the photocurrent. Moreover interference fringes appear in the external quantum efficiency curves for flat CIGSe cells, corresponding to interferences in the ZnO layer. As observed on figure 26, the reflectivity measurements show that the decrease of the roughness of the CIGSe surface leads to the presence of interference fringes. However the reflectivity of the solar cell remains approximatively unchanged after smoothing the surface, and although the interference fringes may have a small contribution in the current drop, this cannot explain the strong EQE decrease observed.

EQE ratio of each etched sample with the reference sample is also presented on figure 27.b. When the surface becomes flat, the losses are increased at higher wavelength, which means that the low energy carriers are either generated or collected less efficiently with a flat surface. Textured surface produces light scattering in the absorber and thus increases light absorption; in this study however, the absorber is more than 2 μm thick and considering the

high absorption coefficient of CIGSe [66], it is unlikely that light trapping is needed for a complete absorption of light in the absorber. This is supported by the reflectivity measurements from figure 26 which show a roughly equivalent absorption between a rough (RMS = 230 nm) and a flat (RMS = 90 nm) complete solar cell.

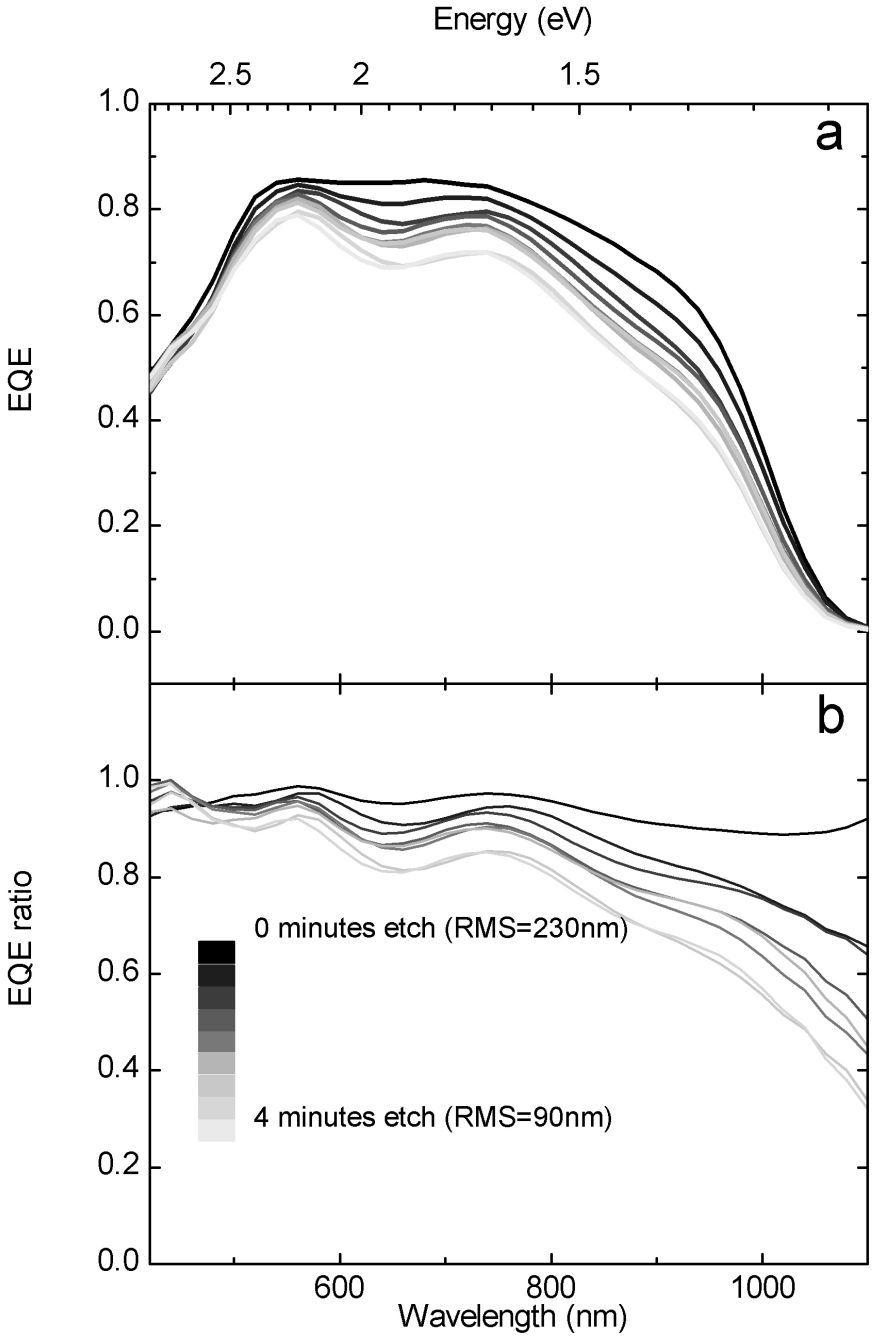

Figure 27. (a): Spectral Response (EQE) for different etching times; (b): EQE ratio for different etching times

III.6.b) Discussion

Smoothing the absorber surface does not significantly reduce the absorption of the solar cell. In order to interpret the reduction of the J_{sc}, one hypothesis would be that the photocurrent decrease has to be related to an incomplete carrier collection at the p-n junction when the absorber surface is smoother. Since the CIGSe surface composition and the structural properties remain unchanged whatever the surface roughness of the absorber (part III..4.a), it is possible to make the assumption that the p-n interface geometry is influencing the effective volume of the space charge region in a way that would favor the carrier collection for a rough interface compared to a flat interface.

The typical roughness peak-to-valley of a co-evaporated as deposited CIGSe is about 1 μm, and the RMS is about 250 nm. In this case where the RMS is of the same order of magnitude as W, it is very likely that the surface morphology will increase the effective volume of the space charge region; by increasing the region width where the electric field is developed, it allows a complete separation of electrons-holes pairs for photons with lower energy and thus increase the short circuit current (J_{sc}) and the efficiency, as it is observed in our rough samples compared to flat samples.

A simple geometrical model that gives a first order insight of the possible influence of the surface roughness of the absorber on the space charge region and the effective diffusion length in the absorber is presented in Figure 28. In this figure W_{flat} is the space charge region width for a flat ZnO-CdS (medium 1) / CIGSe (medium 2) interface and W_{rough} is for a rough interface corresponding to as deposited co-evaporated CIGSe. The rough surface is schematized as a regular pyramid with a top angle 2θ with n_1 corresponding to the refractive index of medium 1 and n_2 to the refractive index of medium 2. When a normal incident photon reaches the interface with an angle of $\varphi = \frac{\pi}{2} - \theta$, the incident angle becomes ζ following the Snell-Descartes law:

$$\sin\varsigma = \frac{n_1}{n_2}\sin(\frac{\pi}{2} - \theta) \Leftrightarrow \varsigma = Arc\sin\left[\frac{n_1}{n_2}\cos\theta\right] \qquad (1)$$

from the scheme figure 28, we immediately deduce the formula:

$$\cos\varsigma = \frac{W_{flat}}{W_{rough}} \Leftrightarrow \frac{W_{flat}}{W_{rough}} = \cos\left\{ Arc\sin\left[\frac{n_1}{n_2}\cos\theta \right] \right\} \quad (1)$$

It is possible to make the same consideration on the diffusion length L_n, however it is very likely that it won't be affected at the same level than the space charge region which is in direct contact with the p-n junction. A more realistic behavior of the space charge region and diffusion region is shown with dotted lines on figure 28.

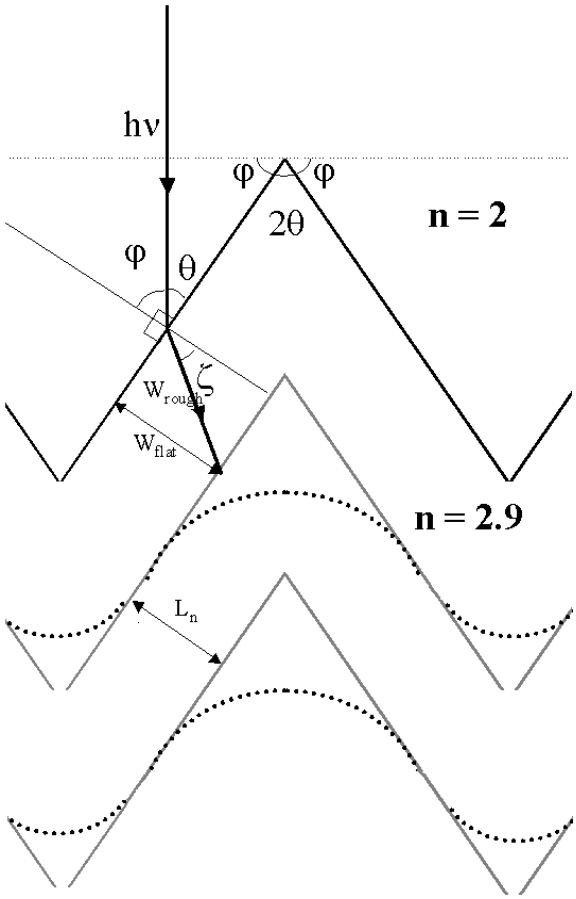

Figure 28. Schematic representation of the space charge region for a rough p-n interface

To support this hypothesis, we plot on Figure 29 the experimental internal quantum efficiency (IQE) extracted from the formula

$$IQE(\lambda) = \left[1 - R(\lambda)\right] EQE(\lambda) \quad (3)$$

with R(λ) being the reflection coefficient of the complete solar cell device, given on figure 27 for the different samples, and EQE(λ) being the experimentally measured External Quantum Efficiency given on figure 28. We observe on figure 29 a moderate decrease of the IQE for high energy photons, with an IQE at 550 nm passing from 0.92 for the non etched (rough) sample to 0.87 for the 4 minutes etched sample (smooth). The IQE decrease becomes however more important for the low energy photons; at 900 nm, it drops from 0.74 for the non etched sample down to 0.54 for the etched sample. Since the reflectivity contribution is eliminated, this drop of the quantum efficiency has to be related to the carrier collection mechanism which is influenced by the roughness of the CdS/CIGSe interface.

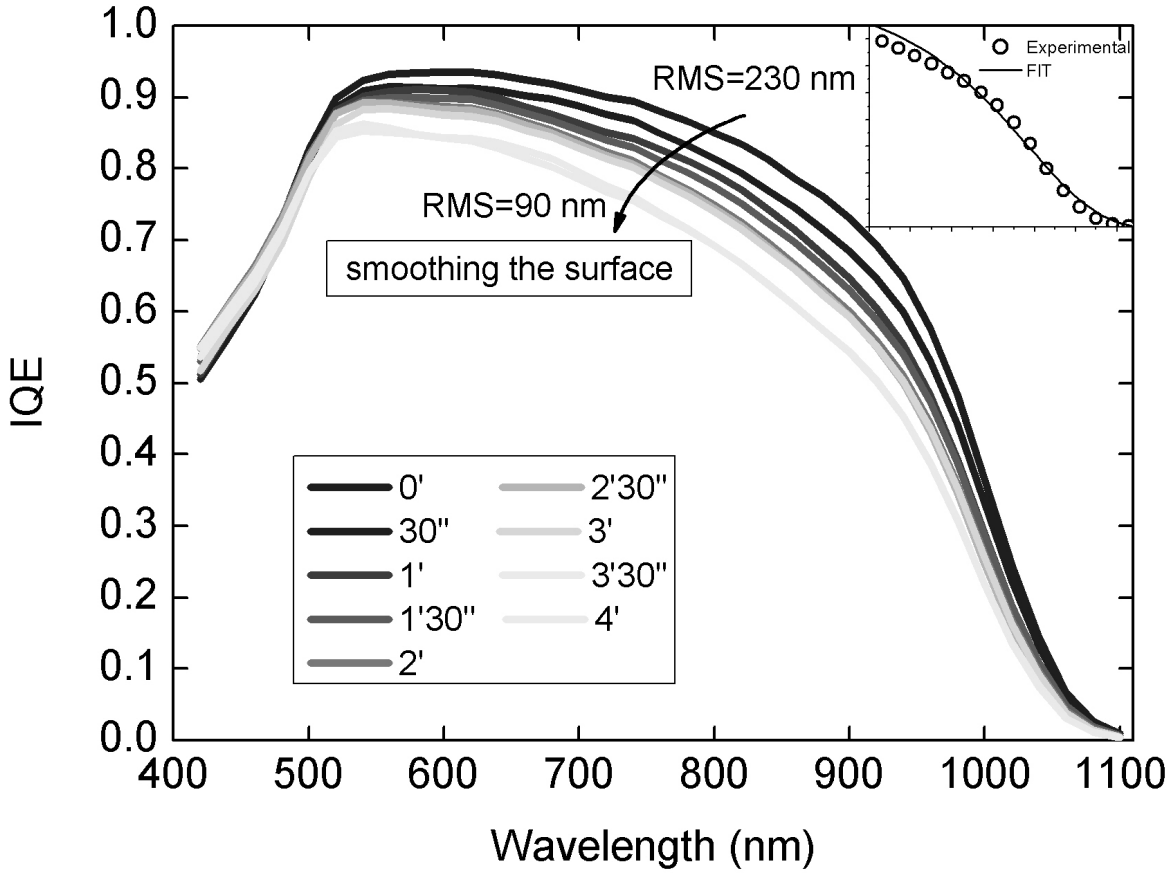

Figure 29. Internal Quantum Efficiency (IQE) for different etching times; inset: fitting of the tail of the IQE for a smooth CIGSe sample.

III.6.c) Analytical expression of the Spectral Response

In the following, we simulate the IQE of a CIGSe solar cell depending on the space charge region width W and the minority carrier diffusion length L_n. For an incident light with a wavelength λ on the surface of a semiconductor absorber, the generation function is defined as follows:

$$G(\lambda,x)=\alpha(\lambda)F(\lambda)[1-R(\lambda)]\exp(-\alpha(\lambda)x) \tag{4}$$

where $R(\lambda)$ is the reflectivity of the surface, $F(\lambda)$ is the number of incident photons per cm^2 per sec per unit bandwidth, $\alpha(\lambda)$ is the absorption coefficient of the material, and x is the distance in material from the surface. For low injection level condition (no concentration), the minority carrier continuity equation is:

$$\left(\frac{1}{q}\right)\left(\frac{dJ_n}{dx}\right)+G-\frac{(n-n_0)}{\tau_n}=0 \tag{5}$$

And the electron current is:

$$J_n=q\mu_n nE+qD_n\left(\frac{dn}{dx}\right) \tag{6}$$

Where E is the electric field, q is the elemental charge $q = 1.6.10^{-19}$ C, μ_n is the electron mobility in the absorber, τ_n is the electron lifetime in the absorber, D_n is the diffusion coefficient of the electrons in the material, n is the photogenerated electron density and n_0 is the electron density in equilibrium in the dark. In our model, we consider that both sides of the p-n junction have are uniform in doping, mobility and lifetime. When combining equation (5) and (6) and after resolution of the differential equation, we obtain the general equation:

$$(n-n_0)=A\cosh\left(\frac{x}{L_n}\right)+B\sinh\left(\frac{x}{L_n}\right)-\frac{\alpha F(1-R)\tau_n}{(\alpha^2L_n^2-1)}\exp(-\alpha x) \tag{7}$$

where L_n is the diffusion length $L_n=\sqrt{D_n\tau_n}$. The boundary conditions are:

$n-n_0=0$ for x = W where W is the width of the space charge region.

$S_n(n-n_0) = -D_n\left[\frac{d(n-n_0)}{dx}\right]$ for x = x_{BC} where S_n is the back contact recombination velocity, and x_{BC} is the abscissa of the back contact (equal to the absorber thickness when the origin is taken at the p-n junction).

This leads to the following equation for the photocurrent due to the electrons:

$$J_n = \frac{qF(1-R)\alpha L_n}{(\alpha^2 L_n^2 - 1)} \exp(-\alpha W) \times \left\{ \alpha L_n - \frac{\frac{S_n L_n}{D_n}\left[\cosh\left(\frac{\bar{x}}{L_n}\right) - \exp\left(-\alpha(\bar{x})\right)\right] + \sinh\left(\frac{\bar{x}}{L_n}\right) + \alpha L_n \exp(-\alpha \bar{x})}{\frac{S_n L_n}{D_n}\sinh\frac{\bar{x}}{L_n} + \cosh\frac{\bar{x}}{L_n}} \right\} \quad (8)$$

where $\bar{x} = x_{BC} - W$. When recombination is neglected, this equation can be written in the simple form:

$$J_n = qF(1-R)\frac{\alpha L_n}{(1+\alpha L_n)}\exp(-\alpha W) \quad (9)$$

which is the well known Gärtner's equation [67]. Both for equation (8) and (9), the internal spectral response is obtained by $IQE = \frac{J_n}{qF(1-R)}$

In the case of the CIGSe solar cells, the Mo back contact is well known for its ohmic behavior thanks to the formation of a $MoSe_2$ interfacial layer. In this case, the back contact is considered as a perfect trap for the electron and the recombination velocity $S_n \to \infty$. The Taylor's development of equation (8) with $S_n \to \infty$ leads to the analytical formula:

$$IQE = 1 - \exp(-\alpha W)\left[\frac{1}{1+\alpha L_n} - \frac{L_n \alpha}{L_n^2 \alpha^2 - 1}\frac{\exp(-\alpha \bar{x}) - \exp\left(-\frac{\bar{x}}{L_n}\right)}{\sinh\left(\frac{\bar{x}}{L_n}\right)}\right] \quad (10)$$

This is the equation that will be used in this part to simulate the influence of the space charge region width on the IQE. Figure 30 summarizes the geometry and the boundary conditions in the following.

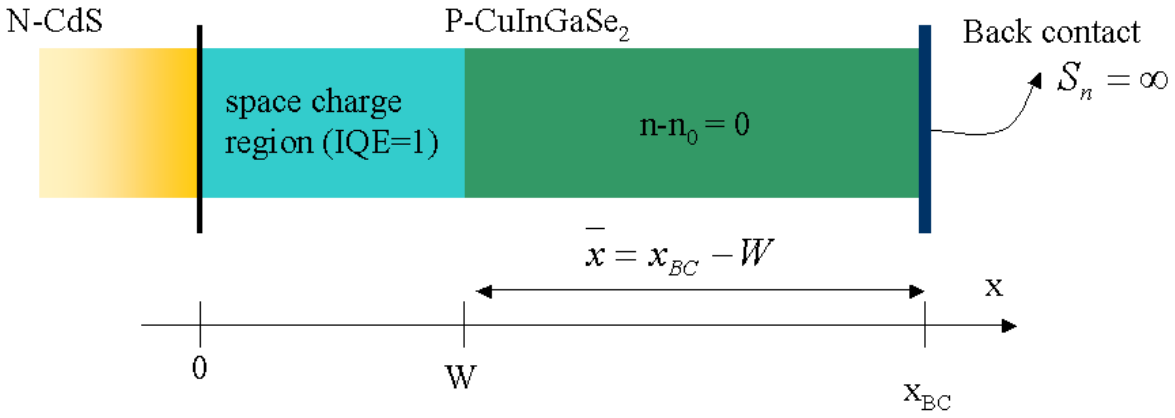

Figure 30. Schematic geometry and boundary conditions for analytical approximation of photocurrent collection

From Capacitance-Voltage measurements at ambient temperature, we have deduced the CIGSe acceptor density being $N_a=2.10^{16}$; the space charge region W for a flat interface is determined with the following simplified equation:

$$W = \sqrt{\frac{2\varepsilon_r \varepsilon_0}{qN_a}(V_{BI} - V)} \qquad (11)$$

Where V_{BI} is the built-in potential (V_{BI}~1), N_a the acceptor density, ε_r the relative permittivity of the CIGSe (ε_r = 13.6), ε_0 the absolute vacuum permittivity, and V an applied potential. When no voltage is applied, the W is equal to W_{flat} = 275 nm. It is then possible to determine L_n for a flat interface by fitting the tail of the IQE of the 4 minutes etched sample with the Gärtner's equation [67]:

$$IQE = 1 - \frac{e^{-\alpha W_{flat}}}{1 + \alpha L_n} \qquad (12)$$

where α is the absorption coefficient of the CIGSe deduced from ellipsometry measurements [68]. The fit is presented as an inset in figure 29 and the value for L_n is $L_n = 380nm$.

In order to evaluate the preeminence of W and L_n the one over the other, we simulate the IQE of a CIGSe solar cell using equation (12) and vary both parameters while keeping $L_{eff} = W + L_n = 275 + 380 = 655nm$ at a constant value. The simulated IQE are presented in figure 31. As we can see, the lowest IQE is obtained for a $W = 0$ and $L_{eff} = L_n = 655nm$ (configuration 1). In this extreme case, the generated electrons are not assisted by any potential when diffusing to the p-n junction and the carrier collection is less efficient. As observed on Figure 31, when increasing W and reducing L_n, the IQE increases, mainly between 520 nm and 950 nm (from 0.68 to 0.89 at $\lambda = 800nm$), because of the potential which enhances carrier collection for photons absorbed in the space charge region; when $L_n = 0$ and $L_{eff} = W = 655nm$ (configuration 2), the best IQE is achieved. This clearly highlights the preeminence of W over L_n as a critical parameter enhancing the IQE. This is in direct relation with the fact that the separation of electron-hole pairs in the space charge region is complete due to the assistance of the electric field while the diffusion region is electrically neutral (E=0).

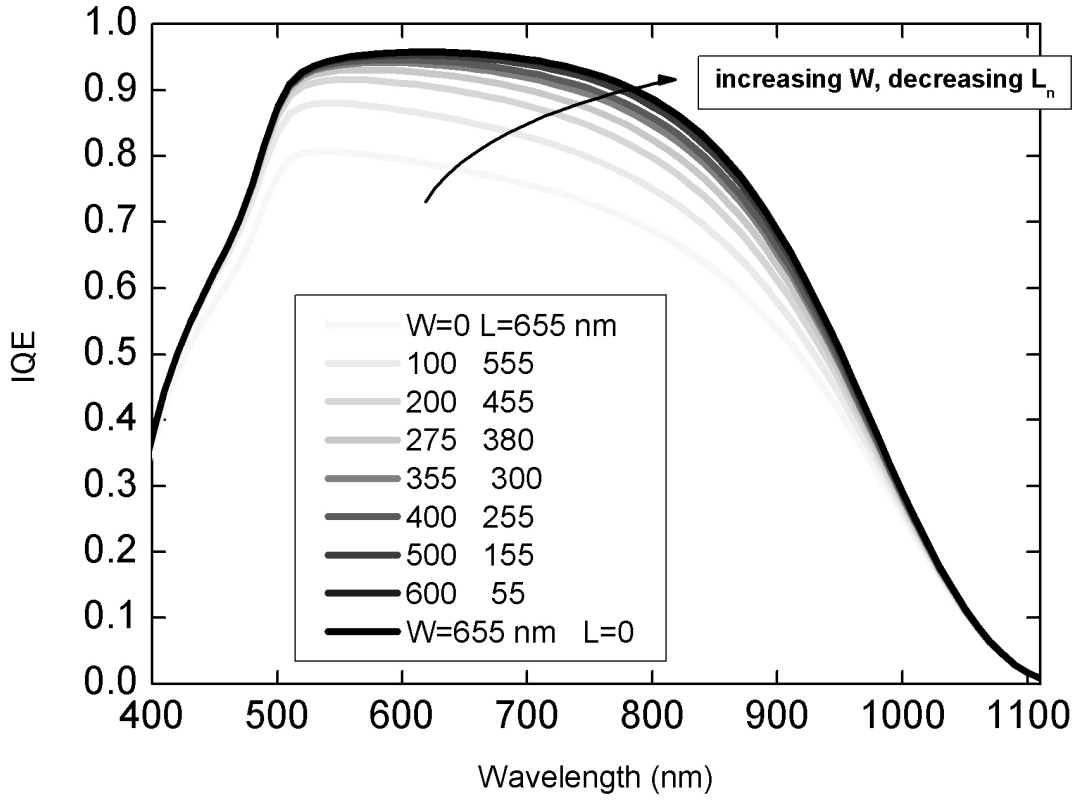

Figure 31. Simulated IQE curves where the space charge region W and the minority carriers diffusion length L_n are varied while keeping W + L_n at a constant value L_{eff}.

In the hypothesis of the roughness influencing L_{eff}, it is clear that the space charge region will be the most affected parameter, being much thinner and closer to the p-n junction than L_n. It results in an effective volume of the space charge region more important for a very rough CIGS/CdS interface compared to a flat surface. The preeminence of W over L_n as a critical parameter influencing the carrier collection have been demonstrated, leading to a behavior of the simulated IQE when increasing W comparable to what is observed in our experimental data. The penetration depth increases with the wavelength, therefore, the absorption in the space charge region and so the carrier collection is reduced in the case of a flat surface compared to a highly textured surface.

This situation points out the interest of having a low doped region where the electric field can develop. This situation is similar to the n-i-p structure found in thin film silicon solar cells. To maintain the voltage, it is important to maintain a higher doped p-type region in the back of the CIGSe layer, which is indeed the case. An additional effect which has not been considered in this study is the driving force created by bandgap grading, which enhance the effective diffusion length in the quasi-neutral region of CIGSe [65 69].

III.6.d) Conclusion

CIGSe surfaces have been chemically etched to reduce their surface roughness from a RMS of 230 nm to 90 nm, while keeping approximately the same structure, surface composition and absorber thickness (over 2 µm). The influence of the CIGSe roughness over the electrical and optical properties of CIGSe solar cells have been investigated. Reflectivity measurements shows that the reflectivity of the smooth solar cells (completed with CdS and ZnO) slightly increases. J(V) measurements and spectral response show that both FF and Voc are constant with the surface roughness, whereas the Jsc and thus the efficiency decreases with the decrease of the roughness RMS, indicating a strong dependence between CIGSe roughness and short circuit current. This Jsc decrease with the surface smoothing is more important than expected from the losses due to the increased reflectivity. We made the hypothesis that the surface roughness influences the effective space charge region width, leading to an increased carrier collection for the case where the absorber is textured compared to a flat absorber. Numerically simulated IQE highlight the importance of the space charge region width compared to the diffusion length as a critical parameter to enhance the carrier collection in the

solar cell and show results comparable to the results observed in the experiments. The roughness of the CIGSe/CdS interface is therefore found to be a major parameter for efficient state of the art solar cells. Moreover, this situation highlights the interest of having a low doped absorber region at the CdS/CIGSe to increase the space charge region and thus the carrier collection.

III.7) Chapter Conclusion

A chemical etching process, based on oxidation of the CIGSe by Br_2, has been developed for the purpose of reducing the absorber thickness without altering the properties of the film. The work from Institut Lavoisier shows that it is possible to have a remarkable control on the etching rate of the CIGSe, and Atomic Absorption Spectrometry allows to precisely monitor the etched thickness. A precision of $\pm 50nm$ over the etched thickness is possible, which is in the range of what is needed for ultrathin < 500 nm CIGSe solar cells.

XPS analysis, along with Raman spectroscopy and X ray diffraction analysis show a very good stability of the surface chemistry and the material composition and crystallinity. The KCN treatment enables to reconstruct on etched CIGSe the initial surface configuration of as-deposited CIGSe. In agreement with literature, the chemical etching of the absorber has a strong smoothing effect which was characterized by Atomic Force Microscopy. This smoothing of the surface results in a modification of the optical properties of the films.

A systematic study of the photovoltaic properties of the solar cells when varying the absorber thickness has been carried out. As expected, the main limitation of the efficiency when thinning the absorber comes from the reduced absorption and the increased back contact recombination, which affect directly the photocurrent. For ultrathin devices (<500 nm), the incomplete quasi Fermi level splitting limits the Voltage and the Fill Factor is also reduced.

The surface roughness is also of great influence over the photocurrent generation of CIGSe solar cells, regardless of the thickness of the absorber. Very short etching of the surface allowed to precisely monitor the smoothing of the CIGSe without affecting its thickness in significant proportions; a study of the parameters of the cells with the variation of the roughness of the CIGSe/CdS interface was performed, and surprising findings showed that the decrease of the photocurrent was not only related to the increased reflectivity of the solar cell, but also to the carrier collection which is different for a flat and a rough CIGSe surface. An interpretation consisting in a modification of the Space Charge Region effective width for a rough interface is proposed, and numerical simulations of Internal Quantum Efficiency by varying the space charge region width confirm the observed trend.

The decrease of the efficiency, from 14% for a reference as-deposited solar cell down to less than 10% for ultrathin devices, has to be overcome with an engineering both on the front side and on the back side of the solar cell. The Quantum Efficiency measurements show that there is a significant room for improvement of the properties of the cell, especially in the absorption of IR photons.

Chapter IV

Front contact engineering of thin CIGSe solar cells

IV.1) Introduction

In Chapter II and III, we had an overview of the phenomena responsible of the decrease of the photovoltaic performances of CIGSe solar cells when reducing the absorber thickness from its initial value (2500 nm) down to an ultrathin level (100 nm). We highlighted the fact that non absorption of incident photons in the thinned CIGSe is the main issue that needs to be solved, by an optical engineering of the device. In this Chapter, we will study the aspects concerning front contact optical engineering.

We briefly recall the principle behind an Anti-reflection coating (ARC) which is already a widely used technique to increase the proportion of the incident light entering in the solar cell. Besides the classically used ARC, we suggested in Chapter II the replacement of the U.V. absorbing CdS buffer layer by a wider bandgap material such as ZnS. This already proven technology [47,48,70–74] showed a great potential enhancement for the absorption of U.V. light inside the absorber and thus for an efficiency improvement. To the best of our knowledge, this type of buffer layer has never been used on an etched CIGSe surface; in this chapter, we will compare the photovoltaic properties of CIGSe solar cells with different absorber thickness between a standard CdS buffer layer and an alternative ZnS buffer layer.

However, the best to expect from the alternative ZnS buffer is an absorption enhancement in the U.V. range (about 400 nm to 500 nm) whereas the whole spectrum, and particularly the low energy IR photons, are concerned by the reduced absorption of the CIGSe when reducing its thickness. It is therefore needed to increase the optical path in the absorbing layer by light scattering. This problem, which is common to every ultrathin solar cell, is already widely studied for the amorphous silicon (a:Si) technology in order to obtain “optically thick, electrically thin” materials. The random texturation of the front Transparent Conducting Oxide (TCO) has been increasingly developed in the past decades [75–77], even at the industrial level with the Asahi U-type SnO_2:F (which is a standard in the a:Si technology) and more recently the VU-type and the HU-type [78]. In this chapter, we investigate on the possibility to transfer similar techniques to thinned and ultrathin CIGSe solar cells, and we give an overview of the limitations encountered during this study.

An alternative solution could come by using nanowires and nanorods [79–82]. These TCO pillar-shaped structures are well known for their extremely high light scattering properties [83–86] and thus could provide an alternative and more efficient way to improve ultrathin devices than random texturation of flat TCO layers. This option will also be studied in this Chapter.

IV.2) State of the art

IV.2.a) Anti-reflecting coating layers

An anti-reflecting coating (ARC) is a thin film coating applied on the top of a surface to reduce its reflectivity in a particular wavelength range. The basic principle is that the reflected light from different interfaces cancel each other by destructive interferences, maximizing the light transmission. In the simplest case, an ARC is a single layer deposited on the top of the surface of which the reflectivity has to be reduced; the goal is to obtain a quarter-wave layer of a material, with a refractive index close to the average value of the refractive indexes of the two adjacent media (air and ZnO:Al in our case). In that situation, two reflections of equal magnitude arise at the two interfaces, and cancel each other by destructive interference. An illustration of this particular effect is shown figure 1.

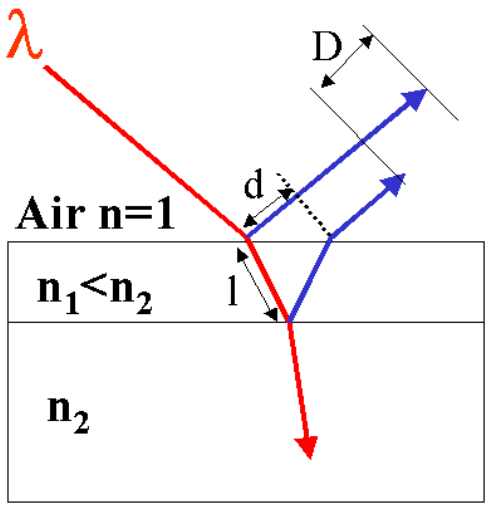

Figure 1. Schematic representation of anti reflecting effect

The layer 1 increase the optical path of one of the two reflected rays. If the layer thickness e is

$$e = \frac{\lambda}{4n_1} \qquad (1)$$

and if

$$n_1 = \frac{1+n_2}{2} \qquad (2)$$

then the shift D between the two reflected rays is

$$D = 2l \times n_1 - d = \frac{\lambda}{2} \qquad (3)$$

and the two rays are in opposite phase which leads to destructive interferences at the wavelength λ. However, this type of ARC is centered on a certain wavelength λ while a solar cell needs a broadband anti-reflecting effect. A multi-stack of ARC layers with intermediate optical indexes is required to achieve broadband antireflection. It is also possible to use a coating with a graded optical index.

An alternative option is to create an optical gradient with pyramidal shaped ARC layer,with dimensions of the order of the incident wavelength to the layer of which one wants to reduce the reflectivity. This particular shape gives a pseudo-progressive index to the medium in the vicinity of the surface, simulating a smooth transition of the refractive index by smoothly reducing the amount of solid material in a plane parallel to the surface [87] [88]. It provides an antireflection effect on a fairly large spectral and angular range.

The most commonly used ARC in CIGSe solar cells is single layer MgF_2 ARC [89] with an optical index of about $n_{MgF2} = 1.38$ in the CIGSe absorption spectral region, deposited on the front ZnO:Al window.

IV.2.b) Light scattering effect by texturation of the front ZnO:Al window

IV.2.b.i) Theoretical aspect

Scattering light at the front interface aims to increase the optical path in the absorber as schematized figure 2. The surface morphology of a film is defined by the RMS roughness σ_r and the height function $\eta(x, y)$ which can be randomly or periodically modulated. The light scattering properties of the film are characterized by the haze factor $H(\lambda)$ given by the ratio between scattered light with total light; the angular distribution function $ADF(\theta, \lambda)$ where θ is the scattering angle, defines the intensity distribution of scattered light as a function of the angle at which the scattered light propagates. It is given by the magnitude of the Poynting vector. K. Jäger and M. Zeman [90] predicted the $ADF(\theta, \lambda)$ of a surface from its morphology, using $\eta(x, y)$ as an input parameter and the first order Born approximation:

$$ADF(\lambda, \theta) = \frac{A_{opt}}{A} \cos\theta \left| \frac{F}{r} \iint_A Z e^{-i(K_x x + K_y y)} dx dy \right|^2 \qquad (4)$$

where $\frac{A_{opt}}{A}$ is the normalization of the surface of the sample depending on the optical measurement system, $K_{x,y}$ is the wave vector in the x and y directions, and Z contains the height function and is given by

$$Z = \frac{1}{iK_Z} \{1 - \exp[-iK_Z \eta(x, y)]\} \qquad (5)$$

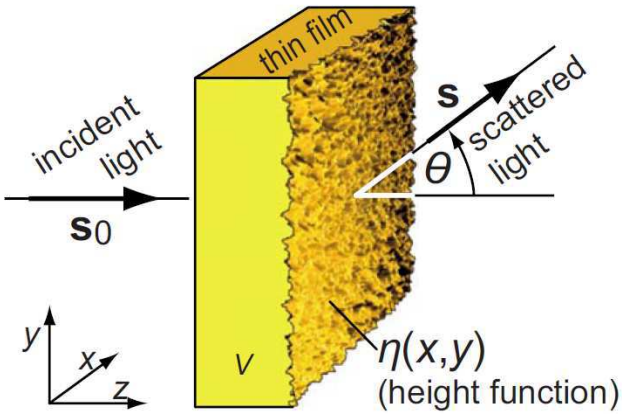

Figure 2. Illustration of the scattering of light on a thin film with a rough surface [90]

4 different samples are tested to validate the model; a Fluorine-doped tin oxide (FTO) Asahi U-type with a $\sigma_r \approx 40nm$, two ZnO:Al layer etched in HCl for 20'' and 40'' leading to $\sigma_r \approx 50nm$ and $\sigma_r \approx 100nm$ respectively (AZO 20'' and AZO 40''), and a boron doped zinc oxide with a pyramidal structure and a $\sigma_r \approx 220nm$ (BZO).

This theoretical model is in reasonable agreement with experimental data of AZO 20'' and FTO as shown figure 3.a, but doesn't match for AZO 40'' and BZO. It is known that the Born first order approximation works better for moderate RMS roughness [91], and equation (5) was modified for higher σ_r leading to the equation

$$Z^{(II)} = \frac{1}{ik}\{1 - \exp[-ik\eta(x,y)]\} \qquad (6)$$

where $k = K_{x,y,z}$. In this case, known as modified Fraunhofer scattering, the measured and calculated intensities for AZO 40'' and BZO match much better than with the Born first order approximation as shown figure 3.b.

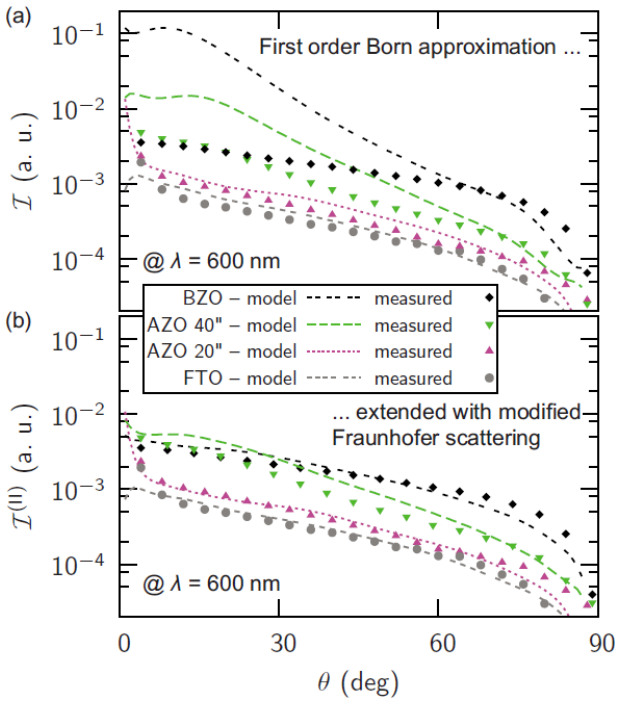

Figure 3. Four samples at λ = 600 nm (Color line) (a) Measurements and the application of equation (4) with first order Born approximation (equation (5)); (b) With a modified Fraunhofer scattering extension (equation (6)) [90]

Numerical tools allows to predict the light scattering behavior of a textured rough surface. Different types of structures have been investigated to achieve broadband and efficient light scattering, especially for Silicon thin film solar cells; in the following, we will present an overview of recent progresses in the field.

IV.2.b.ii) Light scattering by texturation of the front ZnO

Texturing the front transparent conducting oxide (TCO) has been reported as one of the most effective solution to increase the light trapping in very thin absorbers, leading to the development of the reference industrial SnO_2:F substrate in thin film silicon solar cells Asahi U-type [78]. Kluth and Löffl reported a method that allows to texture a magnetron sputtered ZnO:Al layer by wet chemical etching in HCl [75 92] to enhance the light scattering. This method has been widely used since then in the field of a:Si solar cell as one of the most effective one to achieve low cost and efficient light scattering at the front interface of the solar cell [93–99]. Starting from a ZnO:Al film with a thickness typically between 500 nm to 1000 nm, the film is dipped in a HCl solution with a concentration of 0.5 % in most cases [95 94] for a few seconds (less than a minute). This leads to a thickness reduction between 100 nm to about 400 nm, and to the texturation of the ZnO:Al film due to the preferential etching of the material at the grain boundaries. The purpose is to obtain films with high light scattering properties without degrading its electrical properties (i.e. not increasing the resistivity), with a sheet resistance in the range of 5-15 Ω/sq [94]. The two important optical parameters that determine the quality of the light scattering are the haze parameter H and the angular distribution function ADF. The haze parameter is described as the ratio of light that is scattered with the total intensity of light at the interface. The ADF defines the intensity distribution of scattered light as a function of the angle at which the scattered light propagates. In a paper from 2003 [93], J. Krc and M. Zeman report that by varying the etching duration from 1s to 30s in a 0.5% HCl solution, it is possible to vary the root mean square of the surface roughness σr from 25 to 120 nm. Optical measurements using a spectrometer coupled with an integrating sphere show that the haze increases with increasing σr both for the transmitted and reflected light, and decreases with increasing the wavelength λ for both (figure 4). The comparison of H for reflected H_R and transmitted H_T light of the same substrate reveals that the scattering process is more effective in reflection than in transmission. The calculated H_T for transmitted light is much higher than the experimental one, whereas the reflected H_R seems in better agreement with the experiments although far from matching.

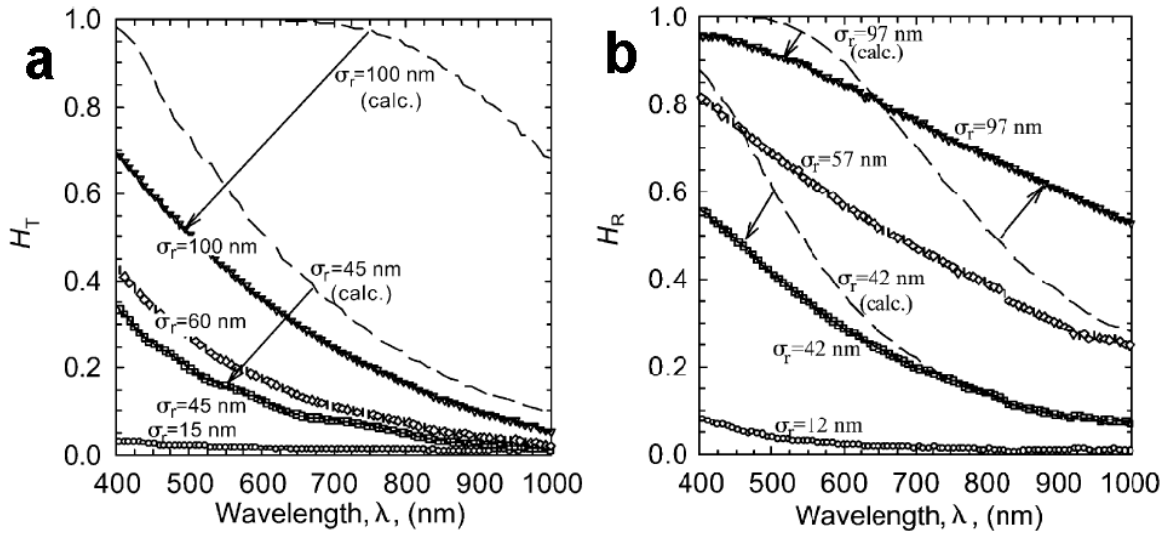

Figure 4. Measured (symbols) and calculated (lines) haze parameters in transmission (a) and reflection (b) of the air/glass/ZnO:Al/air stack. [93]

On the other hand, angular resolved scattering measurements show that increasing σr leads to a decrease of the ADF parameters, i.e. high σ_r samples have a more pronounced light scattering into smaller angles centered around the specular direction (figure 5). Whatever the σ_r, the ADF of the etched ZnO:Al remains lower than for the commercial SnO2:F Asahi U-type, and of course than lambertian light scattering.

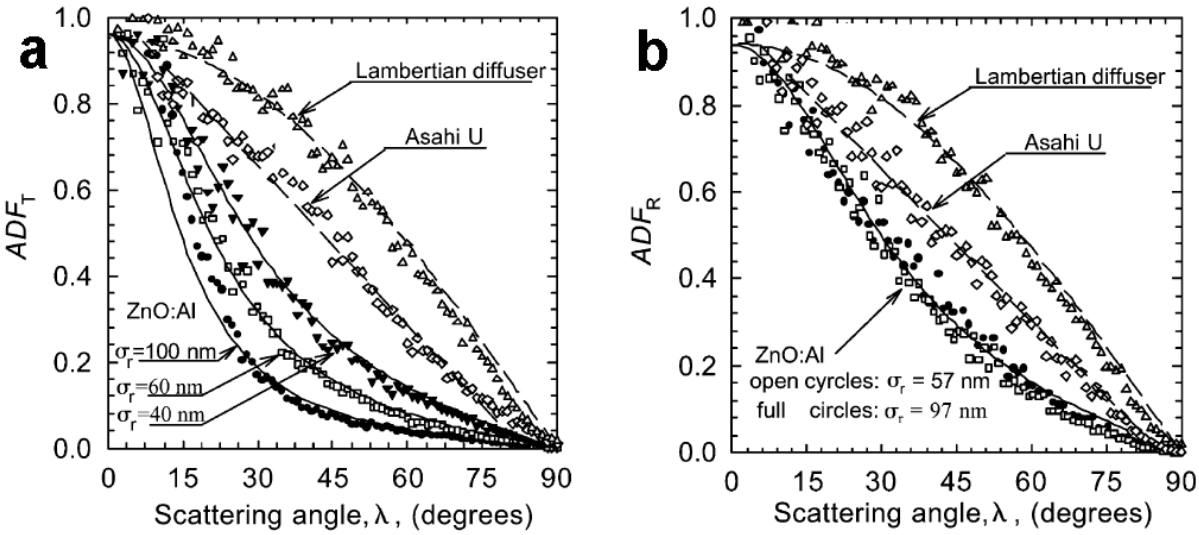

Figure 5. Measured (symbols) and approximated (curves) angular distribution functions of diffused transmitted (a) and reflected (b) light for the glass/ZnO:Al stack with different σr. For comparison, the measured and approximated ADF of an Asahi U-type SnO_2:F and a lambertian diffuser are added. [93]

Although encouraging, these results show that there is still room for improvement in light scattering by the front TCO. In order to evaluate the potential enhancements of the light trapping by textured films, Krc, Smole and Topic [100] performed numerical simulation of the effect of an hypothetic high haze parameter and ADF of a textured conductive oxide on the quantum efficiency and short circuit current on a a:Si solar cell. They observe a significant improvement of the parameters of the cell up to a haze factor of 40%. Beyond that point, optical simulations do not show any significant enhancement on the J_{sc}, indicating saturation with respect to haze parameter. Similarly, a saturation is observed for very broad ADF, due to absorption by the thin p-side of the a:Si instead of the active intrinsic layer. However, this would not be the case for CIGSe solar cells since neither the buffer layer nor the front window are likely to absorb in the same spectral region than CIGSe.

Tuning the surface morphology of ZnO:Al is therefore found to be a key issue in controlling the light scattering properties for photovoltaic applications. In a publication from 2007 [95], F. Ruske and W. Werner showed that it is possible to modify the etching behavior of sputtered ZnO:Al films by changing the oxygen partial pressure during the deposition. Different surface morphologies are realized depending on the pressure as shown in figure 6. For low oxygen partial pressure (10 mPa), the surface shows a low roughness which progressively increases when the pressure is increased up to 17.5 mPa, with a structure size of about 200 nm. Further increase of the oxygen partial pressure above 20 mPa leads to a very rough film with steep structure, which size decreases below 200 nm. Optical characterizations with an integrating sphere (not shown, see reference [95]) indicates that the highest haze value is reached for an oxygen partial of 17.5 mPa.

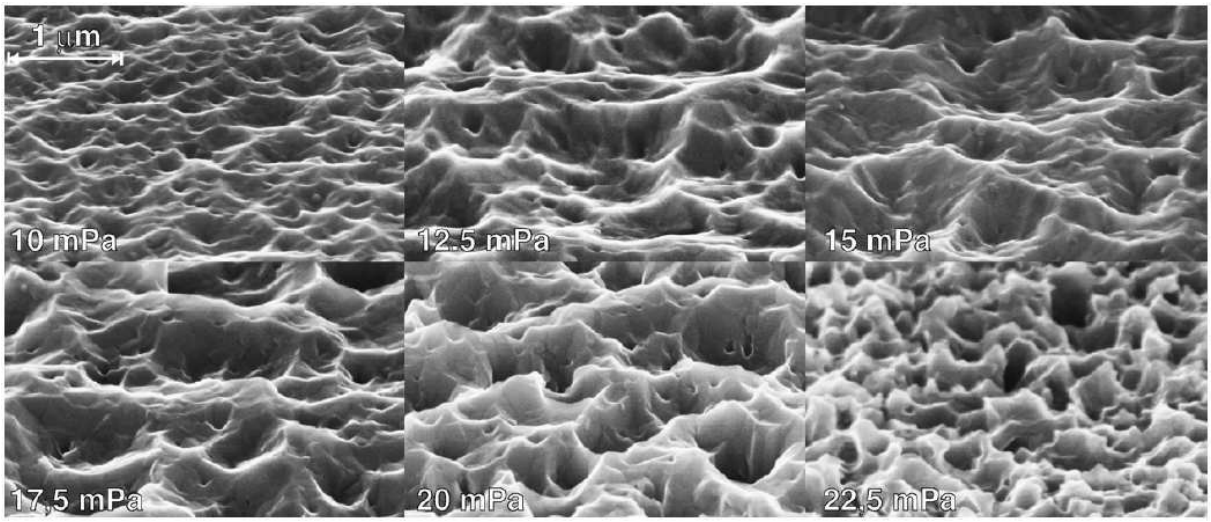

Figure 6. SEM cross section images of the surface structure of ZnO:Al films after HCl etching as a function of the oxygen partial pressure during the deposition [95].

High haze ZnO:Al films such as presented in the papers previously discussed lead to significant improvements in the quantum efficiency of a:Si or µc:Si solar cells. An example from the review of Müller and Vanecek et al. [94] is shown in figure 7. It demonstrates the influence of the ZnO:Al surface roughness for two µc:Si cells deposited on glass/ZnO:Al superstrate. Both the QE and the (1-R) curves are shown (R is the reflectivity). The cell with the rough ZnO:Al shows as expected a much higher QE, and the main gain in the generated J_{sc} comes from the red/IR region due to the introduced light trapping. Additionally, QE is increased due to an antireflection effect which was already reported by reference [101].

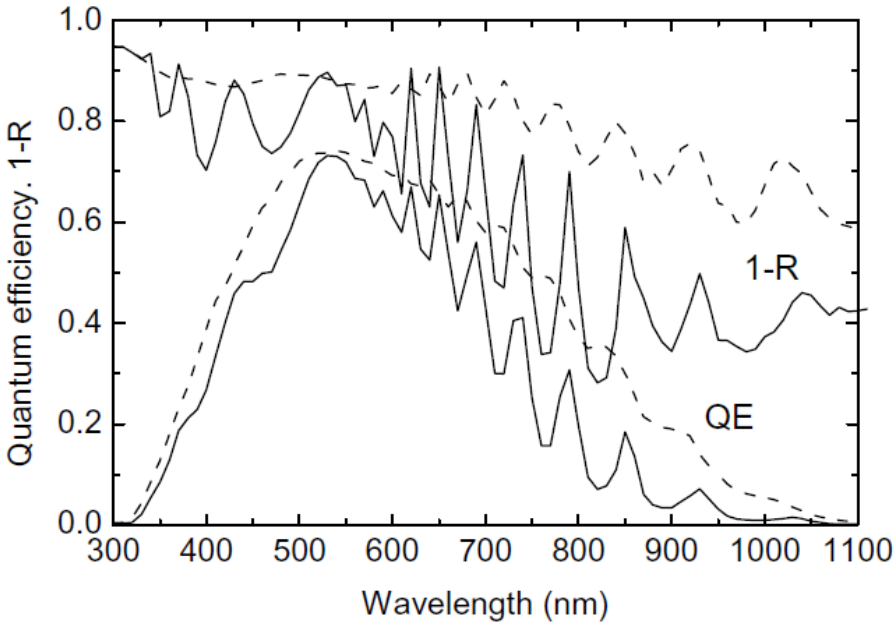

Figure 7. Quantum efficiency and (1-R) curves of μc:Si pin solar cells with thin textured-etched (dashed lines) and smooth ZnO:Al (solid lines). Resulting J_{sc} are 20.8 mA.cm^{-2} and 15.3 mA.cm^{-2} respectively [94].

Unlike thin film Si solar cells, CIGSe is a substrate-only technology since it involves a high temperature process and materials that are incompatible with the superstrate process. Therefore, texturing the front ZnO can only be performed after full deposition of the solar cell stack, and the air/ZnO interface is the only one that can be modified. Moreover, the high absorption coefficient of CIGSe makes light trapping unnecessary in the standard conditions. A recent study based on numerical simulations by Campa and Topic et al. [41] evaluated the potential of a textured front ZnO:Al for CIGSe solar cells application. It is demonstrated that a high haze parameter and broad ADF at the air/ZnO:Al does not lead to large scattering angles in the CIGSe, and so does not significantly enhance the light absorption in this layer. This is due to the refractive index of CIGSe which is $n \approx 2.9$, that is larger than the one of ZnO:Al $n \approx 2$. According to Snell-Descartes law, large scattering angles are transformed into smaller ones when entering in the CIGSe and greatly reduces the impact on the solar cells parameters. However, the authors show that a substantial increase of the QE is expected if the CIGSe/CdS interface is textured, similarly to what happens in the superstrate thin film Si solar cells. The second effect related to additional roughness at air/ZnO:Al interface is the decreased reflectivity of the solar cell, according to the antireflection effect of textured

surface that was discussed in the beginning of this chapter. This effect is observed in the simulations and increases light absorption in the CIGSe [41].

IV.2.b.iii) Light scattering by ZnO nanorods

Although light scattering at the front interface is a lot more complicated in the case of CIGSe solar cells compared to the thin film Si technology, we demonstrated in the simulations chapter II that an effective antireflection (AR) layer on top of the CIGSe has the potential to increase the absorption in the CIGSe by an absolute value of 7 %. AR can be achieved either by etching the ZnO as previously discussed, but it is possible to achieve a much higher surface roughness by deposing ZnO nanorods on top of the ZnO:Al. Previous studies from different groups already investigated on the use of ZnO nanorods and nanotubes for dye sensitized solar cells and ETA cells [81] [83] [84] [102] [103]. The interest is to take advantage of the important developed surface and the light scattering properties of such structures. Moreover, in a 2008 publication from Lee et al. [104], ZnO nanorods (NR) are reported as a very efficient solution to achieve AR effect in solar cells. The authors use a RCWA method to simulate the reflectivity of a NR film, and they demonstrate that control of tip tapering of the NR allows to significantly reduce the reflectivity of the films. A comparison of the reflectivity of differently shaped NR is showed figure 8. We see that a reflectivity lower than optimized SiN ARC can be obtained for highly tapered NR.

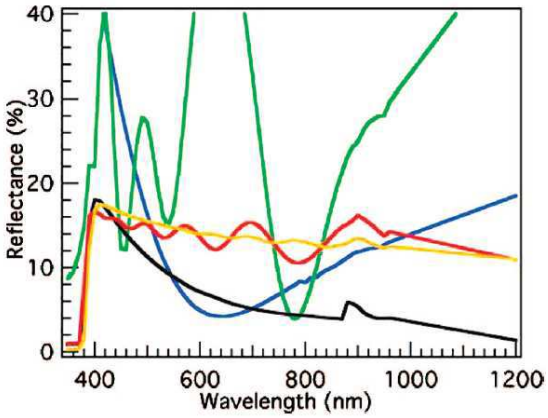

Figure 8. Front reflectance spectra of flat top NR (red), tapered NR (orange), sol-gel ZnO film (green), optimized SiN ARC on Si PV cell with metallic contact (blue), and highly tapered NR (black) [104]

We reported an experimental observation of the reduced reflectivity of vertically oriented ZnO nanorods electrodeposited on ZnO:Al films [86]. A recent study [105] demonstrates experimentally the potential of ZnO NR as an effective ARC on CIGSe solar cell. The NR are deposited by electrodeposition from an aqueous solution of 4.5 mM $Zn(NO_3)_2 \times 6H_2O$ and 70 µM HNO_3 directly on the ZnO:Al front window of the solar cell. As expected, the reflectance of the solar cell is significantly reduced while the EQE in increased and the interference fringes in the ZnO are vanished (figure 9.a). The effect is comparable to standard MgF_2 ARC (figure 9.b) and further improvements are possible with future optimizations.

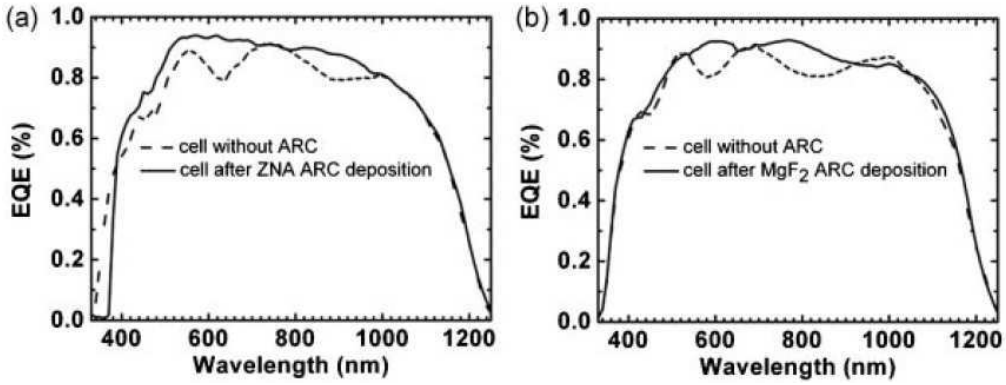

Figure 9. EQE of a solar cell before (dashed line) and after (solid line) deposition of ZnO NR (a); after (solid line) MgF_2 single layer coating (b) [105]

Another solution to improve the light absorption in the CIGSe layer is to replace the CdS buffer layer by a material with a wider bandgap, such as ZnS. Simulations from Chapter II showed that such a buffer layer could greatly improve the efficiency of solar cells; in the following, we will present a summarized state of the art on this topic.

IV.2.c) Alternative ZnS/(Zn,Mg)O buffer layer for CIGSe solar cells

The standard buffer layer used in the CIGSe solar cells is the Cadmium Sulfide (CdS), deposited by chemical bath deposition (CBD). Its excellent band matching with CIGSe (bandgap Eg = 2.4 eV and electron affinity χ=4.2 eV) associated with its very good coverage of the absorber makes it an appropriate material for the p-n junction. However, the Cd toxicity and the relatively low bandgap of the CdS, which absorbs light in the U.V. range, led to an increasing development of alternative solutions [46,48,106–109]. One of the most proven solution of alternative buffer layer is the CBD deposited ZnS buffer layer, which is already used as a standard buffer layer in some industrially produced CIGSe modules [70]. Its high bandgap (3.6 eV), associated to a surface passivation due to the incorporation of sulfur and short deposition times (<10 min) makes it an excellent alternative to CdS.

In 2009, two joint publications [47] [48] investigated on the combination of both a CBD deposited ZnS layer and a sputtered $Zn_{1-x}Mg_xO$ layer, in replacement to the standard CdS/ZnO:i bilayer, leading to significant improvements of the efficiency and the stability compared to previous alternative buffer layer solar cells. The deposition process is as follow: co-evaporated CIGSe films [2] are chemically treated in a KCN solution [35]. The ZnS layer is then grown by CBD from aqueous solutions of zinc sulfate (0.1 M), thiourea (0.4 M), and ammonia (1.5 M). The deposition temperature is tested between 60°C and 90°C. The $Zn_{1-x}Mg_xO$ layer is deposited by radio-frequency magnetron sputtering. Its bandgap varies from 3.3 eV for pure ZnO to 4.1 eV for $Zn_{0.6}Mg_{0.4}O$. In this study, the bandgap of $Zn_{1-x}Mg_xO$ was 3.6 eV. More details on the ZnS/ $Zn_{1-x}Mg_xO$ bilayer deposition and composition can be found in Appendix III.

A comparison with standard CdS buffer is carried out; the devices parameters are summarized in table 1. The higher bandgap of ZnS leads to a higher transmission of the ZnS buffer in the 350-550 nm wavelength range, the Cd-free solar cells show a significantly enhanced quantum efficiency in this spectral region (figure 10). At the absorption edge of the CIGSe, the EQE of the Cd-free cells is identical to the one with CdS buffer, which indicates that the collection length is not affected by the new buffer layer. However, the V_{oc} of Cd free cells is systematically lower by an average of 40 mV compared to standard CdS/ZnO:i buffer solar cells. The relative gain of about 12% in J_{sc} of Cd-free cells leads to a relative increase of about 9% in the efficiency as illustrated table 1.

Buffer layer	CdS/ZnO:i	ZnS/ZnMgO
Voc (mV)	690	665
FF (%)	76.4	77.4
Jsc (mA.cm^{-2})	26.5	29.7
Efficiency (%)	14	15.3

Table 1. Compared photovoltaic parameters for CIGSe solar cells with CdS and ZnS buffer layers [47]

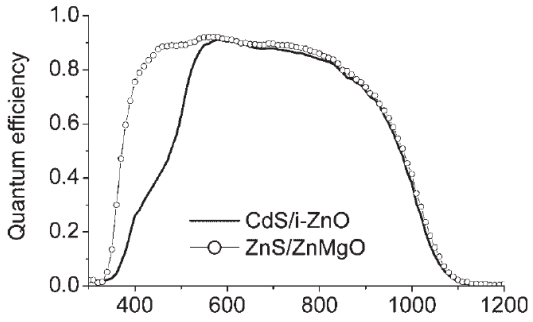

Figure 10. Compared EQE for CdS/ZnO:i and a ZnS/ $Zn_{0.74}Mg_{26}O$ buffer layer [47]

According to Serhan et al. [110], the CIGSe/ZnS interface is the critical parameter that controls the metastabilities observed in the solar cells; we have highlighted in the previous chapter with XPS analysis that the bromine etching of CIGSe surfaces does not lead to any major surface modification of the films, and KCN treatment allows to reconstruct the surface termination of the reference as-grown CIGSe [61]. In the experimental part of this chapter, we will investigate on bromine etched absorber solar cells with an alternative ZnS buffer layer and discuss our results regarding literature and the optical simulations presented in Chapter II.

IV.2.d) Conclusion

Using textured TCO for light scattering has been proven as a very efficient way to improve the light absorption in thin film solar cells such as amorphous silicon base solar cells; Theoretical studies however suggest that one should not expect a gain as important in the CIGSe technology, because of the index matching between the layer that reduces the scattering angle. Recent studies on the influence of ZnO nanorods on the front side of a CIGSe solar cell demonstrated that a very good antireflection effect can be achieved with such a structure.

As already discussed in Chapter II, the replacement of CdS by ZnS as a buffer layer is a key point to increase the short circuit current of the solar cell. Literature however does not report the deposition of ZnS on etched CIGSe surface.

IV.3) Experimental Results

IV.3.a) Light scattering and antireflection effect for ultrathin CIGSe solar cells by ZnO:Al chemical texturation and electrodeposition of ZnO nanorods

Increasing the light broadband absorption is a major issue when reducing the absorber thickness like it was highlighted both in Chapter II and III. The thin film Si solar cells technology developed several ways to texture transparent conducting oxides (TCO) and thus increase the light pathway through the absorber while decreasing the front side reflectivity. In the following, we will transpose these techniques to the CIGSe technology and study the feasibility of increasing the light absorption in very thin absorber. In the first part, we discuss on the optical properties of chemically etched ZnO:Al films, and then apply these etch to the ZnO:Al window layer of thinned absorber CIGSe solar cells. A comparative study with a standard MgF_2 antireflection coating is proposed. In the following part, we push further the surface texturation by electrodeposing ZnO nanorods on ZnO:Al films. We study the optical properties of the nanorods films compared to etched ZnO:Al films, especially their light scattering properties. ZnO nanorods are then applied to thinned absorber CIGSe solar cells and electrical characterizations are performed.

IV.3.a.i) Texturation of ZnO:Al surfaces by chemical etching

Films on glass substrate

ZnO:Al films are deposited by sputtering with the standard solar cell conditions on glass. The film thickness is doubled (800 nm) compared to classic solar in order to avoid full dissolution when etching the films and maintain good electrical properties. The sheet resistance of the films is characterized with a 4 probes Pro4 setup (LUCAS LABS), and the films morphology is observed using SEM. The optical properties of the films are characterized in reflectivity and transmission with a spectrometer (Perkin Elmert lambda 900 UV/VIS/NIR) and an integrating sphere. Both direct and diffused transmission and reflection are measured, unfortunately, angle resolved measurements are not possible with our experimental setup and thus the ADF

cannot be characterized. The etching is performed in an HCl solution and the effect of both the etching time and the concentration of HCl is studied. The chemical reaction involved is

$$ZnO + 2H^+ \rightarrow Zn^{2+} + H_2O$$

The experimental protocol is as follows:

The ZnO:Al surface is rinsed for two minutes with Millipore quality water (18.2 Ω.cm). This is to make sure that the surface is completely wet.

The sample is etched for a given time in the HCl solution (see table 2 for conditions)

The surface is again rinsed for two minutes in Millipore water

The whole process takes place at room temperature.

Sample Number	C1	C2	C3	C4	C5	C6	C7
HCl Concentration (% mass)	0.01%	0.03%	0.05%	0.10%	0.30%	0.50%	0.70%
Etching duration (s)	15	90	5	10	5	2	1
	25	120	20	20	10	5	2
	40	150	50	45	20	10	5
	60		60	60	40	15	10
	90		90	75	60	30	
	120						
	150						
	180						

Table 2. Etching conditions of ZnO:Al on Glass

In order to maintain the good electrical properties of the front TCO, we set the limit of the maximum acceptable sheet resistance of the film at 20 Ω/sq. The sheet resistance of the standard 400 nm ZnO:Al film is about 8-10 Ω/sq, and the one of a 800 nm film as used in this study is about 4 Ω/sq. The sheet resistance being partly related to the film thickness, we expect it to increase when etching the films. Similarly, the preferential etching at the grain boundaries may further affect the electrical transport properties of the films. The variation of the sheet resistance as a function of different HCl concentrations and etching times is presented on figure 11.

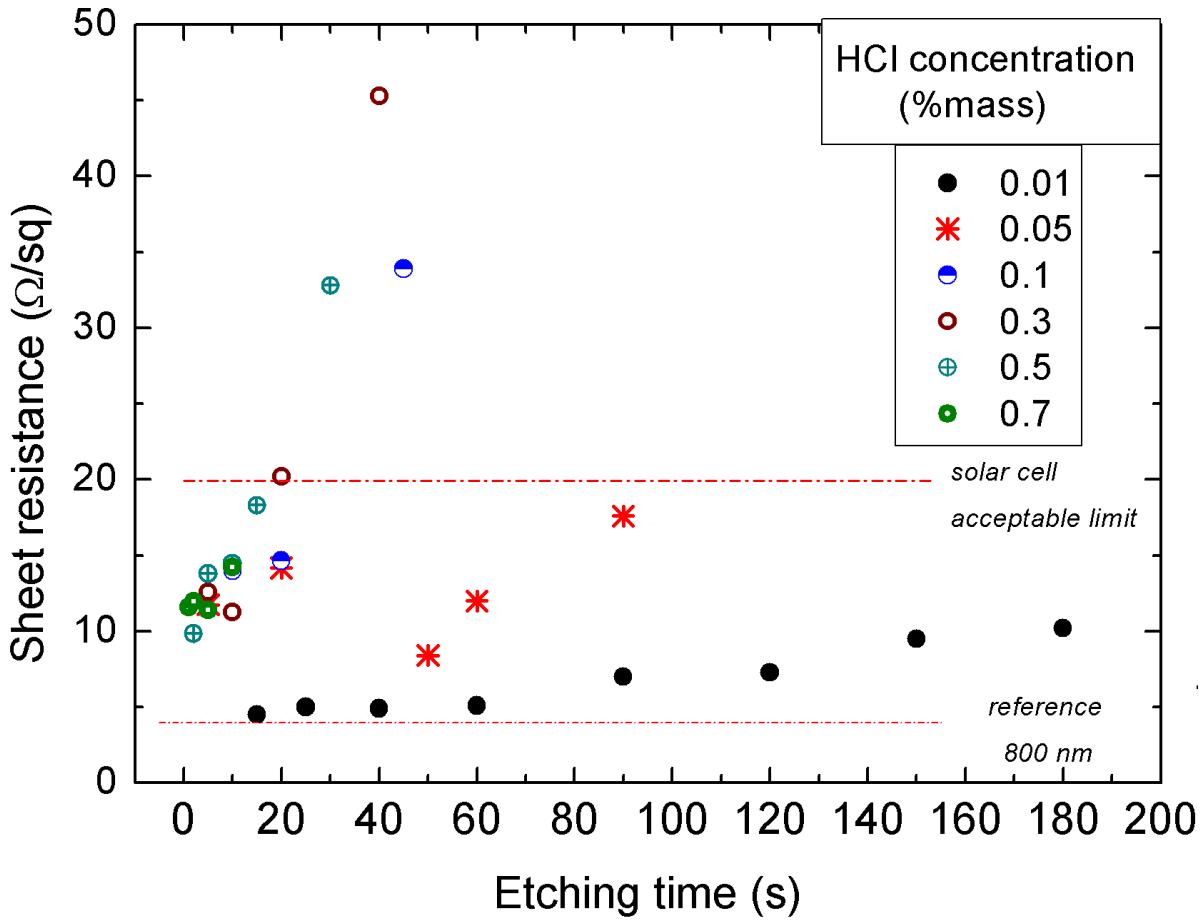

Figure 11. Sheet resistance of etched ZnO:Al films with different HCl concentrations and etching durations

We observe a relatively important spreading of the results. As expected, low HCl concentrations leads to lower sheet resistance, even after a very long etching (> 100 seconds). The 0.01% HCl solution does not seem to significantly affect the surface since its sheet resistance is almost unchanged; The 0.5% HCl solution, which is the most reported concentration in the thin film Si solar cells field, leads to a sheet resistance of ZnO:Al lower

than 20 Ω/sq up to approximatively 20 seconds of etching. The 0.05% HCl solution offers a sheet resistance lower than 20 Ω/sq up to 90 seconds of etching, and the aspect of the film seems very diffusive to the eye. These data have to be compared to optical measurements in order to determine the best etching condition to apply to solar cells. All samples are tested in total and diffuse transmission and reflection. Our purpose is to determine the best conditions in terms of light diffusion, total transmission, along with a low reflectivity. The amount of data being considerable, more details can be found in reference [111]. The optimal films properties are obtained with the following conditions:

- 0.05% HCl and 90 seconds
- 0.1% HCl and 45 seconds
- 0.3% HCl and 40 seconds

Figure 12 presents the diffused transmission curve that is achieved for these three samples.

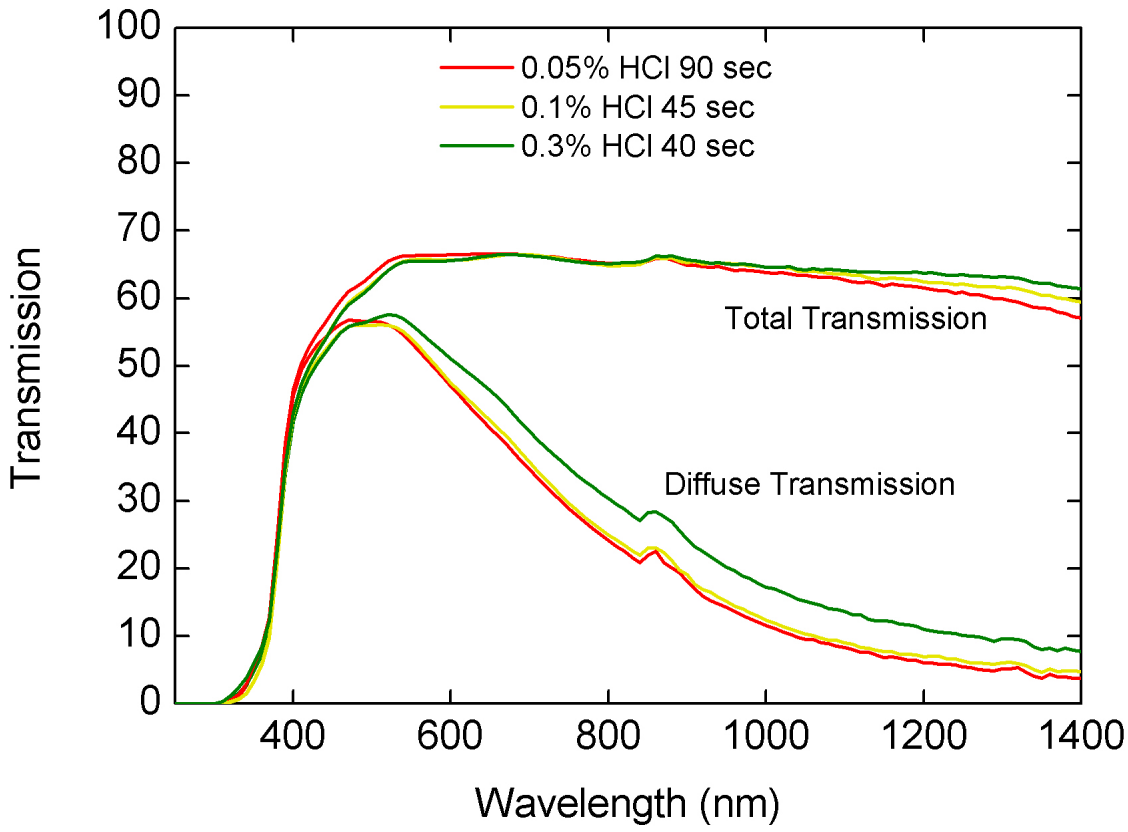

Figure 12. Diffuse transmission for different of etched ZnO:Al films for different HCl concentrations and etching times. The stack is Glass/ZnO:Al.

In these conditions, the reflectivity of the ZnO:Al film is lower than non etched ZnO:Al, while the ratio of scattered transmitted light is remarkably increased. The three sample have almost equivalent light diffusion properties; the diffusion peaks at about 60% for $\lambda = 500nm$ in each sample before decreasing in the red and infrared spectral region. As a result, the diffusion is only 20% for $\lambda = 900nm$ which is the spectral region where light scattering is the most needed for ultrathin absorber CIGSe solar cells.

However, the only condition that leads to a film with a sheet resistance that is acceptable for a TCO application on CIGSe is the 0.05% HCl and 90 seconds of etching. This HCl concentration is surprisingly lower to what is usually reported in literature. We hint that this may be related to the different deposition conditions for the ZnO:Al layer. The SEM cross section view of the surface of each sample is presented on figure 13. We see that the film thickness is much lower (approximatively 200 nm) for 0.1% and 0.3% HCl which explains why the sheet resistance is much higher than for the 0.05% HCl sample (approximatively 500 nm thick). The three films present a high surface texturation with random pyramids about 200 nm wide and 100 nm high.

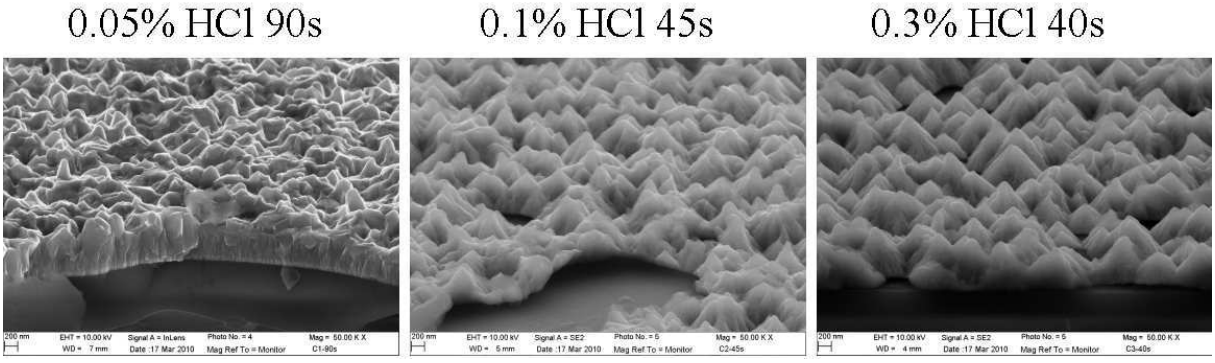

Figure 13. SEM cross section of HCl etched ZnO:Al films on glass substrate

The optical properties of the 90-seconds etched ZnO:Al film with concentration 0.05% HCl compared to the standard non etched ZnO:Al are presented on figure 14.a (reflection) and b (transmission). The interference fringes in the reference sample correspond to the ZnO:Al film thickness and appear due to the smoothness of the film. These interference fringes are still visible for short etching times (not shown), which allowed us to estimate the etching rate

to about 3.5 nm per second for this HCl concentration (0.05% in mass). The interference fringes vanish when the surface is highly textured (etched sample curves on the figure). In the CIGSe absorption range, the reflectivity of the film is lowered (figure 14.b), however in smaller proportion than expected if the films were deposited on CIGSe. This is due to the differences in optical indexes between glass (n~1.5) and CIGSe (n~2.9); while the reflectivity of the air/ZnO interface is as expected reduced by the surface texturation, the inverse effect of antireflection occurs (enhanced reflectivity) at the ZnO/glass interface ($n_{glass} < n_{ZnO}$). The overall reflectivity of the stack is therefore only slightly lowered, meaning that the ZnO:Al texturation overcompensates the enhanced reflectivity effect due to the deposition of ZnO:Al on glass. In both cases (etched and non etched) the ratio between total and diffuse reflectivity is very high; this high reflectivity haze is consistent with previous observations from literature [93].

The average total transmission is almost not affected by the texturation of the films with a transmission plateau of about 70% in the 400 nm – 1100 nm range, which corresponds to an absorption of about 8% on the complete stack for the etched films. This relatively high value can be explained by the fact that the optical path in the ZnO:Al is enhanced by the surface texturation, and the scattering angle is even more increased in the glass substrate because of its lower optical index, which leads to total reflections inside the glass for some rays and so losses in the transverse direction. While the measured diffuse part of the transmission is extremely low for non etched sample, around 5% on the whole spectrum, the etched textured sample has a very high diffuse part which starts at about λ=1000 nm and peaks at 520 nm with a value close to 60% of diffusion. This results in a haze factor H_{etched} that increase from about 30% at λ = 1000 nm to H_{etched} = 90% at 520 nm. In comparison, the haze factor for the reference non textured sample is $H_{ref} < 10\%$ on the whole spectral range. The expected effect on light scattering of the surface texturation is here clearly visible. Unfortunately, all our samples had a diffusion curve centered around 500 nm – 550 nm. The scale of the texturation is related to the average size of the grain. In order to tune the diffusion properties, it would be interesting to vary the size of the ZnO:Al grains, which was not performed in this study.

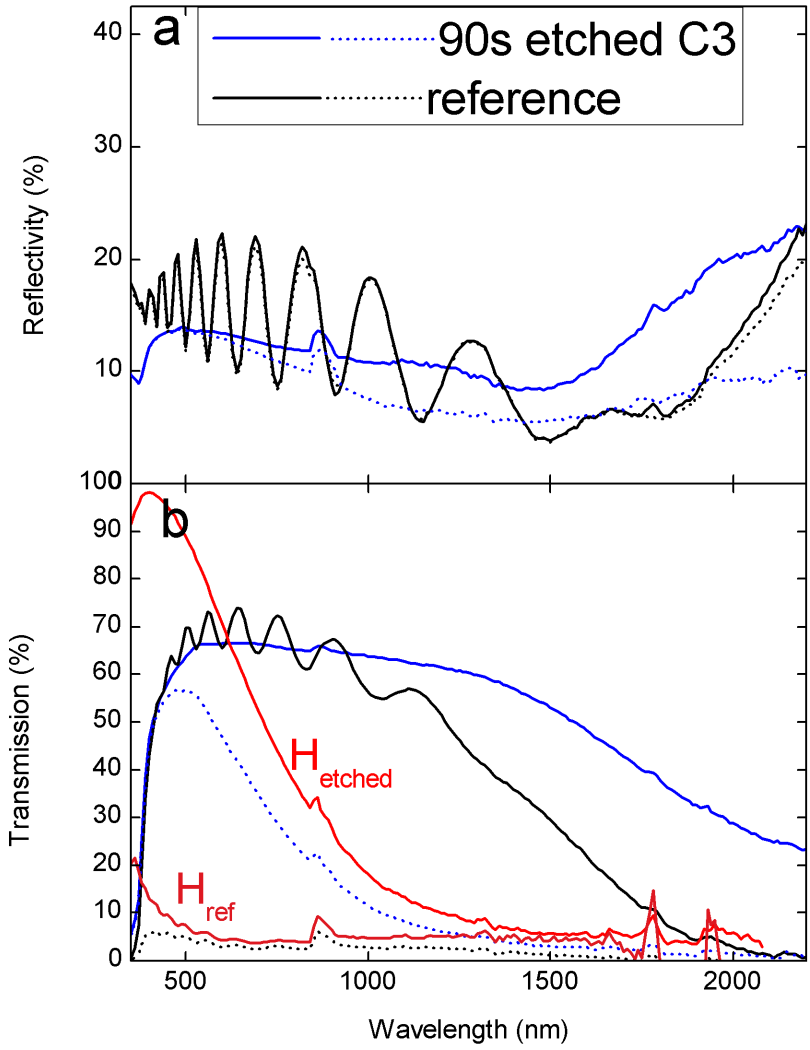

Figure 14. Reflectivity (a) and Transmission (b) of non etched (black) and etched (blue) ZnO:Al films on Glass. Both the total (solid line) and diffuse part (dashed line) are presented. The curves are the total ZnO:Al/Glass stack, and the glass substrate has not been subtracted from the data. The Haze factor H is represented in red for the etched H_{etched} and non etched H_{ref} sample.

These results show the potential of a textured ZnO:Al surface for light scattering and antireflection effect. However, these etching parameters were optimized for a ZnO:Al deposited on a glass substrate; it is very likely that the deposition of the ZnO:Al on the CIGSe/CdS stack may change both the optical properties because of the optical index of CIGSe which is higher than that of glass, but also because of the film morphology which may change when the deposition is done on a different substrate. In the following, we will investigate on texturing the front ZnO:Al window of a 500 nm absorber CIGSe solar cell. We will compare the standard ZnO:Al with the etched one and a classic antireflection coating.

Texturation of the front window of CIGSe solar cells

CIGSe solar cells with different absorber thickness are prepared using chemical Br_2 etching of the absorber, and completed with the standard solar cell process that is described in Chapter III, except that the front ZnO:Al window layer thickness is 800 nm instead of 400 nm. Each solar cell is divided into smaller cells of 0.1 cm x 0.1 cm (8 cells per sample), and the photovoltaic parameters given are average values on the whole sample. The samples are electrically characterized before and after the etching (texturation) of the ZnO:Al. The front window of the solar cells is textured following the method described in the previous paragraph a.1. However, the direct application of the previously optimized process (90 seconds, 0.05% HCl) on the Mo/CIGSe/CdS led to the complete dissolution of the ZnO:Al window layer and new conditions had to be found. The fact that the ZnO:Al dissolution is much faster on CIGSe/CdS than on glass may be related to the fact that the substrate greatly influences the crystallinity and the stresses within the films, which leads to a different etching behavior; such a study is however not carried out in this thesis, and we only focus on optimizing the photovoltaic properties of the solar cells by etching the ZnO:Al films. The concentrations and etching durations have been significantly lowered compared to our previous study about the etching of ZnO:Al on glass substrate. The etching parameters used on this study are summarized in table 3.

HCl concentration (%mass)	0.01	0.025	0.2	0.4
Etching Duration (s)	20	15	3	2
	40	25	6	5
	60	40	10	8
	80	60	15	12

Table 3. Etching conditions of ZnO:Al on Mo/CIGSe/CdS

Firstly, we focus on solar cells with a 500 nm thickness in order to optimize the HCl etching time. In a second part, we study a complete solar cell serie with different absorber thicknesses and the optimized HCl etching.

Optimization of the HCl etching on a 500 nm CIGSe solar cell

J-V characterization

Each solar cell is characterized by J-V measurement under AM 1.5 illumination. The best solar cell serie is achieved for the 0.025% HCl concentration, we therefore present the results obtained for this sample. The average photovoltaic parameters for different etching times are presented in Figure 15 and are compared to the parameters of the same solar cells prior to the etching.

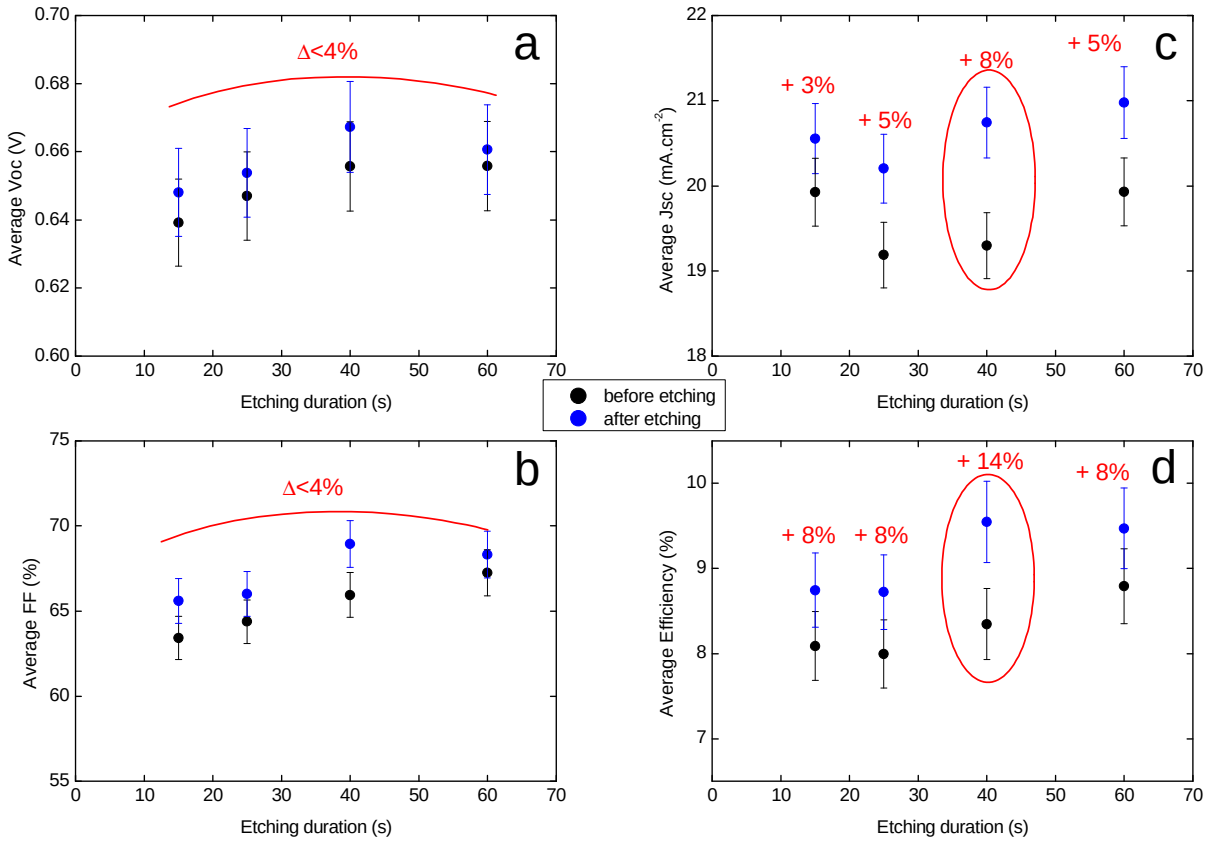

Figure 15. Photovoltaic parameters for a 500 nm CIGSe solar cell before (black dots) and after (blue dots) etching in a 0.025% HCl solution for different etching duration. The error bars are determined with the standard deviation of data on each solar cell with Originlab software.

We clearly see a general increase of all the average photovoltaic parameters after etching of the front ZnO:Al window. However, the increase is below 4% relative to the non etched ZnO:Al film for the V_{oc} and the FF, and cannot be considered as significant when considering the errors bars in the measurements. The only parameters that is enhanced to a value beyond

the error bars is the J_{sc}, with a significant + 8% increase for the 40 seconds etched sample, increasing from 19.3 $mA.cm^{-2}$ for the standard flat ZnO:Al up to 20.8 $mA.cm^{-2}$ for the textured ZnO:Al. Therefore, when texturing the ZnO:Al front window, the efficiency increases from 8.3 % to 9.6 % which represents a relative increase of 14% of the efficiency (figure 16.d) for this etching duration. One may be tempted to consider the +8% relative efficiency increase that is observed for the other etching durations as meaningful, it is however lower than the standard deviation of the data. This relatively important spreading of the results may be related to an insufficient stirring during the etching of the ZnO:Al, which led to inhomogeneities on the samples.

As expected and observed on figure 15, the efficiency enhancement when texturing the front ZnO:Al can only be related to an increase in the short circuit current; evaluation of the spectral region where the absorption and/or the carrier collection is enhanced is a key issue for understanding the effect of the textured ZnO:Al on the thinned solar cell. We performed EQE measurements before and after the ZnO:Al texturation with a 0.025% HCl concentration and a 40 seconds etching time, on a 500 nm CIGSe solar cell. The obtained curve is compared with a standard CIGSe solar cell with the same absorber thickness (500 nm) and no etching of the front ZnO:Al, and with a 500 nm absorber CIGSe solar cell with a standard MgF_2 antireflection coating (ARC) that was deposited at *"Institut des Matériaux de Nantes" (IMN)*. The EQE curves are presented in figure 16. We first notice that the interference fringes are different for the two reference solar cells in figure 16.a and 16.b. This is due to the fact that the ZnO:Al thickness is 400 nm in the first case (standard conditions) and 800 nm in the second case (so that the HCl etching does not completely dissolve the film). By comparing figure 16.a and 16.b, we observe that the MgF_2 ARC and the textured ZnO:Al film have a very similar effect on the quantum efficiency. The interference fringes are suppressed in both cases, and the EQE main increase is in the 400 nm - 700 nm; it also slightly increases in the infrared spectral region for the textured ZnO:Al, while the MgF_2 ARC does not impact these wavelengths. Eventually, the impact of both techniques is very similar. This supports the fact that light scattering at the air/ZnO:Al interface is strongly limited by the optical indexes ($n_{ZnO} \approx 2$ and $n_{CIGSe} \approx 2.9$) when the ZnO:i/CdS/CIGSe interfaces are smooth, as it was previously reported in reference [41]. Textured ZnO:Al is however found to be a very effective broadband antireflection coating. Its pyramid-type high texturation gives a pseudo-progressive optical index at the air/ZnO:Al interface which results in a substantial increase of the short circuit current (+8%), that is confirmed by EQE measurements.

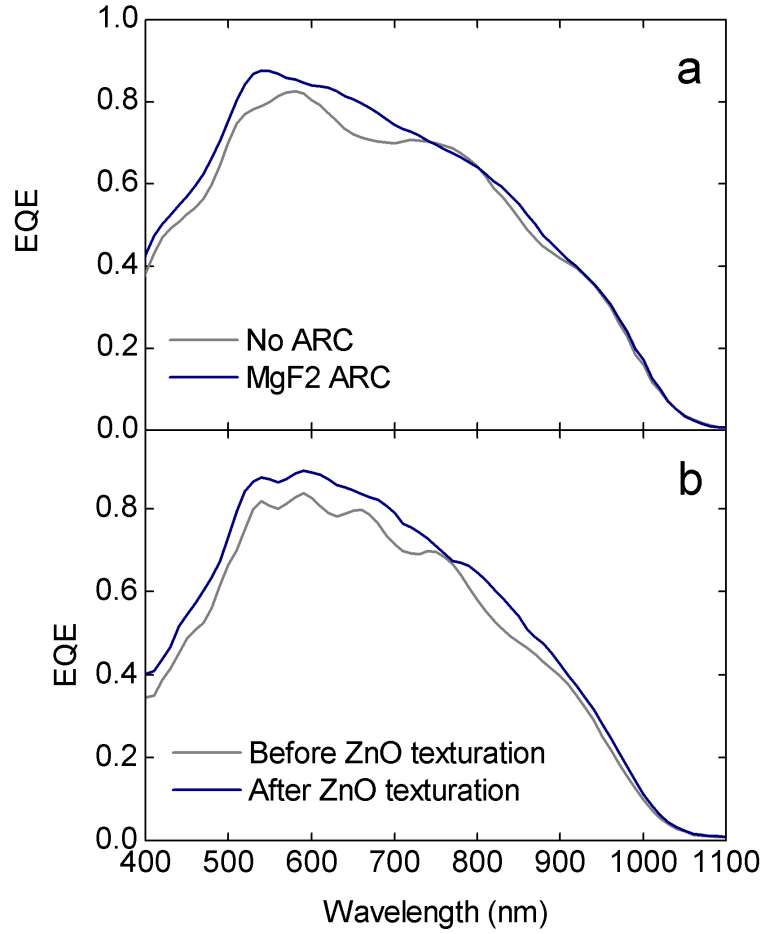

Figure 16. External Quantum Efficiency for a 500 nm CIGSe solar cell. (a) Without ARC (grey curve) and with MgF_2 ARC (dark blue curve); (b) With the standard non etched 800 nm ZnO:Al front window (grey curve) and with a etched textured ZnO:Al front window

Comparison between standard MgF_2 ARC and textured front ZnO:Al for different CIGSe thicknesses

We compare the results obtained with MgF_2 ARC and HCl etching of the front ZnO:Al window, on a solar cell serie with different CIGSe absorber thicknesses: 2 µm, 1.5 µm, 1 µm, 0.5 µm and 0.3 µm. The solar cells have been prepared using the same batch and the same CdS/ZnO process; each sample is cut in two parts, one being coated by the MgF_2 ARC, the other being etched in HCl 0.025% for 40 seconds. The EQE are presented in figure 17.a for the MgF_2 ARC serie, and in figure 17.b for the etched ZnO:Al serie.

It is clear that texturing the ZnO:Al window layer by HCl etching leads to an equivalent antireflection effect than a standard MgF_2 ARC; for each CIGSe thickness, the interference fringes are vanished in both cases and the EQE is slightly increased, especially in the visible spectral region, up to about 750 nm.

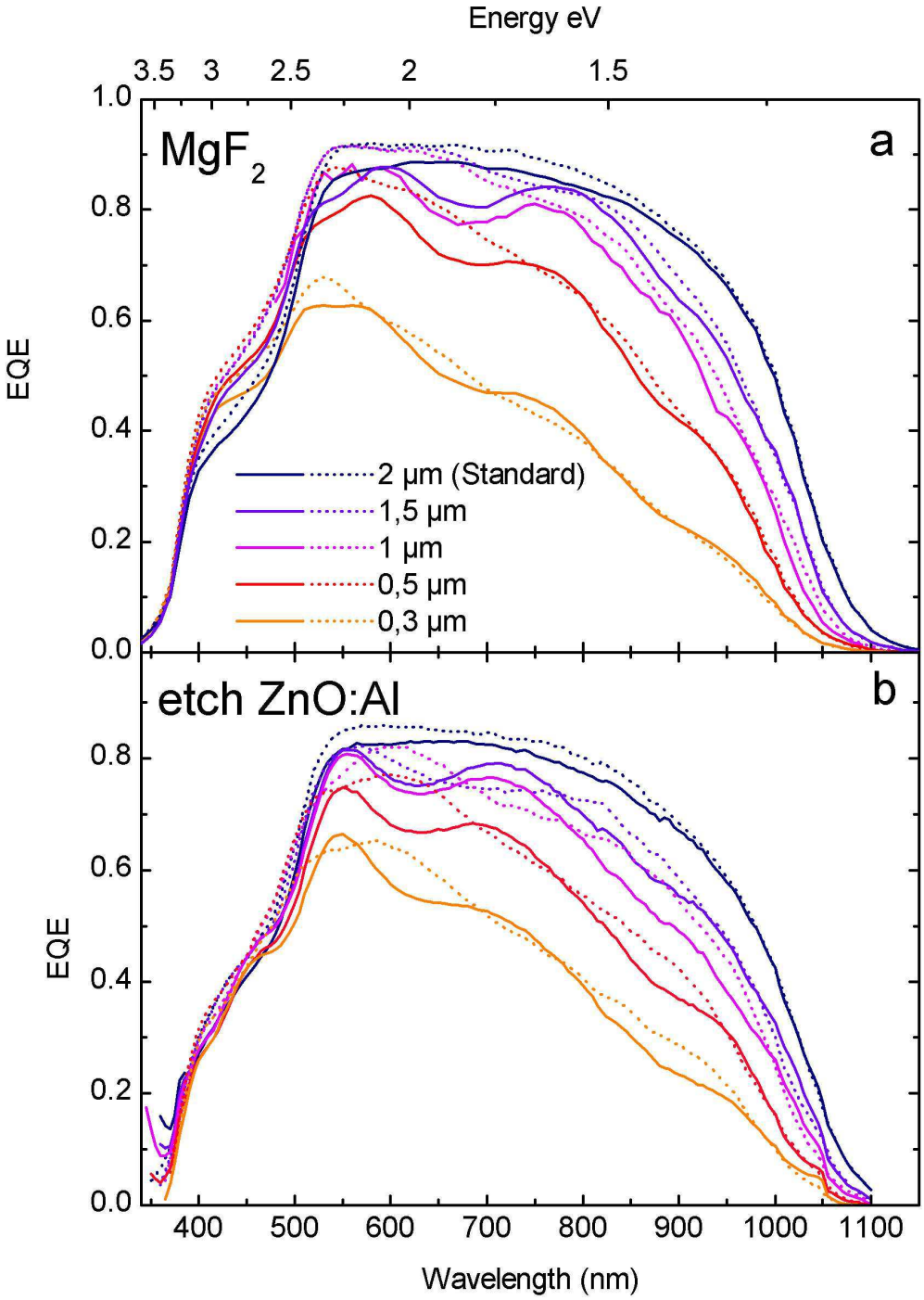

Figure 17. Compared EQE curves for different CIGSe thicknesses with: (a) MgF_2 ARC (dotted lines) and no ARC (solid lines); (b) etched front ZnO (dotted line) and non etched ZnO (solid lines).

The photovoltaic parameters of the solar cells are presented figure 18. We see that both techniques (MgF2 and HCl etched ZnO:Al) lead to comparable results, although an important spreading of the data appears for the FF (figure 18.d). The overall efficiency improvement is very comparable between MgF_2 ARC and HCl etched ZnO:Al.

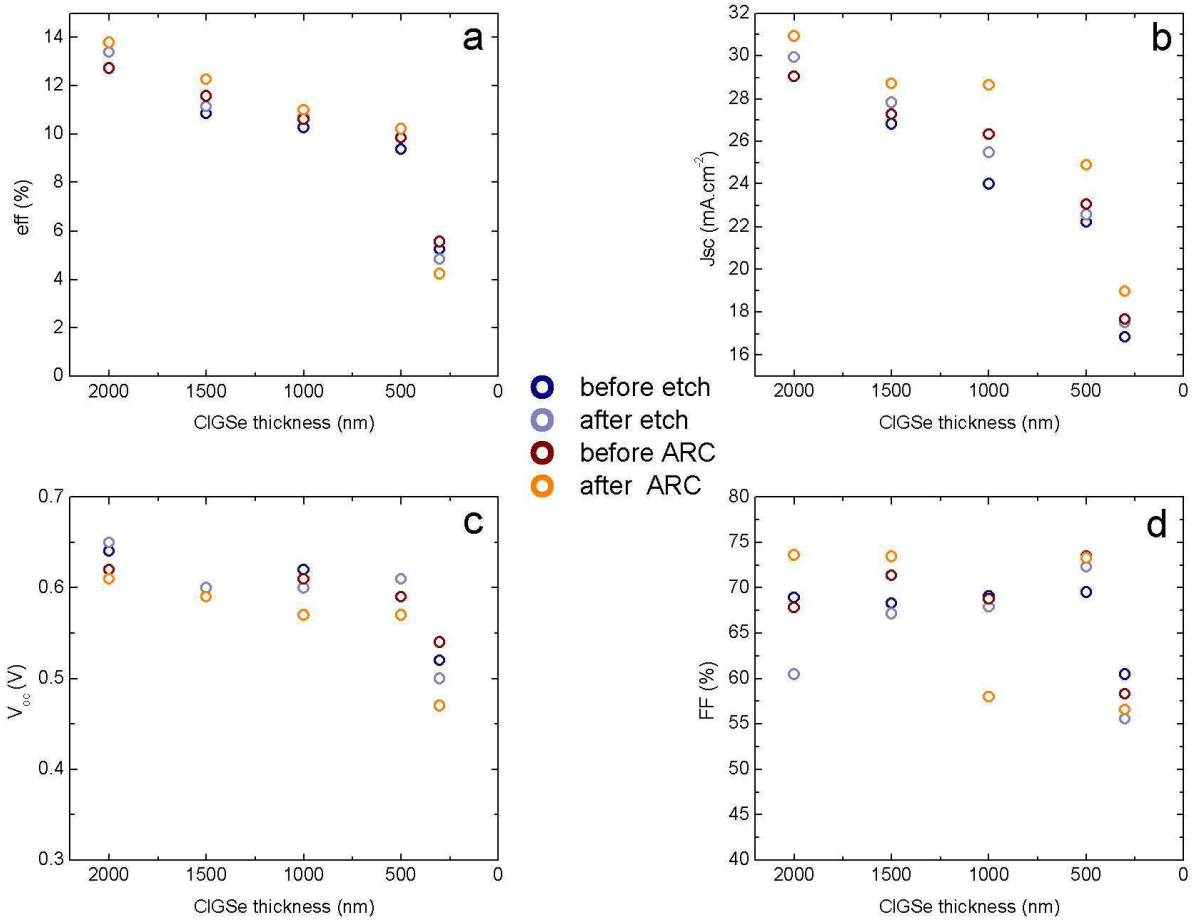

Figure 18. Compared photovoltaic parameters for different CIGSe thicknesses with MgF_2 ARC and ZnO:Al etching. (a) Efficiency; (b) J_{sc}; (c) V_{oc}; (d) FF.

In this part, we evaluated the potential of a textured front ZnO:Al window layer for a thinned absorber CIGSe solar cell. We observed a substantial +14% efficiency increase for an optimized surface texturation on a 500 nm thick absorber, which is related to an increase of the photocurrent of the solar cell. When comparing the quantum efficiency to the EQE of a solar cell with the same absorber thickness and a standard MgF_2 antireflection coating, we see that the effect is almost similar, whatever the CIGSe thickness. While MgF_2 ARC is a well

known and optimized process, it is interesting to note that we obtained results almost similar with texturation of the front ZnO:Al window. However, no improvement specific to a light scattering effect has been observed.

To go beyond the pyramid-type ZnO texturation, we investigate in the following the feasibility of ZnO surface with extreme light scattering properties and antireflection effect.

IV.3.a.ii) Electrodeposited ZnO nanorods on ZnO:Al films for light scattering and antireflection effect

ZnO nanorods aroused a great interest in the past decade because of the large variety of morphology that can be achieved and their resulting interesting optical and electrical properties. Among all the deposition techniques, electrodeposition has emerged as a very flexible effective way to deposit and tune the morphology of nanorods films [112] [113]. In this work, our purpose is to deposit ZnO nanorods on top of the ZnO:Al by electrochemistry, and to optimize the optical properties of the films to increase to the maximum their light scattering properties. We use a $ZnCl_2$/KCl solution for the electrodeposition; this deposition process is based on the reduction of oxygen with the following reactions:

$$O_2 + 4e^- + 2H_2O \rightarrow 4OH^- \text{ and } Zn^{2+} + 2OH^- \rightarrow ZnO + H_2O$$

The solution is O_2 saturated by bubbling, and the deposition temperature is fixed at 80°C. We use a saturated calomel electrode as a reference electrode (SCE), and the applied voltage versus SCE is –1.4V. We have demonstrated in a paper [86], which is at the margin of the subject of this thesis, that it is possible to tune the orientation of the nanorods and so the optical properties of the films by varying the crystalline orientation of the substrate. Varying the deposition time, along with the $ZnCl_2$ concentration are also important parameters that influence the nanorods length and surface density. We performed a complete comparative study about the influence of the substrate and deposition time on the nanorods film morphology and optical properties, and the reader is referred to reference [86] and [111] for further information on this topic.

In this thesis, we only focus on showing the potential of ZnO nanorods as a light scattering film. We deposited the ZnO nanorods with a $ZnCl_2$ concentration of 0.02 mM and a KCl

concentration of 0.1 M. The amount of deposited ZnO is monitored by the Total Charge Exchanged per surface units during the electrodeposition (TCE), which is in direct relation with the length of the nanorods and the amount of deposited material. The substrate used is a 800 nm ZnO:Al film deposited on glass by sputtering. This film has been etched with an HCl solution like described in the previous part of this chapter. The pre-texturation of the substrate is necessary to reduce the density of nucleation sites and thus the density of grown nanorods; it also allows to grow non vertical nanorods. Figure 19 presents the SEM pictures of nanorods when deposited on a non etched ZnO:Al substrate (figure 19.a) and on an etched ZnO:Al substrate (figure 19.b). We clearly see a strong difference between the two films; when deposited on the non etched ZnO:Al, the nanorods are vertical and their density is very high, of the order of 100.μm^{-3}. If the ZnO:Al substrate is pre-etched in HCl, the nanorods grow with a much lower density (20-30.μm^{-3}), and are highly disoriented. We also show (figure 19.c), that is possible to grow vertical nanorods on the top of the pyramids, if the ZnO:Al substrate is HCl etched under certain conditions (very low HCl concentration < 0.02%). In this case, the pyramids have a flat tip, which is the nucleation center for the nanorods. However, this work is at the margin of our subject and we won't expand on this topic.

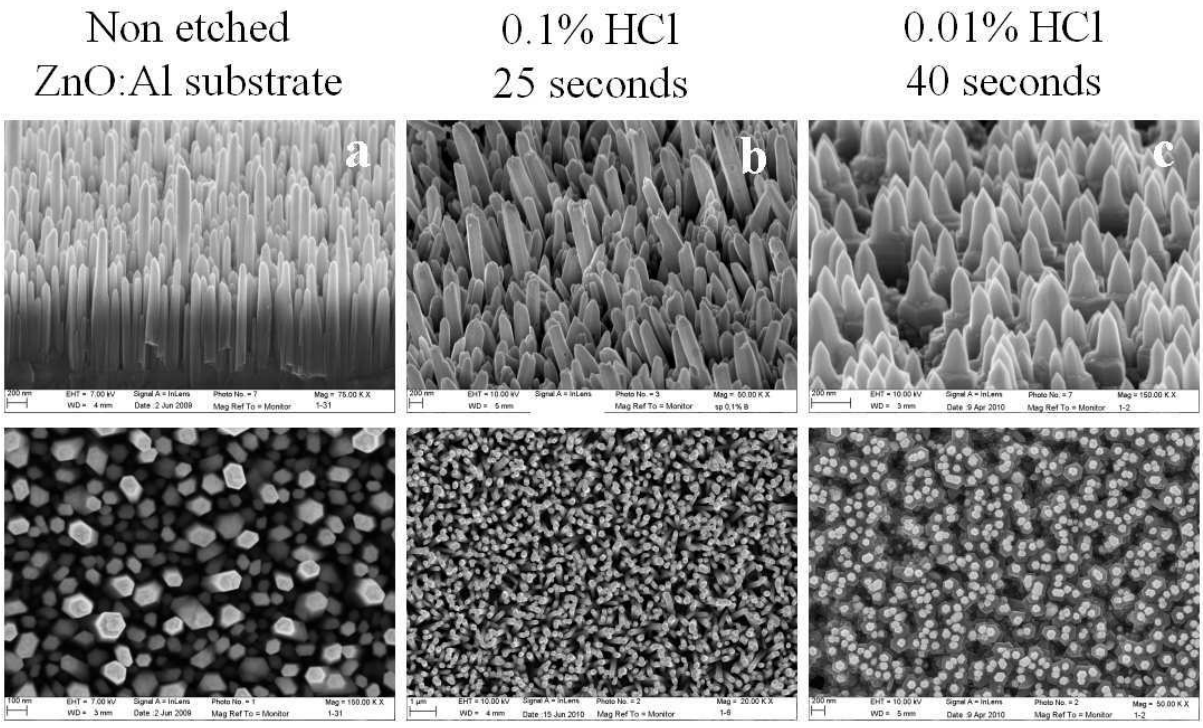

Figure 19. SEM cross section and top view of ZnO nanorods deposited on ZnO:Al substrate; (a) non etched substrate; (b) etched substrate 0.1% HCl and 25 seconds; (c) etched substrate 0.01% HCl and 40 seconds

Growing non vertical and low density nanorods is needed for a maximum light scattering properties of the films as we highlighted it in reference [86]. We present in figure 20 the optical properties (transmission and reflection) of nanorods films grown on a etched ZnO:Al substrate (0.1% HCl for 25 seconds) with a TCE of 30 $C.cm^{-2}$. This film is the one with the highest light scattering properties that was achieved in our study [111].

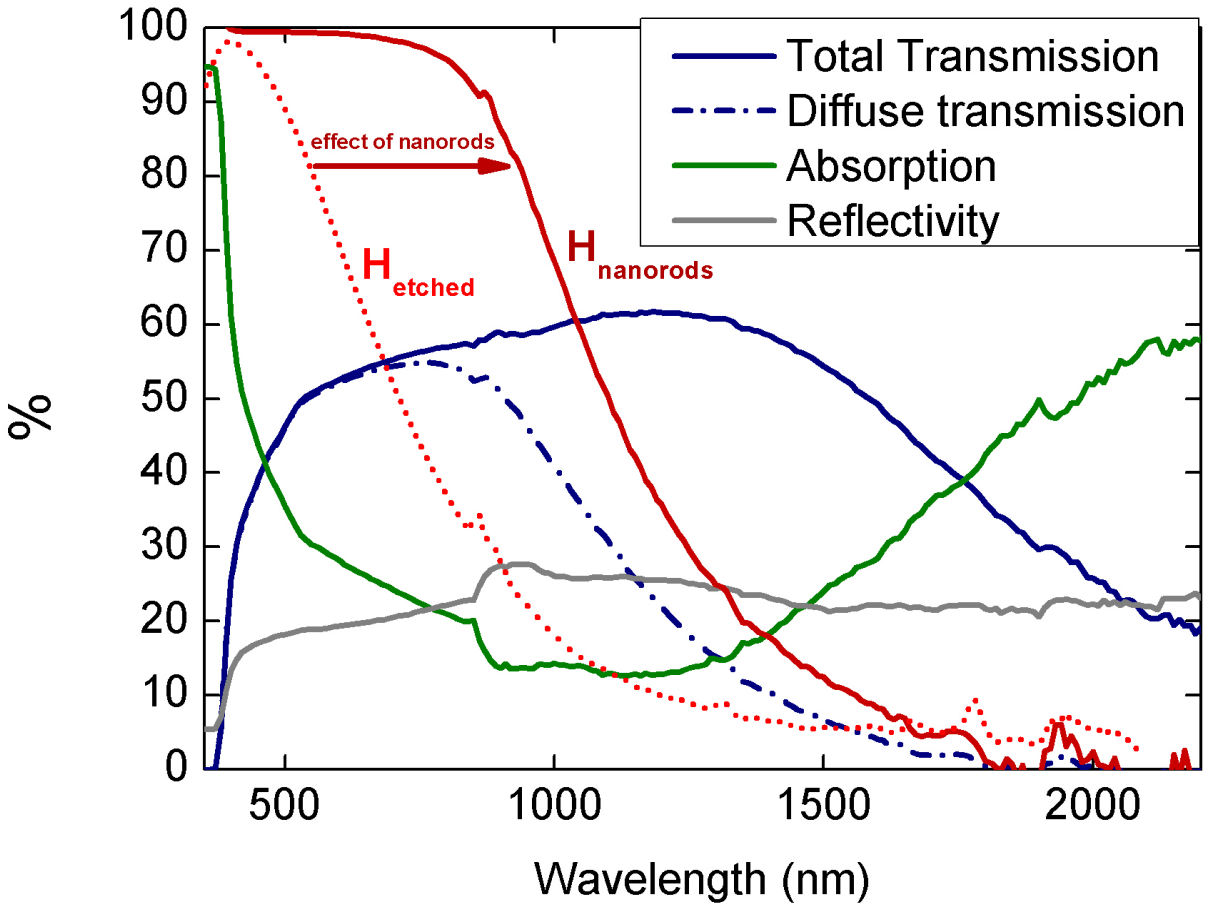

Figure 20. Optical properties of ZnO nanorods electrodeposited on ZnO:Al/Glass substrates. The Haze factors are shown in red.

We first notice that the total transmission is reduced by an approximative value of 5-10% compared to the standard etched ZnO:Al film (see figure 14 for comparison). This might be due to multiple reflections in the highly nanostructured film; it may also be related to the fact that a large part of the scattered photons have a scattering angle higher than the total reflection in the glass and so are lost by multiple transverse reflections inside the glass. In the CIGSe

absorption range, the diffusive transmission curve almost matches the total transmission. The Haze factor is higher than 70% at λ = 1000 nm and increases to about 90-100% at λ = 900 nm. This result is much higher than our previous results with etched ZnO:Al film as can be seen on the figure 20 (solid red line versus dotted red line), and also much higher to what was previously reported in literature [93]. Moreover, the shift of the Haze factor toward the IR spectral range is of major importance for solar cell application as it allows to more efficiently scatter photons that have a lower energy and so are less absorbed when reducing the absorber thickness. In the mean time, the reflectivity of the film with ZnO nanorods remains at a high value (>20 %) when deposited on a glass substrate, for the reasons that are given in part a).

The application of ZnO nanorods on 500 nm thinned absorber CIGSe solar cells has been carried out and the complete set of results is reported in the master thesis of Bo Chang [111]. Figure 21 shows the SEM cross section view of a 500 nm CIGSe solar cell with electrodeposited nanorods on the front side of the cell. The TCE during deposition is 2.5 $C.cm^{-2}$. This relatively low TCE leads to short nanorods of about 500 nm in average value, with an average diameter of about 80 nm. The photovoltaic parameters of the solar cells were determined by J-V measurements. Compared to the solar cell before deposition of the nanorods, the V_{oc} is unchanged at about 630 mV. The FF however is strongly decreased, from 70% to about 60%. The ZnO nanorods are reported to have a lower carrier concentration than the ZnO:Al front window [114] which may therefore influence the making of the contact on the top surface of the solar cell. The Jsc of the solar cell is also roughly unchanged (at about 21 $mA.cm^{-2}$) compared to a solar cell with a HCl-textured ZnO:Al, as can be seen on the EQE curves figure 22. Overall, the addition of nanorods on top of the solar cell decreases the efficiency from 9.7% for a solar cell with a chemically textured ZnO:Al to 8.4% for a solar cell with nanorods, and no enhancement of the current is observed. Although the antireflection effect of the nanorods is confirmed, there is no additional gain due to the higher scattering of light in the IR range, and we also observed a decrease of the FF that was not reported in the paper from Aé et al. [105].

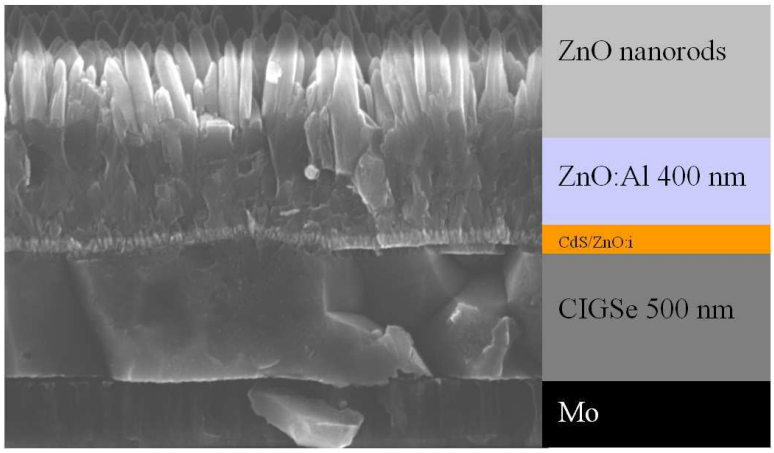

Figure 21. SEM cross section view of a 500 nm CIGSe solar cell with electrodeposited ZnO nanorods of the front window

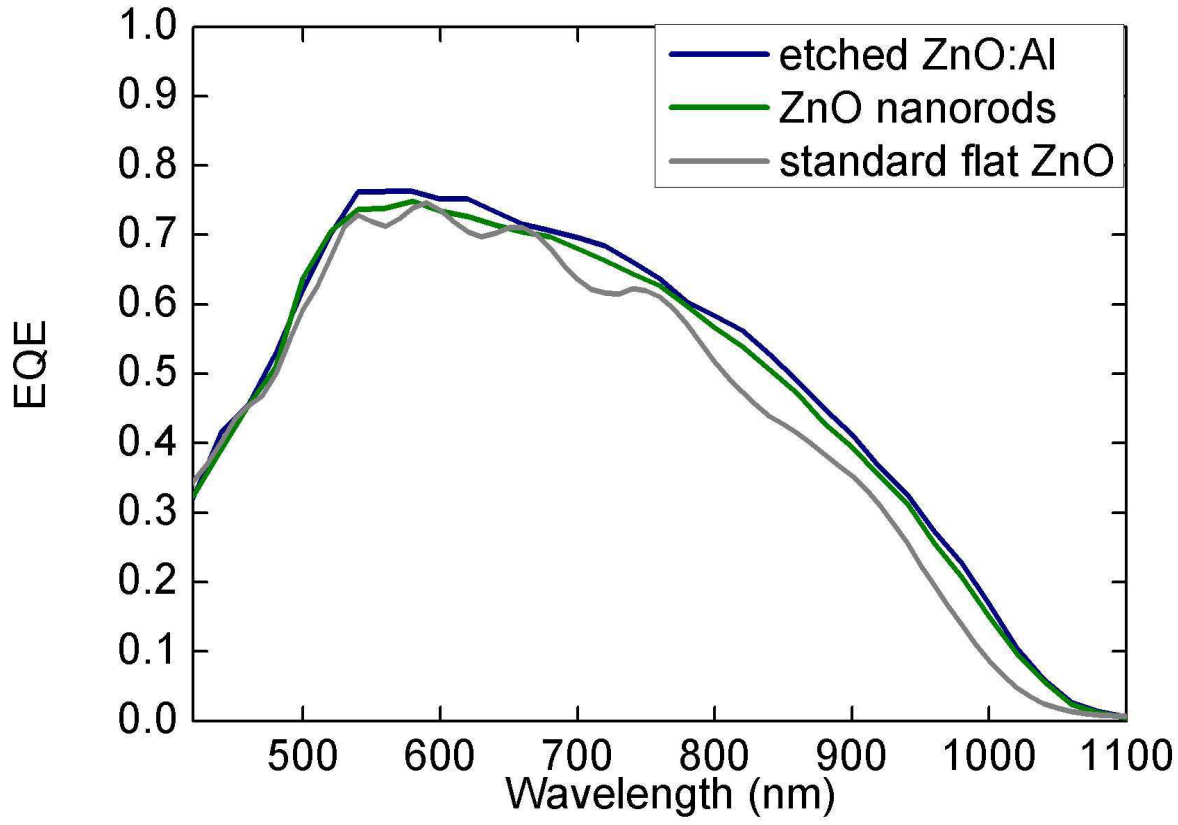

Figure 22. Compared Spectral Response for a 500 nm absorber CIGSe solar cell with a standard non modified ZnO:Al front window (grey curve), an HCl-etched ZnO:Al front window (blue curve) and a ZnO:Al with ZnO nanorods front interface (green curve).

IV.3.a.iii) Conclusion

Texturing a ZnO:Al film by HCl etching or by electrodeposition of ZnO nanorods showed a significant increase of the light scattering properties of the films. A Haze factor of nearly 100% up to $\lambda = 900nm$ has been achieved with ZnO nanorods deposited on a etched ZnO:Al film. However, we believe that light scattering at the air/ZnO interface is not suited for an application to thinned absorber CIGSe solar cells, no matter the haze at the front interface. The different refractive indexes in the layer strongly reduce the light scattering of the air-ZnO interface and thus no gain attributed to the diffusion of light in the absorber layer has been observed in the photovoltaic properties of the solar cells.

Texturing with HCl the air/ZnO:Al interface demonstrated an important potential as a very effective antireflection coating, leading to a relative increase of 14% of the efficiency of a 500 nm absorber solar cell, and the spectral response showed an effect that was comparable to a standard optimized MgF_2 ARC. ZnO nanorods have a similar antireflection effect, although the FF of the solar cells has been degraded probably due to the lower conductivity of the nanorods.

IV.3.b) Comparative study between standard CdS and alternative ZnS buffer layers on chemically thinned CIGSe absorber solar cells

In this part, we compare the photovoltaic parameters of two series of CIGSe solar cells from the same batch (batch J6) etched to different absorber thicknesses. The serie (1) is realized in the standard conditions with CdS-50 nm/ZnO:i-70 nm as buffer layer; serie (2) has an alternative ZnS/$Zn_{1-x}Mg_xO$ buffer layer. The deposition of the alternative buffer layer has been carried out in the frame of the PhD thesis of Thibaud Hildebrandt [115]. The experimental process is as follows: co-evaporated CIGSe surfaces [2] are etched in a bromine solution and treated with a KCN solution, according to the method described in the Chapter III of this thesis. Different absorber thicknesses are realized: 1500 nm (non etched sample), 1000 nm, 800 nm, 500 nm and 300 nm. For serie (2), the ZnS buffer layer is grown by Chemical Bath Deposition (CBD) from an aqueous solution of zinc sulfate (0.1 M), thiourea (0.4 M), and ammonia (1.5 M) at a temperature of 80°C. The deposition time is 8 minutes which leads to a layer thickness of about 40 nm. More details about the preparation of ZnS can be found in references [48] and [116]. The $Zn_{1-x}Mg_xO$ layer is deposited by radio-frequency magnetron sputtering in a Plassys MP 300 device, with a base pressure of 5.10^{-8} mBar and a working pressure of 10^{-3} mBar. More experimental details are given in reference [47]. The ZnO:Al front window layer is grown in the standard conditions (same as chapter III) with a nominal thickness of 400 nm and a sheet resistance of about 8-10 Ω/sq. After deposition of the ZnO:Al, the solar cells are annealed in air for 10 minutes at 200°C and a light soaking under A.M. 1.5 illumination during 1 hour is performed.

The solar cells are analyzed with current-voltage measurements J-V under standard A.M. 1.5 illumination; the external quantum efficiency EQE of the solar cells is also characterized using the same experimental setup as in Chapter III.

IV.3.b.i) J-V characterization

The photovoltaic parameters are extracted from the J-V curves and their average value is presented in Figure 23. An important spreading in the results for the CdS buffer layer solar cell is observed; this is interpreted as inhomogeneities in the CIGSe batch. It is possible to refer to Chapter III for a different set of results in the same conditions without this relatively important spreading of the parameters. From 1500 nm down to 800 nm of CIGSe, the ZnS buffer layer solar cells have a roughly equivalent voltage and fill factor to the CdS buffer layer solar cells, with value of 580 mV and 67-70%. As expected, the short circuit current J_{sc} is much higher with ZnS, decreasing from 31 $mA.cm^{-2}$ (1500 nm absorber) down to 29 $mA.cm^{-2}$ (800 nm absorber), when the J_{sc} of the CdS solar cell decreases from 27.5 $mA.cm^{-2}$ down to 26 $mA.cm^{-2}$ in the same thickness range. This results in an overall efficiency superior for the ZnS buffer layer compared to CdS (figure 21.d) from 1500 nm to 800 nm absorber thickness. For lower thicknesses however, the behavior of the ZnS-buffered solar cells is different compared to the CdS-buffered solar cells. Both the V_{oc} and the FF strongly decrease down to 0.47 V and 55 % respectively for the ZnS-buffered 300 nm absorber solar cell, while the CdS-buffered solar cell has a rather constant trend for those two parameters. The Jsc continues to decrease for both series, and still remains to a higher value with the ZnS buffer layer (24 $mA.cm^{-2}$ versus 22 $mA.cm^{-2}$ at 300 nm of CIGSe). This does not compensate the losses in V_{oc} and FF, and the solar cells with standard CdS buffer layers outperform the ones with ZnS buffer layers for thicknesses lower than 800 nm (ultrathin), with an efficiency for the 300 nm CIGSe of 8.8% versus 6.4% respectively.

The predicted increase of the J_{sc} with the replacement of CdS by ZnS is observed in our results. The fact that the alternative buffer layer is deposited on an etched absorber does not significantly impact the other parameters of the cell, with a roughly identical behavior as previously seen for standard 2500 nm thick CIGSe.

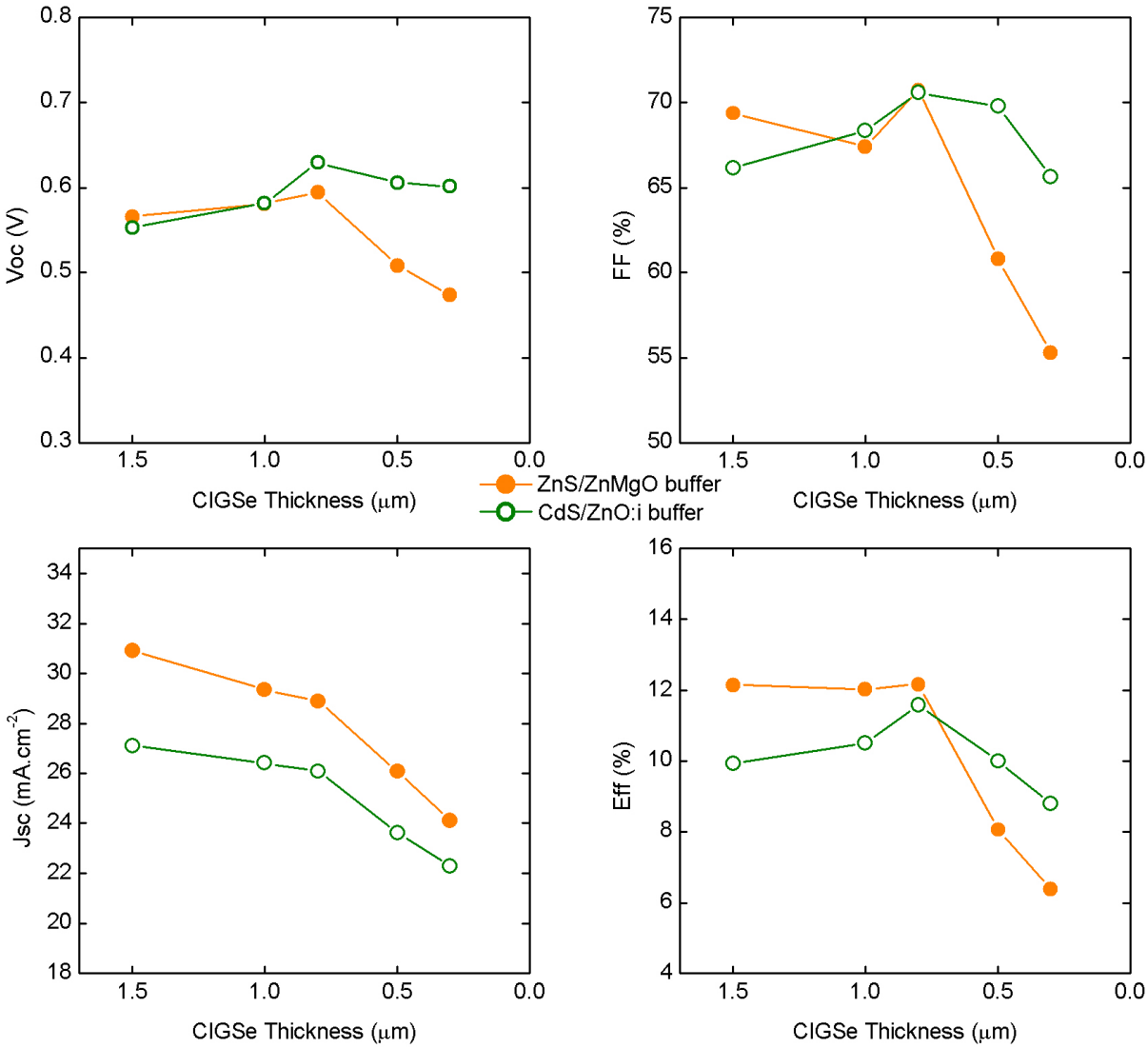

Figure 23. Comparison of the photovoltaic parameters of etched absorber solar cells with CdS and ZnS buffer layers.

IV.3.b.ii) External Quantum Efficiency characterization

To push further the characterization, we perform EQE measurements on both sample series. Figure 24 presents the selected EQE curves for three different absorber thicknesses: reference 2500 nm, etched 1500 nm and etched 500 nm. The CdS and ZnS buffer layers are compared. For the reference thick solar cell, the gain in the U.V. range is visible with the ZnS buffer layer, however, the overall quantum efficiency is lower by about 5% on the rest of the

spectrum (from 550 nm to the bandgap); this may be related to an insufficient carrier collection due to defects at the P-N interface in case of ZnS. Experiments are being performed to fully optimize the ZnS and understand the mechanisms at stake at the absorber/buffer interface.

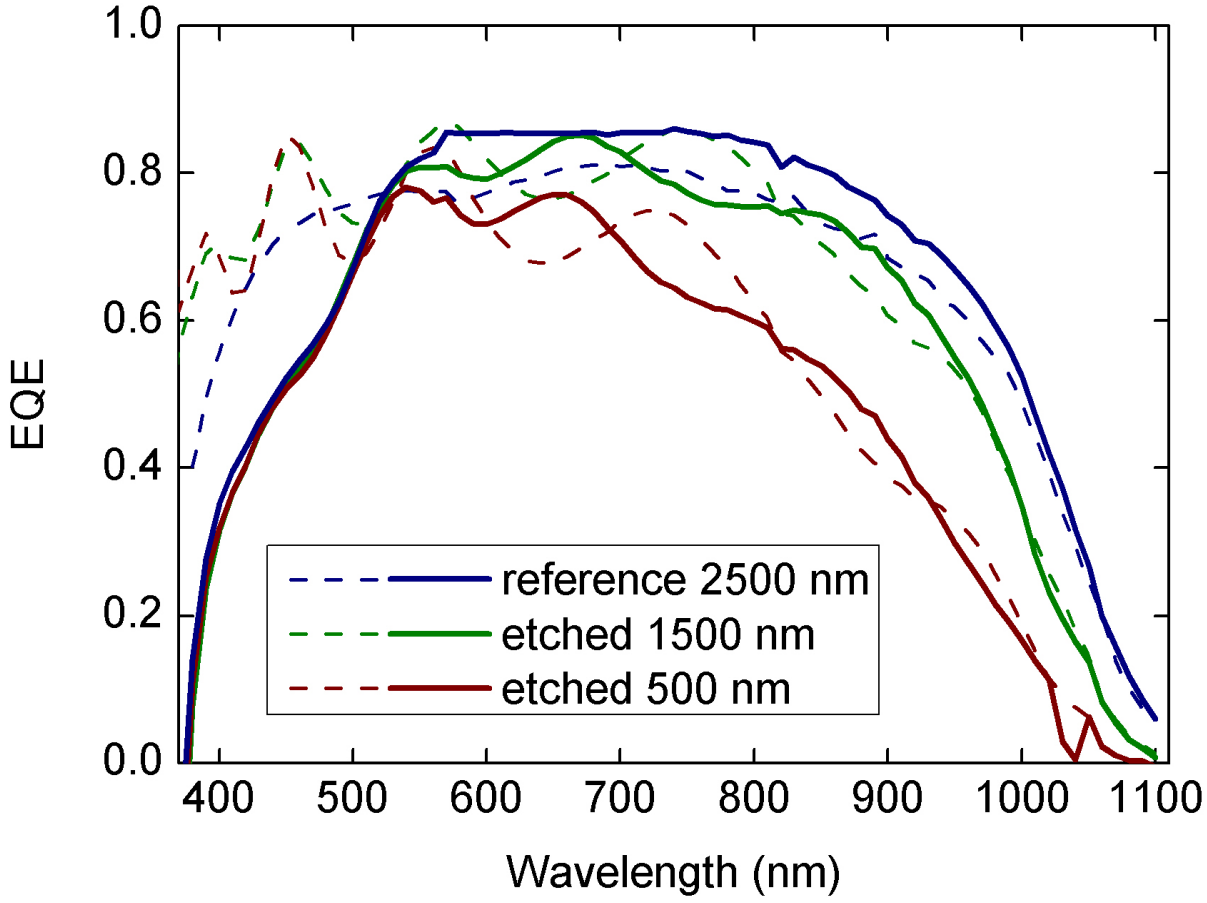

Figure 24. Compared EQE for three different CIGSe thicknesses between a standard CdS buffer layer (solid lines) and an alternative ZnS buffer layer (dashed lines)

This difference between CdS and ZnS in the 550 nm - 1000 nm spectral range is however not found for lower absorber thicknesses; in this case, the interference fringes, mainly due to ZnO window layer, are shifted between CdS and ZnS buffer, but the average EQE is roughly equivalent between the two buffer layers. The shift in the interference fringes is most likely due to the fact that the ZnS/ZnMgO stack has a different thickness than the CdS/ZnO:i. For these the etched CIGSe solar cells (1500 nm and 500 nm), the increase in the U.V. range (from 350 nm to 550 nm) is also clearly visible, and the important absorption of the CIGSe in these wavelengths, combined with two constructive interference fringes, allows the 1500 nm

and 500 nm CIGSe solar cells to surpass the reference 2500 nm solar cell. The measured EQE are consistent with the average J_{sc} that was deduced from the J-V curves, and reproduce well the expected behavior that was observed in the numerical simulations in Chapter II. These results are also in good agreement with the literature [47].

IV.3.b.iii) Conclusion

Similarly to what is commonly observed on state-of-the-art thick absorber CIGSe solar cell, replacement of the CdS buffer layer by ZnS significantly increases the short circuit current due to its higher bandgap that allows the CIGSe to absorb the incident light in the 350 nm - 550 nm spectral range. ZnS was deposited on etched surface without any supplementary optimization compared to the standard conditions, and improvements are very likely in future developments [115]. Similarly, an important drop of both the FF and the V_{oc} are observed for ultrathin absorbers (500 nm and 300 nm) and further experiments are needed.

IV.4) Chapter Conclusion

In this study, our purpose was to increase the short circuit current in a 500 nm CIGSe absorber solar by a front contact engineering of the device. Based on the simulation from Chapter II, and on previous studies especially in the thin film Silicon solar cells field, we investigated on two ways to increase the light absorption in the CIGSe: (1) the texturation of the ZnO:Al front contact by etching and nanorods electrodeposition for antireflection effect and light scattering; (2) the replacement of the standard CdS buffer layer by ZnS which has a higher bandgap energy.

- The texturation of the front ZnO:Al window layer by HCl showed a broadband antireflection effect when applied to CIGSe solar cells, whatever the absorber thickness. The photocurrent increase was already at the same level as an optimized MgF_2 ARC, and it is likely that there is still room for improvements. We also managed to significantly increase the light scattering properties, and shift the haze factor to the infrared wavelength by electrodeposing ZnO nanorods on top of the ZnO:Al; unfortunately, the application to solar cells degraded the fill factor without improving the photocurrent in the device due to the lower conductivity of the nanorods, which reduced the efficiency. ZnO nanorods led to the same antireflection effect that etching the front ZnO:Al window.

- The ZnS buffer layer allowed a substantial increase of the absorption in the U.V. spectral range which led to an increase of the photocurrent and thus the efficiency of the solar cell. However, we noticed that the voltage and the fill factor were degraded when reducing the absorber thickness lower than 800 nm; further improvements are needed to optimize the ZnS/CIGSe interface in the case of an etched absorber, and a PhD thesis including this aspect is currently carried out at IRDEP [115].

The front contact engineering that we used in this study allows to visibly increase the photocurrent in the solar cell, but no increase specific to thinned and ultrathin devices has been observed. Increasing the absorption in the infrared spectral range has been identified in Chapter II and III as the key issue for improving sub-micrometer absorber CIGSe solar cells, and the Spectral Responses here show us that there is still a lot of room for improvements in these wavelengths. In the next Chapter, we will study the back contact engineering of very thin and ultrathin CIGSe absorber solar cells.

Chapter V

Back contact engineering for thin and ultrathin absorber CIGSe solar cells

V.1) Introduction

In Chapter II, we proposed a theoretical insight on solutions to improve the performances of thin and ultrathin absorber CIGSe solar cells by increasing the light trapping and improving the quality of the electrical contacts. Although front contact engineering allowed to substantially enhance the photovoltaic parameters of very thin absorber solar cells, the greatest scope for improvement is in the engineering of the back side of the device.

Previous studies on the back contact of a CIGSe solar cell, especially for the purpose of ultrathin devices, are fairly rare; the high temperature substrate based process for the growth of the CIGSe absorber ($\geq 500°C$) reduces the range of compatible materials. Molybdenum (Mo) has become the reference material as back contact in the field of CIGSe solar cells and alternative metals have most of the time performed poorly in comparison. In this Chapter, we decided to introduce a novel approach based on the lift-off (i.e. peeling) of a CIGSe layer from its original Mo substrate, allowing to process the back surface of CIGSe at low temperature (same approach as the front surface with the CdS). This method significantly broadens the range of compatible materials for back contact application.

In the first part of this chapter, we will give an overview of previous works about alternative back contacts in CIGSe, specifically for ultrathin absorbers application.

In a second part, we characterize chemically, optically and electrically the back surface of CIGSe using the lift-off process, and demonstrate the improvements that can be achieved by using Gold (Au) as a reflective alternative metal back contact with a very thin 300-400 nm absorber CIGSe solar cell. Different metals are also investigated, and their electrical and optical interface with CIGSe is characterized.

In order to further reduce the absorber thickness to a thinner value, we showed in Chapter II that using a classical CIGSe/metal interface was insufficient to achieve enough light trapping, and alternative materials and structures are needed both for optical and electrical considerations. Therefore, in a final part, we investigate on the use of ZnO:Al transparent back contact that will allow to apply more advanced light trapping structures to ultrathin

CIGSe absorber ($d < 300nm$), and electrical characterizations of the CIGSe/ZnO contact are performed. An optical proof of concept device using a lambertian back reflector on a 200 nm absorber CIGSe solar cell will be presented, and compared to numerical simulations. A spectacular increase of the light absorption in a 200 nm CIGSe solar cell structure with a lambertian back reflector will be demonstrated.

V.2) State of the art

V.2.a) Metallic back contact

The "historical" back contact for $CuInSe_2$ solar cells is molybdenum (Mo), although gold (Au) was also used in the first CISe solar cells in the late 70's [117] [118], but was later abandoned in order to meet the low cost objectives of the technology. In the early 80's, Russell et al. [118] investigated on the Mo/CIGSe interface; they showed that the contact has rectifying properties when processed at low temperature. In a paper from 1983, R.J. Matson et al. [119] presented the results about the characterization of the interface between $CuInSe_2$ and different metals including Mo using Electron-Beam-Induced Current, Capacitance-Voltage (C-V) and interface chemical analysis. Highly reflective metals such as silver (Ag) and copper (Cu) performed poorly whatever the deposition method due to interdiffusion of the metal throughout the CIGSe layer even at room temperature. In this paper, they showed that the Mo/CIGSe contact behavior was strongly dependent on the deposition method with a poor reproducibility, and only Au and possibly nickel (Ni) had a reproducible ohmic behavior. However, later studies showed that the high temperature deposition process of the CIGSe on Mo led to a reproducible ohmic contact formation [120] [121] via the formation of an intermediate $MoSe_2$ layer at the metal/semiconductor interface [12]. Over the progress of the research on CISe/CIGSe based solar cells, Mo has become the reference back contact metal for CIGSe, meeting both the low cost requirements and the electrical compatibility with CIGSe. However, in a publication from 1988, Moons et al. showed that the best contact ohmicity on CIGSe can be achieved using Au [53], thanks to the high work function and chemical compatibility of CIGSe with Au.

In standard CIGSe solar cells, the absorber thickness is typically between 1.5 μm and 2.5 μm as previously mentioned, which is sufficient for complete absorption of the incident light because of the high absorption coefficient of CIGSe. However, when the absorber thickness is reduced, the reflectivity of the back contact becomes a key parameter to optimize for not degrading the cell performances. The low reflectivity of Mo [49] does not meet the requirements for application to very thin absorber (<1 μm) solar cells and alternative metals have been considered. In an early publication in 2003, K. Orgassa et al. [122] fabricated $Cu(In,Ga)Se_2$ solar cells with a variety of different back contact metals (W, Mo, Cr, Ta, Nb, V, Ti, Mn) and investigated the influence of reducing the absorber thickness. Three different CIGSe

thicknesses were tested (1800 nm, 900 nm and 450 nm) by direct deposition of CIGSe on the metallic substrate, and scaling of the deposition times. The composition of the CIGSe layer was analyzed by scanning electron microscopy (SEM) and energy dispersive X-ray analysis (EDX); the authors found that during the deposition of the CIGSe, the metal contacts W, Mo, Ta and Nb are almost inert whereas Cr, V, Ti and Mn tend to react with Se. For Ti and Mn, the reaction is total and the metal films are completely consumed whatever the deposited CIGSe thickness; therefore, it was impossible to fabricate a solar cell from these metal substrates. EDX analysis of the metal/semiconductor interface revealed the formation of a thin and well defined selenized metal film for Mo, Ta, and Nb. A similar selenized metal film, but with more graded boundaries, is also observed for Cr and V, in agreement with the fast interdiffusion process with these metals.

The reflectivity of Ta, Nb, W, Mo and Ag in air was calculated (figure 1.a) from the complex refractive index to evaluate the potential of each metal to provide sufficient reflection in the case of very thin absorber layer. Ag was only showed as an example of a very reflective metal, but is not applicable as previously reported [119]. The reflectivity of Ta and Nb was found higher of about 10 % than Mo and W in the red and infrared (IR) part of the spectrum (λ > 700 nm). This spectral region being the most critical in the case of thinned absorber, the authors stated that replacing the back contact by Ta or Nb should allow a significant improvement of the optical properties of very thin CIGSe solar cells.

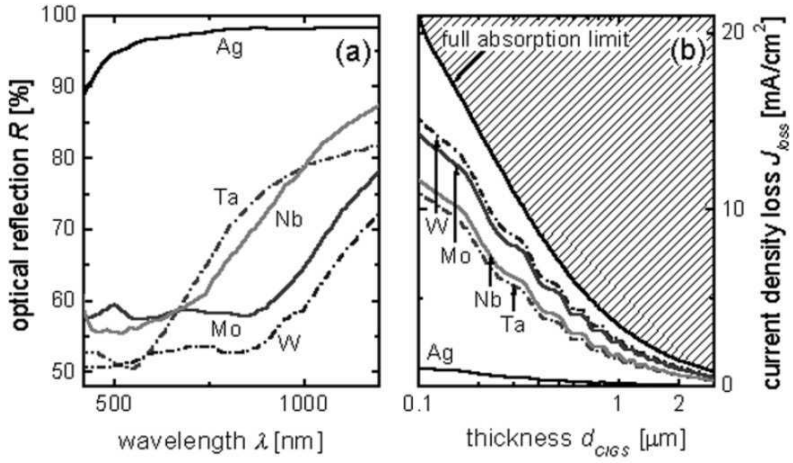

Figure 1. (a) Optical reflectivity spectra for different metals in air; (b) Simulation of the optical absorption of different back contact metals in CIGSe solar cells as a function of the thickness d_{CIGSe}. J_{loss} is the calculated current density that is lost in the back contact by optical absorption [122].

In order to evaluate the current density loss at the back contact depending on the reflectivity of the metal, the author described the solar cell as stack of perfectly smooth plane-parallel layers with abrupt surfaces and used the matrix formalism to calculate the electromagnetic field distribution in the solar cell stack, the optical index and the thickness of the different layer being the only input parameter to fully determine the optical properties of the complete stack [122]. Figure 1.b presents the calculated current density loss J_{loss} under A.M. 1.5 illumination as a function of the absorber thickness d_{CIGSe} for different metallic back contacts. They saw that for absorber with the standard thickness (around 2000 nm), the influence of the reflectivity of the back contact is negligible and the current loss is almost zero whatever the metal. The losses increase when reducing the absorber thickness, and for $d_{CIGSe} \leq 1000nm$, the influence of the back contact reflectivity becomes clearly visible, the most reflective metals allowing to limit J_{loss}. The difference between Ta/Nb compared to Mo/W tends to increase when the absorber thickness is reduced. As mentioned by the authors, a reduction of J_{loss} does not result in an equal increase of the short circuit current of the solar cell J_{sc}, since light reflected from the back contact can escape from the front side of the solar cell if not absorbed in the second pass. They therefore suggest for very sub-micronic absorber devices the replacement of the conventional flat solar cell structure by structures using light trapping or light scattering.

In this paper, the solar cells with alternative back contact were also electrically characterized using J-V measurement under A.M. 1.5 illumination, and the extracted photovoltaic parameters of two sets of solar cells are presented figure 2. The first set had an absorber thickness of $d_{CIGSe} = 900nm$ without bandgap grading, and the second set had an increased bandgap at the back surface (Ga-grading) with an absorber thickness of $d_{CIGSe} = 1400nm$. For the solar cells without graded bandgap, the authors [122] observed a successive decrease of the efficiencies for different back contacts in the order W, Mo, Ta and Nb. The losses are from a decrease in open circuit voltage V_{oc} and fill factor FF, while the J_{sc} scatters from about 27 to 28.5 $mA.cm^{-2}$, most likely due to slight thickness variation of the absorber layer from a sample to an other. When a bandgap gradient is introduced, it causes a “reflection” of the minority carriers diffusing towards the back contact [123]. For the back side graded solar cells, the authors observe that the V_{oc} of devices with W and Mo remains unchanged, whereas the V_{oc} of devices with Ta and Nb increases almost to the level of W and Mo. This indicates that the interfaces CIGSe/Ta and CIGSe/Nb are passivated by the graded bandgap at the back side

of the device while W and Mo seem to provide a sufficient self passivation. The short circuit current in this case differs by approximately 1.5 mA.cm^{-2}, since the absorber is 500 nm thicker in this case (Ga-graded solar cells). However, no effect from the reflectivity of the back contact is observed by the authors in this set of experiment, and it is very likely that more reflective metals like Ag or Au should be used if one wants to increase the absorption in the CIGSe for thinned absorber solar cells.

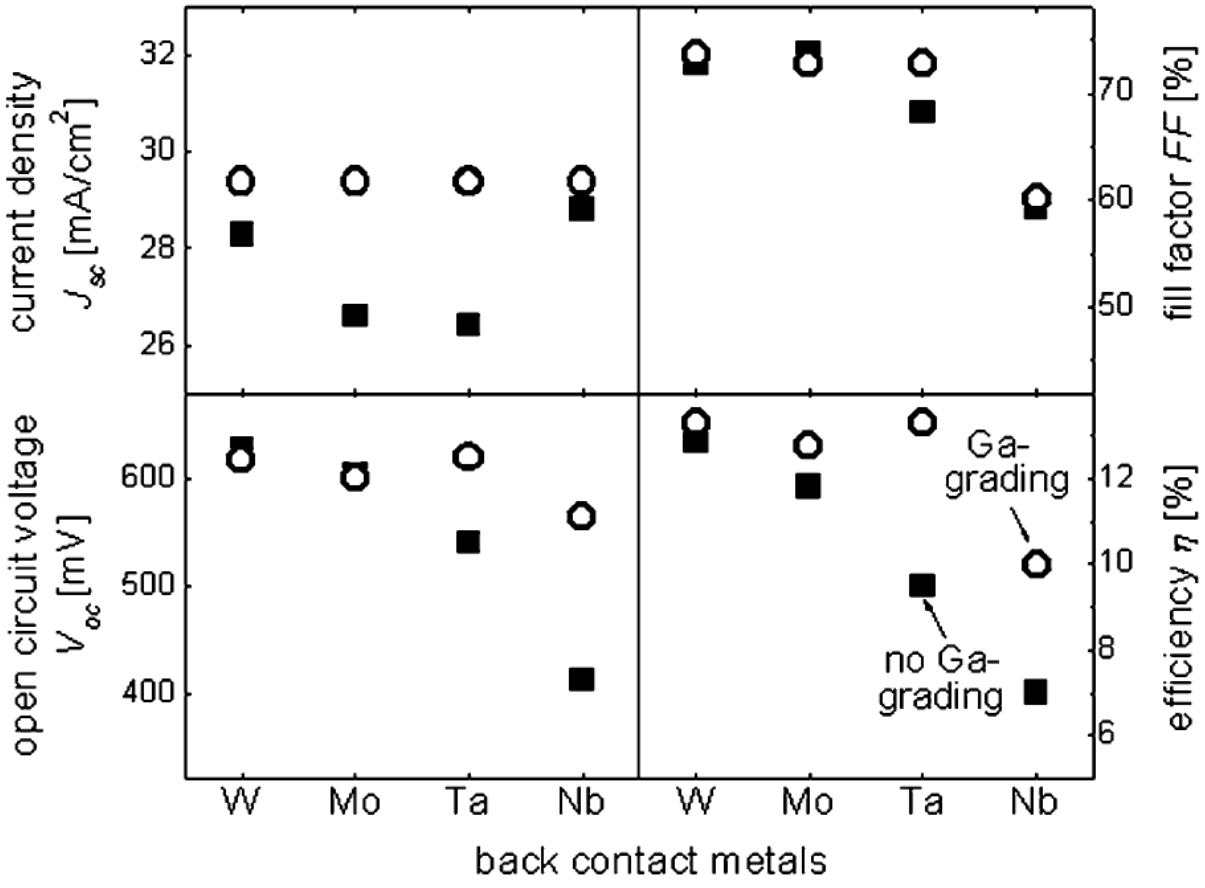

Figure 2. Conversion efficiency η, open circuit voltage V_{oc}, Fill Factor FF and short circuit current Jsc of CIGSe solar cells with back contact W, Mo, Ta and Nb. The open circles presents solar cells with a Ga-grading at the backside ($d_{CIGSe} = 1400nm$), the squares cells without Ga-grading ($d_{CIGSe} = 900nm$) [122]

Such a Ga grading has been widely investigated by M. Edoff's team in reference [27,32,65]. In this case, the Ga grading was introduced during the first stage of the co-evaporation process to produce a $CuGaSe_2$ interfacial layer between the CIGSe and the back contact. As we reported it in Chapter I, this Back Surface Field (BSF) layer on a 2 μm CIGSe solar cell allowed to

increase both the FF of about 5%, and the V_{oc} of 30 mV, but surprisingly the Jsc was unchanged in reference [27]. According to the authors from reference [27], the reduction of back contact recombination was counter balanced by increased bulk recombinations in the CIGSe. In reference [65], Lundberg et al. found that a Ga enrichment at the back side of the CIGSe allowed to increase the low energy photons generated carrier collection by reducing the back contact recombination, as can be observed in the Spectral Response figure 3. They showed that by reducing the CIGSe thickness down to 500 nm, the beneficial effect of the Ga-grading was increased, leading to an average +2.5% relative increase of the efficiency.

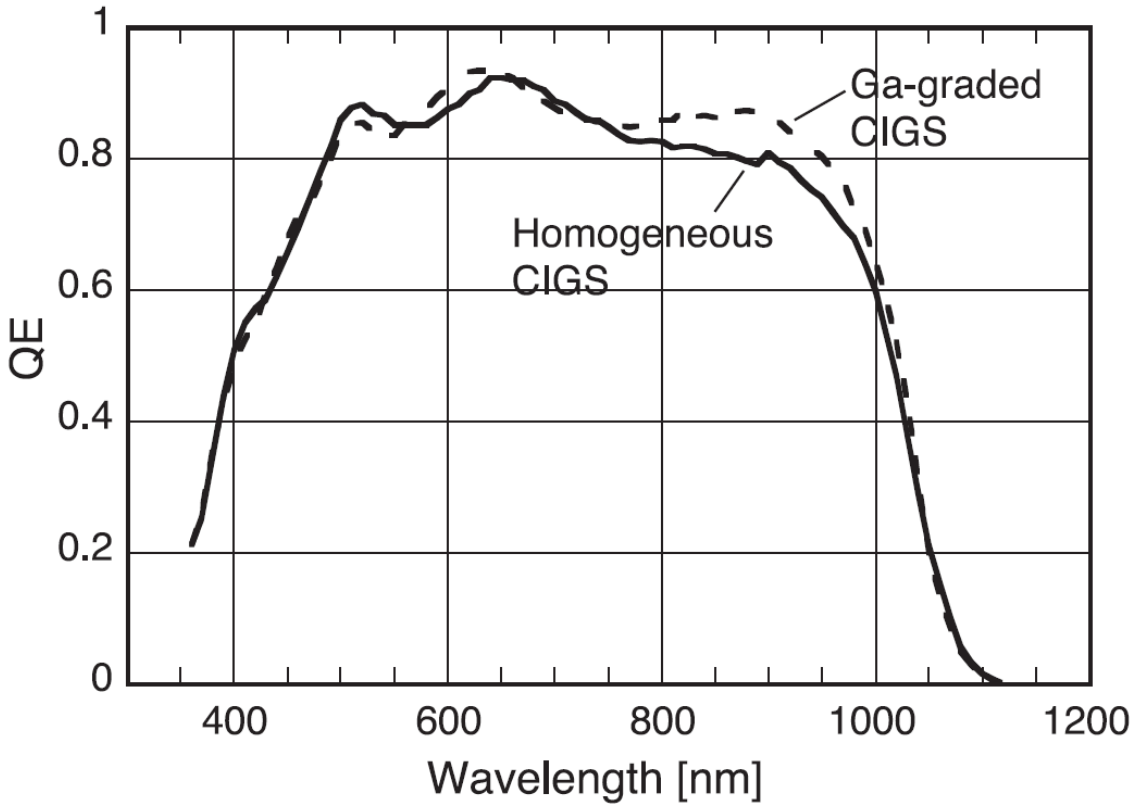

Figure 3. EQE for devices with and without Ga-grading but similar Cu/(In+Ga) ratio. The CIGSe thickness is a standard 2000 nm. [65]

Transition metal nitride are credible alternatives for reflective back contact application, as they combine a relatively high reflectivity and a good chemical stability.

Malmström et al. demonstrated in 2003 [124] an optical gain in the EQE at 500 nm absorber thickness by using a TiN back reflector. However, ZrN yields to a higher reflectivity, and they reported in 2004 the application of ZrN as reflective back contact on a 500-600 nm absorber

CIGSe solar cells [125]. In this study, different solar cell configurations are studied: a standard Mo back contact, a direct ZrN/CIGSe contact (configuration A), a direct ZrN/CIGSe contact with a Ga grading at the back side (configuration B), and a ZrN/CIGSe with an interfacial thin $MoSe_2$ layer (configuration C). Figure 4 compares the specular device reflectance (R (λ)) and the EQE (λ) for the ZrN back contact samples (A,B,C) and the corresponding Mo reference samples. They noted that the reflectivity of all the samples with a ZrN back contact is significantly higher than with the standard Mo back contact; this corresponds to light reflected at the back contact that escapes from the solar cell. The difference between the three ZrN sample is most probably related to slight differences in the absorber thickness between the samples. As expected, the ZrN reflector cells exhibit interferences and an increase of the EQE in long wavelength range compared the solar cells with standard Mo back contact.

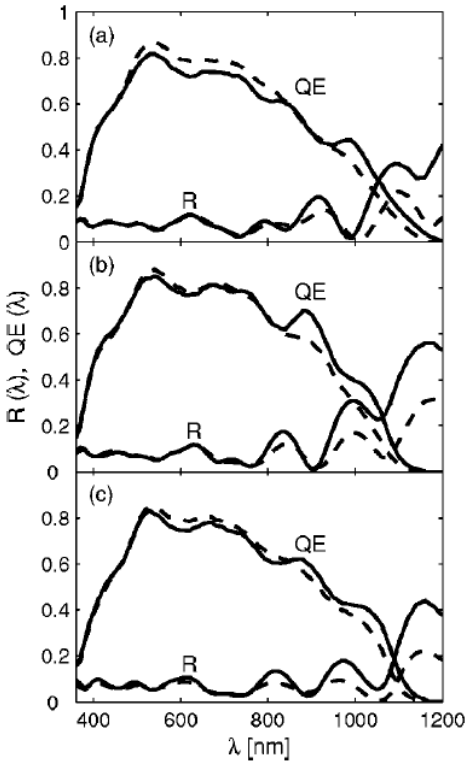

Figure 4. Comparison of specular device reflectance and external quantum efficiency spectra of the best solar cells of reference samples with standard Mo back contact (dashed lines) and ZrN reflector samples (solid lines) in configuration A, B and C [125]

Table 1 summarizes the photovoltaic properties of the different solar cells. It is observed that unfortunately, the gain in the EQE is partly offset by a degradation of the V_{oc} and the FF for configuration A and B. This indicates that the electronic properties of the device have been modified by the introduction of the new ZrN back contact. As pointed by the authors, the

band structure of the metal/CIGSe interface is determined by the difference in work functions and density of interface states, which directly impact the back contact recombination rate of the electrons as well as the contact resistance R_c of the holes. The FF and V_{oc} decrease is interpreted as being related to the fact that the work function of ZrN is significantly lower (4.7 eV) than the work function of CIGSe (5.3-5.5 eV) [125]. With a Mo back contact, it is well known that a MoSe2 interfacial layer that lowers the recombination rate of the electrons and the contact resistance of the holes is formed during the CIGSe deposition process, which is not the case when deposing CIGSe on a ZrN substrate. Therefore, with the introduction of a thin MoSe2 layer at the ZrN/CIGSe interface (configuration C), it is possible to retrieve a series resistance equivalent to the reference solar cell with Mo back contact, as well as increase the V_{oc} and FF. On the other hand, and despite the better optical properties of the ZrN back reflector, the average J_{sc} is at the same level as the reference solar cell, which is an indication of collection losses. In configuration B, the introduction of a Ga grading at the back side of the CIGSe allows to significantly increase the J_{sc} of the ZrN solar cell compared to the reference Mo back contact (26.9 $mA.cm^{-2}$ versus 25.5 $mA.cm^{-2}$). The authors anticipate further improvement of the performances of the solar cells by combining the Ga grading with the interfacial $MoSe_2$ layer on a ZrN back reflector.

Configuration	A	B	C
Voc (mV)	456 (535)	572 (637)	580 (518)
FF (%)	62.8 (72.5)	66 (70.9)	70.5 (69.8)
Jsc (mA.cm-2)	24.9 (25)	26.9 (25.5)	25.4 (25.5)
η (%)	7.2 (7.9)	10.2 (11.4)	10.4 (9.2)

Table 1. Average A.M. 1.5 solar cell parameters open circuit voltage (V_{oc}), fill factor (FF), short circuit current (J_{sc}) and conversion efficiency (η) of the ZrN back contact solar cells (in parentheses: Mo reference devices for each configuration). The CIGSe thickness is 500-600 nm. [125]

In order to further enhance the reflectivity of the back interface, different studies suggested the introduction of a Transparent Conducting Oxide (TCO) at the interface between the metal and the CIGSe.

V.2.b) Transparent back contact

In a publication from 2007, Campa et al. [41] studied from a theoretical point of view the potential of a flat highly reflective TCO/metal back contact in thin CIGSe solar cells. The introduction of a thin TCO layer - in this case ZnO – allows to increase the reflectivity of the back interface thanks to an optical index matching. Moreover, the ZnO can be used as a protective layer to prevent diffusion of metal atoms in the CIGSe, and thus allows to use metals such as Ag. The authors used the optical simulator Sunshine [126] to carry out the simulations. In this study, a very thin 360 nm absorber CIGSe solar cell is simulated and the influence of different back contact configurations is analyzed. The ZnO layer at the back side is 100 nm thick and the metals considered are Mo and Ag. Figure 5 presents the simulated External Quantum Efficiency for the 360 nm absorber solar cell with three back contact configurations: ZnO/Ag, ZnO/Mo and a standard Mo back contact. The authors observed a slight improvement of the EQE for the ZnO/Mo configuration compared to the standard Mo back contact solar, with a $\Delta J_{sc} = 0.33 mA.cm^{-2}$. The increase is much more important for the ZnO/Ag configuration due to the much higher reflectivity of Ag, and a significant enhancement of the EQE is obtained in the long wavelength range compared to the standard solar cell ($\Delta J_{sc} = 2.48 mA.cm^{-2}$). However, the authors also underline the fact that a large amount of the light that is reflected at the back contact still escapes from the solar cell due to the insufficient light trapping.

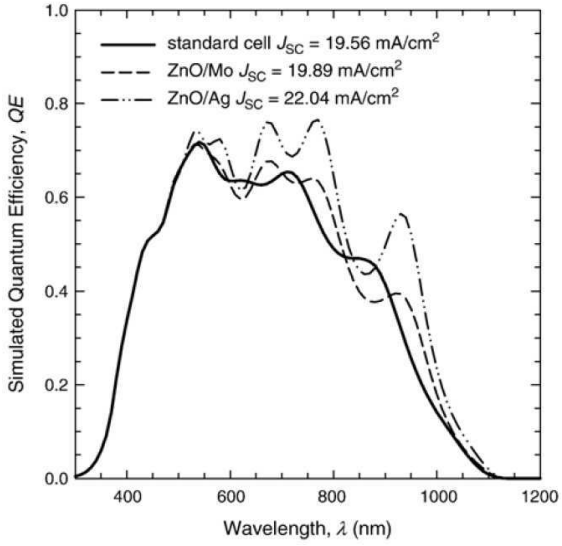

Figure 5. Simulation of the effect of different back contacts on the EQE of a 360 nm CIGSe solar cell [41]

Introducing a transparent conductive spacer at the back side of the solar cell is of particular interest in the scope of using alternative electrical insulator materials as back reflector; moreover, it could act as a barrier to prevent the interdiffusion of undesired species throughout the absorber during the high temperature process. Most TCOs are n-doped semiconductor, and interface with the p-CIGSe could lead to a rectifying behavior instead of ohmicity, which would irreversibly degrade the properties of the solar cell. The most extensive work on the topic of transparent back contact for CIGSe solar cell has been carried out by the team of Prof. Nakada during the last decade [127–129]. They demonstrated that it was possible to achieve efficiency comparable to Mo back contact by using highly doped SnO_2:F (FTO) or SnO_2:In (ITO) as transparent back electrode in a standard 2.5 μm CIGSe solar cell [127]. The best efficiency achieved were about 15% both for FTO and ITO, although ITO showed a better temperature stability which is critical to further enhance the efficiency. Using these TCO back contacts, it was possible to fabricate bi-facial 1000 nm thick CIGSe solar cells for tandem application [128] with a 11.3 % efficiency for front side illumination and 8.9 % efficiency for back side illumination. This result is remarkable given the relatively low absorber thickness and the fact that the back contact is a n-doped semiconductor.

ZnO:Al offers interesting properties if used as a back contact in CIGSe solar cells; it is both highly conductive, very low cost and is already used a front electrode in CIGSe solar cells. However, n-type ZnO:Al and p-type CIGSe interfaces forms a rectifying junction rather than an ohmic junction. Rostan et al. reported the realization of a transparent and ohmic ZnO:Al/$MoSe_2$ contact for CIGSe solar cells [130] by selenizing a very thin Mo layer (less than 20 nm) on top of the ZnO:Al using a NaF precursor film prior to the deposition of the CIGSe. The MoSe2 layer allows to modify the contact properties between n-ZnO:Al and p-CIGSe and leads to an ohmic behavior; figure 6 shows the dark current-voltage characteristic of different interfaces with CIGSe: Mo/CIGSe, ZnO:Al/Mo/NaF($MoSe_2$)/CIGSe, and a direct ZnO:Al/CIGSe interface. They saw that the ZnO:Al/$MoSe_2$/CIGSe had a purely ohmic behavior with a contact resistance of $R = 0.6\Omega.cm^2$ while the direct ZnO:Al/CIGSe interface forms a junction with a rectifying p-n diode characteristics and a zero voltage resistance of $R = 27.2\Omega.cm^2$. The lowest resistance was however achieved with the standard Mo/CIGSe interface with a resistance of $R = 0.045\Omega.cm^2$. By using the alternative transparent back contact, the authors realized a solar cell which photovoltaic parameters are listed in table 2, and compared to the parameters of a standard CIGSe solar cell with Mo back contact. The short circuit current and the open circuit voltage with the transparent back contact are even

higher than those of the Mo reference back contact device. However, the FF is degraded with the transparent ZnO:Al/$MoSe_2$ (FF = 65.4%) back contact compared to standard Mo back contact (73.3%); this is directly related to the higher serie resistance in the first case ($R = 2.9\Omega.cm^2$ versus $R = 0.39\Omega.cm^2$ for the reference solar cell).

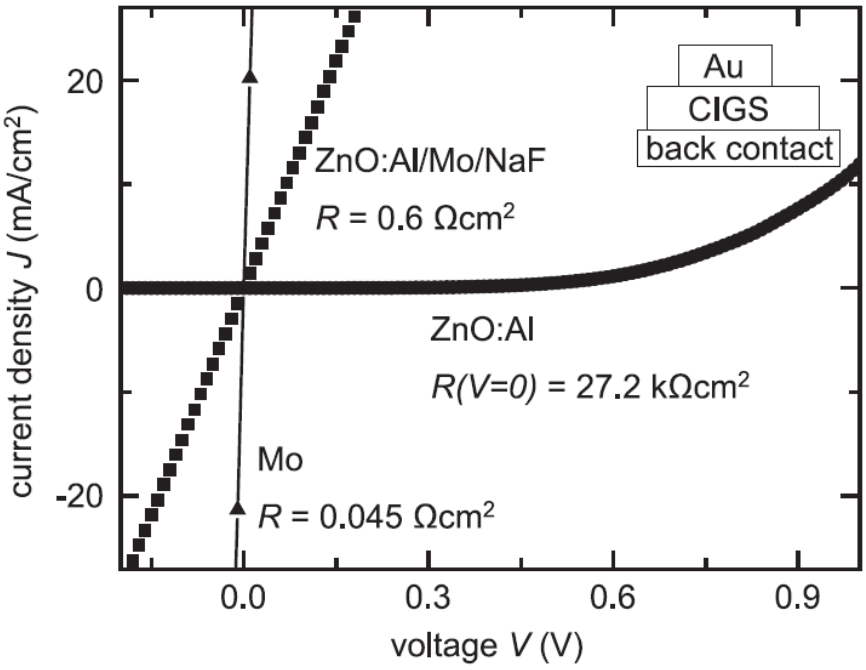

Figure 6. Dark current-voltage characteristics of CIGSe/Au structures with different back contacts (inset). The considered back contacts are ZnO:Al, ZnO:Al/MoSe2, and as reference, pure Mo [130].

Back contact	Voc (mV)	Jsc ($mA.cm^{-2}$)	FF (%)	η (%)	Rs ($\Omega.cm^{-2}$)
Molybdenum	601.2	31.3	73.3	13.8	0.37
ZnO:Al + 10 nm $MoSe_2$	613.8	33.5	65.4	13.4	2.9

Table 2. Photovoltaic parameters of CIGSe solar cells on different back contact, from reference [130]

As previously reported, the high temperature substrate-based process of the CIGSe deposition is a problem for using alternative materials as back contact. Another idea is to process the back contact at low temperature after deposition of the CIGSe, in a superstrate-like process, although standard superstrate process is not applicable to CIGSe without an important decrease of the performances of the solar cell. Minemoto and Anegawa et al. used a lift-off technique [131] [132] to peel a CIGSe layer originally grown on Molybdenum from its substrate and transfer it to a polymer substrate, in the scope of realizing high performance flexible solar cells. The lift-off process that is used in these studies unfortunately creates damages in the CIGSe layer (cracks) that irreversibly decreases the solar cells performances. The authors proposed different techniques to reduce the strains in the material during the lift-off, and a efficiency of 6.6% is achieved after lift-off, starting from a reference 11.4% solar cell [132].

V.2.b) Conclusion

In the literature, we have seen that replacement of the back contact of a CIGSe solar cell is a key issue to design high performance thinned absorber and ultrathin CIGSe solar cells. However, the high temperature substrate based process complicates the use of alternative materials, and previous studies could not take advantage of the best candidates materials as light-trapping efficient layers; therefore, the gains in efficiency were only moderate compared to the reference Mo substrate. An extensive work has been done in the past decade to achieve ohmic transparent back contacts for CIGSe. This is very interesting since it significantly broadens the range of materials that can be used as a back contact for CIGSe solar cells. The lift-off process that has been used for flexible solar cells by Minemoto and Anegawa is an interesting path as it would allow us to process the back contact at room temperature, but it is necessary to control the technique sufficiently to avoid the degradation of the CIGSe films during the lift-off.

V.3) Metallic back contact

V.3.a) Introduction

In this section, we consider the use of alternative metals as reflective and ohmic back contacts on very thin absorber solar cells, down to 300 nm. A lift-off technique is used to separate the CIGSe layer from its original Mo substrate, and a material characterization of the back side of the solar cell is performed (SEM, Spectroscopic Ellipsometry, XPS). From these characterizations and based on literature data, we study the optical potential of a wide range of metals as reflective materials for the back side of CIGSe solar cells. Also, the different metals are electrically tested on CIGSe by Transmission Line Measurement (TLM) to evaluate their potential as low resistivity ohmic contact. The material that combines low resistivity and high reflectivity is used as an alternative back contact on a solar cell serie with different absorber thicknesses, from 1800 nm down to 300 nm, and compared to standard Mo back contact solar cells with the same absorber thicknesses. The complete serie is electrically characterized, and the alternative reflective back contact solar cells show an important increase in the performance of very thin absorber devices compared to the default configuration.

V.3.b) Experimental

The $Cu(In,Ga)Se_2$ absorber samples are prepared on Mo/soda lime glass substrate by coevaporation at Würth Solar [2] (same as in Chapter III and IV). The absorber layers are etched from the front side using the chemical bromine process that was described in the Chapter III and the solar cells are completed with the standard CdS – 50 nm/ZnO:i – 70 nm/ZnO:Al – 400 nm stack and a Ni contact grid (200 nm) is deposited on top of the device. The solar cells are encapsulated using a commercial 2 components epoxy (Araldite 2020) and a 2 mm soda lime glass, and the lift-off is performed by mechanical separation of the two glasses. When separated from its Mo substrate, both sides (Mo side and CIGSe back side) are characterized by X-ray Photoelectron Spectroscopy using a monochromatized AlKα excitation and a Thermo Scientific K-Alpha analyzer and spectroscopic Ellipsometry without

any additional treatment in order to investigate the properties of the Mo/CIGSe interface. It is possible to etch with the bromine solution the back side of the lifted-off CIGSe solar cell, thus combining front side and back side etching. The alternative metals on the back side of the solar cell are deposited by thermal evaporation at room temperature directly on the CIGSe surface. The solar cells are characterized using dark and under A.M. 1.5 illumination Current Voltage (J-V) measurements, and the resulting curves are fitted using a two diodes model. The ohmicity of the different metals on CIGSe are realized by Transmission Line Measurements after deposition of metal pads on the back side of a directly lifted-off CIGSe layer (no CdS or ZnO on the front side).

The lift-off of the CIGSe consists in a mechanical separation of the CIGSe layer from its original Mo substrate. The different steps of the lift-off are schematically represented figure 7. After deposition of the CdS/ZnO:Al front window, we mechanically scratch the solar cell down to the Mo with a doctor blade at one edge (with a width of about 2 mm) of the sample before deposition of the Ni grid (figure 7 step a). By doing this, the Ni also deposits on a small area of the Mo, which is important for the following. The Ni grid is then evaporated on top of the solar cell (figure 7 step b); a 2 mm thick soda lime glass is bound on the device with the epoxy (figure 7 step c, the epoxy is represented transparent on this scheme). When the epoxy is completely dry (typically after 12 hours, although annealing at 60°C speeds up the process), we cut the epoxy on the edges with a doctor blade (figure 7 step d) to ease the cleaving. The final step consists in the lift-off itself. We started by applying a lateral opposite strain between the two glasses, but we noticed that a vertical strain leads to the same results and doesn't degrade the CIGSe layer either (figure 7 step e). Our best results were achieved with a vertical strain that cleaves the two parts. The Ni/Mo interface having a low adhesion, the two metals separates during the lift-off as seen figure 7 step e. This allows to keep the electrical contact with the front side of the solar cell which is now recovered by epoxy and glass. If the operator performs correctly the different steps, the strength needed for the lift-off is very low because of the relatively weak interface between CIGSe and Mo. However, some relatively rare samples seemed much harder to lift-off than others without any relation to their efficiency and quality. Additional experiments are needed to determine the reason why some samples are more adherent than others. It is probable that the lamellar sheet structure of $MoSe_2$ is beneficial for the lift-off. However, according to reference [133], it is possible to grow either vertically or horizontally oriented $MoSe_2$ sheets depending on the CIGSe deposition

conditions. Such change may modify the adhesion properties of the CIGSe to the Mo substrate.

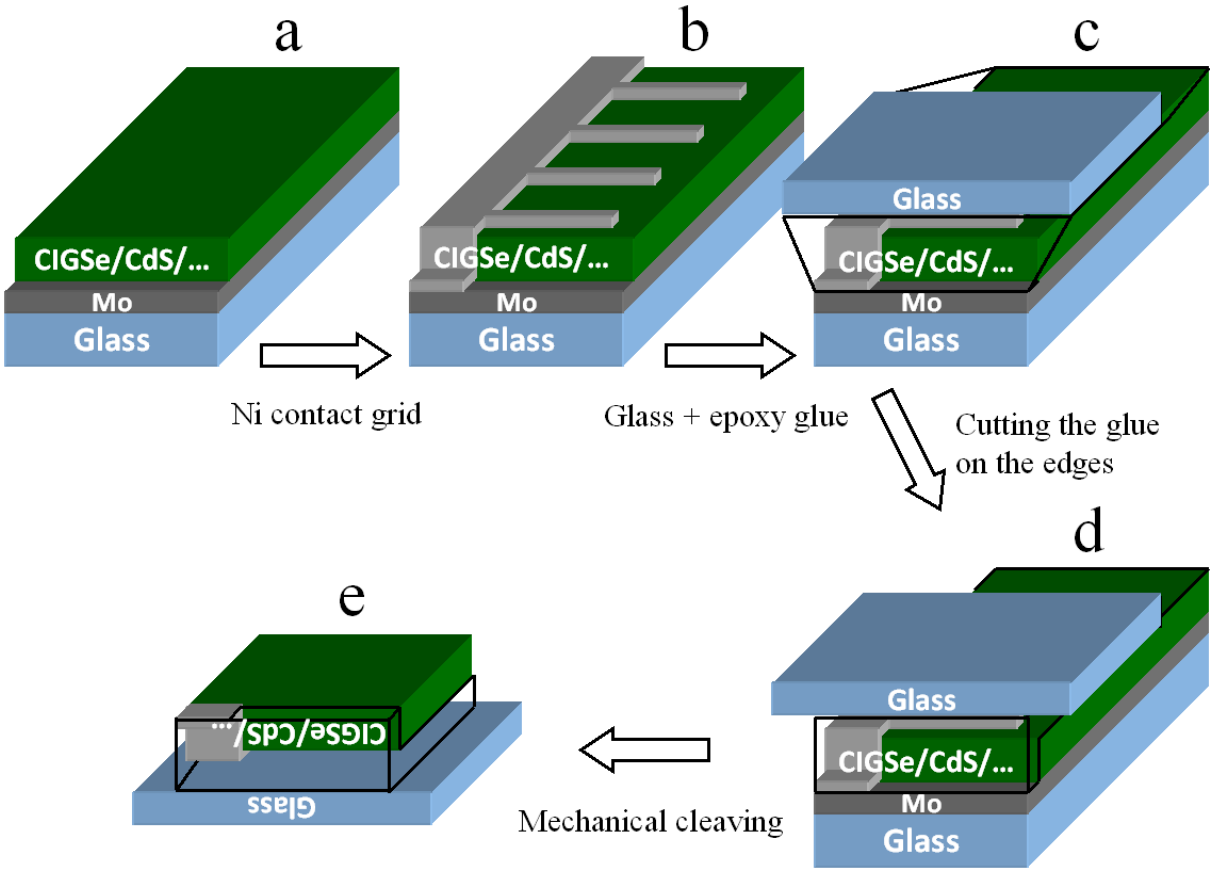

Figure 7. Schematic representation of the different steps of a mechanical lift-off of a CIGSe solar cell

It is also possible to perform a direct lift-off on a single CIGSe layer without CdS or ZnO:Al. In this case, there is no constraint due to the necessity of keeping an access to the front electrical contact, and the lift-off just consist in bonding the glass with the epoxy directly on top of the CIGSe and cleaving mechanically the CIGSe from its Mo substrate. This method is used for material characterization of the Mo/CIGSe interface (XPS), optical characterization (ellipsometry) and electrical characterization of the different metal contacts (TLM).

V.3.c) Chemical analysis of the Mo/CIGSe back contact interface

After the lift-off of a single CIGSe layer, the sample is similar to what is shown figure 8 and both part (Mo side and CIGSe side) can be analyzed separately by XPS measurements. This XPS study has been done in collaboration with our colleagues from “Institut Lavoisier de Versailles”.

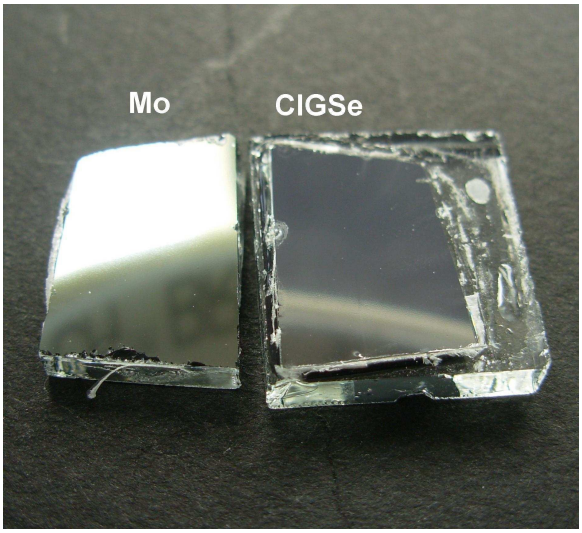

Figure 8. Picture of a CIGSe single layer (right) after lift-off from its original Mo substrate (left)

Figure 9 shows the XPS survey spectra of both CIGSe and Mo surfaces after the lift-off. The spectrum of the initial Mo back contact in Figure 9.a is dominated by core levels and Auger lines of Mo and Se, demonstrating the diffusion of Se into the Mo back contact. The Se/Mo ratio is estimated with the Se 3d and Mo 3d core levels. The Mo 3d peak is corrected from the Se 3s overlapping contribution. Quantification is performed with the Thermo Avantage© software using respective peak areas (Shirley type background subtraction) and taking into account the respective photo-ionization cross sections, inelastic mean free paths and the transmission factor of the spectrometer. The Se/Mo ratio is found to be close to 1.9 which indicates the formation of a $MoSe_2$ layer on top of the Mo back contact, as it has been investigated by various groups [13] [134] [133]. This interfacial layer has been reported as essential for a quasi–ohmic contact between the Mo back contact and the absorber layer [121] [11] [26] [135] despite the low work function of Mo. The three detail spectra (insets) show the high resolution Ga 2p and In 3d spectra, whereas the Cu 2p lines are not detected. This is an indication of the diffusion of In and Ga into the Mo back contact, which, with an atomic

concentration of <1%, remains considerably weaker than the diffusion of Se. These results are coherent with investigations by Weinhardt et al. [136], who also reported the diffusion of Ga into the back contact, whereas a Cu diffusion was not observed.

The XPS spectrum of the CIGSe back surface in Figure 9.b shows the core level and Auger lines of the absorber elements Cu, In, Ga, and Se. Using the intensities of the core level lines Se3d, Ga3d, In4d and $Cu2p_{3/2}$, $Ga2p_{3/2}$, respectively the overall XPS composition of the CIGSe back surface was calculated leading to Ga/In = 0.6, Cu/(Ga + In) = 0.2 and Se/(Cu + Ga + In) = 1.2 corresponding to 2Se/(Cu + 3Ga + 3In) = 0.9. The standard composition for front surface $Cu(In_{1-x},Ga_x)Se2$ absorbers is determined by atomic absorption spectroscopy (see Chapter III) titration and corresponds to 0.5, 0.5, 1.1 and 0.9 which are the reference values. In comparison to these values, we observe a Cu depletion and a Ga enrichment at the CIGSe back surface. At this surface, only traces of Na and a small amount of O are detected.

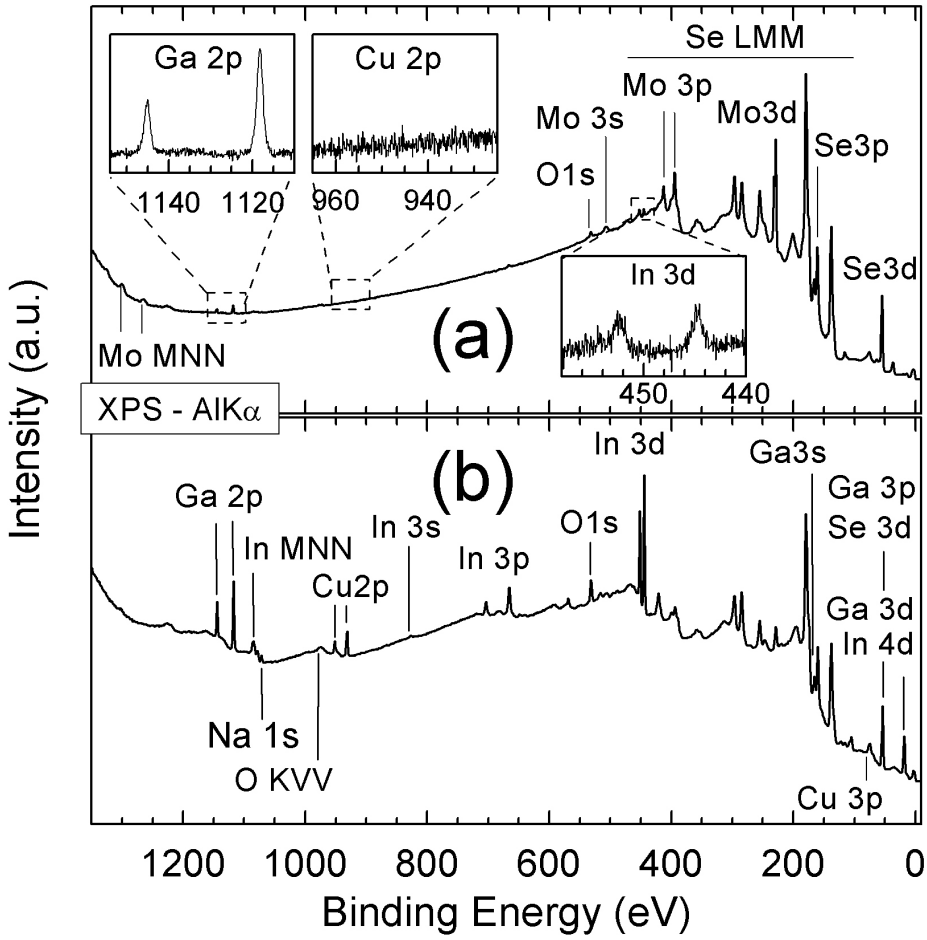

Figure 9. (a) XPS survey spectra of the Mo back contact after lift-off. The three insets show detail spectra of the Ga2p, Cu2p and In 3d core level lines. (b) XPS survey spectra of the CIGSe absorber back surface

Figure 10 compares spectra in the energy range of Mo 3p and Mo 3d core levels for a reference front side CIGSe surface, a reference Mo surface and for the lifted CIGSe back surface. The CIGSe reference surface (front side) is prepared by wet chemical etching in a bromine solution which does not modify the composition and leaves a de-oxidized surface as previously studied in Chapter III. The Mo is dipped in HCl before reference spectra acquisition. Despite the presence of Se LMM and Ga LMM Auger lines and the overlapping between Se 3s and Mo 3d peaks [137], the comparison between the respective energy distributions in these spectral regions exclude the presence of Mo at the back side of CIGSe (within the 0.1 at.% detection limit of XPS) and thus a possible diffusion of Mo atoms into the absorber layer. This finding, combined with the absence of Cu on the back contact surface, shows that the lift-off technique allows to precisely separate the CIGSe from its substrate at the very interface between the two layers. This process is therefore directly applicable for the replacement of the back contact. Moreover, the lift-off as we perform it is a very powerful tool that opens the way for sharp and realistic optical characterizations of the back interface.

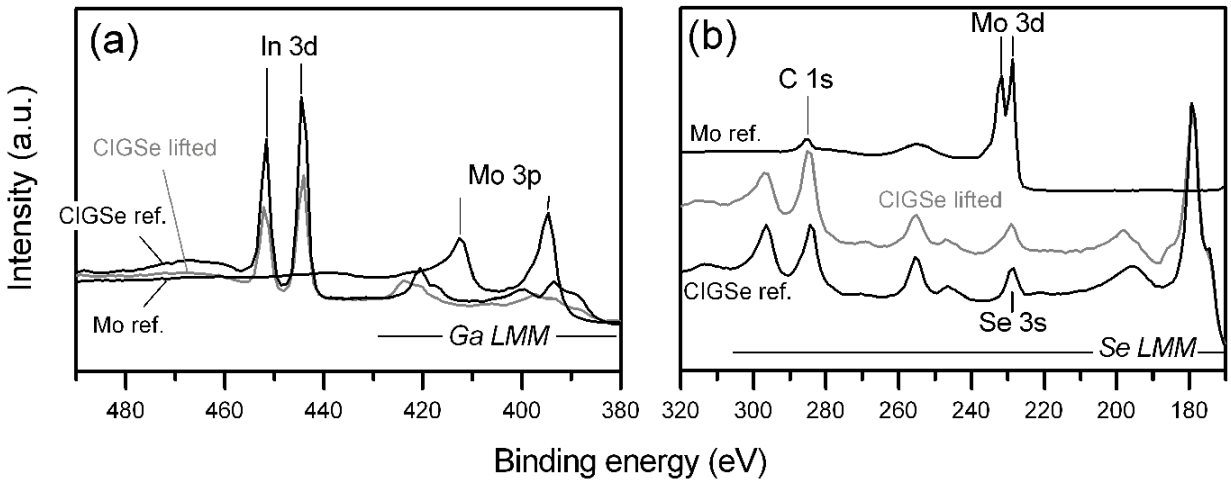

Figure 10. XPS spectra of the CIGSe absorber back surface, CIGSe (front side) and Mo references in the Mo 3p (a) and Mo 3d (b) energy range windows

In the following part, we optically analyze the Mo/CIGSe interface by using the lift-off and the potential of alternative metals as more reflective back contacts is also discussed.

V.3.d) Optical characterization of the Mo/CIGSe interface and alternative back contact interface

In order to calculate the optical reflectivity of the Mo/CIGSe interface, we used Spectroscopic Ellipsometry measurements on both sides of a CIGSe samples after lift off (figure 8). We determine the complex refractive index $\tilde{n} = n - ik$ from measurements of the real and the imaginary parts ($n_{Mo}, k_{Mo}, n_{CIGSe}, k_{CIGSe}$) for the Mo side and the CIGSe side. In both cases the determined values describe the entire material compounds considering the intermixing at the interface and the resulting interface chemistry that is discussed in the previous part. Due to the high absorption of the 2500 nm CIGSe material, which inhibits the contribution of the epoxy/glass substrate, we assumed an infinite absorber film thickness and thus did not perform a multi-layer analysis as commonly done for ellipsometry data. The optical functions of CIGSe (n_{CIGSe}, k_{CIGSe}) are plotted in Figure 11 together with literature data. The extinction coefficient k_{CIGSe} is in good agreement with the data by Alonso et al. [138], and is between the values of Orgassa et al. [122] and Theodoropoulou et al. [139]. The values of n_{CIGSe} are comparable to the data by Theodoropoulou et al. [139] and are considerably smaller than the data by Alonso et al. [138] and Orgassa et al. [122]. In the range $\lambda \geq 1000nm$, interference fringes appear caused by the low absorption of the CIGSe material for low energy photons and the resulting reflection of light in the substrate. The assumption of a semi-infinite condition on the CIGSe film is no longer valid and the data become inaccurate; they are therefore shown as grey lines. Our data still show however a reasonable agreement with literature data.

According to the simulations presented in Chapter II, increasing the reflectivity at the back interface of the solar cell is a key issue to significantly increase the absorption in a very thin CIGSe layer. High reflectance at the back contact can be obtained by a large contrast in refractive indexes between the absorber and the back contact material. In order to evaluate the potential of different metals as back contact reflectors, we simulate the reflectivity R_i at the metal/CIGSe interface by using the optical data that we previously obtained by ellipsometry on the back side of the CIGSe and on the Mo substrate, and refractive indexes for different metals from Palik [49] (Ag, Al, Cu, Au, Ni, Pt, pure Mo) computed in the Fresnel's equation for normal incident direction on a flat interface: $R_i = \left| \frac{\tilde{n}_{Metal} - \tilde{n}_{CIGSe}}{\tilde{n}_{Metal} + \tilde{n}_{CIGSe}} \right|^2$

Figure 12 is the calculated reflectivity for those different metals on a lift-off CIGSe layer. The curve referred to as “real interface” is the calculated reflectivity on CIGSe of the Mo side of the sample (figure 8) after lift-off, i.e. the “real back contact”. As observed, the real back contact shows a very poor reflectivity, below $R_i = 20\%$ on the whole absorption spectrum of the CIGSe (~ 400 nm to 1100 nm) and it is even in the 0%-5% range for wavelength lower than 800 nm. This is attributed to the $MoSe_2$ interfacial layer that was previously observed by XPS. Pt, Ni and metallic Mo show better reflectivity properties, but still with values below 50% on the CIGSe absorption spectrum, decreasing down to $R_i \approx 20\%$ for a wavelength of $\lambda = 500nm$, which means that these metals are not suitable as reflective back contacts for application to very thin absorber CIGSe solar cells. However, very high reflectivity values are obtained for Ag, Cu, Au and Al on CIGSe with a reflectivity $R_i > 60\%$ for wavelength $\lambda > 700nm$, which even increases up to $R_i > 80\%$ for $\lambda > 1000nm$. The long wavelength spectral region is critical for ultra-thin absorber devices due to the weak absorption of low energy photons [27] [140] [141], and these metals could significantly improve the absorption in very thin absorber CIGSe solar cells in this range.

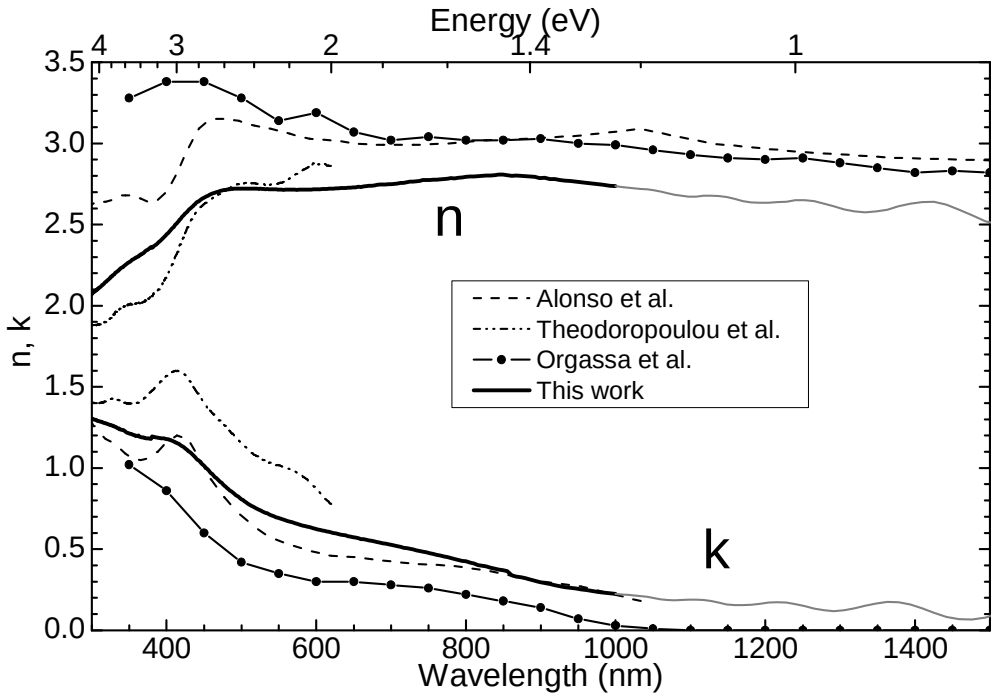

Figure 11. Refractive index and extinction coefficient measured on the back side of a lifted-off CIGSe layer by spectroscopic ellipsometry. Literature data from different sources are also represented [122] [138] [139].

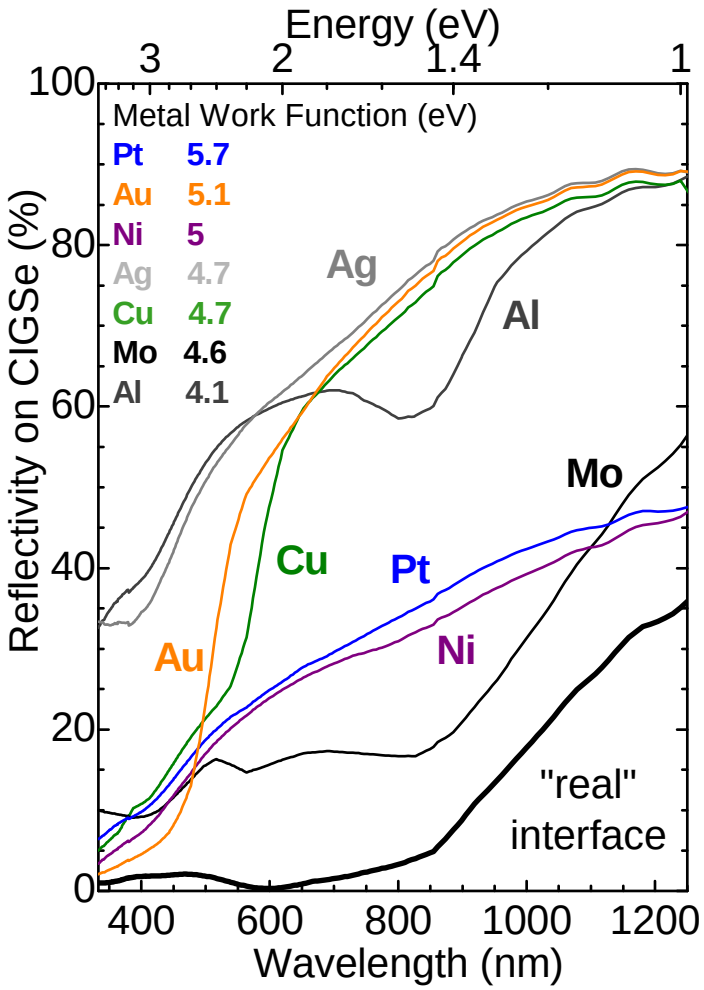

Figure 12. Reflectivity of different metals at the CIGSe/metal interface calculated with Fresnel's equation. The corresponding electron work functions are indicated on the top left of the figure

V.3.e) Electrical characterization by Transmission Line Measurements of the metal/CIGSe interface for different metals

Up to now, none of these metals has been used as an effective back contact in standard CIGSe solar cells mostly because of their incompatibility with the high temperature deposition process of CIGSe layer. In this study, they can be deposited at room temperature on the back side of the solar cell thanks to the lift-off process, which will strongly reduce the probable intermixing. It is well known that to obtain high quality solar cells, it is important to achieve an ohmic contact formation on a p-doped semi-conductor such as p-CIGSe. According to the Anderson model [51], the Fermi level of the metal has to be close to the hole quasi Fermi level of the semi-conductor and therefore a metal with a high work function is desired. We studied in Chapter II the theoretical influence of the metal work function on the metal/CIGSe contact. A comparison between the work functions of different metals from reference [142] is shown on figure 12, and Kelvin probe measurements from literature indicate that the work function of CIGSe is about 5.3 eV [28]; we see that Au has a much higher work function than Al (5.1 eV versus 4.1 eV at room temperature); this is more favorable to the Au/p-CIGSe contact, which leads to a better ohmic behavior than the Al/p-CIGSe contact. Pt (5.7 eV) and Ni (5 eV) contacts can also offer good ohmicity with p-CIGSe absorbers but their reflectivity remains much lower than Au. Ag and Cu also have a relatively low work function (4.7 eV), and it is well know that they both diffuse in the CIGSe absorber even at room temperature [119]. Therefore, Au combines both electrical (ohmic behavior) and chemical (limited diffusion in CIGSe at room temperature) compatibility with the CIGSe material [53], along with the very high reflectivity that is required for very thin absorber CIGSe solar cells.

However, the Anderson model which we based our assumptions on to discriminate which metal can or cannot form an ohmic contact with CIGSe is at fault when an interfacial layer is formed between the metal and the CIGSe; we see that the Mo has a low work function (4.6 eV) but still forms an excellent ohmic contact on CIGSe [130] thanks to the presence of $MoSe_2$ at the interface. Although such an interfacial layer is most probably related to the high temperature of the CIGSe deposition process, it is also possible that other metals form such an interfacial layer even at room temperature, which may therefore change their contact properties on CIGSe.

In order to investigate on the contact properties of the different metals on CIGSe, we performed Transmission Line Measurements (TLM) on the CIGSe back surface (after lift-off)

with the following metals: Pt, Au, Ni, Al, Mo, Cu and Ag. The TLM method consists in performing current-voltage measurement between two metal pads deposited on a semiconductor [143]. The resistance measured is a linear combination of the contact resistance of the first pad, the contact resistance of the second pad, and the sheet resistance of the semiconductor in-between the pads $R_{total} = 2 \times R_{contact} + \frac{L}{l} R_{sheet}$ where L and l are the length and width of the area between the pads. By varying the distance between the metal pads, it is possible to plot the contact resistance versus the contact separation. The plot is linear, the slope being the sheet resistance R_{sheet} and the intercept of the plot with the y-axis is $2 \times R_{contact}$. Figure 13 shows a picture from an optical microscope of the TLM structure that we use in this study. The metallic pads are 50 µm x 200 µm..

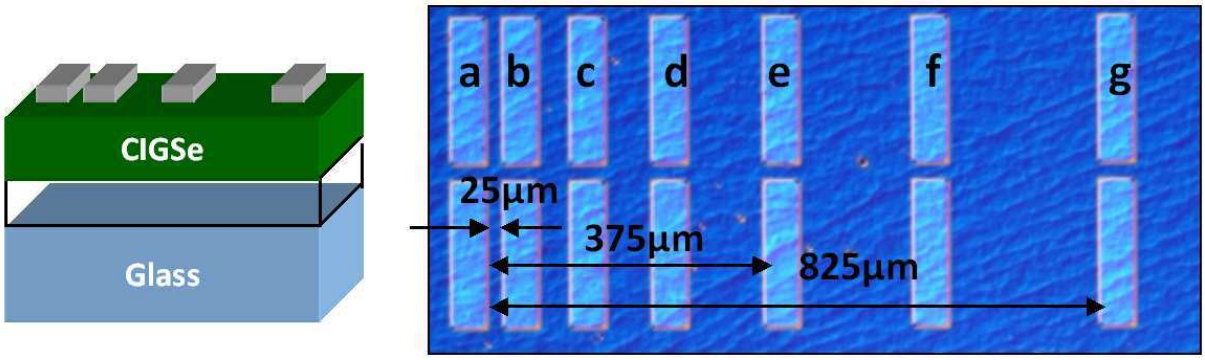

Figure 13. Optical microscope image of the TLM structure used in this study. A 3-dimensionnal representation of the stack is also shown on the left.

The Figure 14 shows the current-voltage curves for the different metals between the pads a and b (distance = 25 µm, figure 13). Both Ag and Cu show an extremely low contact resistance and their plots could not be represented on this figure. This is due to the interdiffusion of the metal's atoms through the CIGSe layer which gives a metallic behavior to the surface. These two metals can therefore not be considered as credible alternatives to Mo for direct application to CIGSe. Beside those two metal, we see that the lowest contact resistances are obtained for the highest work function, in good agreement with the Anderson model. As anticipated, Pt and Au both have an ohmic behavior and a relatively low contact resistance. Mo has a much lower contact resistance than expected from the Anderson model even though the metal deposition was performed at room temperature. This is an indication of

the formation of an interfacial layer between Mo and CIGSe, most likely $MoSe_2$, which strongly reduces the contact resistance. Al has a very high contact resistance on CIGSe and we see (inset figure 14) that it also have a rectifying behavior; this is due to the low work function of Al (4.1 eV).

When compared to the simulations from Chapter II, we see that both Mo and Au have a much different behavior than predicted, due to the probable formation of a very thin interfacial layer that was not taken in account.

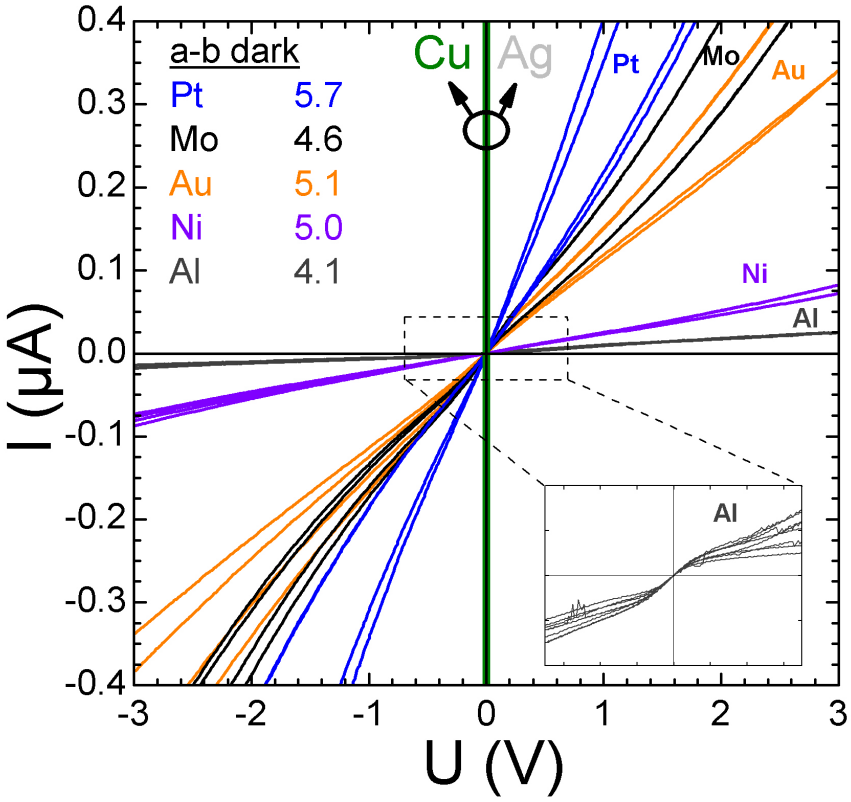

Figure 14. Current-Voltage characteristic measured in the dark between the contact pads a and b (distance = 25 µm) for the different metals

By measuring the current-voltage between the different pads, we plot on figure 15 the contact resistance versus contact separation curves for Pt, Mo and Au. The surface of the metallic pads is 10^{-4} cm^2. Pt and Mo give reproducible results and the contact resistance of these metal on CIGSe are 1.10^{-2}-$2.5.10^{-2}$ $\Omega.cm^{-2}$ and 2.10^{-2}-$3.5.10^{-2}$ $\Omega.cm^{-2}$ respectively. On the other hand, the Au plot is not linear and the contact resistance found is between $2.5.10^{-2}$-10.10^{-2} $\Omega.cm^{-2}$ depending on the measurement set; this result is quantitatively unusable because of the

too important uncertainties in the measurement. These problems are due to the fact that the metal contact pads have been deposited on the CIGSe, but no engraving of the CIGSe around the pattern was done. Therefore, some non linear electric field lines exist at the extremity of the pads, which disrupts the current measurement. However, when the distance between the pads is increased, the influence of these curved field lines is reduced. Consequently, if the a-b measurement (distance = 25 µm on the figure) is removed from the figure, the Au plot seems more linear with a slope comparable to Pt and Mo, and the contact resistance is in this case about $6.5.10^{-2}$-10.10^{-2} $\Omega.cm^{-2}$.

In conclusion, the contact resistance values from these TLM measurements should be taken with precaution, and a more accurate study is needed to obtain quantitative values. However, they give an interesting qualitative insight on the behavior of each metallic contact when the metal is deposited on the CIGSe at room temperature. Au, Pt and Mo seem to be the only compatible metals that could be considered as efficient back contact for CIGSe solar cells.

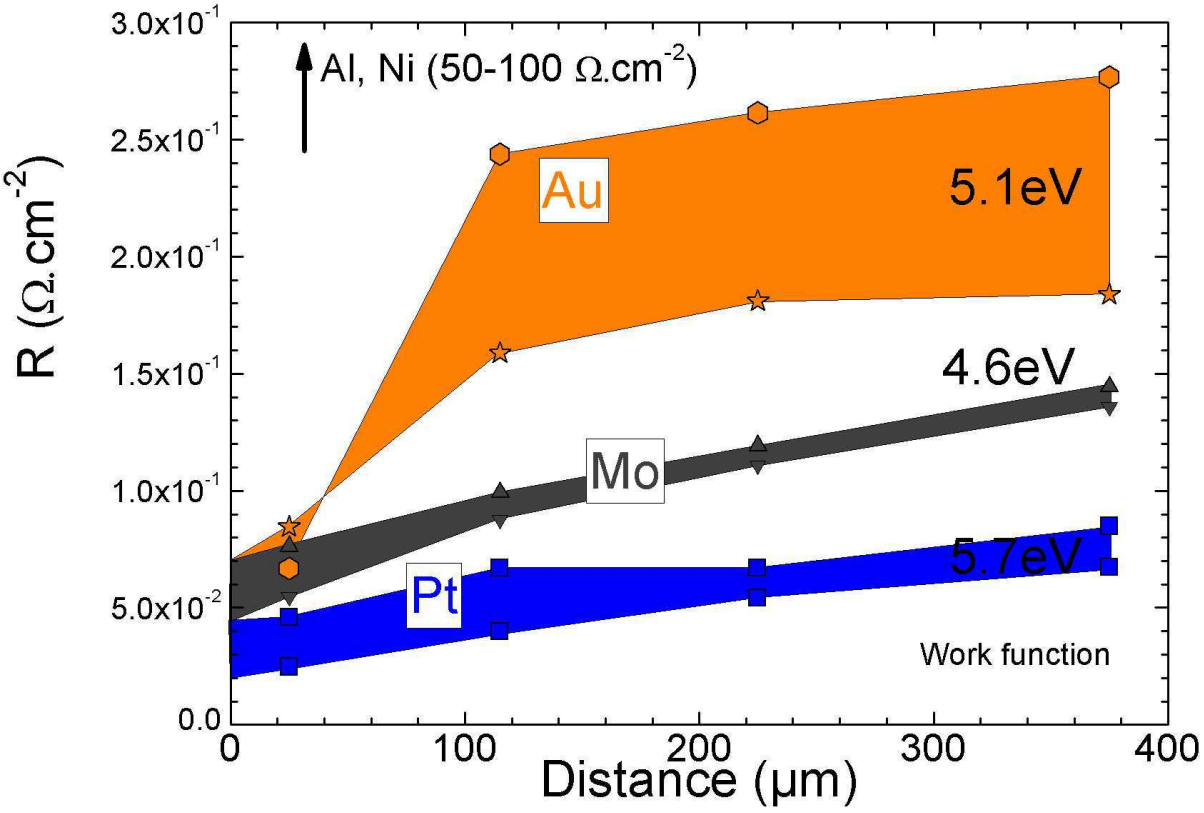

Figure 15. Resistance versus Distance between the metallic pads plotted for Au, Mo and Pt. The slope of the lines is the sheet resistance of the CIGSe, the intercept with the y-axis is 2 times the contact resistance of the metal/CIGSe interface.

From the previous experiments, we see that Au combines chemical compatibility with CIGSe (no or limited interdiffusion of species through the layer), electrical ohmic behavior on CIGSe, and a very high reflectivity especially in the visible and near infrared spectral region where it matches the Ag reflectivity. Au is therefore our metal of choice in the scope of realizing efficient solar cells with a very thin sub-micrometer absorber and a highly reflective back contact. In the following part, we will study the influence of a highly reflective Au back contact on CIGSe solar cells with different absorber thicknesses. A comparative study with standard Mo back contact will be done.

V.3.f) Electrical characterization of thin absorber solar cells with Au back contact and comparative study with standard Mo back contact

In order to compare the influence of a reflective Au back contact on very thin absorber solar cells with a standard Mo back contact, we realize a complete set of samples of different absorber thicknesses with the two back contacts. Two types of solar cells are realized: (1) Front etched solar cells with Mo back contact (figure 15.a); (2) Front etched and back etched solar cells with Au back contact (figure 15.b).

V.3.f.i) Experimental

For type (1) solar cells, as-deposited CIGSe is etched from the front side [141] [144] [61] to different thicknesses (1.8 µm, 1.2 µm, 0.8 µm, 0.4 µm and ~0.3 µm, ± 100 nm) as shown in figure 16.a, then the solar cell is completed using a standard process with a chemical bath deposited cadmium sulfide (CdS) buffer layer and a sputtered ZnO:i/ZnO:Al front window. No anti-reflection coating (ARC) or encapsulation is done on these samples. For type (2) solar cells, as-deposited CIGSe is etched for 3 minutes from the front side in order to obtain a flat interface [141]. Then the solar cell is completed using the classic CdS/ZnO:i/ZnO:Al process and encapsulated using a transparent epoxy (Araldite 2020) and a 2 mm glass. The lift-off is then performed to separate the solar cell stack from its Mo substrate, using the technique previously reported in this thesis. After the lift-off, the back side of the absorber is etched for different durations, resulting in the following CIGSe thicknesses as illustrated in figure 16.b: 1.8 µm, 1.2 µm, 0.8 µm, 0.4 µm and ~0.3 µm, ± 100 nm. The Au back contact is then evaporated with a thickness of ~ 0.3 µm. Etching the absorber both from front and back side for the type (2) samples results in a small bandgap shift of the absorber compared to type (1). Figure 16.c shows a SEM cross section view of a 400-500 nm thick absorber CIGSe solar cell with a 2-sides etching and an alternative Au back contact.

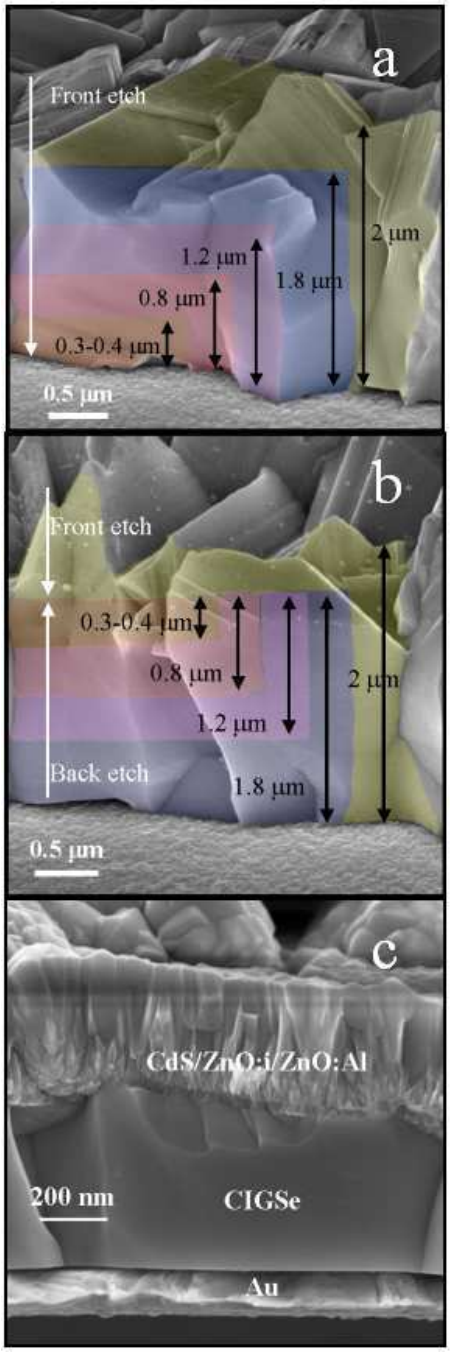

Figure 16. Scanning electron microscopy (SEM) cross-section view of CIGSe illustrating: (a) front side etching of different slabs as performed for samples type (1); (b) the front side etching and back side etching of different slabs as performed for samples type (2); (c) SEM cross-section view of a 2 side etched CIGSe solar cell with Au back contact

V.3.f.ii) Results

J-V measurements under standard A.M. 1.5 illumination are performed on the two series of samples, and the extracted photovoltaic parameters are presented in figure 17. The open circuit voltage (V_{oc}) and the Fill Factor (FF) are not significantly affected (~650 mV and ~64% respectively) down to a 400 nm absorber thickness with the same values for both Au and Mo back contact (figure 17.a and 17.b), indicating that the CIGSe etching process does not affect the properties of the material. The FF however is degraded in both cases for a CIGSe thickness below 400 nm. On the contrary of what is observed for a CIGSe/Mo back contact, the short circuit current (J_{sc}) of Au back contact solar cells is almost not affected by the absorber thickness reduction, and remains in the 25-26 mA.cm^{-2} range. The comparison between the two types of solar cells (figure 17.c) shows that the J_{sc} interval between Au and Mo increases as the absorber thickness is reduced. The influence of the back contact reflectivity becomes prominent for a CIGSe thicknesses lower than 1200 nm, with a $\approx 4.5 mA.cm^{-2}$ difference between a Mo back contact and an Au back contact solar cell at a 400 nm CIGSe estimated thickness. However, the J_{sc} shift for relatively thick absorber (> 1200 nm) cannot be explained only by the replacement of the Mo back contact by the more reflective Au back contact.

The first reason for that is the encapsulation effect; as previously detailed, the Au back contact solar cells are encapsulated for the lift-off, which is not the case of the Mo back contact solar cells. The encapsulation is done with an epoxy glue that has a refractive index of about n~1.5, which results in an effective anti-reflection effect for type (2) solar cells. It has been observed on previous experiments that the encapsulation increases the J_{sc} by an absolute value between 0.8 and 1.2 mA.cm^{-2} depending on the smoothness of the absorber layer. The second reason is the small bandgap shift because of the different etched region between the two type of solar cells (front etch for type (1), front and back etch for type (2)). We previously showed in Chapter III that our material had a + 50 meV bandgap shift from its front side to its back side. This leads to an extreme $\Delta J_{sc} \leq 1 mA.cm^{-2}$ in term of J_{sc} shift. These two statements lead to a maximum $\Delta J_{sc} \leq 2.2$ mA.cm^{-2} when combining encapsulation and bandgap shift.

It is however noticeable that the Au back contact makes it possible to maintain the J_{sc} at a high value, along with the voltage and the FF, which leads the efficiency (η) to remain above 10 % for an absorber thickness down to 400 nm (η = 10.2%). However, for the same CIGSe

thickness solar cell with a Mo back contact, the efficiency drops down to η = 7.9 % (8.6% for maximum ΔJ_{sc} correction taking in account the encapsulation and the bandgap shift) (figure 17.d). We notice that the reference solar cell with Mo back contact has a lower efficiency than what was reported in the Chapter III. This is due to the fact that a different CIGSe batch is used in this study.

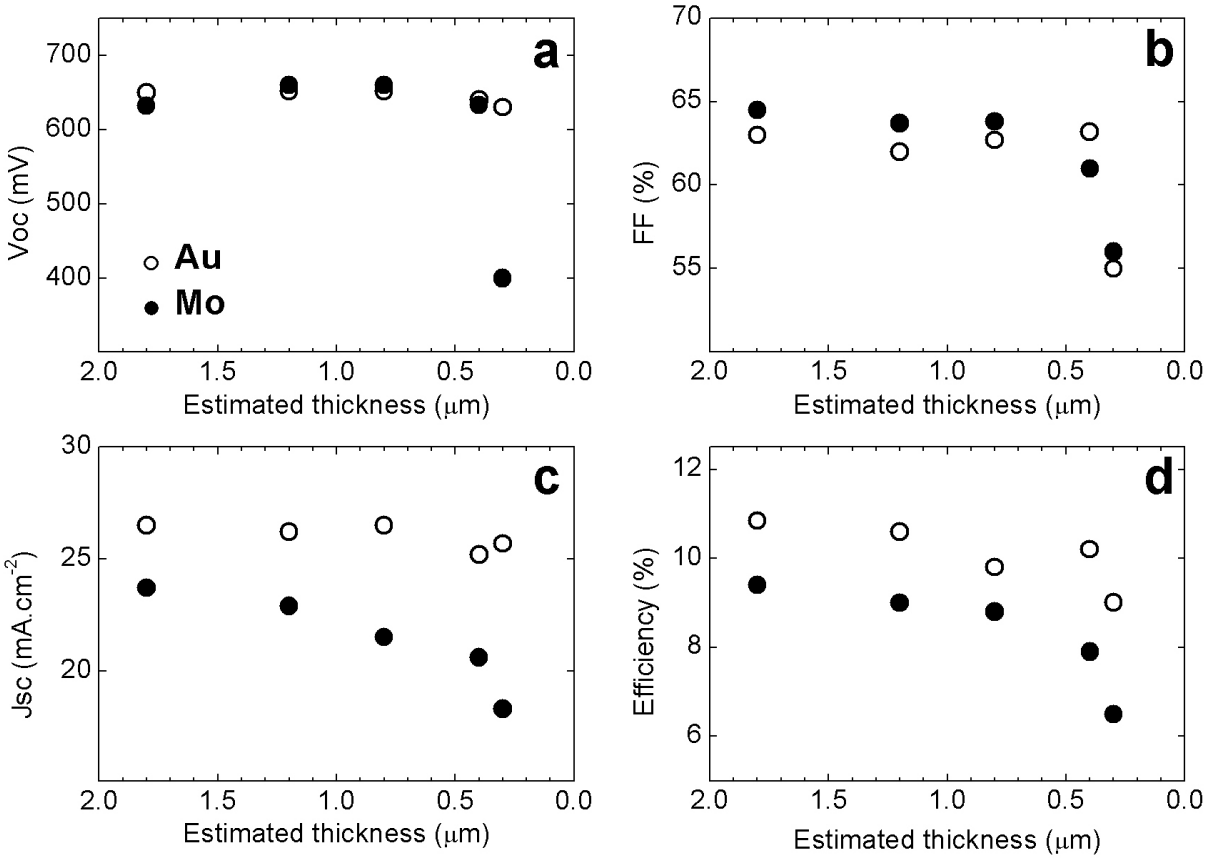

Figure 17. Photovoltaic parameters versus CIGSe thickness deduced from J-V measurements under A.M. 1.5 illumination for Mo back contact cells (filled circles and Au back contact cells (empty circles): (a) open-circuit voltage, (b) fill factor, (c) short-circuit current, and (d) efficiency.

To eliminate the encapsulation effect in the spectral response, we decide to plot the internal quantum efficiency IQE using the first order formula:

$$IQE = \frac{EQE}{1-R}$$

R being the reflectivity of the complete solar cell device as measured in the Chapter III (see references [141] [144]), EQE being the measured External Quantum Efficiency. The J_{sc} improvement with the Au back contact compared to the Mo back contact is nicely illustrated by figure 18, showing the IQE measurements for a 400 nm thick CIGSe solar cell with Mo and Au back contacts, compared to a standard 2500 nm absorber solar cell. In this figure, we observe that when Mo is replaced by Au, the current increase occurs mainly for low energy photons (infrared region), where the absorption of CIGSe is weaker. Au back contact allows a major enhancement of the optical path in the ultrathin absorber especially for low energy photons; subsequently, this leads to a significant enhancement of the absorption probability, and so to an increased photocurrent in the device. However, the current of the reference non etched thick solar cell (29 $mA.cm^{-2}$) is not fully recovered; being one-dimensional, the Au back contact mirror cannot enhance absorption to a higher value than an absorber with twice the thickness would have. As a comparison, the IQE curve of a 800 nm cell with a standard Mo back contact is also shown in figure 18; we notice that the 400 nm CIGSe with Au back contact is very close to the 800 nm with Mo back contact, which nicely illustrates this "doubling" of the effective absorber thickness with a highly reflective back contact.

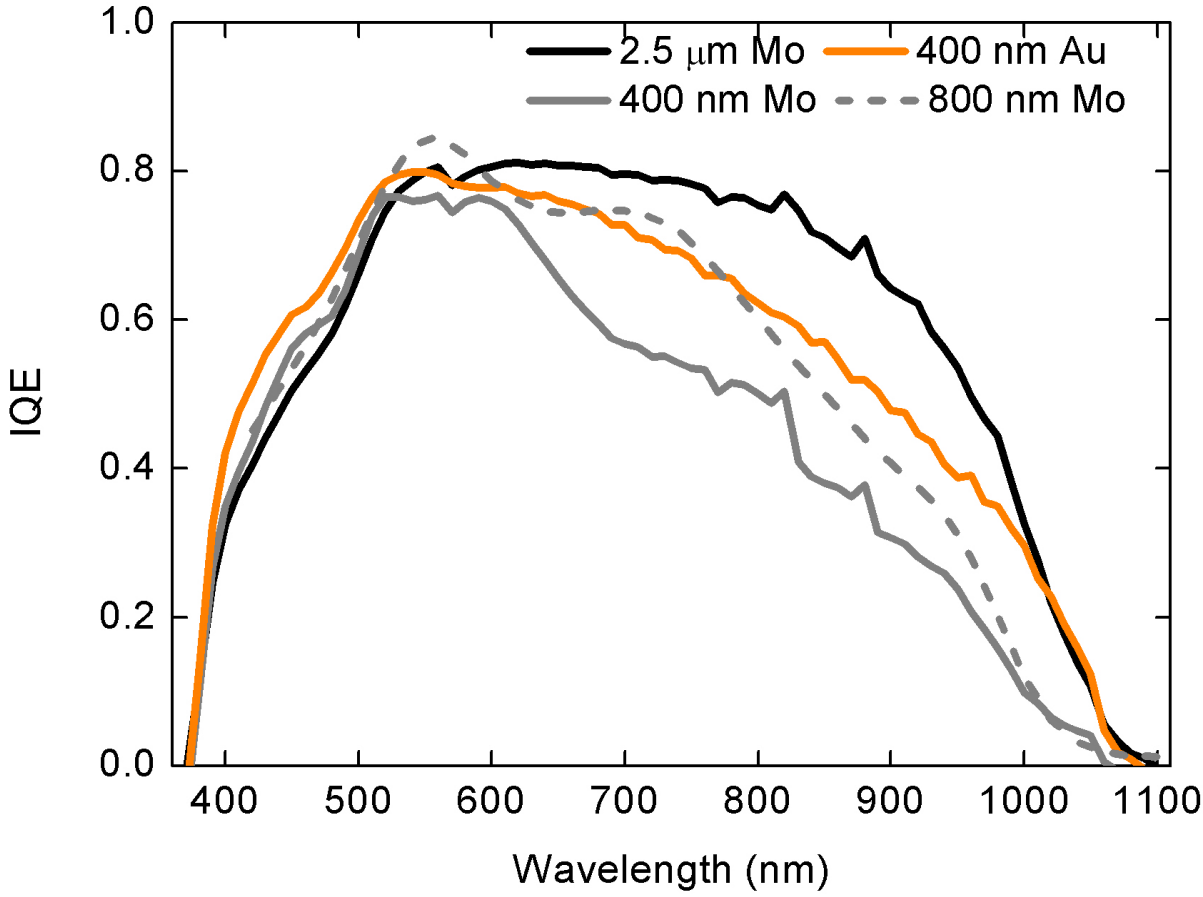

Figure 18. Internal Quantum Efficiency (IQE) curves for a reference 2.5 μm CIGSe solar cell with Mo back contact (solid black line), etched 400 nm CIGSe with Mo back contact (solid grey line), etched 800 nm CIGSe with Mo back contact (dashed grey line) and etched 400 nm CIGSe with Au back contact (orange solid line)

The increase of the absorption of low energy photons with the Au back contact is in good agreement with the simulations from Chapter II. The expected theoretical ΔJsc increase was 3.3 mA.cm^{-2} when using Au back contact instead of Mo back contact. In our experiment, we obtain a $\Delta Jsc \approx 4.5 mA.cm^{-2}$ (figure 17), which however must be balanced by a maximum $2.2 mA.cm^{-2}$ value coming from the encapsulation effect and the bandgap grading; this brings the minimum ΔJsc only due to the Au back contact to $\Delta Jsc \approx 2.3 mA.cm^{-2}$. This result is much higher to what was previously obtained in literature by using alternative reflective back contacts. By using a ZrN back reflector instead of Mo, Malmström et al. reported a maximum $\Delta Jsc = 1.4 mA.cm^{-2}$ [125]. This result is consistent with the higher reflectivity of Au compared to ZrN [125] (and TiN [145]). The Au back contact does not seem to lead to a higher back recombination rate than the Mo back contact. This leads us to believe that a thin $AuSe_x$ layer

may be formed at the interface between CIGSe and Au, similarly to what happens for the Mo with the formation of the $MoSe_2$ interfacial layer.

In order to investigate the electronic properties of the devices, we carried out dark J-V measurements on the Au back contact solar cells. The dark J-V curves of solar cells with different absorber thicknesses and Au back contact have been fitted using a classic two diodes model [146], where the ideality factors n_1 and n_2 are 1 and 2 respectively, and the reverse saturation current J_1 and J_2 are calculated, as well as the serie resistance (R_{serie}) and the parallel resistance ($R_{parallel}$). We can see on figure 19.a that R_{serie} is independent of the CIGSe thickness and remains remarkably stable at a low value in the range of 4-6 $\Omega.cm^2$ down to 300 nm absorber thickness, which confirms the very good quality and ohmicity of the alternative Au back contact. On the opposite, $R_{parallel}$ is degraded when thinning the CIGSe layer (figure 19.b); this decrease becomes critical when the $R_{parallel}$ decreases from 2.10^4 $\Omega.cm^2$ for the 400 nm absorber down to 760 $\Omega.cm^2$ for the 300 nm thick absorber, and it explains the observed FF degradation (from 63 % to 55 %) in figure 17.b. This “shunt” effect probably comes from the chemical etching process which most likely reveals some pre-existing “pinholes” in the absorber when the etching goes below 300 nm. It is consistent with the AFM measurements previously done on etched CIGSe layers (Chapter III, reference [141]) which indicated a peak-to-valley of ~150 nm and a ~40 nm RMS after etching. The existence of these pinholes is also confirmed in SEM observations of the back side of the CIGSe absorbers.

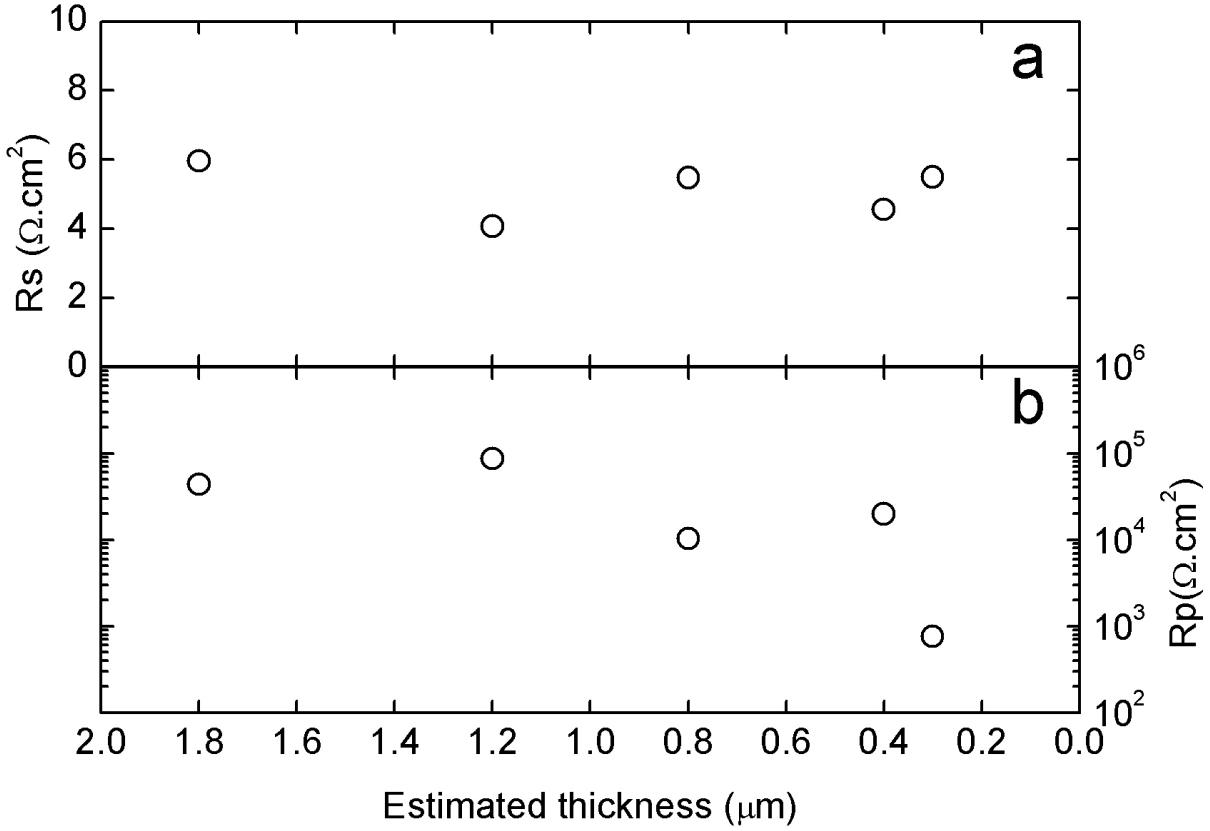

Figure 19. (a) Serie and (b) Parallel resistance deduced from a two-diode fit versus estimated CIGSe thickness for solar cells with Au back contact.

V.3.g) Conclusion

In conclusion, we developed a lift-off process that allows to separate the CIGSe absorber from its original Mo substrate with a high reproducibility and no significant damages in the film. This allowed us to study with high precision the chemical composition of the CIGSe back side, and the Mo substrate, and we characterized the presence of an interfacial $MoSe_2$ layer on the substrate-side, while no interdiffusion of Mo atoms was observed in the CIGSe back surface. Spectroscopic ellipsometry analysis of the lift-off CIGSe allowed us to simulate the reflectivity of the back interface of the solar cell for different alternative metals back contact. By using Transmission Line Measurements, we also characterized the electric contact on CIGSe for each metal. Finally, from the optical and electrical characterization, we deduced that Au was the metal with the highest potential to increase the light absorption in a very thin CIGSe absorber without degrading the electrical properties of the cells.

A serie of CIGSe solar cells with different thicknesses down to 300 nm has been realized with an alternative Au back contact. The cells are characterized by current-voltage measurements and Spectral Response, and are compared with CIGSe solar cells with the same absorber thicknesses and standard Mo back contact. For each absorber thickness, the Au back contact solar cells have a significantly higher J_{sc} than the Mo back contact solar cells while the other parameters (V_{oc}, FF) are unchanged. When the thickness is reduced, the shift in J_{sc} between Au and Mo back contact increases; as a result the efficiency of Au back contact solar cells is much higher than the efficiency of Mo back contact solar cells. For a 400 nm absorber CIGSe solar cell, the Au back contact brings a remarkable +2.5 % absolute efficiency increase compared to standard Mo back contact with the same absorber thickness. This increase is much higher than what was ever reported in literature when using an alternative back contact for thin CIGSe solar cells and it is consistent with our theoretical results from simulations in Chapter II.

V.4) Transparent back contact based on ZnO:Al

V.4.a) Introduction

Beyond the fact that we realized an efficient proof of concept device with an alternative back contact, we demonstrated that the lift-off process allows to use materials that usually have compatibility issues with CIGSe as back contacts, and thus to significantly increase the efficiency of a very thin device compared to standard Mo back contact. In the scope of reducing the absorber thickness to an ultrathin level (100-200 nm), we have seen in Chapter II that a more advanced back contact engineering is required, and it would be convenient to use a transparent back contact applicable to CIGSe. With that, the use of advanced light trapping structures would be greatly facilitated.

Transparent back contacts on CIGSe have been widely investigated by Nakada et al. in the past decade [127,128]. They demonstrated that it was possible to achieve high efficiency CIGSe solar cells by using both Indium Tin Oxide (ITO) and Fluoride Tin Oxide (FTO) as substrates in a co-evaporation process. In our laboratory, the Transparent Conducting Oxide that we use is highly n-doped ZnO:Al ($N_d = 10^{20} cm^{-3}$); Rostan et al. showed that although the ZnO:Al/CIGSe contact has a rectifying behavior, it is possible to turn it to an ohmic contact by adding a thin transparent interfacial $MoSe_2$ layer [130]. The bandgap of this $MoSe_2$ is only 1.2 eV [147], but the minor thickness of this layer allows to maintain the transparency of the ZnO:Al/MoSe2/CIGSe contact. However, we have shown by SCAPS simulations in Chapter II that when the CIGSe thickness becomes smaller than the Space Charge Region width (W), a wider bandgap semi-conductor is necessary at the back contact if one wants to increase the quasi-Fermi levels splitting and maintain the V_{oc} at a high value. In this part, we propose to introduce a novel copper based back contact buffer layer which purpose is twofold:

- To allow ohmic contact formation between the transparent ZnO:Al and CIGSe film
- To increase the quasi Fermi level splitting in the absorber

To achieve both conditions, a p+ doping (ohmicity on p-CIGSe) along with a relatively wide bandgap (quasi Fermi level splitting) are required. Figure 20 presents the band diagram of the

contact between a low doped p-type (p) semi-conductor such as CIGSe (solid green line) with a highly n-doped (n+) semi-conductor such as ZnO:Al (solid green line). We see that in this case, we obtain a rectifying behavior, blocking the holes diffusion from the p semi-conductor toward the n+ semi-conductor. The valence band band-bending acts as a sink for the electrons. When the doping rate of the p semi conductor is increased, turning the material into a p+ semi conductor (solid black line), the depletion region is almost vanished as shown on the black lines figure 20. In that case, the carriers can diffuse from the p+ semi-conductor to the n+ semi-conductor by tunneling leading to an ohmic behavior of the contact.

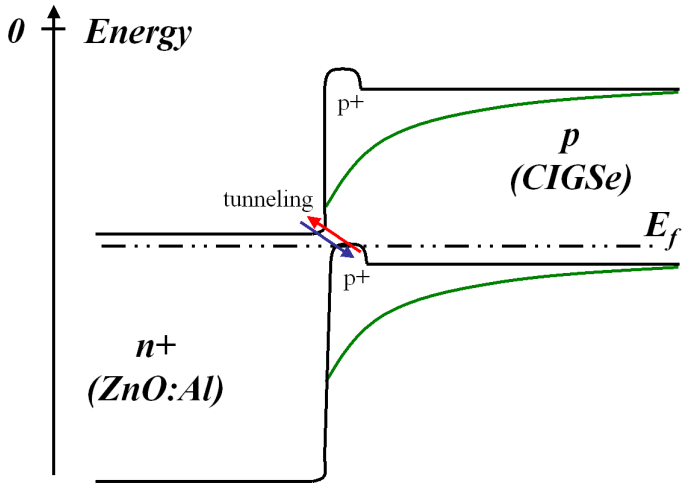

Figure 20. Schematic representation of the effect of increasing the doping rate at the back interface of a p-type semi-conductor, turning the rectifying junction with a n+ type semi-conductor into a tunnel junction

It is well known that a copper enrichment on CIGSe strongly increases the doping rate of the material. To achieve such a contact, we deposit a very thin copper layer on the back side of the CIGSe by electrodeposition (less than 100 nm). The goal is to increase the carrier density at the CIGSe surface in order to realize a tunnel junction between p+ CIGSe and n+ ZnO:Al.

In a second section, we will present the first results on the influence of an interfacial electrodeposited thin Cu_2O buffer layer at the ZnO:Al/CIGSe interface for ohmic back contact application. Cu_2O is know for its high p+ doping rate, but also for its large bandgap that may help us to increase the quasi fermi level splitting issue in ultrathin devices.

V.4.b) Electrodeposited thin Cu layer at the CIGSe/ZnO:Al interface

In this part, we investigate on the potential benefits of deposing an extremely thin (less than 100 nm) metallic Cu layer on the CIGSe before the deposition of a ZnO:Al layer, in order to turn the rectifying ZnO:Al/CIGSe contact into an ohmic contact.

V.4.b.i) Experimental

The Cu layer is electrodeposited on a CIGSe surface at room temperature and a potential $E = -0.6V$ versus the saturated calomel electrode (SCE) in a three electrodes electrochemical setup. The solution is a 0.1 M Cu^{2+} from $CuSO_4$ and 0.034 M HCl (pH = 1.46) at room temperature. A Pt wire is used as counter electrode, and a standard CIGSe sample on Mo is the working electrode. The contact is taken on the Mo (the CIGSe is removed on a small portion of the sample with a doctor blade) and the sample is illuminated during the electrodeposition with a tungsten lamp. The solution is stirred during the deposition using a magnetic bar. After electrodeposition on the thin Cu layer, a 200 nm thick ZnO:Al layer is deposited by sputtering in the same conditions as the front ZnO:Al in a CIGSe solar cell. The final stack is Glass/Mo/CIGSe/Cu/ZnO:Al, and the visual aspect of the sample is almost unchanged compared to a CIGSe/ZnO:Al sample. The device is characterized by J-V measurement in the dark.

V.4.b.ii) Electrochemical study

The nature of the thin Cu layer on CIGSe is still unclear; being very thin, it is very likely that it is partly or even fully oxidized. However, its aspect needs to be investigated. The observation of the electrodeposition deposition chronoamperograms (current during the deposition versus time) gives us an insight on the deposition mechanism and the shape of the layer. Figure 21 is a chronoamperogram of a relatively thick Cu layer on CIGSe. This sample had a metallic copper aspect after deposition (orange). We clearly see that two different regimes co-exist during the electrodeposition. During the first regime, from 0 to about 10 seconds, the deposition current strongly increases in absolute value. This is characteristic of a coalescent regime; during this early stage, it is very probable that small pads grow in 2D or

3D from the nucleation sites on the CIGSe. When they merge into a flat single metallic Cu film, the current reaches an asymptotic value of about 12.5 mA.cm^{-2}. This relatively constant trend of the current is characteristic of a 2 dimensional growth. Consequently, it is possible that the metallic or oxidized Cu pads establish the ohmic contact pathways between CIGSe and ZnO:Al.

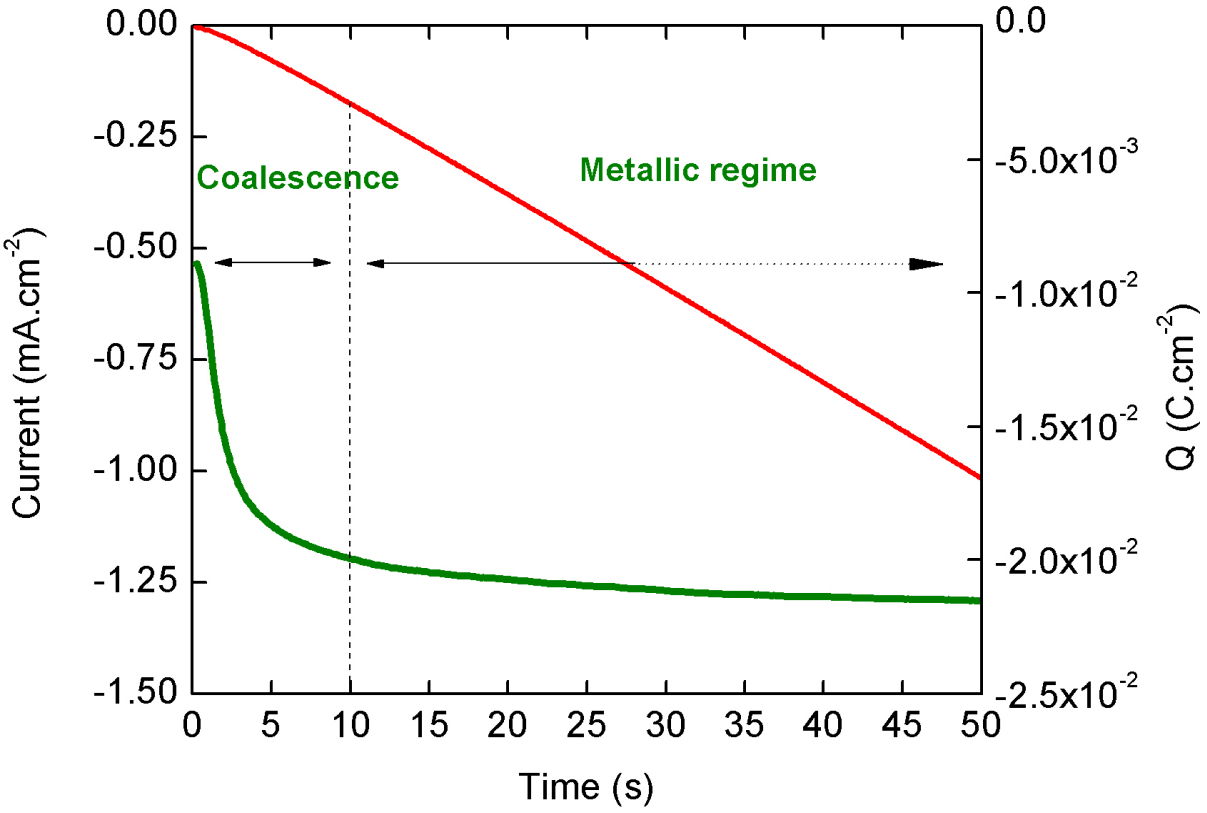

Figure 21. Chronoamperogram of an electrodeposited Cu layer on a CIGSe surface (green). Total charge exchanged during the deposition (red).

The equivalent copper thickness d electrodeposited on the CIGSe after t seconds of deposition is calculated by considering a 100% faradic efficiency. The reaction is as follow:

$$Cu^{2+} + 2e \rightarrow Cu$$

After t seconds, the charge exchanged per surface units (red curve Figure 21) is Q(t), in Coulomb per cm^{-2}. The number of copper atoms deposited per surface units on the CIGSe is therefore:

$$N_{Cu} = \frac{Q(t)}{2 \times 1.6.10^{-19}} \text{ in .cm}^{-2}$$

The molar volume of Cu is $7.11 \times 10^{-6} m^3.mol^{-1}$. The equivalent electrodeposited Cu thickness d is:

$$d = \frac{N_{Cu}}{N_A} \times V_{mol}$$

The numerical application leads to the following thicknesses (table 3).

Time (sec)	Charge exchanged per surface units ($C.cm^{-2}$)	Equivalent Cu thickness (nm)
0.5	9.1E-5	0.33
1	1.78E-4	0.65
5	1.28E-3	4.6
10	2.9E-3	10.6

Table 3. Calculated equivalent Cu thickness for different deposition times

However, these thicknesses are most probably not representative of the real interface. Indeed, the film did not appear metallic after deposition on CIGSe (no orange characteristic color); it had a dark blue aspect, characteristic of the 2nd oxidation degree of Cu. This was confirmed by XPS analysis of the surface which did not reveal any metallic copper on the surface for each sample. However, the analysis of the valence band (Figure 22) reveals a “metallic” behavior of the surface, indicating a degenerated region at the surface. As we can see, the onset of the valence band of the reference CIGSe (without deposited Cu) is at about +0.5 eV. For the two samples with electrodeposited Cu, the Fermi level is after the valence band onset, which is an indication of a degenerated material. It is therefore probable that the film is completely oxidized, or diffuses through the CIGSe to forms a degenerated region at the interface.

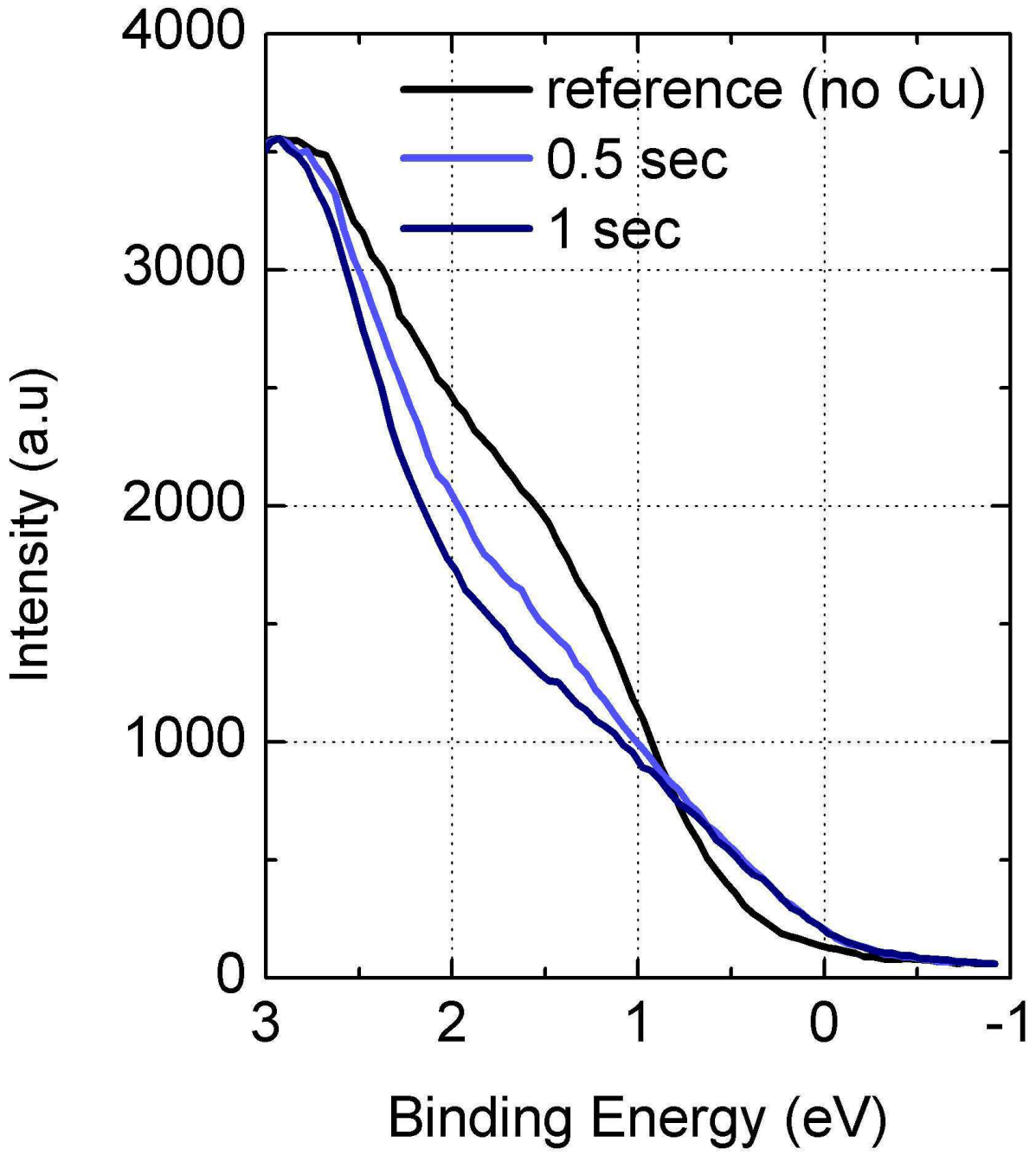

Figure 22. Valence band from XPS for three different samples: reference CIGSe (black), 0.5 sec Cu (light blue) and 1 sec Cu (dark blue)

V.4.b.iii) Characterization of the ZnO:Al/CIGSe interface with a thin Cu interfacial layer

Figure 23 shows the a schematic view of the J-V characterization of the device. We assume that the Mo/CIGSe contact has a contact resistance of R_{Mo} = 0.045 Ω.cm^2 based on reference [130]. The device is mechanically scribed in squares of 0.1 cm x 0.1 cm and the measurement is performed in the dark in several points of the samples.

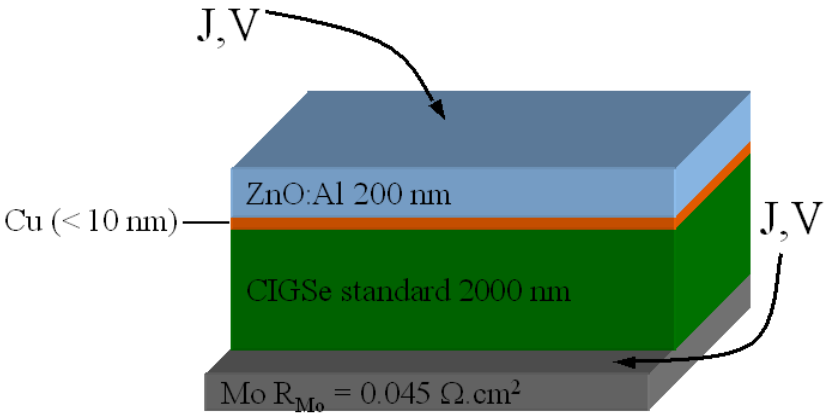

Figure 23. Schematic representation of the J-V characterization of test-device for the CIGSe/ZnO:Al contact

Different Cu deposition times are studied, from 0.5 seconds to 10 seconds. After that duration, the sample turns to an orange color characteristic of metallic copper which we reported as unsuited for back contact application. The thickness of the layer is very difficult to estimate, because it is very unlikely that such thin copper layer stays in its metallic form; however calculations based on the faradic efficiency during the deposition showed that a 10 seconds deposition roughly corresponds to a 12 nm Cu film. Figure 24 shows the current voltage curves of Mo/CIGSe/Cu/ZnO:Al stack with 4 different deposition durations: 0.5, 1, 5 and 10 seconds. A direct rectifying CIGSe/ZnO:Al interface is shown in comparison. We observe that for each deposition duration, the presence of a thin interfacial Cu film turns the CIGSe/ZnO:Al contact into an ohmic contact with a relatively low contact resistance. The contact resistance decreases from 1.8 Ω.cm^2 for 0.5 seconds of electrodeposition down to 0.9 Ω.cm^2 for 5 seconds of electrodeposition. It is however slightly increased up to 1.3 Ω.cm^2 for

10 seconds of deposition, for reasons that are still unclear. Although still superior to the contact resistance of the Mo/CIGSe contact (R_{Mo} ~ 0.03 Ω.cm^2), Rostan et.al demonstrated that it was possible to achieve very efficient solar cells with a contact resistance of the same magnitude and a $MoSe_2$/ZnO:Al back contact [130]. Consequently, extremely thin Cu buffer layer could be considered for transparent ZnO:Al back contact solar cell application.

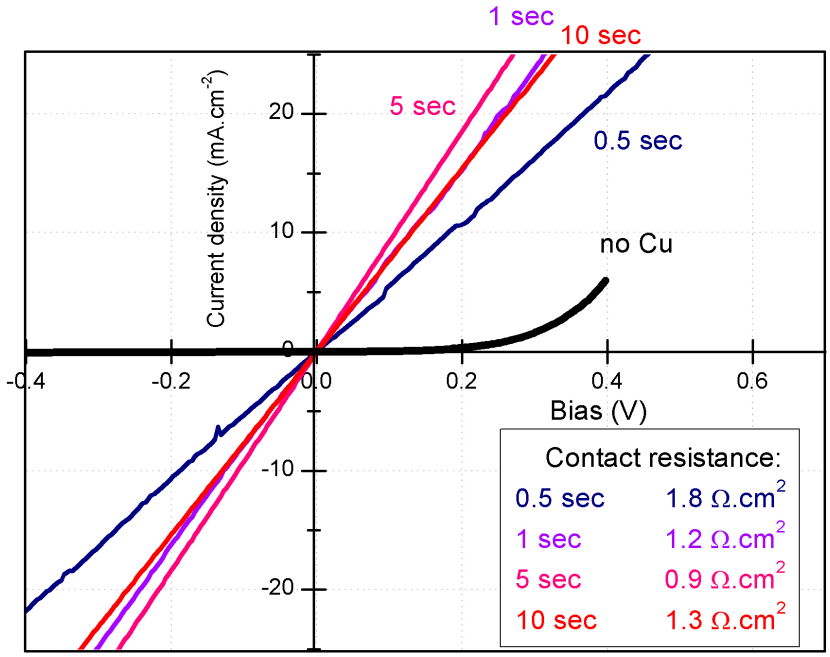

Figure 24. Voltage versus Current density curves for different electrodeposition duration of interfacial Cu layer and transparent CIGSe/ZnO:Al contact

We have demonstrated that it was possible to turn a rectifying ZnO:Al/CIGSe junction into an ohmic contact by electrodeposing even an extremely thin Cu interfacial layer. Low contact resistance, in the magnitude of 1 Ω.cm^2 has been achieved, which is comparable to results that are obtained with the addition of a $MoSe_2$ interfacial layer. Although this study is still preliminary, we tried to realize a 500 nm CIGSe solar cell with a transparent ZnO:Al back contact and an interfacial Cu thin layer (5 seconds deposition). The efficiency is still very low, but the comparison with a structure without Cu interfacial layer shows that the double diode effect is vanished when using the Cu interfacial layer (figure 25). The V_{oc} and the FF are slightly improved from 260 mV to 310 mV and 31% to 44% respectively, while the short circuit current is unchanged at 20 mA.cm^{-2}. The efficiency increases from 1.6% without Cu interfacial layer to 2.7% with the Cu interfacial layer.

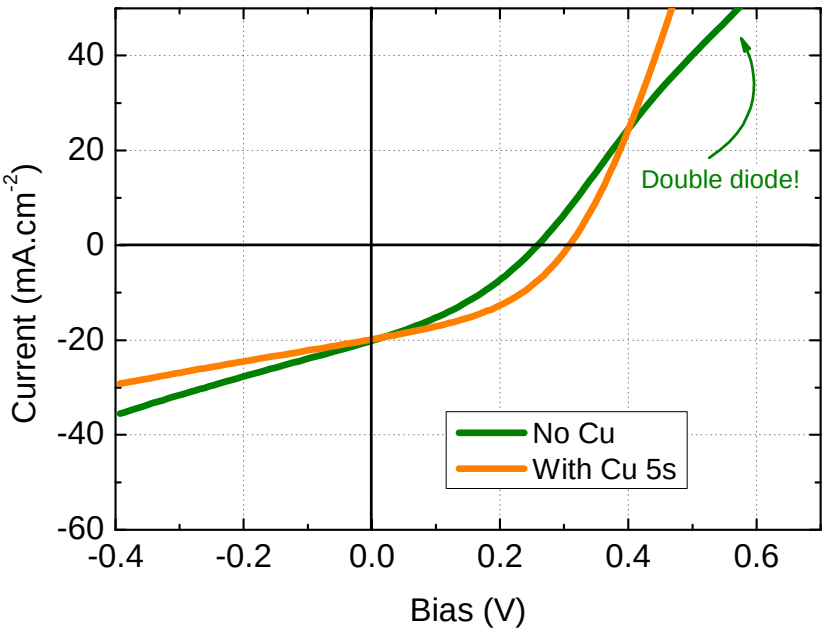

Figure 25. Lifted-off 500 nm CIGSe solar cells with Cu/ZnO:Al back contact (orange curve) and ZnO:Al only back contact (green curve)

The application of extremely thin Cu layer at the ZnO/CIGSe interface to solar cells is not conclusive at the moment, and the nature of the Cu interfacial layer is still unclear to us. As a result, the lack of control in the parameters of this layer (thickness, band alignment…) makes it difficult to apply it to solar cells. However, the introduction of a thin Cu layer at ZnO:Al/CIGSe interface showed an interesting potential for transparent ohmic back contact formation.

V.4.c) Electrodeposited Cu_2O interfacial buffer layer

In this section, we propose to deposit on the back surface of the CIGSe a copper based p-type TCO, Cu_2O, which electronic and optical properties may fulfill the condition required to increase the ohmicity of the ZnO:Al/CIGSe contact. The study is still at an early stage and very preliminary results will be presented.

Cu_2O is a p-type semiconductor with a 2.5 eV indirect bandgap and 2.9 eV direct transition; these values decrease to 2.0 eV and 2.4 eV for thicker films (more than ~500 nm) as reported by Alkire et al. [148]. It is well known for its important doping rate [149] and extensive researches have been carried out in the past decades for its very promising properties as a semi-transparent conducting oxide. In this section, we electrodeposited Cu_2O layers using a methodology that is reported elsewhere [150]. The applied potential versus the SCE is E = -1.4 V, and the source materials are copper sulfate (25 g) and lactic acid (125 mL) dissolved in 500 mL of deionized water. Concentrated sodium hydroxide solution is then slowly added to adjust the pH value to ~13 while stirring. When it is thick enough (more than 300 nm), the color of the films turns to a light orange/red color, characteristic from a direct ~2.6 eV transition. Firstly, the films have been deposited on FTO for optical characterizations by another group from our institute [151], and the transmission curve of a 300 nm film is presented on figure 26. We observe important interference fringes, with a minimum centered at 950 nm; however, this sample is much thicker than what we will use for solar cells applications, which will suppress the interference effects and so will not affect the transmission. The bandgap of the film is calculated (inset figure 26) at 2.6 eV, which is consistent with literature data [148]. The fact that the photons of energies lower than 500 nm are absorbed is not harmful in the scope of back contact application of Cu_2O, because these photons are for the vast majority absorbed in the first pass through the absorber.

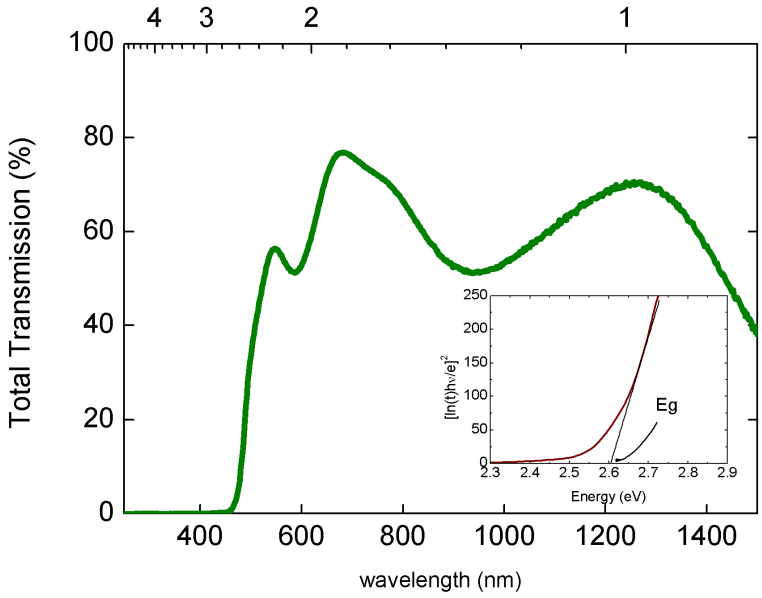

Figure 26. Total Transmission curve of a 300 nm thick Cu_2O layer deposited on a FTO coated glass (Asahi standard); (inset) bandgap calculation.

In a second step, the Cu_2O films have been electrodeposited on standard CIGSe surfaces under illumination for different durations, in order to vary the thickness of the films. A 200 nm ZnO:Al film is then deposited, leading to a stack identical to Figure 23 with a Cu_2O layer instead of the Cu layer, and the obtained device are mechanically scribed to 0.33 cm x 0.33 cm squares (1 cm^2). The Cu_2O thickness is determined from the Total Charge Exchanged during the electrodeposition assuming a 100% faradic efficiency. The deposition times are: 30 seconds (2-4 nm), 1 minute (8-10 nm), 4 minutes (30-40 nm) and 10 minutes (~80 nm). The device are electrically characterized using dark J-V measurements (figure 27), in the same configuration as reported in the previous section. Similarly to what was obtained in the previous section, we see that the rectifying behavior of the ZnO:Al/CIGSe contact is turned to ohmic when with the addition of a Cu_2O interfacial buffer layer. The contact resistance decreases from 2.6 Ω.cm^2 to 0.9 Ω.cm^2 when increasing the Cu_2O deposition time (thickness) up to 4 minutes (30-40 nm) and then increases for the 10 minutes deposition sample to 14 Ω.cm^2. This increase for thicker layer may be related to the low carrier mobility of the Cu_2O layer; however the study is still very preliminary and more experiments are needed.

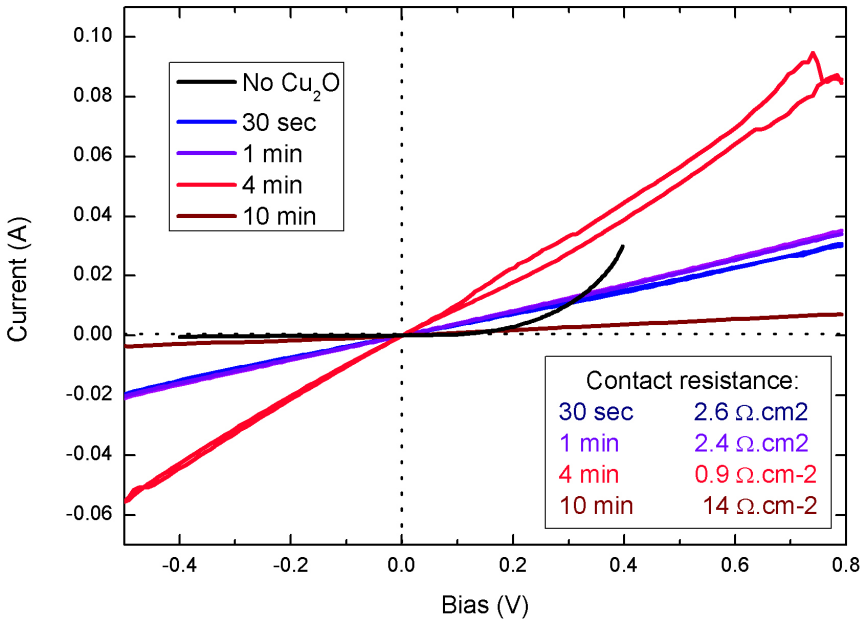

Figure 27. Current Voltage curves for ZnO/Cu_2O/CIGSe/Mo stack for different Cu_2O deposition time. The stack without Cu_2O is shown in comparison (black curve)

In conclusion, our results showed an alternative route to achieve ohmicity of the ZnO:Al/CIGSe contact while keeping maintaining the transparency of the contact, by using an extremely thin electrodeposited Cu layer at the interface. Low contact resistance (less than 1 $\Omega.cm^{-2}$) comparable to state of the art devices have been achieved, and the first application to solar cells showed a suppression of the double diode effect that is observed for direct CIGSe/ZnO:Al back contact when using interfacial Cu.

Moreover, we demonstrated in a very preliminary study that ohmicity could also be achieved with p-type wide gap semiconductor, Cu_2O. In the scope of a back contact application for ultrathin CIGSe solar cells, such a wide gap layer may solve the quasi Fermi level splitting issue that occurs when the absorber thickness is lower than the space charge region width.

If a transparent back contact is designed on ultrathin CIGSe solar cell without electrical degradation of the device, new materials could be used as back reflectors to increase the light pathway through the absorber. In the following part, we will experimentally demonstrate the feasibility of an ultrathin CIGSe solar cell having the same light absorption than a standard CIGSe solar cell by using lambertian light scattering on a proof of concept device.

V.5) Ultrathin CIGSe solar cell with lambertian light scattering back reflector

As highlighted in Chapter II, the CIGSe absorption in an ultrathin absorber device configuration (less than 400 nm) is too low to achieve full spectrum absorption by only using 2 dimensional flat layers. In order to increase the light absorption in such a solar cell, new designs have to be developed not only to reflect the light at the back interface, but also to dramatically increase the optical path of reflected light in the absorber. Lambertian light scattering reflection is known to be the ideal light scattering back reflector; it means that the radiance of the reflected light is assumed equal for all possible directions in the scattering hemisphere. A schematic representation of the effect of a lambertian back reflector in an ultrathin 200 nm CIGSe solar cell is presented in figure 28. In Chapter II, by using data from the theoretical investigation from Malmström et al. [28], we demonstrated that it could be possible to enhance the light absorption in a 100 nm ultrathin device by using lambertian back reflection; in this case, the photocurrent of the 100 nm ultrathin absorber solar cell matched the photocurrent of the reference thick absorber solar cell.

In the following part, we investigate on the potential of a lambertian back reflector for ultrathin CIGSe cell. The absorption of a 100 nm CIGSe slab with and without reflective lambertian back scattering is first theoretically analyzed, and a comparison of the calculated absorption in CIGSe with calculated absorption in a thicker layer is done. These simulations have been performed by Nir Dahan and Jean Jacques Greffet at “Institut d’Optique”. Based on this theoretical study, we realize an experimental proof of concept device for optical characterizations only, consisting in a lifted-off 200 nm thick CIGSe absorber completed with the full solar cell stack (i.e. CdS/ZnO:i/ZnO:Al…); this optical demonstrator solar cell is optically characterized by spectroscopic reflection/transmission/absorption, and the results are compared with optical simulations of the same material stack in order to identify the role of each layer in the optical properties of the device.

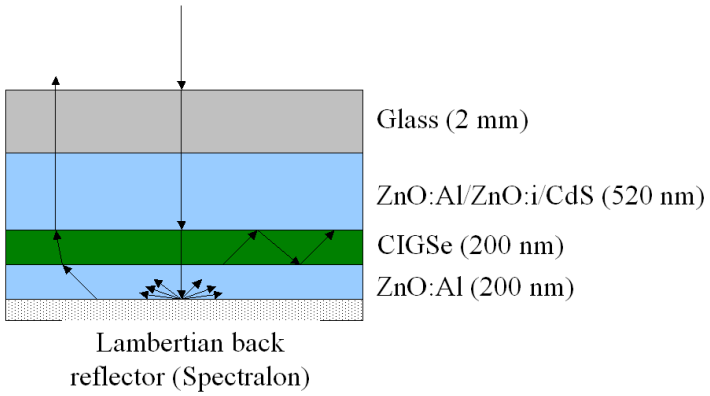

Figure 28. Schematic representation of a normal incident light ray entering the solar cell structure with a lambertian back reflector. On the right side of the figure, the ray light is scattered and trapped in the absorber. On the left side, the ZnO:Al spacer reduces the scattering angle and the ray light can escape from the structure.

V.5.a) Optical simulation of a 100 nm CIGSe slab with lambertian back reflection

To evaluate the potential of a lambertian back reflector in a 100 nm CIGSe slab, our colleagues from the "Institut d'Optique" first simulated the absorption of a single CIGSe slab with various back reflectors. In these simulations, the CIGSe thickness and the nature of the back interface are the only parameters that are varied. The absorption of the slab with a thickness of 100 nm is modeled considering a specular front interface and a perfect lambertian back reflector. The calculations are performed with the following assumptions:

- The system is azimuthally symmetric.
- The incident light associated with the solar spectrum AM 1.5 is unpolarized.
- The diffuse light reflected or transmitted from the back surface is unpolarized and is not correlated with the impinging light. Therefore, no interferences effects are considered.

To follow the ray in the slab, the notation of radiative transfer equation (RTE) [152] is adopted. Although RTE assumes geometrical optics, it is still valid in slab thickness which is comparable to the wavelength [153] and so applicable to our 100 nm CIGSe slab. More details

on the calculations are given in Appendix IV of this thesis. The absorption of a 100 nm and a 1 µm CIGSe slabs with standard Mo back contact, Ag back contact and perfect lambertian back reflector is shown in figure 29. The absorption of the 100 nm slab is very poor, below 20 % after λ = 750 nm. The Ag back contact, although very reflective, does not increase the absorption in the CIGSe sufficiently to consider an application to solar cells since only the 450 – 600 nm range is noticeably enhanced. When using a lambertian back reflector, the absorption in the CIGSe is significantly larger than with a flat interface on the back contact and even higher than the absorption of the 1 µm CIGSe slab with standard Mo back contact. This enhancement results from the dramatic increase of the optical path in the absorber by the lambertian diffusion effect. The 1 µm CIGSe slab also takes great advantage of using of the lambertian back reflector, with an almost constant 80% absorption from λ = 400 nm to λ = 1000 nm.

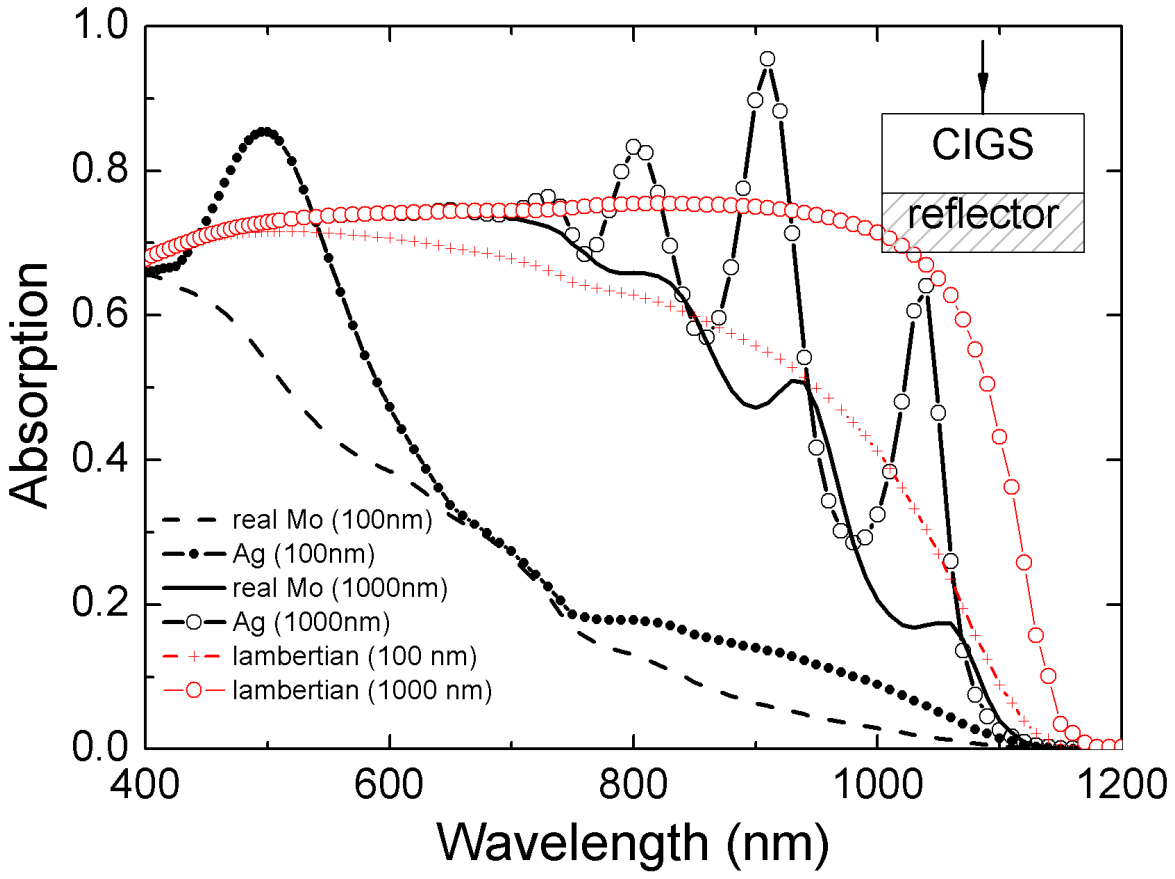

Figure 29. Simulated absorption in a single CIGSe slab for different thicknesses and back reflectors. Flat Mo and Ag back contact are shown in comparison (black) to a perfect lambertian back reflector (red). Two different CIGSe thicknesses (100 nm and 1000 nm) are presented

The lambertian back reflector has a very high potential to increase light absorption in ultrathin CIGSe layer. In the following section, we realize an experimental demonstrator device with a complete ultrathin solar cell stack (200 nm CIGSe), in order to experimentally investigate the behavior of an ultrathin device in real conditions with a lambertian back reflector. As a comparison, we will present the results from simulations of an equivalent material stack.

V.5.b) Light absorption in an ultrathin 200 nm CIGSe solar cell structure

Real lambertian back reflectors are often Fluoropolymers, known as Spectralon, which are known to be the materials with the highest diffuse reflectance in the U.V., visible and I.R. ranges [154]. In this section, we realize an experimental proof of concept solar cell structure for optical measurements to demonstrate the very high light absorption that can be achieved in an ultrathin 200 nm CIGSe layer in the real solar cell conditions.

The structure is realized with the following process: a standard CIGSe film on Mo substrate is etched down to 1000 nm from the front side in the bromine solution, as described in Chapter III. The standard solar cell stack (CdS/ZnO:i/ZnO:Al) is then deposited on the absorber, and the encapsulation is performed as previously described in this Chapter (part V.3.b). After the lift-off of the structure, a back side etching of the CIGSe is performed down to a final thickness of 200 nm, ± 50 nm. At this stage, the structure is semi-transparent due to the extreme thinning of the absorber (see Figure 30).

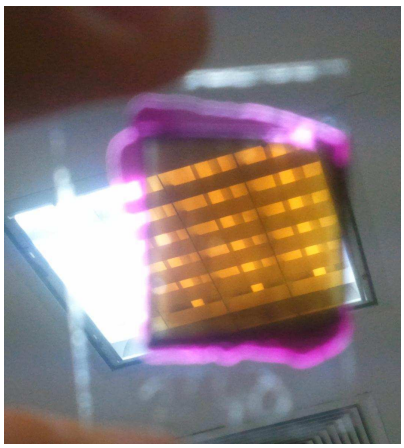

Figure 30. Picture of a 200 nm-CIGSe/50 nm-CdS/70 nm-ZnO:i/400 nm-ZnO:Al/2 mm Glass stack, showing the transparency of the device

In a realistic configuration, a transparent back contact is needed because the lambertian back reflector is an electrical insulator. Therefore, we have deposited a 200 nm ZnO:Al spacer layer at the back side of the CIGSe by sputtering; the ohmicity of the contact is not considered in this work, and only the optical properties of the stack are studied. The structure is then characterized by transmission/reflection spectroscopy using an integrating sphere set-up (see part III.4.b.i). After this first characterization, a Spectralon is mechanically bonded at the back side of the device, leading to the following structure: Spectralon/ZnO:Al-200 nm/CIGSe-200 nm/CdS/ZnO:i/ZnO:Al/Glass-2 mm. We then perform the same spectroscopic characterizations, and compare with simulation results of an equivalent material stack. The total reflectivity of the Spectralon is about 90% on the whole spectral region.

Figure 31 summarizes the transmission/reflection/absorption measured on the ultrathin solar cell structure (200 nm CIGSe) with and without the lambertian back reflector. The absorption is calculated by $A = 100 - R - T$. With no reflector on the back side, we see that the transmission of the structure starts to increase at a wavelength of about 600 nm to reach 40% at 980 nm. These photons are lost and cannot contribute to the photocurrent. The reflectivity is stable at about 20%. The absorption of the structure is 80% in the wavelength range of 400-600 nm, but it is very likely that absorption from the CdS buffer layer accounts for this value. After 600 nm wavelength, the absorption of lower energy photons starts to decrease in correspondence with the increasing transmission of the structure and at 920 nm, the absorption is only 53%.

When the Spectralon is added at the back side of the structure, we see that the absorption curve becomes remarkably stable, only decreasing from 80% to 76% for λ = 600 nm to λ = 900 nm respectively. By scattering light at the back interface, the optical path is greatly enhanced in the absorber, increasing its effective optical thickness and thus the absorption. The gain in absorption for the Spectralon back reflector is symbolized by hatching on the graph figure 29. After 900 nm, the reflectivity of the structure with Spectralon starts to increase significantly; this corresponds to photons that are not absorbed in the second pass through the absorber and escape from the structure. This effect may be partly related to the ZnO:Al spacer layer that reduces the effective scattering angle of light entering the absorber after reflection by the Spectralon, following the Snell-Descartes law (left side of figure 28).

After the bandgap of the CIGSe, the absorption of the structure is still at an unintuitive high level: 45% and 18% at λ = 1070 nm with and without Spectralon respectively. However, we

identified this absorption as the absorption coming from the free carrier electrons in both highly doped layers 400 nm front side ZnO:Al and 200 nm back side ZnO:Al. The fact that the absorption of the structure is increasing when increasing the wavelength from 1070 nm to 1400 nm also supports this assumption. Moreover, a ~10% absorption is attributed to the Spectralon.

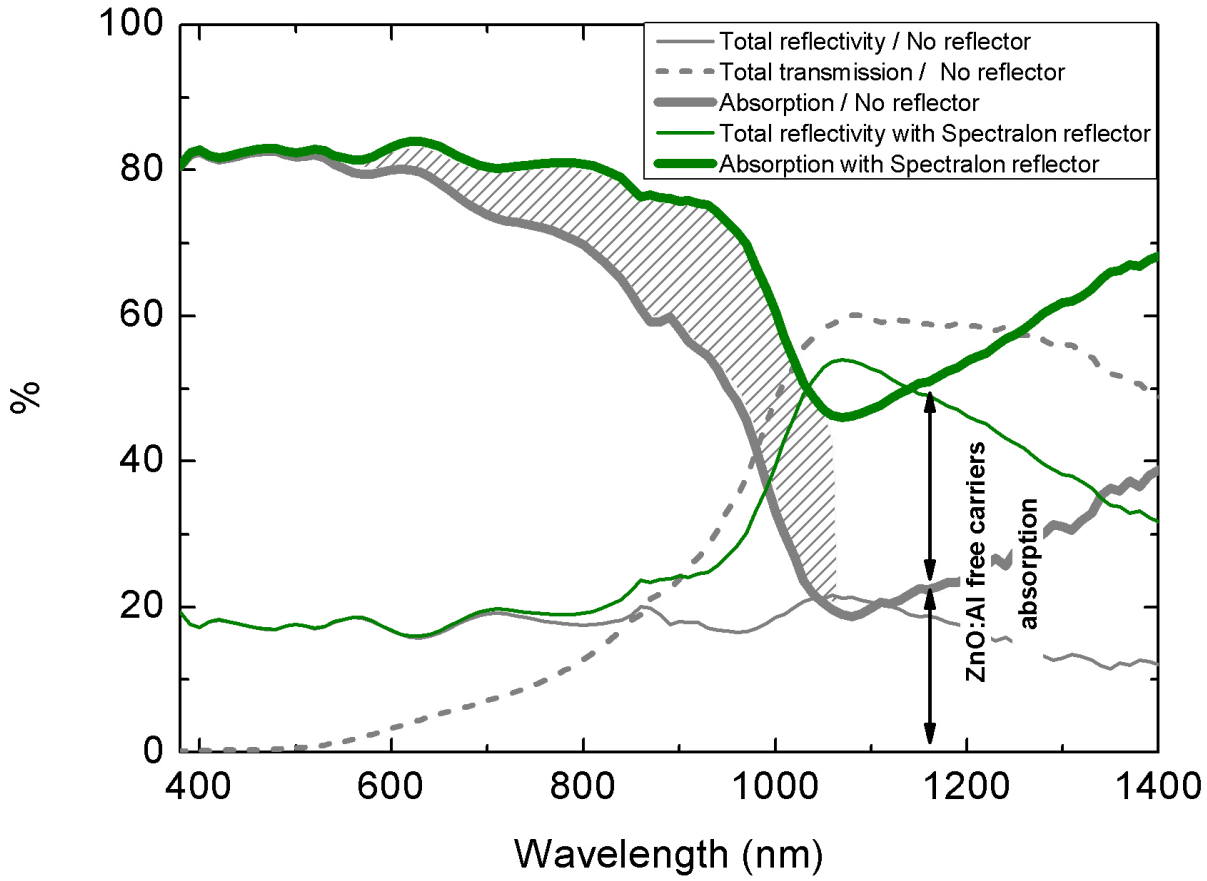

Figure 31. Transmission/Reflection/Absorption for the 200 nm absorber solar cell structure without back reflector (grey curves) and with a Spectralon lambertian back reflector (green curves)

To investigate the region of the solar cell structure where the light absorption occurs, the spectroscopic transmission/reflection/absorption properties of an equivalent material stack are simulated, using the Radiative Transfer Equation (RTE) methodology previously described. The figure 32 compares the simulated absorption of the complete stack with a lambertian back reflector with the experimentally measured absorption from figure 31. Simulation of specific absorption in the 200 nm CIGSe layer is also performed to identify the photons that will contribute to the photocurrent. The lambertian reflector (Spectralon) is taken with a total reflectivity of 91% and full lambertian light scattering.

In the following, the data corresponding to simulations are represented in red, and the data from experiments are in green (figure 32). We see that the simulated absorption of the complete stack $A_{stack} = 1 - R$ curve (red solid line) has a similar aspect as our experimental absorption curve (green solid line), with a stable trend up to λ = 950 nm, and an important absorption after the bandgap. The simulated specific absorption in the CIGSe A_{CIGSe} (red dotted line) shows that the CIGSe layer contribute to the extremely largest part in the absorption of the complete stack. We define the CIGSe absorption factor A_f by the ratio of the specific absorption of the CIGSe A_{CIGSe} with the total absorption of the stack 1-R: $A_f = \frac{A_{CIGSe}}{1-R}$. By multiplying the experimental absorption of the complete stack from figure 31 with this A_f factor, we obtain the experimental estimation of the absorption in the CIGSe in our experimental proof of concept structure (green dotted line). For our experimental 200 nm CIGSe solar cell structure, we observe an absorption in CIGSe higher than 70% up to λ = 800 nm, and higher than 60% up to λ = 900 nm. This curve can be considered as the first order estimation of the External Quantum Efficiency of the solar cell assuming that all generated carriers in the CIGSe are extracted. In comparison, we also plot the simulated specific absorption in the CIGSe layer without any reflector at the back side of the structure (thin red line). After determining the A_f factor that corresponds to the stack without back reflector, it is also possible to calculate the experimental specific absorption in the CIGSe that corresponds to the structure without back reflector (thin green line). We clearly see, in the experimental data (green), that the lambertian back reflector remarkably increases the specific absorption in the CIGSe layer especially in the red and infrared spectral range. In each case (with and without lambertian reflector), the corresponding photocurrent is determined by integrating these data with the A.M. 1.5 solar spectrum. Without any reflector, the calculated photocurrent of the experimental 200 nm CIGSe solar cell structure is $J_{sc} = 15.47 mA.cm^{-2}$.

When the Lambertian back reflector is added, the photocurrent increases up to $J_{sc} = 25.72 mA.cm^{-2}$, which corresponds to a +66 % relative increase. This photocurrent value with lambertian back reflector roughly matches the value that we previously obtained for an etched 2000 nm CIGSe solar cell (part III.5) with a standard Mo back contact. If we assume a 650 mV V_{oc} and a 70% Fill Factor (average values for standard CIGSe solar cells), it corresponds to a conversion efficiency of $\eta = 11.7\%$ (7% in the structure without back reflector). In comparison, the reference non etched 2500 nm thick solar cell from the sample batch that we used in this study had a $\eta = 12.4\%$ standard average efficiency.

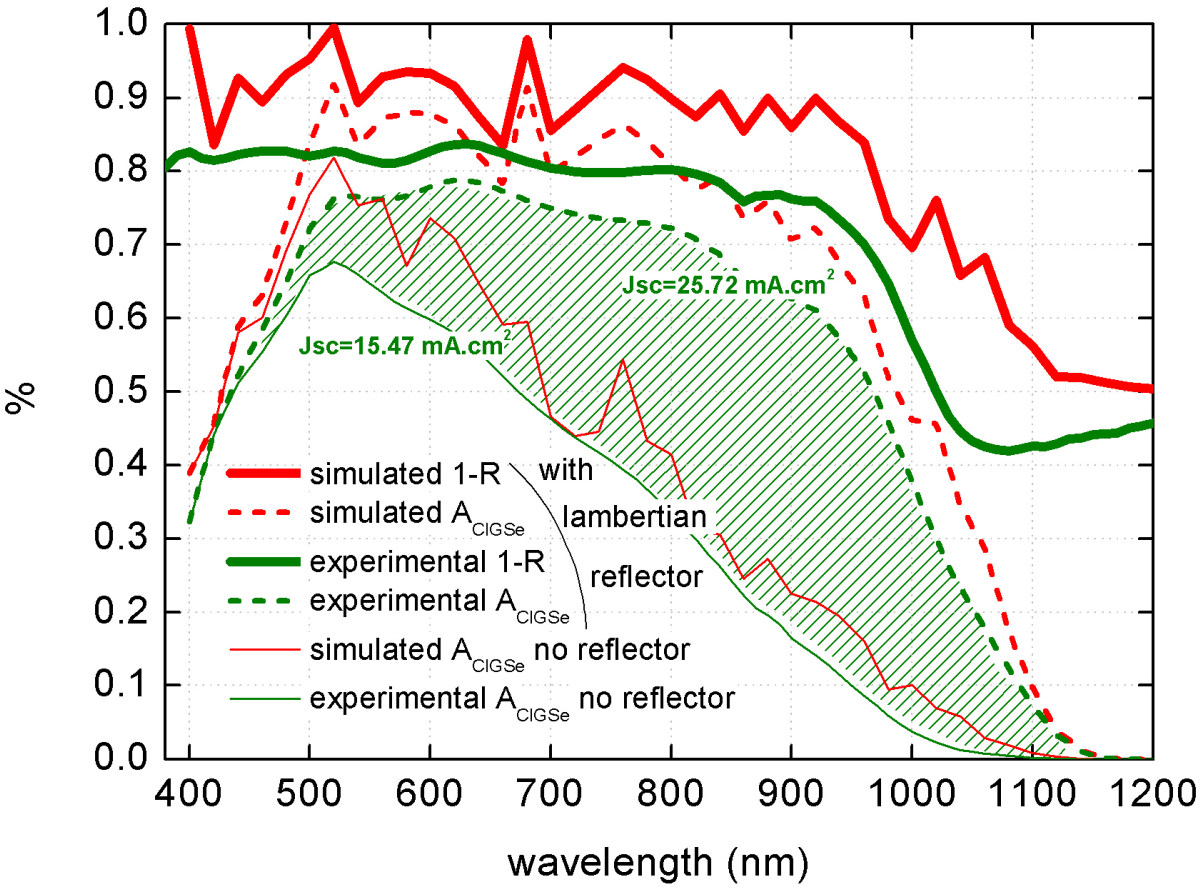

Figure 32. Optical properties of the complete 200 nm CIGSe solar cell structure with a lambertian back reflector: Simulated absorption of the stack (red solid line), simulated specific absorption in the CIGSe (red dotted line), experimentally measured absorption in the complete stack (green solid line), experimentally calculated specific absorption in the CIGSe layer (green dotted line). The simulated specific absorption in the CIGSe without back reflector (thin red line) and experimentally calculated specific absorption in the CIGSe layer without back reflector (thin green line) are also shown in comparison.

For a 200 nm CIGSe absorber, Malmström [28] evaluated from numerical simulations that an increase of the J_{sc} of 10 mA.cm^{-2} was possible with a lambertian back reflector. This is in good agreement with our optical measurements on the experimental solar cell stack (figure 32). However, the absolute value of the J_{sc} calculated in reference [28] was 32.mA.cm^{-2}, whereas in our experiments, we found a much lower value of 25.7 mA.cm^{-2}. This is attributed to the fact that our data are experimental and not simulated, although we relied on simulation results to estimate the photocurrent. Additional parameters such as the absorption coming from the glass, the ZnO:Al spacer and the non ideal lambertian reflector (absorption of about 10%) are taken into account in our J_{sc} value. The fraction of reflected light escaping the structure is also more important when using a ZnO spacer between the CIGSe and the lambertian back reflector as shown figure 28.

V.5.c) Conclusion

Numerical calculations in a single 100 nm CIGSe slab showed that a lambertian back reflector allowed to remarkably enhance the absorption in the layer up to the level of a 1000 nm CIGSe slab, while a 1D Ag mirror was proven insufficient for light trapping in such an ultrathin layer. On the basis of these results, we realized an ultrathin 200 nm CIGSe proof of concept solar cell structure for optical characterizations, and we studied the influence of a lambertian back reflector by performing spectroscopic transmission/reflection/absorption measurements on the device. The lambertian reflector allows to significantly increase the absorption of the structure in the red and infrared spectral regions, leading to an almost constant trend of the absorption curve of the device to the bandgap. The simulation of an equivalent material stack allows calculating the fraction of the absorbed light in the complete structure that is actually absorbed by the CIGSe layer only. Based on these results, we calculated the specific absorption in CIGSe in our experimental 200 nm CIGSe solar cell structure with and without lambertian back reflector. A major increase with the lambertian back reflector is observed especially in the red and infrared spectral region, leading to an increase of the estimated photocurrent of +66 %, from 15.47 mA.cm^{-2} without back reflector to 25.72 mA.cm^{-2} with a lambertian back reflector. From these results, we estimate that the efficiency of the 200 nm solar cell increases from 7% to 11.7% if no electrical losses are considered, which is very close to the reference efficiency of the non-etched thick solar cell (12.4%).

V.6) Chapter Conclusion

In this final Chapter, we investigated the use of alternative back reflectors for very thin absorber and ultrathin absorber CIGSe solar cells. For that matter, we introduced a novel approach by combining chemical etching of the absorber to reduce its thickness, and a lift-off technique that allows to process the back contact of the solar cell at low temperature. With the lift-off of the absorber, it was possible to precisely characterize the chemistry of the Mo/CIGSe interface by X-ray Photoelectron Spectroscopy, and the interface is characterized optically by ellipsometry. We highlighted the formation of an interfacial $MoSe_2$ layer in the substrate, while the analysis of the absorber back revealed no interdiffusion of Mo atoms in the CIGSe.

A set of alternative metals have been characterized on CIGSe back surface both optically and electrically, and Au has been found to be the metal with the highest potential as back contact for very thin absorber CIGSe solar cell; spectroscopic ellipsometry measurements showed that the Au/CIGSe interface has an excellent reflectivity in the absorption spectral region of the CIGSe, and transmission line measurements (TLM) demonstrated that Au forms a low resistive ohmic contact on CIGSe. The effect of a gold (Au) back reflector on the solar cell parameters as a function of the CIGSe thickness has been studied. We observed that the alternative Au back contact allows to significantly enhance the short circuit current of the solar cells when reducing the absorber thickness. This effect is particularly remarkable for sub-micrometer absorbers, and a net increase of $\Delta J_{sc} = 4.5 mA.cm^{-2}$ is observed for a 400 nm CIGSe absorber without degradation of the other parameters of the cell, leading to an absolute efficiency increase of 2.3% (η = 10.2% for Au back contact versus η = 7.9% with standard Mo back contact). This enhancement of the efficiency nicely demonstrates the potential of highly reflective metals in the scope of realizing very thin absorber CIGSe solar cells.

To realize thinner absorber devices, down to 100 nm – 200 nm CIGSe thickness, a more advanced light trapping structure is needed at the back side of the solar cell. We proposed the introduction of a transparent ZnO:Al back contact. Our preliminary results show that it is possible to turn the rectifying ZnO:Al/CIGSe junction with the addition of an interfacial very thin Cu-based buffer layer. Using a transparent back contact allows to consider electrical insulator materials as back reflector in ultrathin absorber CIGSe solar cells.

Optical comparative simulations on a single 100 nm CIGSe slab showed that the addition of a perfect lambertian back reflector at the back side of a CIGSe significantly increases the light absorption in the absorber, up to the level of a 1000 nm CIGSe film, while a flat Ag mirror is proven insufficient at this extreme level of CIGSe thinning. We realized a 200 nm CIGSe solar cell structure with a 200 nm ZnO:Al layer at the back side (spacer), and studied the optical properties of the complete material stack. When a lambertian back reflector (Spectralon) is added on the back side, the analysis of the optical properties of the structure reveals that the absorption is significantly increased in the red and infra-red spectral region with the lambertian reflector. Modeling of an equivalent material stack are performed, and demonstrate that most of the gained absorption comes from an enhanced absorption by the CIGSe. A factor between the light absorbed in the complete stack and the light specifically absorbed in the CIGSe layer is determined from these simulations, which gives the possibility to calculate the spectral response of our solar cell structure based on experimental data; we found that the short circuit current could increase from $J_{sc} = 15.5 mA.cm^{-2}$ without back reflector up to $J_{sc} = 25.7 mA.cm^{-2}$ when adding the Spectralon at the back interface, leading to a calculated efficiency increase from $\eta = 7\%$ to $\eta = 11.7\%$ respectively. This efficiency, obtained for a 200 nm CIGSe solar cell experimental structure, is very close to that of the reference non etched 2500 nm CIGSe solar cell ($\eta = 12.4\%$). Lambertian back reflectors are proven to be the most effective solution to improve the light absorption in an ultrathin absorber CIGSe solar cell.

General Conclusion and Perspectives

Main results

In these three years of research, we investigated the possibility to reduce the indium consumption in the CIGSe technology by significantly reducing the thickness of the CIGSe absorber down to an “ultrathin” layer thickness. This work was done in the frame of the Ultracis project supported by the French Research Agency (ANR). The literature from the past decade shows that an increasing attention has been brought in reducing the absorber thickness both in the CIGSe and CdTe technology to limit the consumption of rare and expensive elements. Most of the studies have been performed by adapting the material deposition process to shorter deposition times, and so thinner layer. This technique presents the advantage of direct applicability to industrial process, however the induced changes in the CIGSe absorber and standard deposition process are limiting the possibilities of upstream researches on ultrathin absorber solar cells. In this study, we decided to introduce a novel approach to study well controlled very thin and ultrathin CIGSe films.

In a preliminary study (Chapter II), we modeled by numerical tools the influence of reducing the absorber thickness in a well controlled CIGSe solar cell, from the reference 2500 nm absorber thickness down to 100 nm absorber thickness. For that matters, we defined the parameters of a “state of the art” reference solar cell from experimental and literature data. The behavior of this solar cell is found to be very close to experimental results obtained on a standard CIGSe solar cell prepared at Würth Solar and ZSW in Germany; therefore, the parameters that we used in the model are taken as “baseline” parameters for further simulations. When simulating the reduction of the absorber thickness, we clearly identify two regimes:

- the first one is the reduction of the thickness from 2500 nm (reference) down to 500 nm; the short circuit current (J_{sc}) is the only parameter that is affected by the thickness reduction, from 28 mA.cm^{-2} (2500 nm absorber reference) to 20 mA.cm^{-2} (500 nm absorber), and the Open Circuit Voltage (V_{oc})and Fill Factor (FF) remain stable at

about 650 mV and 72% respectively. Consequently, the efficiency (Eff) undergoes a moderate decrease, from 14% to about 11%. The reduction of the J_{sc} is attributed to a combination of increased back contact recombination, as observed by the increase of back contact recombination current, and to a light absorption limitation due to the thickness reduction of the active layer (CIGSe).

- In a second regime, from 500 nm CIGSe down to 100 nm, the absorber is fully depleted which blocks the back contact recombination; in this case, the J_{sc} is almost only dependent on the absorption of the CIGSe. The material is however transparent to the majority of red and infrared photons due to its extreme thinning, and the Jsc is reduced down to 12 $mA.cm^{-2}$ for a 100 nm absorber. The V_{oc} is also limited when the CIGSe thickness becomes smaller than the space charge region width (W), which limits the quasi Fermi level splitting. Consequently, the efficiency drops down to less than 4% for a 100 nm absorber.

To overcome these issues we proposed to engineer both the front and the back interfaces of the CIGSe solar cell. Optical simulation on a 500 nm absorber device shows that the use of a wide gap buffer layer like ZnS in replacement of CdS allows to significantly increase the absorption in CIGSe in the 350-550 nm spectral range (+6 % absolute absorption increase). More importantly, the replacement of the low reflective Mo back contact by a highly reflective Au back contact leads theoretically to an absolute absorption increase in the CIGSe of +7%, especially in the red and infrared spectral ranges. Combined with an anti reflection coating (ARC), we showed that it is theoretically possible to increase the J_{sc} of the solar cell up to 33.80 $mA.cm^{-2}$ in a 500 nm CIGSe solar cell. The problem of back contact recombination is also addressed, by tuning the energy band diagram. We show that in the Anderson model, a high work function metal such as Pt is required to form an ohmic contact on CIGSe, and that the introduction of an interfacial electron blocking layer helps to suppress the back surface recombination.

For 100 nm ultrathin CIGSe solar cells, conventional metal reflectors have been found insufficient; we proposed to use a lambertian back reflector to increase to the maximum the optical path of the light through the absorber, along with a wide gap p-doped semi conductor contact that would allow complete splitting of the quasi Fermi levels and thus solve the V_{oc} issue. We demonstrate that in these ideal conditions, it is theoretically possible to increase the efficiency of a 100 nm CIGSe solar cell up to the level of a standard 2500 nm solar cell.

In Chapter III, we used a novel approach to experimentally reduce the absorber thickness by using a chemical HBr/Br_2 etching of the CIGSe. This technique allows to precisely monitor the remaining material thickness. Etching experiments and X ray Photoelectron Spectroscopy (XPS) have been carried out at Institut Lavoisier and we demonstrated that the surface chemical composition is almost not affected by etching. Similarly, X-ray diffraction and Raman spectroscopy showed that etching had minor influence on the CIGSe crystalline structure and bulk composition. Observation of the CIGSe etched surfaces by Scanning Electron Microscopy (SEM) revealed that etching had a dramatic smoothing effect; this was confirmed by Atomic Force Microscopy (AFM) which showed a decrease of the Root Mean Square (RMS) of the surface from about RMS = 200-250 nm for non etched absorbers down to about RMS = 40-50 nm for etched absorbers. Optical characterization of the absorbers showed an increased specular reflectivity of the surface after etching, and photoluminescence characterization highlighted a bandgap shift through the absorber, which is attributed to the Ga-grading in the CIGSe.

Solar cells with different absorber thicknesses from the reference 2500 nm down to 200 nm CIGSe have been realized in standard conditions. Current-Voltage characterization showed very similar trends to what was previously simulated, with two distinct regimes from 2500 nm to 500 nm absorber thickness, and from 500 nm to 200 nm absorber thickness. A solar cell of 500 nm absorber thickness with an efficiency of 10.3% has been achieved, starting from a 13.7 % reference thick absorber solar cell. Since the etching of the CIGSe has a strong smoothing effect, we also investigated on the influence of the surface roughness on the Jsc decrease that is observed when the absorber thickness is not varied. We proposed an interpretation based on the influence that the roughness may have on the effective width of the space charge region.

In Chapter IV, we focused on possible engineering of the front interface of very thin absorber CIGSe solar cells to increase light absorption in CIGSe. We first implemented in experimental devices the solutions that were proposed in Chapter II. The CdS buffer layer has been successfully replaced by a ZnS buffer, which led to substantial increase of the J_{sc} by an increased light absorption in the 350-550 nm spectral range. The gain is however partly offset for sub-micrometer absorbers (< 800 nm in our experiments) by the decrease of the V_{oc} and FF, and optimizations of the contact are still needed. Similarly to what has been done in the amorphous silicon solar cells field, we developed a high haze ZnO:Al by HCl etching for light scattering at the front interface of the solar cell. Moreover, we also increased the light

scattering by electrodeposing ZnO nanorods on top of the ZnO:Al window layer, which led to a significant increase of the light diffusion properties of the films. In both cases however, the optical index difference between ZnO and CIGSe led to a strong decrease of the light scattering angle, and the only effect that is observed in antireflection at the air/ZnO interface. Compared to standard MgF_2 ARC, the effect on the light absorption of textured ZnO:Al is even slightly higher. By texturing the front ZnO:Al layer, we observed a relative increase of +14% in the J_{sc} compared to flat standard ZnO:Al, and an increase of the efficiency from 8.3% to 9.6%. For a 500 nm CIGSe solar cell, the ZnO nanorods on ZnO:Al had a similar ARC effect. Their very high haze factor could however be useful for other applications.

In the last Chapter, we investigated the replacement of the Mo back contact by an alternative material to improve the efficiency of very thin absorber CIGSe solar cells (down to about 400 nm), but also for ultrathin absorbers (200 nm). For that, we developed a new technique that is based on the combination of lift-off of the CIGSe from its original Mo substrate, and chemical etching of both the front and the back side of the absorber. The lift-off process allowed us to consider alternative materials as back contact, that were incompatible with the CIGSe high temperature deposition. Thanks to this approach, it was also possible to precisely characterize the chemical composition of the back interface of the solar cell; XPS observations indicated the formation of the well known $MoSe_2$ interfacial layer, but no diffusion of the Mo atoms in the CIGSe has been observed. We performed an ellipsometric analysis of both the CIGSe back surface and the substrate after lift-off to determine the complex refractive indexes of both samples, and we noticed that the reflectivity at the real CIGSe/Mo interface (therefore including the $MoSe_2$ layer) is very poor. We then calculated the reflectivity that can be achieved with alternative metals: Au, Ag, Cu, Ni, Pt and Al. Au, Ag, Al and Cu significantly improve the reflectivity of the back interface in a CIGSe solar cell, but the nature of the CIGSe/metal being of high importance for an efficient solar cell device, these metals were characterized on CIGSe using Transmission Line Measurements (TLM). From the TLM data, we concluded that Au and Pt form a low resistive ohmic contact on CIGSe, which is consistent in the Anderson model with their relatively high work function. Since Au combines both a good electrical compatibility with CIGSe, and a very high reflectivity, we realized a serie of CIGSe solar cells with different absorber thicknesses, down to 300 nm, and compared the photovoltaic parameters between a standard Mo back contact and an Au alternative back contact. We found that the Au back contact allows to significantly increase the light absorption of low energy photons in the CIGSe, and thus the J_{sc} of solar cells especially when

the thickness of the absorber is reduced to the sub-micrometer scale, without affecting neither the V_{oc} nor the FF. For a very thin 400 nm CIGSe solar cell, we achieved an absolute efficiency increase of + 2.3%, from $\eta = 7.9\%$ to $\eta = 10.2\%$.

We also investigated the feasibility of alternative transparent back contact using ZnO:Al, by introducing a Cu based buffer layer at the ZnO:Al/CIGSe interface. We demonstrated that it was possible to turn the rectifying junction into an ohmic contact, and the application on a solar cell shows a suppression of the double diode effect in the J-V curve. These results are however very preliminary and the efficiency of the solar cells remains at a low level.

In the final part of our work, we studied the feasibility of an ultrathin CIGSe solar cell device, by focusing on the optical absorption in the CIGSe layer. Simulations performed by our colleagues of the Institut d'Optique on a 100 nm CIGSe single layer showed that the addition of a lambertian back reflector at the back side allows to reflect and diffuse light very efficiently in the layer, which increases the absorption of this 100 nm slab up to the level of a 1000 nm CIGSe film. We realized a proof of concept 200 nm CIGSe solar cell structure that we characterized by transmission/reflection/absorption spectroscopy, and studied the influence of a lambertian back reflector (Spectralon) at the back side of the structure. We observed a major enhancement of the absorption of the structure for low energy photons, and compared our experimental data with simulated data from an equivalent material stack. It was possible to estimate for our experimental structure the ratio of light that is specifically absorbed in the CIGSe film, and so the calculated spectral response. We estimated from these data that the addition of a lambertian back reflector on the structure increases the J_{sc} from $J_{sc} = 15.47 mA.cm^2$ to $J_{sc} = 25.72 mA.cm^2$, leading to a spectacular increase of the efficiency from 7% to 11.7% if no other losses are considered, which is comparable to the reference efficiency of the standard 2500 nm CIGSe solar cell (12.4% in this study). Based on these simulations and experiments, lambertian back reflectors are found to be one of the most effective way to achieve a near to perfect light trapping in an ultrathin absorber layer, where conventional metals are insufficient.

Perspectives

For very thin absorber solar cells, down to 400 nm absorber thickness, we demonstrated with several techniques that it was possible to significantly increase the efficiency of the solar cell. The next step would be to combine all these techniques (ZnS, ARC/Textured ZnO:Al, and reflective back contact) in order to match the efficiency of a reference thick solar cell. Experiments in this direction are currently being carried out in our laboratory. Moreover, using a less expensive metal than Au as a back contact, such as Cu, is required to meet the low cost expectations of the industry. It will be therefore of great interest to find a compatible barrier layer between the CIGSe and the metal that would prevent the diffusion of metal atoms in the absorber.

We also believe that the results from this study pave the way for further investigations in the field of ultrathin CIGSe solar cells. For future development, we think that the main challenge is to realize a working device with an ultrathin absorber thickness, less than 200 nm, with an efficiency comparable to thick absorber solar cells. To achieve this, it is very important to improve the control of the chemical etching process, both in terms of surface roughness and film thickness. Our partners from Laboratoire de Photonique and Nanostructures recently achieved an impressive 6 nm surface RMS by etching CIGSe by a mechano-chemical process, which will be applied for very precise etching of CIGSe films down to 100 nm. More researches are also needed to improve the electrical properties of the back contact, and achieve wide gap transparent hole-ohmic contact at this interface. This would not only increase the voltage of ultrathin CIGSe solar cells, but also allow to use a lambertian back reflector which has been demonstrated in this study as extremely effective for light trapping in ultrathin absorbers. Another light trapping technique based on plasmonic resonators, which is not mentioned in this thesis, is also being developed by our partners from “Laboratoire de Photonique and Nanostructures”. Simulations showed that a very important light absorption in CIGSe can be achieved with such a structure, and its application to ultrathin solar cells is currently being carried out in the frame of two PhD Thesis.

Finally, another objective is to make very thin and ultrathin CIGSe solar cells compatible with an industrial process. Directly growing ultrathin CIGSe absorber on alternative substrates without degradation of the absorber or electric contact quality is highly desired.

References

1. Jackson, P. *et al.* New world record efficiency for Cu(In,Ga)Se_2 thin film solar cells beyond 20%. *Progress in Photovoltaics: Research and Applications* **19**, 894–897 (2011).

2. Powalla, M. *et al.* Large-area CIGS modules: Pilot line production and new developments. *Solar Energy Materials and Solar Cells* **90**, 3158–3164 (2006).

3. Fthenakis, V. Sustainability of photovoltaics: The case for thin-film solar cells. *Renewable and Sustainable Energy Reviews* **13**, 2746–2750 (2009).

4. Todorov, T. K., Reuter, K. B. & Mitzi, D. B. High Efficiency Solar Cell with Earth Abundant Liquid Processed Absorber. *Advanced Materials* **22**, E156–E159 (2010).

5. Paire, M., Lombez, L., Guillemoles, J.-F. & Lincot, D. Toward microscale Cu(In,Ga)Se2 solar cells for efficient conversion and optimized material usage: Theoretical evaluation. *Journal of Applied Physics* **108**, 034907–034907–7 (2010).

6. Repins, I. *et al.* 19·9% efficient ZnO/CdS/CuInGaSe_2 solar cell with 81·2% fill factor. *Progress in Photovoltaics: Research and Applications* **16**, 235–239 (2008).

7. Stanbery, B. J. Copper indium selenides and related materials for photovoltaic devices. *Critical Reviews in Solid State and Material Sciences* **27**, 73–117 (2002).

8. Pianezzi, F. *et al.* Electronic properties of Cu(In,Ga)Se_2 solar cells on stainless steel foils without diffusion barrier. *Progress in Photovoltaics: Research and Applications* doi:10.1002/pip.1247

9. Chirilă, A. *et al.* Highly efficient Cu(In,Ga)Se_2 solar cells grown on flexible polymer films. *Nat Mater* **10**, 857–861 (2011).

10. Scofield, J. H., Duda, A., Albin, D., Ballard, B. & Predecki, P. Sputtered molybdenum bilayer back contact for copper indium diselenide-based polycrystalline thin-film solar cells. *Thin Solid Films* **260**, 26–31 (1995).

11. Kohara, N., Nishiwaki, S., Hashimoto, Y., Negami, T. & Wada, T. Electrical properties of the Cu(In,Ga)Se_2/ $MoSe_2$/Mo structure. *Solar Energy Materials and Solar Cells* **67**, 209–215 (2001).

12. Wada, T., Kohara, N., Negami, T. & Nishitani, M. Chemical and structural characterization of Cu(In,Ga)Se_2/Mo interface in Cu(In,Ga)Se2 solar cells. *JAPANESE JOURNAL OF APPLIED PHYSICS PART 2 LETTERS* **35**, 1253–1256 (1996).

13. Nishiwaki, S., Kohara, N., Negami, T. & Wada, T. $MoSe_2$ layer formation at Cu(In,Ga)Se_2/Mo Interfaces in High Efficiency Cu($In_{1-x}Ga_x$)Se_2 Solar Cells. *Japanese Journal of Applied Physics* **37**, L71–L73 (1998).

14. Thornton, J. A. Reactive sputtered copper indium diselenide films for photovoltaic applications. *Journal of Vacuum Science & Technology A: Vacuum, Surfaces, and Films* **2**, 307 (1984).

15. Nakada, T., Migita, K., Niki, S. & AkioKunioka Microstructural Characterization for Sputter-Deposited CuInSe Films and Photovoltaic Devices. *Japanese Journal of Applied Physics* **34**, 4715–4721 (1995).

16. Lincot, D. *et al.* Chalcopyrite thin film solar cells by electrodeposition. *Solar Energy* **77**, 725–737 (2004).

17. Taunier, S. *et al.* Cu(In,Ga)(S,Se)$_2$ solar cells and modules by electrodeposition. *Thin Solid Films* **480-481**, 526–531 (2005).

18. Kapur, V. K., Bansal, A., Le, P. & Asensio, O. I. Non-vacuum processing of CuIn1-xGaxSe2 solar cells on rigid and flexible substrates using nanoparticle precursor inks. *Thin Solid Films* **431-432**, 53–57 (2003).

19. Contreras, M. A. *et al.* Optimization of CBD CdS process in high-efficiency Cu(In,Ga)Se2-based solar cells. *Thin Solid Films* **403-404**, 204–211 (2002).

20. Shockley, W. & Read Jr, W. Statistics of the recombinations of holes and electrons. *Physical Review* **87**, 835 (1952).

21. Hall, R. N. Electron-hole recombination in germanium. *Physical Review* **87**, 387 (1952).

22. Shafarman, W. N. *et al.* Effect of reduced deposition temperature, time, and thickness on Cu(InGa)Se$_2$ films and devices. , *Conference Record of the Twenty-Sixth IEEE Photovoltaic Specialists Conference, 1997* 331–334 (1997).doi:10.1109/PVSC.1997.654095

23. Negami, T., Nishiwaki, S., Hashimoto, Y., Kohara, N. & Wada, T. Effect of the absorber thickness on performance of Cu(In,Ga)Se$_2$ solar cells. *Proceedings of the 2nd WCPEC, Vienna* 1181–1184 (1998).

24. K. Ramanathan *et al.* Processing and Properties of Sub-Micron CIGS Solar Cells. *Conference Record of the 2006 IEEE 4th World Conference on Photovoltaic Energy Conversion* **1**, 380–383 (2006).

25. Delahoy, A. & Chen, L. Advanced CIGS Photovoltaic Technology. (2005).

26. Dhere, N. High Throughput, Low Toxic Processing of Very Thin, High Efficiency CIGSS Solar Cells. (2009).

27. Lundberg, O., Bodegaard, M., Malmström, J. & Stolt, L. Influence of the Cu (In, Ga) Se$_2$ thickness and Ga grading on solar cell performance. *Progress in Photovoltaics: Research and Applications* **11**, 77–88 (2003).

28. Malmström, J. On generation and recombination in Cu (In, Ga) Se$_2$ thin-film solar cells, PhD Thesis. (2005).

29. Karpov, V. G., Cooray, M. L. C. & Shvydka, D. Physics of ultrathin photovoltaics. *Applied Physics Letters* **89**, 163518 (2006).

30. Gloeckler, M. & Sites, J. R. Potential of submicrometer thickness Cu(In,Ga)Se_2 solar cells. *Journal of Applied Physics* **98**, 103703 (2005).

31. Wei, S. H., Zhang, S. & Zunger, A. Effects of Ga addition to CuInSe on its electronic, structural, and defect properties. *Applied physics letters* **72**, 3199 (1998).

32. Dullweber, T. *et al.* Back surface band gap gradings in Cu(In,Ga)Se_2 solar cells. *Thin Solid Films* **387**, 11–13 (2001).

33. Rau, U. Tunneling-enhanced recombination in Cu(In,Ga)Se_2 heterojunction solar cells. *Applied Physics Letters* **74**, 111–113 (1999).

34. Birkmire, R. W. & McCandless, B. E. Specular $CuInSe_2$ films for solar cells. *Applied Physics Letters* **53**, 140–141 (1988).

35. Canava, B., Guillemoles, J. F., Vigneron, J., Lincot, D. & Etcheberry, A. Chemical elaboration of well defined Cu(In,Ga)Se_2 surfaces after aqueous oxidation etching. *Journal of Physics and Chemistry of Solids* **64**, 1791–1796 (2003).

36. Shafarman, B. Thin Cu(InGa)Se2 Solar Cells. Visual Presentation. Institute of Energy Conversion, University Center of Excellence for Photovoltaic Research and Education (2006).

37. Plotnikov, V., Kwon, D. H., Wieland, K. & Compaan, A. 10% efficiency solar cells with 0.5 μm of CdTe. *Photovoltaic Specialists Conference (PVSC), 2009 34th IEEE* 001435–001438 (2009).

38. Plotnikov, V. *et al.* Thin-film CdTe cells: Reducing the CdTe. *Thin Solid Films* **519**, 7134–7137 (2011).

39. Bai, Z., Yang, J. & Wang, D. Thin film CdTe solar cells with an absorber layer thickness in micro-and sub-micrometer scale. *Applied Physics Letters* **99**, 143502 (2011).

40. Burgelman, M., Nollet, P. & Degrave, S. Modelling polycrystalline semiconductor solar cells. *Thin Solid Films* **361-362**, 527–532 (2000).

41. Čampa, A. *et al.* The potential of textured front ZnO and flat TCO/metal back contact to improve optical absorption in thin Cu(In,Ga)Se_2 solar cells. *Thin Solid Films* **515**, 5968–5972 (2007).

42. Gloeckler, M., Fahrenbruch, A. L. & Sites, J. R. Numerical modeling of CIGS and CdTe solar cells: setting the baseline. *Proceedings of 3rd World Conference on Photovoltaic Energy Conversion, 2003* **1**, 491–494 Vol.1 (2003).

43. Repins, I. *et al.* Required material properties for high-efficiency CIGS modules. *Proc. SPIE* **7409**, 74090M

44. Adachi, S. *Optical properties of crystalline and amorphous semiconductors: Materials and fundamental principles*. (Kluwer Academic Pub: 1999).

45. Hajjar, J. *Modélisation de la photoluminescence d'un empilement planaire de semiconducteurs*. Master Thesis, IRDEP(2010).

46. Naghavi, N. *et al.* Buffer layers and transparent conducting oxides for chalcopyrite Cu(In,Ga)(S,Se)$_2$ based thin film photovoltaics: present status and current developments. *Progress in Photovoltaics: Research and Applications* **18**, 411–433 (2010).

47. Hariskos, D. *et al.* The Zn(S,O,OH)/ZnMgO buffer in thin film Cu(In,Ga)(Se,S)2 based solar cells part II: Magnetron sputtering of the ZnMgO buffer layer for in line coevaporated Cu(In,Ga)Se$_2$ solar cells. *Progress in Photovoltaics: Research and Applications* **17**, 479–488 (2009).

48. Hubert, C. *et al.* The Zn(S,O,OH)/ZnMgO buffer in thin film Cu(In,Ga)(S,Se)$_2$ based solar cells part I: Fast chemical bath deposition of Zn(S,O,OH) buffer layers for industrial application on Coevaporated Cu(In,Ga)Se$_2$ and electrodeposited CuIn(S,Se)$_2$ solar cells. *Progress in Photovoltaics: Research and Applications* **17**, 470–478 (2009).

49. Palik, E. D. *Handbook of optical constants of solids II*. **2**, (Academic press: 1991).

50. Sze, S. M. & Ng, K. K. *Physics of semiconductor devices*. (John Wiley and Sons: 2007).

51. Anderson, R. L. Germanium-Gallium Arsenide Heterojunctions [Letter to the Editor]. *IBM Journal of Research and Development* **4**, 283–287 (1960).

52. Michaelson, H. B. Relation Between an Atomic Electronegativity Scale and the Work Function. *IBM Journal of Research and Development* **22**, 72–80 (1978).

53. Moons, E., Engelhard, T. & Cahen, D. Ohmic contacts to p-CuInSe$_2$ crystals. *Journal of Electronic Materials* **22**, 275–280 (1993).

54. Devaney, W. E. & Mickelsen, R. A. Vacuum deposition processes for CuInSe$_2$ and CuInGaSe2 based solar cells. *Solar Cells* **24**, 19–26

55. Noufi, R. & Dick, J. Compositional and electrical analysis of the multilayers of a CdS/CuInSe2 solar cell. *Journal of Applied Physics* **58**, 3884–3887 (1985).

56. Dimmler, B. & Schock, H. W. Scaling up of CIS technology for thin film solar modules. *Progress in Photovoltaics: Research and Applications* **4**, 425–433 (1996).

57. Canava, B., Vigneron, J., Etcheberry, A., Guillemoles, J. . & Lincot, D. High resolution XPS studies of Se chemistry of a Cu(In, Ga)Se2 surface. *Applied Surface Science* **202**, 8–14 (2002).

58. William. N. Shafarman, Rongxue S. Huang & Scott H. Stephens Characterization of Cu(InGa)Se2 Solar Cells using Etched Absorber Layers. *Conference Record of the 2006 IEEE 4th World Conference on Photovoltaic Energy Conversion* **1**, 420–423 (2006).

59. Paulson, P. D., Birkmire, R. W. & Shafarman, W. N. Optical characterization of CuIn$_{1-x}$Ga$_x$Se$_2$ alloy thin films by spectroscopic ellipsometry. *Journal of Applied Physics* **94**, 879 (2003).

60. Hildebrant, T. *Etude de couches minces de CIGS: determination de la cinétique d'attaque, caractérisation de la surface et de piles*. Master Thesis, University of Versailles (ILV) (2009).

61. Bouttemy, M. *et al.* Thinning of Cu(In,Ga)Se_2 solar cells: Part I: Chemical processing in acidic bromine solutions. *Thin Solid Films* (2011).

62. Poortmans, J. & Arkhipov, V. *Thin film solar cells: fabrication, characterization and applications*. **18**, (John Wiley & Sons Inc: 2006).

63. Swanepoel, R. Determination of the thickness and optical constants of amorphous silicon. *Journal of Physics E: Scientific Instruments* **16**, 1214–1222 (1983).

64. Krc, J. *et al.* Optical and electrical modeling of Cu(In,Ga)Se_2 solar cells. *Optical and quantum electronics* **38**, 1115–1123 (2006).

65. Lundberg, O., Edoff, M. & Stolt, L. The effect of Ga-grading in CIGS thin film solar cells. *Thin Solid Films* **480-481**, 520–525 (2005).

66. Meakin, J. D. Status of $CuInSe_2$ solar cells. *Society of Photo-Optical Instrumentation Engineers (SPIE) Conference Series* **543**, 108–118 (1985).

67. Gärtner, W. W. Depletion-layer photoeffects in semiconductors. *Physical Review* **116**, 84 (1959).

68. Erfurth, F. *et al.* Mo/Cu(In, Ga)Se_2 back interface chemical and optical properties for ultrathin CIGSe solar cells. *Applied Surface Science* doi:10.1016/j.apsusc.2011.11.037

69. Decock, K., Lauwaert, J. & Burgelman, M. Characterization of graded CIGS solar cells. *Energy Procedia* **2**, 49–54 (2010).

70. Kushiya, K. Development of Cu(InGa)Se2-based thin-film PV modules with a Zn (O, S, OH) $_x$ buffer layer. *Solar energy* **77**, 717–724 (2004).

71. Nakada, T., Mizutani, M., Hagiwara, Y. & Kunioka, A. High-efficiency Cu (In, Ga) Se_2 thin-film solar cells with a CBD-ZnS buffer layer. *Solar energy materials and solar cells* **67**, 255–260 (2001).

72. Ennaoui, A. *et al.* Highly-efficient Cd-free $CuInS_2$ thin-film solar cells and mini-modules with Zn (S, O) buffer layers prepared by an alternative chemical bath process. *Progress in Photovoltaics: Research and Applications* **14**, 499–511 (2006).

73. Contreras, M., Nakada, T., Hongo, M., Pudov, A. & Sites, J. ZnO/ZnS (O, OH)/Cu (In, Ga)Se_2/Mo solar cell with 18.6% efficiency. *Photovoltaic Energy Conversion, 2003. Proceedings of 3rd World Conference on* **1**, 570–573 (2003).

74. Bhattacharya, R. N., Contreras, M. A. & Teeter, G. 18.5% copper indium gallium diselenide (CIGS) device using single-layer, chemical-bath-deposited ZnS (O, OH). *Japanese journal of applied physics* **43**, 1475 (2004).

75. Kluth, O. *et al.* Texture etched ZnO:Al coated glass substrates for silicon based thin film solar cells. *Thin Solid Films* **351**, 247–253 (1999).

76. Kambe, M. *et al.* Improvement of light-trapping effect on microcrystalline silicon solar cells by using high haze transparent conductive oxide films. *Proceedings of 3rd World Conference on Photovoltaic Energy Conversion, 2003* **2**, 1812–1815 Vol.2 (2003).

77. Konagai, M., Hiza, S., Ohki, K. & Yamada, A. 0.5 μm-thick μc-Si solar cell grown by photo-CVD on highly textured SnO_2. *Proceedings of 3rd World Conference on Photovoltaic Energy Conversion, 2003* **2**, 1605–1610 Vol.2 (2003).

78. ASAHI website http://www.agc.com/english/csr/environment/products/positive_seihin1.html.

79. Könenkamp, R., Word, R. C. & Godinez, M. Ultraviolet Electroluminescence from ZnO/Polymer Heterojunction Light-Emitting Diodes. *Nano Lett.* **5**, 2005–2008 (2005).

80. Willander, M. *et al.* Zinc oxide nanorod based photonic devices: recent progress in growth, light emitting diodes and lasers. *Nanotechnology* **20**, 332001 (2009).

81. Umar, A., Al-Hajry, A., Hahn, Y. & Kim, D. Rapid synthesis and dye-sensitized solar cell applications of hexagonal-shaped ZnO nanorods. *Electrochimica Acta* **54**, 5358–5362 (2009).

82. Suh, D. I. *et al.* The fabrication and characterization of dye-sensitized solar cells with a branched structure of ZnO nanowires. *Chemical physics letters* **442**, 348–353 (2007).

83. Law, M., Greene, L. E., Johnson, J. C., Saykally, R. & Yang, P. Nanowire dye-sensitized solar cells. *Nature materials* **4**, 455–459 (2005).

84. Tena-Zaera, R., Elias, J. & Lévy-Clément, C. ZnO nanowire arrays: Optical scattering and sensitization to solar light. *Applied Physics Letters* **93**, 233119 (2008).

85. Woosuk Jun, Hong Tak Kim, Dongwook Kim & Chinho Park Optical and electrical properties of ZnO thin films synthesized by sol-gel method for the application in three-dimensional junction photovoltaics. *2009 34th IEEE Photovoltaic Specialists Conference (PVSC)* 000629–000631 (2009).doi:10.1109/PVSC.2009.5411605

86. Jehl, Z. *et al.* Electrodeposition of ZnO nanorod arrays on ZnO substrate with tunable orientation and optical properties. *Nanotechnology* **21**, 395603 (2010).

87. CLAPHAM, P. B. & HUTLEY, M. C. Reduction of Lens Reflexion by the Moth Eye Principle. *Nature* **244**, 281–282 (1973).

88. Southwell, W. H. Pyramid-array surface-relief structures producing antireflection index matching on optical surfaces. *J. Opt. Soc. Am. A* **8**, 549–553 (1991).

89. Onoki, F. & Kamiya, H. *Method for coating anti-reflection film on surface of optical material*. (Google Patents: 1978).

90. Jager, K. & Zeman, M. A scattering model for surface-textured thin films. *Applied Physics Letters* **95**, 171108–171108–3 (2009).

91. Simonetti, F. Multiple scattering: The key to unravel the subwavelength world from the far-field pattern of a scattered wave. *Physical Review E* **73**, 036619 (2006).

92. Kluth, O. *et al.* Texture etched Al-doped ZnO: a new material for enhanced light trapping in thin film solar cells. , *Conference Record of the Twenty-Sixth IEEE Photovoltaic Specialists Conference, 1997* 715–718 (1997). doi:10.1109/PVSC.1997.654189

93. Krč, J., Zeman, M., Kluth, O., Smole, F. & Topič, M. Effect of surface roughness of ZnO: Al films on light scattering in hydrogenated amorphous silicon solar cells. *Thin Solid Films* **426**, 296–304 (2003).

94. Müller, J., Rech, B., Springer, J. & Vanecek, M. TCO and light trapping in silicon thin film solar cells. *Solar Energy* **77**, 917–930 (2004).

95. Ruske, F., Jacobs, C., Sittinger, V., Szyszka, B. & Werner, W. Large area ZnO: Al films with tailored light scattering properties for photovoltaic applications. *Thin Solid Films* **515**, 8695–8698 (2007).

96. Krč, J., Zeman, M., Smole, F., Metselaar, J. & Topič, M. Analysis of light scattering in a-Si: H-based solar cells with rough interfaces. *Solar energy materials and solar cells* **74**, 401–406 (2002).

97. Zeman, M. Advanced amorphous silicon solar cell technologies. *Thin Film Solar Cells* 173–236 (2006).

98. Berginski, M. *et al.* The effect of front ZnO:Al surface texture and optical transparency on efficient light trapping in silicon thin-film solar cells. *Journal of Applied Physics* **101**, 074903–074903–11 (2007).

99. Söderström, T., Haug, F.-J., Niquille, X. & Ballif, C. TCOs for nip thin film silicon solar cells. *Progress in Photovoltaics: Research and Applications* **17**, 165–176 (2009).

100. Krč, J., Smole, F. & Topič, M. Potential of light trapping in microcrystalline silicon solar cells with textured substrates. *Progress in Photovoltaics: Research and Applications* **11**, 429–436 (2003).

101. Frammelsberger, W. *et al.* Effects of TCO surface texture on light absorption in thin-film silicon solar cells. *Proceedings of the 16th European Photovoltaic Solar Energy Conference, Glasgow, UK* 389–392 (2000).

102. Baxter, J. B. & Aydil, E. S. Nanowire-based dye-sensitized solar cells. *Applied Physics Letters* **86**, 053114–053114 (2005).

103. Martinson, A. B. F., Elam, J. W., Hupp, J. T. & Pellin, M. J. ZnO nanotube based dye-sensitized solar cells. *Nano letters* **7**, 2183–2187 (2007).

104. Lee, Y.-J., Ruby, D. S., Peters, D. W., McKenzie, B. B. & Hsu, J. W. P. ZnO Nanostructures as Efficient Antireflection Layers in Solar Cells. *Nano Letters* **8**, 1501–1505 (2008).

105. Aé, L. *et al.* ZnO nanorod arrays as an antireflective coating for $Cu(In,Ga)Se_2$ thin film solar cells. *Progress in Photovoltaics: Research and Applications* **18**, 209–213 (2010).

106. Siebentritt, S. Alternative buffers for chalcopyrite solar cells. *Solar energy* **77**, 767–775 (2004).

107. Naghavi, N., Spiering, S., Powalla, M., Cavana, B. & Lincot, D. High-efficiency copper indium gallium diselenide (CIGS) solar cells with indium sulfide buffer layers deposited by atomic layer chemical vapor deposition (ALCVD). *Progress in Photovoltaics: Research and Applications* **11**, 437–443 (2003).

108. Hariskos, D., Spiering, S. & Powalla, M. Buffer layers in Cu (In, Ga) Se_2 solar cells and modules. *Thin Solid Films* **480**, 99–109 (2005).

109. Törndahl, T., Platzer, Björkman, C., Kessler, J. & Edoff, M. Atomic layer deposition of $Zn_{1-x}Mg_xO$ buffer layers for Cu(In,Ga)Se_2 solar cells. *Progress in Photovoltaics: Research and Applications* **15**, 225–235 (2007).

110. Serhan, J. *et al.* Electrical characterization of CIGSe solar cells metastability with Zn (S, O, OH)-ZnMgO interface buffer layers. *Solar Energy Materials and Solar Cells* **94**, 1884–1888 (2010).

111. Chang, B. "*Etude de la texturation des couches de ZnO pour des applications aux cellules solaires à base de CIGSe*". Master Thesis, IRDEP (2010).

112. Xu, L., Guo, Y., Liao, Q., Zhang, J. & Xu, D. Morphological Control of ZnO Nanostructures by Electrodeposition. *J. Phys. Chem. B* **109**, 13519–13522 (2005).

113. El Belghiti, H., Pauporté, T. & Lincot, D. Mechanistic study of ZnO nanorod array electrodeposition. *physica status solidi (a)* **205**, 2360–2364 (2008).

114. Mora-Seró, I. *et al.* Determination of carrier density of ZnO nanowires by electrochemical techniques. *Applied physics letters* **89**, 203117 (2006).

115. Hildebrandt, T. Master Thesis, IRDEP (2010).

116. Hubert, C. *et al.* A better understanding of the growth mechanism of Zn(S,O,OH) chemical bath deposited buffer layers for high efficiency Cu(In,Ga)$(S,Se)_2$ solar cells. *physica status solidi (a)* **205**, 2335–2339 (2008).

117. Piekoszewski, J. *et al.* RF-sputtered $CuInSe_2$ thin films. *Solar Energy Materials* **2**, 363–372 (1980).

118. Russell, P. E. Properties of the Mo-$CuInSe_2$ interface. *Applied Physics Letters* **40**, 995 (1982).

119. Matson, R. J. *et al.* Metal contacts to $CuInSe_2$. *Solar Cells* **11**, 301–305 (1984).

120. Shafarman, W. & Phillips, J. Direct current-voltage measurements of the Mo/CuInSe2 contact on operating solar cells. *Photovoltaic Specialists Conference, 1996., Conference Record of the Twenty Fifth IEEE* 917–919 (1996).

121. Wada, T., Kohara, N., Nishiwaki, S. & Negami, T. Characterization of the Cu(In,Ga)Se_2/Mo interface in CIGS solar cells. *Thin Solid Films* **387**, 118–122 (2001).

122. Orgassa, K., Schock, H. W. & Werner, J. H. Alternative back contact materials for thin film Cu(In,Ga)Se_2 solar cells. *Thin Solid Films* **431-432**, 387–391 (2003).

123. Contreras, M. A. *et al.* High efficiency graded bandgap thin-film polycrystalline Cu (In, Ga) Se_2-based solar cells. *Solar energy materials and solar cells* **41**, 231–246 (1996).

124. Malmstrom, J., Lundberg, O. & Stolt, L. Potential for light trapping in Cu(In,Ga)Se_2 solar cells. *Proceedings of 3rd World Conference on Photovoltaic Energy Conversion, 2003* **1**, 344–347 Vol.1 (2003).

125. Malmstrom, J., Schleussner, S. & Stolt, L. Enhanced back reflectance and quantum efficiency in Cu(In,Ga)Se_2 thin film solar cells with a ZrN back reflector. *Applied Physics Letters* **85**, 2634 (2004).

126. Krč, J., Smole, F. & Topič, M. Analysis of light scattering in amorphous Si:H solar cells by a one dimensional semi coherent optical model. *Progress in Photovoltaics: Research and Applications* **11**, 15–26 (2003).

127. Nakada, T., Hirabayashi, Y., Tokado, T., Ohmori, D. & Mise, T. Novel device structure for Cu (In, Ga) Se_2 thin film solar cells using transparent conducting oxide back and front contacts. *Solar energy* **77**, 739–747 (2004).

128. Miyano, T., Hashimoto, R., Kanda, Y., Mise, T. & Nakada, T. Bifacial CIGS thin film solar cells using TCO back contacts. *Technical Digest of the International PVSEC-17, Fukuoka Japan* (2007).

129. Tokado, T. & Nakada, T. Semi-transparent Cu (In_{1-x}, Gax) Se_2 thin film solar cells using an indium tin oxide back electrode. *Photovoltaic Energy Conversion, 2003. Proceedings of 3rd World Conference on* **1**, 539–542 (2003).

130. Rostan, P. J., Mattheis, J., Bilger, G., Rau, U. & Werner, J. H. Formation of transparent and ohmic ZnO:Al/$MoSe_2$ contacts for bifacial Cu(In,Ga)Se2 solar cells and tandem structures. *Thin Solid Films* **480-481**, 67–70 (2005).

131. Anegawa, T., Oda, Y., Minemoto, T. & Takakura, H. Comparison of lift-off processes and rear-surface characterization of Cu(In,Ga)Se_2 thin films for solar cells. *Journal of Crystal Growth* **311**, 742–745 (2009).

132. Minemoto, T., Abe, Y., Anegawa, T., Osada, S. & Takakura, H. Lift-Off Process for Flexible Cu(In,Ga)Se_2 Solar Cells. *Japanese Journal of Applied Physics* **49**, 04DP06 (2010).

133. Würz, R. *et al.* Formation of an interfacial $MoSe_2$ layer in CVD grown $CuGaSe_2$ based thin film solar cells. *Thin Solid Films* **431–432**, 398–402 (2003).

134. Assmann, L. *et al.* Study of the Mo thin films and Mo/CIGS interface properties. *Applied Surface Science* **246**, 159–166 (2005).

135. Bär, M. *et al.* Electronic level alignment at the deeply buried absorber/Mo interface in chalcopyrite-based thin film solar cells. *Applied Physics Letters* **93**, 042110–042110–3 (2008).

136. Weinhardt, L. *et al.* Chemical properties of the Cu(In,Ga)Se_2/Mo/glass interfaces in thin film solar cells. *Thin Solid Films* **515**, 6119–6122 (2007).

137. Wagner, C., Riggs, W., Davis, L., Moulder, J. & Muilenberg, G. Handbook of X-Ray photoelectron spectroscopy. 1979. *Eden, MN Perkin-Elmer Corp., Physical Electronics Division*

138. Alonso, M. I., Garriga, M., Durante Rincon, C. A., Hernandez, E. & Leon, M. Optical functions of chalcopyrite $CuGa_xIn_{1-x}Se_2$ alloys. *Applied Physics A: Materials Science & Processing* **74**, 659–664 (2002).

139. Theodoropoulou, S., Papadimitriou, D., Anestou, K., Cobet, C. & Esser, N. Optical properties of $CuIn_{1-x}Ga_xSe_2$ quaternary alloys for solar-energy conversion. *Semiconductor Science and Technology* **24**, 015014 (2009).

140. Delahoy, A., Chen, L. & Sang, B. Uniform, High Efficiency, Hybrid CIGS Process with Application to Novel Device Structures. (2006).

141. Jehl, Z. *et al.* Thinning of CIGS solar cells: Part II: Cell characterisations. *Thin Solid Films* **519**, Issue 21, pp 7212-7215 (2011).

142. Tipler, P. A. & Llewellyn, R. A. *Modern physics*. (WH Freeman: 2003).

143. Berger, H. Models for contacts to planar devices. *Solid-State Electronics* **15**, 145–158 (1972).

144. Jehl, Z. *et al.* INFLUENCE OF THE SURFACE ROUGHNESS ON CIGS-BASED SOLAR CELL PARAMETERS. 25th EUPVSEC, Valencia, SPAIN (2010)

145. Claesson, Y., Georgson, M., Roos, A. & Ribbing, C.-G. Optical characterisation of titanium-nitride-based solar control coatings. *Solar Energy Materials* **20**, 455–465 (1990).

146. Guillemoles, J. F. *et al.* Solution Processing Route to High Efficiency $CuIn(S,Se)_2$ Solar Cells. *Journal of Nano Research* **4**, 79–89 (2008).

147. Coehoorn, R., Haas, C. & de Groot, R. A. Electronic structure of $MoSe_2$, MoS_2, and WSe_2. II. The nature of the optical band gaps. *Phys. Rev. B* **35**, 6203–6206 (1987).

148. Alkire, R. C. & Kolb, D. M. *Advances in Electrochemical Science and Engineering*. (John Wiley & Sons: 2006).

149. Martínez-Ruiz, A., Moreno, M. G. & Takeuchi, N. First principles calculations of the electronic properties of bulk Cu_2O, clean and doped with Ag, Ni, and Zn. *Solid State Sciences* **5**, 291–295 (2003).

150. Cui, J. & Gibson, U. J. A Simple Two-Step Electrodeposition of Cu_2O/ZnO Nanopillar Solar Cells. *J. Phys. Chem. C* **114**, 6408–6412 (2010).

151. Haller, S. PhD Thesis, IRDEP. (2009-2012).

152. Thomas, G. E. & Stamnes, K. *Radiative transfer in the atmosphere and ocean*. (Cambridge Univ Pr: 2002).

153. Roux, L., Mareschal, P., Vukadinovic, N., Thibaud, J. B. & Greffet, J. J. Scattering by a slab containing randomly located cylinders: comparison between radiative transfer and electromagnetic simulation. *JOSA A* **18**, 374–384 (2001).

154. Goldstein, D. H. *Polarimetric characterization of Spectralon*. (Air Force Research Laboratory, Munitions Directorate: 2003).

155. Siegbahn, Nordling & Fahlman ESCA, atomic, molecular and solid state structure studied by means of electron spectroscopy. at http://cdsweb.cern.ch/record/269524

156. Kumar, S., Gupte, V. & Sreenivas, K. Structural and optical properties of magnetron sputtered $Mg_xZn_{1-x}O$ thin films. *Journal of Physics: Condensed Matter* **18**, 3343 (2006).

Appendix

I) Modeling parameters of the reference solar cell

The parameters used for simulations of a standard CIGSe solar cell are summarized in the following table.

Front contact	flatband : 1 (1: flatband contact imposed; 0: fixed Phi_m value)	
	Recombination velocity Sn [cm/s]	1.00E+07
	Recombination velocity Sp [cm/s]	1.00E+07
	Metal work function (eV)	4.45E+00
	Majority carrier barrier height relative to Ef (eV)	-2.00E-01
	Majority carrier barrier height relative to Ev or Ec (eV)	-5.95E-02
	optical filter	from file

ZnO:Al	Thickness d (μm)	0.4
	Bandgap E_g (eV)	3.5
	Electronic affinity χ (eV)	4.65
	Dielectric permittivity ε_r	9
	Conduction band effective density of state Nc (1/cm^3)	2.2E+17
	Valence band effective density of state Nv (1/cm^3)	1.8E+19
	Electron thermal Velocity v_{thN}	10000000
	Hole thermal Velocity v_{thP}	10000000
	Electron mobility μ_n (cm²/Vs)	100
	Hole mobility μ_p (cm²/Vs)	25
	Acceptor density N_a (1/cm^3)	1
	Donor density N_d (1/cm^3)	1E+20
	Absorption	Numos ZnO
B to B defect	Radiative (cm^3/s)	0
	Auger hole capture coefficient (cm^6/s)	0
Defect	Type (neutral/acceptor/donor)	neutral
	Nt (1/cm^3)	1.77E+16
	cross section e (cm²)	1E-12
	cross section h (cm²)	1E-12
	energetic distribution (single gauss…)	gauss
	level above Ev (eV)	1.65
	Characteristic Energy Wg (eV)	0.1

ZnO:i	Thickness d (μm)	0.07
	Bandgap E_g (eV)	3.3
	Electronic affinity χ (eV)	4.45
	Dielectric permittivity ε_r	9
	Conduction band effective density of state Nc (1/cm^3)	2.20E+17
	Valence band effective density of state Nv (1/cm^3)	1.80E+19
	Electron thermal Velocity v_{thN}	1.00E+07
	Hole thermal Velocity v_{thP}	1.00E+07
	Electron mobility μ_n (cm²/Vs)	1.00E+02
	Hole mobility μ_p (cm²/Vs)	2.50E+01
	Acceptor density N_a (1/cm^3)	1
	Donor density N_d (1/cm^3)	1.00E+17
	Absorption	Numos ZnO
B to B defect	Radiative (cm^3/s)	0
	Auger hole capture coefficient (cm^6/s)	0
Defect	Type (neutral/acceptor/donor)	neutral
	Nt (1/cm^3)	1.77E+16
	cross section e (cm²)	1.00E-12
	cross section h (cm²)	1.00E-12
	energetic distribution (single gauss…)	gauss
	level above Ev (eV)	1.65
	Characteristic Energy Wg (eV)	0.1

CdS	Thickness d (μm)	0.05
	Bandgap E_g (eV)	2.4
	Electronic affinity χ (eV)	4.2
	Dielectric permittivity ε_r	10
	Conduction band effective density of state Nc (1/cm^3)	2.20E+18
	Valence band effective density of state Nv (1/cm^3)	1.80E+19
	Electron thermal Velocity v_{thN}	1.00E+07
	Hole thermal Velocity v_{thP}	1.00E+07
	Electron mobility μ_n (cm²/Vs)	1.00E+02
	Hole mobility μ_p (cm²/Vs)	2.50E+01
	Acceptor density N_a (1/cm^3)	1
	Donor density N_d (1/cm^3)	1.00E+17
	Absorption	Numos CdS
B to B defect	Radiative (cm^3/s)	0
	Auger hole capture coefficient (cm^6/s)	0
Defect	Type (neutral/acceptor/donor)	neutral
	Nt (1/cm^3)	1.77E+17
	cross section e (cm²)	1.00E-13
	cross section h (cm²)	1.00E-13
	energetic distribution (single gauss…)	gauss
	level above Ev (eV)	1.2
	Characteristic Energy Wg (eV)	0.1

CIGSe	Thickness d (μm)	2.5
	Bandgap E_g (eV)	1.15
	Electronic affinity χ (eV)	4.5
	Dielectric permittivity ε_r	13.6
	Conduction band effective density of state Nc (1/cm^3)	2.20E+18
	Valence band effective density of state Nv (1/cm^3)	1.80E+19
	Electron thermal Velocity v_{thN}	1.00E+07
	Hole thermal Velocity v_{thP}	1.00E+07
	Electron mobility μ_n (cm²/Vs)	1.00E+02
	Hole mobility μ_p (cm²/Vs)	2.50E+01
	Acceptor density N_a (1/cm^3)	2.00E+16
	Donor density N_d (1/cm^3)	1
	Absorption	Numos CIGS
B to B defect	Radiative (cm^3/s)	0
	Auger hole capture coefficient (cm^6/s)	0
Defect	Type (neutral/acceptor/donor)	neutral
	Nt (1/cm^3)	1.77E+13
	cross section e (cm²)	5.00E-13
	cross section h (cm²)	1.00E-15
	energetic distribution (single gauss…)	gauss
	level above Ev (eV)	0.6
	Characteristic Energy Wg (eV)	0.1

Back surface field	Thickness d (μm)	0.01
	Bandgap E_g (eV)	1.4
	Electronic affinity χ (eV)	4.3
	Dielectric permittivity ε_r	13.6
	Conduction band effective density of state Nc (1/cm^3)	2.20E+18
	Valence band effective density of state Nv (1/cm^3)	1.80E+19
	Electron thermal Velocity ν_{thN}	1.00E+07
	Hole thermal Velocity ν_{thP}	1.00E+07
	Electron mobility μ_n (cm²/Vs)	1.00E+02
	Hole mobility μ_p (cm²/Vs)	2.50E+01
	Acceptor density N_a (1/cm^3)	2.00E+19
	Donor density N_d (1/cm^3)	1
	Absorption	1.00E+05
B to B defect	Radiative (cm^3/s)	0
	Auger hole capture coefficient (cm^6/s)	0
Defect	Type (neutral/acceptor/donor)	neutral
	Nt (1/cm^3)	1.772E+15
	cross section e (cm²)	5.00E-13
	cross section h (cm²)	1.00E-13
	energetic distribution (single gauss…)	gauss
	level above Ev (eV)	0.6

	Characteristic Energy Wg (eV)	0.1
Back contact	flatband : 1 (1: flatband contact imposed; 0: fixed Phi_m value)	
	Metal work function (eV)	5.4
	Majority carrier barrier height relative to Ef (eV)	0.15
	Majority carrier barrier height relative to Ev or Ec (eV)	0.0335
	Sn [m/s]	1.00E+07
	Sp [m/s]	1.00E+07
	optical filter	reflection from file ($MoSe_2$)

II) Characterization tools

Scanning Electron Microscopy (SEM)

This type of electron microscope, mainly developed in the 60's by Charles Oatley's group based on the work of Max Knoll and Manfred von Ardenne in the 30's, consists in an electron beam scanning the surface to analyze. The interaction with the material leads to re-emission of particles that are detected, allowing a three-dimensional image reconstruction of the surface. The most commonly detected particles are secondary electrons as they allow a precise topography of the surface with very high precision (close to 4 nm) , and back-scattered electron for the analysis of the chemical composition and homogeneity of the surface with a much lower precision (in the order of 1μm). Characteristic X-rays, cathodoluminescence, and transmitted electrons can also be measured, but it is rare that a single machine would have detector for all possible signals.

In this work, the SEM setup used was based on a Leo Supra 35 field emission gun (FEG).

Atomic Force Microscopy (AFM)

This type of microscopy is based on the attraction (Van der Waals)/repulsion (electron cloud) occurring between atoms at a certain distance. The surface to analyze is scanned by a very sharp tip (down to ~10-20 nm) mounted on a micro-lever; the atomic force between the tip and the lever lead to a deflection of the micro-lever according to Hooke's law $F = -kx$ where x is the displacement of the spring end from its equilibrium position, F is the restoring force exerted by the spring on that end and k is a constant called spring constant, which depends on the material used for the micro-lever (typically silicon or silicon nitride). By measuring the deflection of the micro-lever (usually by laser reflection on the micro-lever), it is possible to quantify the interaction between the tip and the surface of the sample to analyze, and thus the topography of the surface. Generally, the lateral resolution of an AFM is in the magnitude of a

few 10^{th} of nanometers, however, the vertical resolution is on the magnitude of the Å, which allows detection of an atomic march on a clean and smooth surface.

In this study, the AFM images are obtained on 50 x 50 mm2 zones with a D3100 microscope and nanoscope IIIa controller, using contact mode with DNP-20 tips (20 nm nominal tip radius).

X-Ray Photoelectron Spectroscopy

X-Ray Photoelectron Spectrometry (XPS) is a widely use surface characterization technique developed in the 60's at the Uppsala University (Sweden) by Kai Siegbahn and his group [155]. This spectroscopic method is based on the photoelectric effect: the sample is irradiated by monochromatic X-ray photons leading to atoms ionization at the surface of the sample. The kinetic energy of the photo-generated electrons is measured; it depends on the binding energy of the electrons following the equation

$$E_{bind} = E_{h\nu} - (E_{kinetic} + \varphi)$$

where E_{bind} is the binding energy of the electron, $E_{h\nu}$ is the energy of the X-ray photons being used, $E_{kinetic}$ is the kinetic energy of the electron (measured in the experimental setup) and φ is the work function of the spectrometer (known). It is possible to plot the number of electrons at each kinetic energy value, i.e. at each binding energy; since each element produces a characteristic set of XPS peaks at characteristic binding energy values, we can identify precisely each elements on the surface of the material. The peak's shape gives informations about the chemical bonding between different elements. The typical analyzed depth is from 8 nm to 12 nm, and all the deeper photo-generated electrons are either recapture by the material or trapped in excited states. The analysis is performed under ultra-high vacuum ($P<10^{-9}$ mbar) since the electron-counting device is almost 1 meter spaced from the analyzed sample.

This quantitative spectroscopic non-destructive technique allows a sharp measurements of the empirical formula of chemical compounds, elemental composition, chemical state and electronic state of the elements within a material.

Electrical Characterization

The J(V) measurements is the most important characterization technique for solar cells. It consists in measuring the current, or the current density, versus an applied voltage, under a specific illumination. When the illumination is the standard A.M. 1.5 illumination, the experimental setup is called a “solar simulator”. A normalized light source illuminates the sample to analyze; the voltage is applied with two needles connected to the front and the back contact respectively, in a range from –0.4 V to +0.8 V for CIGSe typically. Two different needles (in order to avoid parasitic serie resistance) measure the resulting current delivered by the solar cell. Figure 1 is schematic view of an experimental solar simulator device. From this J(V) curve, it is possible to extract the open circuit voltage (V_{oc}), the Fill Factor (FF), the short circuit current (J_{sc}) and so the efficiency (Eff). Series resistance (R_s) and shunt resistance (R_{sh}), along with ideality factor (n) of the diode and dark current (J_0), are also parameters that are accessible with this characterization; however, numerical fitting of the J(V) is needed and measurements in the dark are preferred, as it will be discussed later.

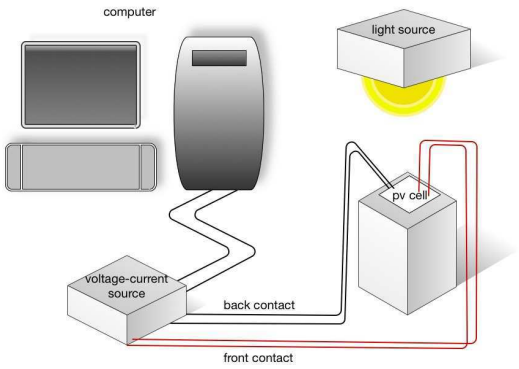

Figure 1. Experimental setup of the IV measurement tool under AM 1.5 illumination

Spectral Response measurements allow to quantify the photon-material interaction depending on the photon energy. In a solar cell, this interaction results in the generation of an electron-hole pair; therefore, by counting the number of generated photons per incident photons at different wavelength (i.e. energies), we measure the Internal Quantum Efficiency of the cell, IQE(λ). Since the solar cell as a specific reflectivity, and the front layer a specific absorption, some photons are lost and does not contribute to the photo-current. As a result, the experimental device measure the External Quantum Efficiency of the cell, EQE(λ). The Spectral Response device we used for this study in a home-made setup; it consists in a source

of polychromatic light, which passes through a monochromator and a chopper, and is focus through an optical fiber directed on the sample to analyze. Two metal needles connected to the front and back contact of the cell measure the extracted current, which is then analyzed with a lock-in technique.

III) State of the art insights for ZnS/(Zn,MgO) deposition

In 2009, two joint publications [48] [47] investigated on the combination of both a CBD deposited ZnS layer and a sputtered $Zn_{1-x}Mg_xO$ layer, in replacement to the standard CdS/ZnO:i bilayer, leading to significant improvements of the efficiency and the stability compared to previous alternative buffer layer solar cells. Reference [48] focuses on the study of the chemical process involved in the deposition of the ZnS layer, along with its compositional and morphology analysis. The deposition process is as follow: co-evaporated CIGSe films [2] are chemically treated in a KCN solution [35]. The ZnS layer is then grown by CBD from aqueous solutions of zinc sulfate (0.1 M), thiourea (0.4 M), and ammonia (1.5 M). The deposition temperature is tested between 60°C and 90°C. The samples are washed in a solution of NH_4OH 1M to avoid an incontrollable precipitation of $Zn(OH)_2$. The solar cells are then completed by sputtered (Zn,Mg)O/ZnO:Al window layer. The $Zn_{1-x}Mg_xO$ layer is deposited by radio-frequency magnetron sputtering. Six different $Zn_{1-x}Mg_xO$ targets are used with different Mg contents of x = 0 (pure ZnO:i), 0.15, 0.22, 0.26, 0.33 and 0.4.

The deposition behavior of the ZnS is studied by calculating the solubility diagrams as a function of the pH, in presence of ammonia and as a function of the temperature (25, 60, 70, 80 and 90 °C). These results are presented in Figure 2. One can notice that regardless of the pH and the temperature, the solubility curves of ZnO and $Zn(OH)_2$ are very close to each other. This means that it may not be easy to deposit either pure ZnO or pure $Zn(OH)_2$ since both species can precipitate together. Moreover, figure 2.a and 2.b show that when increasing the temperature, there is a clear displacement of the solubility region of the three solid phases (ZnS, ZnO and $Zn(OH)_2$) towards lower pH, which means that in the standard deposition conditions ($9<pH<11$ and $T \geq 70°C$), the ZnS deposition implies a significant amount of oxides and hydroxides (see figure 2.b). The influence of the stirring rate on the growth of the ZnS shows a similar behavior to standard CdS. The growth rate is roughly independent from the stirring rate, which indicates that the growth rate of the ZnS is controlled not by a diffusional mechanism but by chemical reactions at the surface of the CIGSe. This is particularly favorable for a large area industrial application.

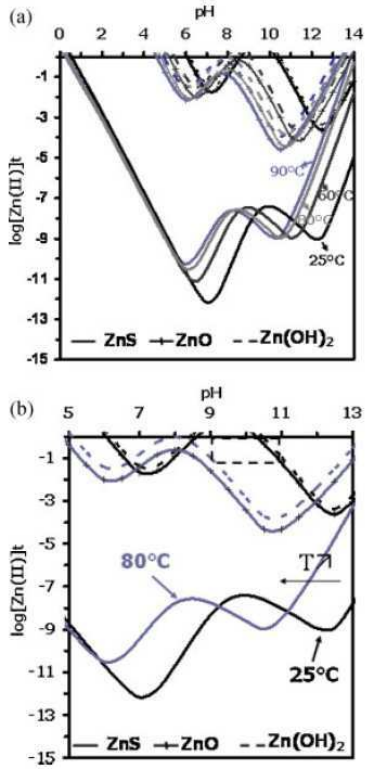

Figure 2. Effect of temperature (T=25°C, T=60°C, T=80°C, and T=90°C) on solubility curves of Zn(II) species in aqueous medium and in presence of thiourea and ammonia as function of pH ($[ZnSO_4]=10^{-1}$ M, $[S^{2-}]=4.10^{-1}$ M, and $[NH_3]=1.5$M) considering ZnS (solid line), ZnO (cross line) and Zn(OH)2 (dashed line). (a) Full diagram. (b) Enlarged view of the CBD-Zn(S,O,OH) deposition region for T=25 and 80°C (the arrow shows the effect of increasing temperature) [48]

The structure of the $Zn_{1-x}Mg_xO$ layers is investigated by XRD measurements. When the Mg concentration is between x = 0 and x = 0.4, the layers exhibit a hexagonal wurzite structure (single phase region); a cubic phase segregation (two phase region) takes place at x between 0.4 and 0.48. which is in good agreement with the reported two phase region observed between x = 0.43-0.55 reported in the literature [156]. With transmission measurements, it is possible to estimate the bandgap of the $Zn_{1-x}Mg_xO$ films extracted from the $[\alpha(E)E]^2$ versus E dependency, where α is the absorption coefficient and E is the photons energy. The bandgap varies linearly with the Mg concentration from $E_g = 3.3eV$ for pure ZnO to a maximum bandgap of $E_g = 4.1eV$ for x = 0.4, which is in good agreement with previous literature [156].

After completing the solar cells with the standard ZnO:Al window layer, the following procedure is applied in order to stabilize the transient effects: the completed cells are post-annealed in air at 200°C for 30 minutes and subsequently light soaked at one sun for 1 minutes at room temperature. The solar cells are then characterized by J-V analysis under A.M. 1.5 illumination, and the photovoltaics parameters are extracted. Figure 3 presents the photovoltaic parameters dependence on the Mg content in the $Zn_{1-x}Mg_xO$ target. We clearly see that the optimum Mg concentration in the $Zn_{1-x}Mg_xO$ buffer is between x = 0.15 and 0.26 with a solar cell efficiency higher than 14%. The cells without Mg (ZnS/ZnO:i buffer) show poor performances mainly because of a limited FF and V_{oc} around 40-50 % and 510 mV-580 mV respectively. For Mg concentration higher than 0.26 (x = 0.33 and 0.4), an increased spread of the results and a strong decrease in average of the parameters is observed.

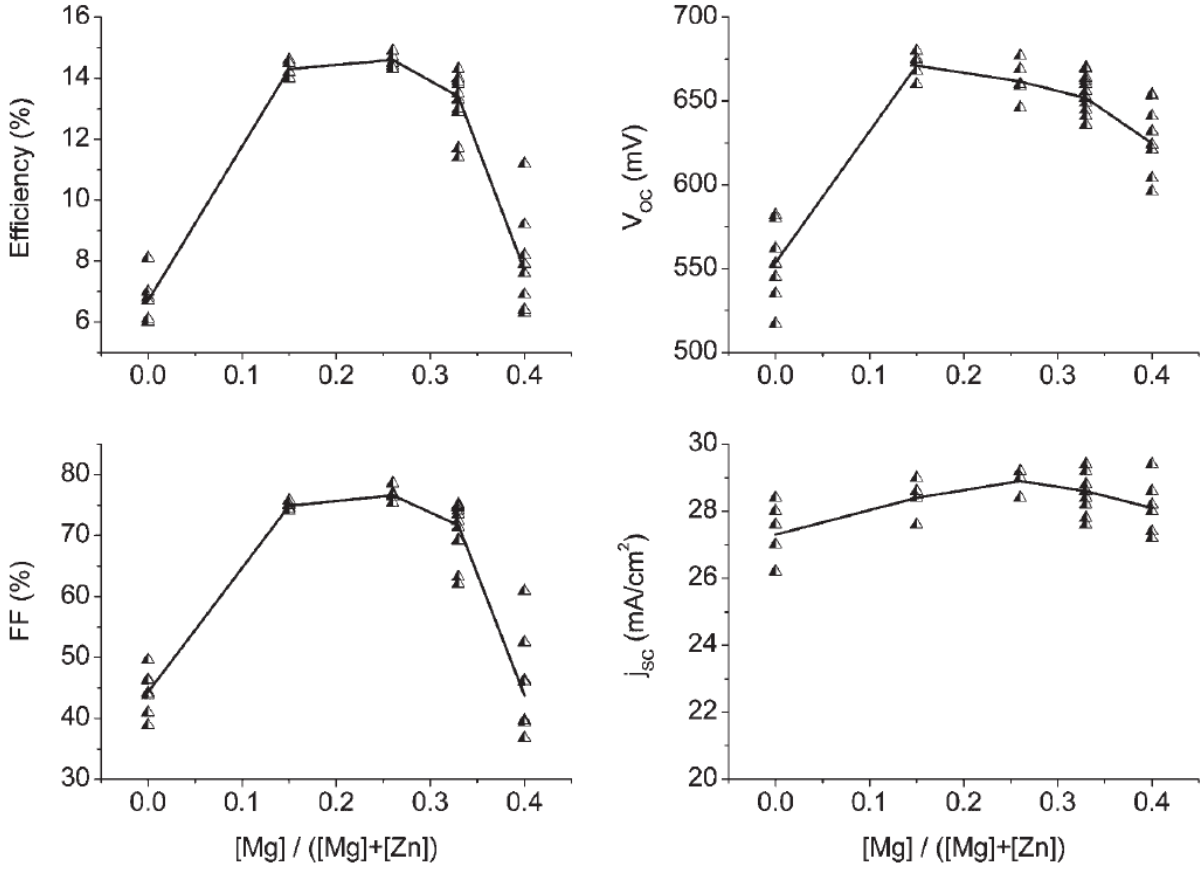

Figure 3. Influence of the Mg concentration on the performances of CIGSe/ZnS/ $Zn_{1-x}Mg_xO$/ZnO:Al solar cells [47]

IV) Optical simulation of a solar cell stack using the radiative transfer equation

*(from Dr. Nir Dahan, Institut d'Optique)

In this section, we show the calculation for a CIGSe slab of thickness d with a specular front interface and diffuse surface on the back reflector. Let us introduce the parameters as in the figure below

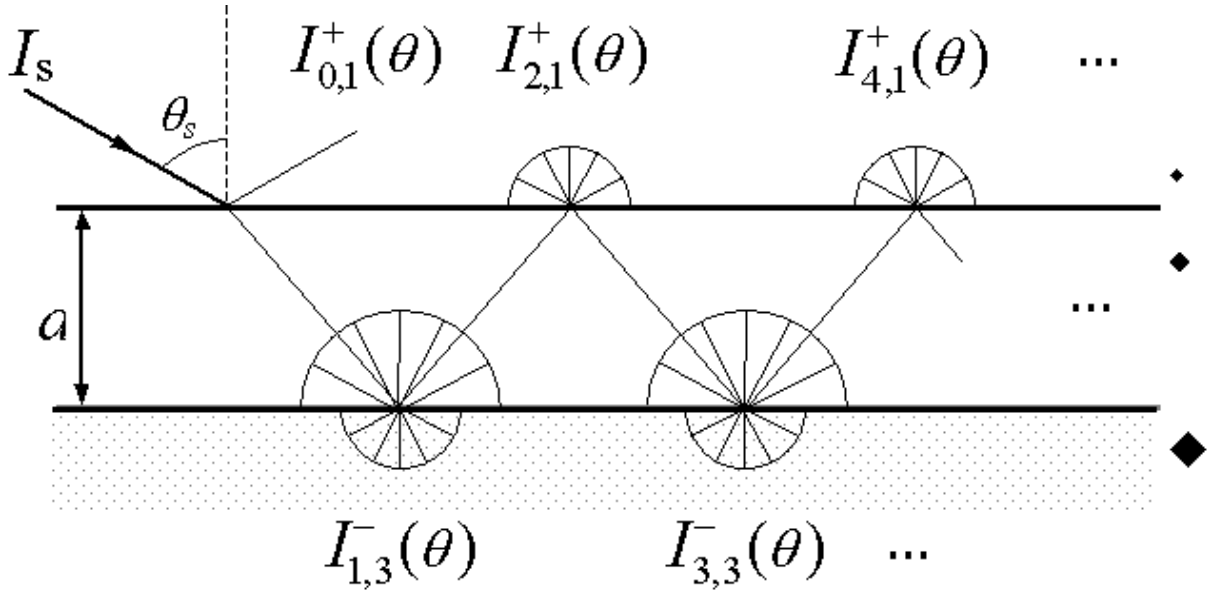

Figure 2. CIGSe slab deposited on white paint (lambertian reflector)

$I(\theta)$ denotes the specific intensity given in units of $\text{Watt}/(m^2 \cdot \mu\text{m} \cdot sr)$, R_F (T_F) the Fresnel's reflection (transmission), and θ is the angle between the direction of the ray and the surface normal. The reflection of the back reflector can be described, in general, by the *bidirectional reflectance distribution function* $\rho(\mathbf{s},\mathbf{s}')$. It relates the reflected intensity $I_r(\mathbf{s})$ in direction $\mathbf{s}$ to the incident intensity $I_{inc}(\mathbf{s}')$ in direction $\mathbf{s}'$ by

$$I_r(\mathbf{s}) = \int \rho(\mathbf{s},\mathbf{s}') I_{inc}(\mathbf{s}') \cos\theta' \, d\Omega'$$

where $d\Omega$ is the solid angle and the integration is over a hemisphere. Herein, we assume that the reflected intensity is isotropic, such that it does not depend on the angle of incident or observation,

$$\rho(\mathbf{s},\mathbf{s}') = \rho_L$$

where ρ_L is the Lambertian reflectivity. The same arguments hold for the transmission τ_L.

In our calculation we make the following assumptions:

- The system is azimuthally symmetric.

- The incident light associated with the solar spectrum AM1.5 is unpolarized.

- The diffuse light reflected or transmitted from the back surface is unpolarized and is not correlated with the impinging light. Therefore, we do not consider interference effects.

According to energy conservation, the absorption in the slab is

$$A = 1 - R_{total} - T_{total}$$

where R_{total} (T_{total}) is the total energy reflected (transmitted) from the slab normalized by the incident energy. Therefore, our aim is to calculate the reflectivity and transmission from the slab.

To follow the rays in the slab, we adopt the notation of radiative transfer equation (RTE) [1,2] using $\mu = \cos\theta$ and $I^{\pm}_{p,\mathrm{l}}$ the intensity in upward direction (+) or downward direction (–) at point p (p = 0, 1, 2, …) in layer l ($\mathrm{l} = 1, 2, 3$). It is interesting to note that although the RTE assumes geometrical optics, it is valid in slab thickness which is comparable to the wavelength scale [3].

The relationship between the intensity and the spectral flux F [units of Watt$/(m^2 \mu\mathrm{m})$] is defined by

$$F^{\pm} = \int I^{\pm}(\mathbf{s}) \cos\theta d\Omega.$$

In our axial symmetry case, we can express the spectral flux as

$$F^{\pm} = \iint I^{\pm}(\mathbf{s})\cos\theta\sin\theta d\theta d\phi = 2\pi\int I^{\pm}(\mu)\mu d\mu$$

where ϕ is the azimuthal angle. The solar intensity is approximately collimated thus it can be written as

$$I_s(\mathbf{s}) = F_s\delta(\mathbf{s}-\mathbf{s}_s)$$

where F_s is the solar flux and $\delta(\mathbf{s}-\mathbf{s}_s)$ is the Dirac δ-function. The spectral flux of the incident intensity is thus

$$F_1^- = \int I_s(\mathbf{s}')\mu' d\omega = F_s\mu_s.$$

The reflected intensity on the front surface (from layer ① to layer ②), at point (0) is

$$I_{0,1}^+(\mathbf{s}) = R_{F12}(\mathbf{s})I_s(\mathbf{s})$$

with a spectral flux

$$F_{0,1}^+ = \int I_{0,1}^+(\mathbf{s}')\mu' d\Omega' = R_{F12}(\mathbf{s}_s)F_s\mu_s.$$

The intensity transmitted into the slab and reaching point (1) is

$$I_{1,2}^-(\mathbf{s}) = T_{F12}(\mathbf{s},\mathbf{s}_s)I_s(\mathbf{s}_s)e^{-\alpha/\mu}\delta(\mathbf{s}-\mathbf{s}_2)$$

where $T_{F12}(\mathbf{s}_2,\mathbf{s}_1)$ is the transmission coefficient on the front interface from layer ① in direction $\mathbf{s}_1$ to layer ② in direction $\mathbf{s}_2$. The relation between $\mathbf{s}_1$ and $\mathbf{s}_2$ is given by Snell's law. The attenuation of the beam intensity is addressed in the exponential term, $\alpha = 2\frac{2\pi}{\lambda}\mathrm{Im}(n_2)d$, with a factor of $1/\mu$ for the actual optical path length of the ray, $\mathrm{Im}(n_2)$ is the imaginary part of the refractive index of layer ②, and λ is the wavelength in vacuum. The reflected light at this point is

$$I_{1,2}^+ = \int \rho_L I_{1,2}^-(\mathbf{s}')\mu' d\Omega' = \rho_L T_{F12}(\mathbf{s}_2,\mathbf{s}_s)F_s\mu_2 e^{-\alpha/\mu_2}.$$

The intensity reaching point (2) is azimuthally symmetric given by

$$I_{2,2}^+(\mu) = I_{1,2}^+ e^{-\alpha/\mu}.$$

The spectral flux emerging from point (2) is therefore

$$F_{2,1}^{+} = 2\pi \int_0^1 T_{F21}(\mu,\mu') I_{2,2}^{+}(\mu')\mu' \, d\mu' = 2\pi I_{1,2}^{+} \int_0^1 T_{F21}(\mu,\mu') e^{-\alpha/\mu'} \mu' \, d\mu'$$
$$F_{2,1}^{+} = 2\pi I_{1,2}^{+} E_T$$

where the integral noted by E_T can be computed numerically. Similarly, the intensity at point (3) is

$$I_{3,2}^{-}(\mu) = I_{1,2}^{+} R_{F21}(\mu) e^{-2\alpha/\mu}$$

$$I_{3,2}^{+} = 2\pi \int_0^1 \rho_L I_{3,2}^{-}(\mu')\mu' \, d\mu' = 2\pi I_{1,2}^{+} \rho_L \int_0^1 R_{F21}(\mu') e^{-2\alpha/\mu'} \mu' \, d\mu'$$
$$I_{3,2}^{+} = 2\pi I_{1,2}^{+} \rho_L E_R$$

Here, the integral is noted by E_R. Following the ray to point (4) the intensity is

$$I_{4,2}^{+}(\mu) = I_{3,2}^{+} e^{-\alpha/\mu}$$

and the associated spectral flux is

$$F_{4,1}^{+} = 2\pi \int_0^1 T_{F21}(\mu,\mu') I_{4,2}^{+}(\mu')\mu' \, d\mu'$$
$$F_{4,1}^{+} = 2\pi I_{3,2}^{+} \int_0^1 T_{F21}(\mu,\mu') e^{-\alpha/\mu'} \mu' \, d\mu' = 2\pi I_{3,2}^{+} E_T$$
$$F_{4,1}^{+} = 2\pi \left(2\pi I_{1,2}^{+} \rho_L E_R\right) E_T .$$

The reflected energy (spectral flux) from the slab is the sum of all the fluxes up-welling from the front interface,

$$F_1^{+} = F_{0,1}^{+} + F_{2,1}^{+} + F_{4,1}^{+} + \ldots$$
$$F_1^{+} = F_{0,1}^{+} + F_{2,1}^{+}(1 + q + q^2 + \ldots)$$
$$F_1^{+} = F_{0,1}^{+} + \frac{F_{2,1}^{+}}{1-q}$$

where $q = \frac{F_{4,1}^{+}}{F_{2,1}^{+}} = 2\pi\rho_L E_R$.

The total reflection from the slab is thus,

$$R_{total} = \frac{F_1^+}{F_1^-} = R_{F12}(\mathbf{s}_s) + \frac{2\pi\rho_L T_{F12}(\mathbf{s}_2,\mathbf{s}_s)e^{-\alpha/\mu_2}E_T}{1-2\pi\rho_L E_R}$$

where the Fresnel reflections or transmissions are computed as an average for both polarizations. Similarly, we calculate the transmission from the slab as

$$T_{total} = \frac{F_3^-}{F_1^-} = \frac{\pi\tau_L T_{F12}(\mathbf{s}_2,\mathbf{s}_s)\frac{\mu_2}{\mu_s}e^{-\alpha/\mu_2}}{1-2\pi\rho_L E_R} \quad .$$

In general, the absorption in the slab is $A = 1 - R_{total} - T_{total}$. However, we assume a perfect Lambertian reflection on the back reflector, i.e., all the incident light is reflected:

$$2\pi\int_0^1 \rho_L \mu d\mu = 1$$
$$\rho_L = 1/\pi \quad (\tau_L = 0).$$

Thus, $T_{total} = 0$ and the absorption at each wavelength reduces to

$$A_\lambda = 1 - R_{total}\big|_{\pi\rho_L=1} = 1 - R_{F12}(\mathbf{s}_s) - \frac{2T_{F12}(\mathbf{s}_2,\mathbf{s}_s)e^{-\alpha/\mu_2}E_T}{1-2E_R},$$

and the integrated absorption shown in the table is calculated by

$$A = \frac{\int_{400}^{1200} A_\lambda I_s(\lambda)d\lambda}{\int_{400}^{1200} I_s(\lambda)d\lambda}.$$

References:

[1] S. Chandrasekhar, *Radiative Transfer* (Dover Publications, Inc. New-York, 1960).

[2] G. E. Thomas and K. Stamnes, *Radiative Transfer in the Atmosphere and Ocean*, (Cambridge University Press, New-York, 1999).

[3] L. Roux, P. Mareschal, N. Vukadinovic, J.-B. Thibaud and J.-J. Greffet, "Scattering by a slab containing randomly located cylinders: comparison between radiative transfer and electromagnetic simulation," J. Opt. Soc. Am. A 18, 374 (2001).